



Doctoral Thesis

Numerical and Experimental Study of a Small Cryogenic Pulsating Heat Pipe

Author

Marcin Opalski

Prepared under a co-tutelle agreement between

Wrocław University of Science and Technology and

Université Paris-Saclay

Under the supervision of

Sławomir Pietrowicz Supervisor

PhD, DSc, Assoc. Prof.

Bertrand Baudouy Supervisor

PhD, DSc, HDR

Wrocław – Paris-Saclay

A	bstra	ıct		V
\mathbf{A}^{\cdot}	bstra	ict in I	Polish - Streszczenie	vi
N	omer	ıclatur	re	vii
1	Inti	roducti	ion	1
	1.1	Backg	round on Pulsating Heat Pipes	1
	1.2	Curre	nt State of Knowledge on Cryogenic PHPs	3
	1.3	Factor	rs influencing on performance of PHP	5
		1.3.1	Working Fluid	6
		1.3.2	Number of Loops	7
		1.3.3	Condenser and Evaporator Design	8
		1.3.4	Diameter	9
		1.3.5	Gravity	10
		1.3.6	Filling Ratio	11
		1.3.7	Limitations of Criterial Numbers	11
	1.4	Summ	nary and Research Gap	12
2	Nııı	morica	l Modeling	14

	2.1	What	is CFD and What Topics Does it Cover	14
		2.1.1	Available Numerical Methods	15
		2.1.2	Multiphase Flow Modeling	17
	2.2	Phase	Change Modeling	19
	2.3	State o	of the Numerical Art	22
		2.3.1	General Approaches to PHP Modeling using CFD Methods	22
		2.3.2	Cryogenic PHP Modeling	23
	2.4	Model	description	24
		2.4.1	Determination of Time Step	28
		2.4.2	Phase Change Modeling	29
		2.4.3	Transport Equation For Void Fraction	31
		2.4.4	Momentum Matrix and Momentum Predictor	33
		2.4.5	Energy Equation	34
		2.4.6	Conjugate Heat Transfer and Turbulence	37
		2.4.7	Momentum Conservation and Pressure Correction	40
	2.5	Model	Validation through Benchmarks	42
		2.5.1	Stefan Problem	42
		2.5.2	Scriven Single Bubble Growth	43
3	Exp	erimer	ntal Test Facility	48
	3.1	Design	Principles in Cryogenics	48
	3.2	Cryoco	poling and Operating Ranges	49
	3.3	Design	of the Experiment	52
		3.3.1	PHP design	52

		3.3.2 Cryocooler Connection and Radiation Shield Design	 	56
	3.4	Selection of Sensors and Measurement Instruments	 	64
	3.5	Condenser Temperature Control	 	67
	3.6	Filling Process	 	71
	3.7	Error Analsyis	 	72
		3.7.1 Uncertainty in Thermal Resistance Measurement \dots	 	72
		3.7.2 Uncertainty in Average Pressure Measurement	 	74
		3.7.3 Filling Ratio Calculation Based on Mass Balance $\ \ldots \ \ldots$	 	74
	3.8	Data Acquisition system	 	81
	3.9	Cooling Process and Temperature Regulation	 	83
4	Exp	perimental Analysis Results		86
	4.1	Experimental Results	 	86
		4.1.1 Nitrogen	 	87
		4.1.2 Argon	 	97
		4.1.3 Neon	 	105
	4.2	Summary of Experiment and Parametric Analysis	 	113
5	CFI	D Analysis Results		122
	5.1	Mesh Independence Study	 	122
	5.2	Numerical Setup and Initialization	 	126
	5.3	Model Limitations	 	129
	5.4	Numerical Results	 	130
		5.4.1 Contour Plots of Representative Fields	 	131
		5.4.2 Quantitative Validation of the Numerical Model	 	135

6	Sun	nmary, Conclusions and Perspectives	162
	6.1	Summary	162
	6.2	Conclusions	164
	6.3	Perspectives	167

Abstract

The dissertation integrates experimental investigations with numerical modeling of pulsating heat pipes (PHP), which are passive heat exchangers without moving parts. The primary objective is to develop a numerical PHP model for cryogenic conditions. The experimental part provides a consistent high-quality reference data set for model validation and extends the description of heat and mass transfer mechanisms at low temperatures. Heat rejection was provided using a two-stage cryocooler with two dedicated thermal interfaces matched to the cold ends of both stages and with radiation shielding that limited parasitic heat fluxes to the cryostat. The campaign covered two inner diameters of the capillary channel, three working fluids, namely neon, nitrogen, and argon, and selected filling ratios. Measurements were carried out over 27.3 to 105 K and the operating window depended on the working fluid. The pressure in the tube and the temperatures in the evaporator and condenser were recorded, enabling the determination of thermohydraulic characteristics complemented by a full uncertainty analysis. The modeling was carried out in OpenFOAM using the Volume of Fluid (VOF) method with the MULES algorithm in a fully compressible formulation with thermophysical properties dependent on temperature and local saturation parameters. In cryogenics, the properties of liquids and vapors depend strongly and non-linearly on temperature and pressure and differ markedly from those of fluids under ambient conditions. Therefore, a compressible approach was adopted with precise property correlations and strict control of mass and energy balances. The phase change was described by the Tanasawa relation and the Hardt and Wondra approach, treated as a mass flux across the phase interface resulting from interfacial kinetics and controlled by superheat or subcooling relative to saturation. The solver includes in-house modifications that are tailored to cryogenic conditions and to the specific operation of PHP. Validation was carried out in stages, from reference tests and benchmarks to comparisons with experimental data. The parametric analyzes covered the effects of the working fluid, the filling ratio and the inner diameter on a prescribed heat flux. The calculations were performed in parallel using an MPI environment, enabling a systematic parameter survey and sensitivity analyzes within the desired turnaround time. The results showed how the choice of fluid, filling ratio, and channel diameter governs PHP operating regimes, thermal resistance, and the evolution of pressure and temperature. Parameter regions that minimize thermal resistance and thresholds for loss of pulsation stability were identified. Comparison of the model with experiments indicated agreement within acceptable error bounds. Recommendations were developed to select the working fluid, diameter, and filling ratio for cryogenic systems, and directions were defined for further model development.

Abstract in Polish - Streszczenie

Rozprawa integruje badania eksperymentalne z modelowaniem numerycznym (CFD) pulsacyjnych rurek ciepła (PHP), które są pasywnymi wymiennikami pozbawionymi elementów ruchomych. Zasadniczym celem jest opracowanie modelu numerycznego PHP dla warunków kriogenicznych. Część doświadczalna dostarcza spójnego i wysokiej jakości zbioru danych referencyjnych do walidacji oraz rozszerza opis mechanizmów cieplnoprzepływowych w niskich temperaturach. Odbiór ciepła realizowano w dwustopniowej kriochłodziarce z dwoma dedykowanymi interfejsami termicznymi dopasowanymi do zimnych końców obu stopni oraz z ekranowaniem promieniowania ograniczającym dopływ ciepła do kriostatu. Kampania objęła dwie średnice wewnętrzne kanału kapilarnego, trzy media robocze neon azot i argon oraz wybrane wartości stopnia wypełnienia. Pomiary prowadzono w zakresie od 27.3 do 105 K, a okno pracy zależało od medium. Rejestrowano ciśnienie oraz temperatury parownika i skraplacza, co pozwoliło wyznaczyć charakterystyki termohydrauliczne uzupełnione pełną analizą niepewności. Modelowanie wykonano w OpenFOAM metodą objętości płynów VOF z algorytmem MULES w ujęciu w pełni ściśliwym i z właściwościami termofizycznymi zależnymi od temperatury oraz lokalnego nasycenia. W kriogenice własności cieczy i pary silnie i nieliniowo zależą od temperatury oraz ciśnienia i wyraźnie odbiegają od mediów w warunkach otoczenia, dlatego przyjęto podejście ściśliwe z precyzyjnymi korelacjami właściwości oraz ze ścisłą kontrolą bilansów masy i energii. Przemiane fazowa opisano relacją Tanasawy oraz podejściem Hardta i Wondry jako strumień masy przez powierzchnię międzyfazową wynikający z kinetyki na granicy faz i zależny od przegrzania lub dochłodzenia względem nasycenia. W solverze wprowadzono autorskie modyfikacje dostosowane do kriogeniki i specyfiki pracy PHP. Walidację prowadzono etapowo od testów referencyjnych i benchmarków do porównań z danymi eksperymentalnymi. Analizy parametryczne objęty wpływ medium roboczego, stopnia wypełnienia i średnicy wewnętrznej przy zadanym strumieniu ciepła. Obliczenia realizowano równolegle w środowisku (MPI), co umożliwiło systematyczny przeglad parametrów oraz analize wrażliwości modelu w pożadanym czasie. Uzyskane wyniki pokazały, jak dobór medium, stopnia wypełnienia i średnicy kanału kształtuje reżimy pracy PHP, opór cieplny oraz przebiegi ciśnień i temperatur. Wyznaczono obszary parametrów sprzyjające minimalizacji oporu cieplnego i progi utraty stabilności pulsacji. Zestawienie wyników modelu z eksperymentem wskazało zakresy zgodne w granicach akceptowalnego błędu. Określono zalecenia doboru medium, średnicy i stopnia wypełnienia dla układów kriogenicznych oraz wyznaczeno kierunki dalszej rozbudowy modelu.

Nomenclature

\mathbf{Symbol}	Meaning	Units
Latin symbo	ls	
t	time	S
x, r	spatial / radial coordinate	m
$V,~\Delta V$	control volume and its measure	m^3
A_f	face area	m^2
\mathbf{S}_f	face area vector	m^2
\mathbf{U}	velocity vector	m/s
p	pressure	Pa
$p_{ m rgh}$	pressure reduced by hydrostatic head	Pa
gh	hydrostatic head	Pa
${f g}$	gravitational acceleration	$\mathrm{m/s^2}$
T	temperature	K
T_e, T_c	evaporator / condenser temperature	K
c_p	specific heat (at constant p)	J/(kgK)
c_v	specific heat (at constant v)	J/(kgK)
k	thermal conductivity	W/(mK)
$\kappa_{ ext{eff}}$	effective thermal conductivity	W/(mK)
q	heat flux	$ m W/m^2$
ϕ	volumetric face flux	m^3/s
ϕ_{lpha}	VOF flux with compression	m^3/s
\dot{m}	interfacial mass flux	$\mathrm{kg/(m^2s)}$
\dot{v}	volumetric phase–change source	s^{-1}
h_{lv}	latent heat of vaporisation	J/kg
M	molar mass	kg/mol
R_g	gas constant	J/(mol K)

Symbol	Meaning	Units
D	thermal diffusivity	$\mathrm{m^2/s}$
D_c	diffusion coeff. in scalar transport	m^2/s
R(t)	bubble radius	m
Co	Courant number	_
GV	inverse capillary–viscous timescale	s^{-1}
rAU	reciprocal of momentum–matrix diagonal	_
S	generic source term	_
J	volumetric mass flux	$\mathrm{kg/(m^3s)}$
d	diameter	m
$T_{\rm sat},\ p_{\rm sat}$	local saturation temperature/pressure	K, Pa
$\hat{\mathbf{n}}_f$	unit normal to interface at face	_
Greek symb	ools	
α	volume fraction	_
ho	density	${ m kg/m^3}$
μ	dynamic viscosity	Pas
ν	kinematic viscosity	m^2/s
σ	surface tension	N/m
ψ	isothermal compressibility	Pa^{-1}
β	relaxation/tuning coefficient	s^{-1}
eta_T	thermal expansion coefficient	K^{-1}
ϵ	turbulent dissipation rate	$\mathrm{m}^2/\mathrm{s}^3$
γ	accommodation coefficient	_
$ au_{\mu}, au_{ ho}$	viscous / capillary timescales	S
ζ	Stefan similarity parameter	_
$\Theta(\cdot)$	Heaviside step function	_
ϕ_r	interface–compression flux	m^3/s
Experiment	-specific symbols	
	41 1	K/W
R	thermal resistance	11/ //
$R \ \hat{R}$	model approximation of thermal resistance	K/W

Symbol	Meaning	${f Units}$
$Q_{\rm cool}$	net heat removed by cryocooler (PID readback)	W
$K_{ m eff}$	effective thermal conductivity (experiment)	$\mathrm{W}/(\mathrm{m}\mathrm{K})$
L_{PHP}	effective conduction length $\frac{1}{2}(l_e + l_c) + l_a$	m
l_e, l_c, l_a	evaporator, condenser, adiabatic segment length	m
A	total cross–sectional area carrying heat	m^2
n	number of capillaries	_
D_i	inner diameter of capillary	m
Bo	Bond number = $g(\rho_l - \rho_v)d^2/\sigma$	_
La	Laplace number = $\rho \sigma d/\mu^2$ (form used in sensitivity study)	_
$\mathrm{Co}_{\mathrm{conf}}$	Confinement number (convenience symbol; distinct from Courant Co)	_
$d_{ m crit}$	critical diameter at $Bo = 4$	m
FR	filling ratio = $V_l/(V_l + V_g)$	%
$V_l,\ V_g$	liquid and vapour volume inside PHP	m^3
V_{PHP}	internal volume of PHP	m^3
$V_{\rm orange}$	buffer-side control volume (supply section)	m^3
$V_{ m blueCryo}$	cryostat segment of feed line	m^3
$V_{ m blueOut}$	ambient segment of feed line	m^3
$V_{ m buffer}$	buffer tank volume	m^3
Δm	gas mass transferred from buffer to PHP during filling	kg
$ar{p}$	time-averaged pressure over analysis window	Pa
T_{cond}	condenser temperature ($Cernox^{\oplus}$)	K
$T_{ m buffer}$	buffer/ambient temperature (PT100)	K
$ ho_l,\; ho_g$	liquid and vapour density (from REFPROP)	${\rm kg/m^3}$
$(\rho c_p)_l, \ (\rho c_p)_v$	liquid and vapour volumetric heat capacity	$J/(m^3 K)$
$\Delta(\rho c_p)$	volumetric heat–capacity contrast $(\rho c_p)_l - (\rho c_p)_v$	$J/(m^3 K)$
u_R	standard uncertainty of R	K/W
$u_{Q_{\mathrm{evap}}}$	standard uncertainty of Q_{evap}	W
$u_{T_e}, \ u_{T_c}$	standard uncertainties of T_e , T_c	K

 $continued\ on\ next\ page$

Symbol	Meaning	Units
$u_{ar{p}}$	standard uncertainty of \bar{p}	Pa
u_V	standard uncertainty of volume	m^3
$u_ ho$	standard uncertainty of density (incl. REFPROP)	${\rm kg/m^3}$
u_{FR}	standard uncertainty of filling ratio	%
$\sigma_{T_e},~\sigma_{T_c},~\sigma_p$	sample st. dev. of T_e , T_c , p	K, K, Pa
N	number of samples in averaging window	_
$K_p,~K_i$	PID gains (proportional, integral)	$-, s^{-1}$
Subscripts ar		
l, v	liquid, vapour	_
1, 2	phase index (VOF)	_
e, c, ad	evaporator, condenser, adiabatic	_
f, s	fluid, solid	_
sat	saturation state	_
lv, vl	${\it liquid} {\rightarrow} {\it vapour} / {\it vapour} {\rightarrow} {\it liquid}$	_
eff	effective (turbulent + molecular)	_
f (suffix)	face—interpolated value	_
*	predicted (uncorrected) field	_

Chapter 1

Introduction

This dissertation focuses on the modeling and analysis of heat and mass transfer in pulsating heat pipes (PHPs) under cryogenic conditions. It is the result of a collaboration between the "Accelerator, Cryogenics and Magnetism Department" of CEA Paris-Saclay associated with the Université Paris-Saclay and Wrocław University of Technology. The thesis combines experimental research with numerical CFD (Computational Fluid Dynamics) analyses to develop a computational algorithm to predict the thermal operating parameters of PHPs. This approach reduces the need for costly and time-consuming experiments, particularly at cryogenic temperatures, and facilitates design optimization. This dissertation also aims to improve the understanding of PHP thermal behavior and enhance their performance in practical applications.

1.1 Background on Pulsating Heat Pipes

As technological advances in low-temperature cooling continue, thermal management systems such as pulsating heat pipes are receiving growing attention. Their ability to transfer heat efficiently, combined with the simplicity of design, ease of implementation and low operating cost, could make them attractive for applications in aerospace, superconducting magnets, or quantum devices, where cryogenic operation is often required. The concept of the PHP was introduced in the early 1990s by Akachi (1). Since then, PHPs have been widely studied thanks to their compact design, which allows them to compete with other passive heat transfer solutions. Being passive, a PHP relies on natural processes—conduction, convection and phase change rather than external power sources such as pumps or fans. In its typical form, a capillary tube is bent into a serpentine shape and partially filled with a working fluid. The device is usually divided into three main

sections: the evaporator, where heat input initiates the vapor formation, the adiabatic zone, which provides a neutral region for fluid oscillations, and the condenser, where heat is removed as the vapor condenses. A schematic of this configuration is presented in Fig. 1.1.

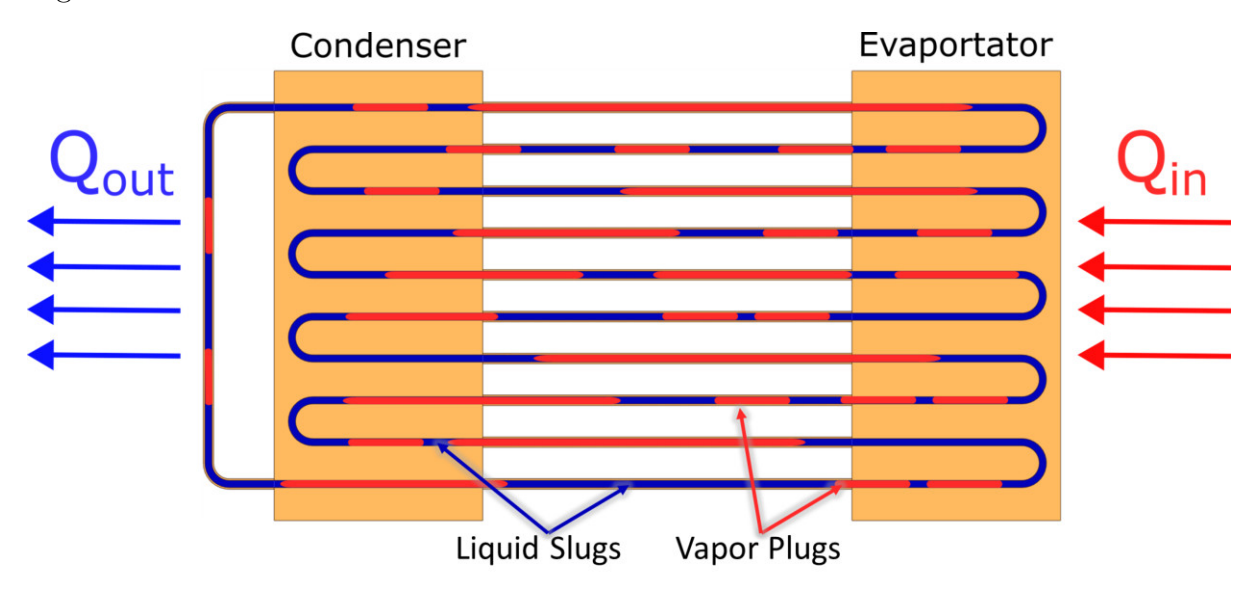


Figure 1.1: Schematic layout of the pulsating heat pipe investigated in the experiments

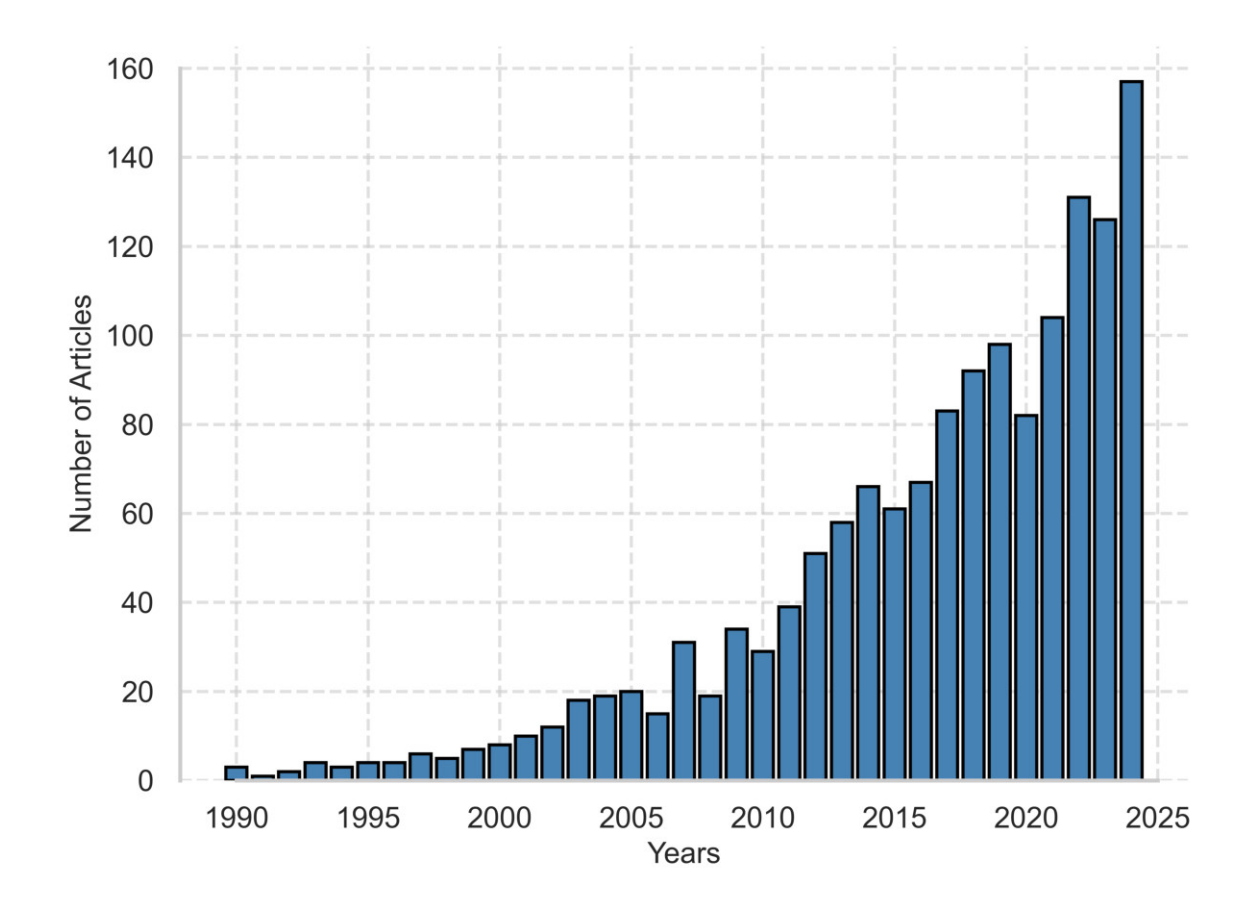


Figure 1.2: Amount of the articles about PHPs over the years

The referenced data indicates not only a growing interest, but also a rising demand for passive heat exchangers. Counting all the research groups working on PHPs would be difficult, yet certain individuals and their teams have made particularly influential contributions.

- M.B. Shafii, in collaboration with Zhang, was among the first to propose lumped and distributed models of PHPs (2; 3). Beyond numerical modeling, he investigated performance enhancement with nanoparticles together with Nazari et al. (4) and explored applications to solar panel cooling in collaboration with Arab et al. (5).
- S. Khandekar was one of the first to link thermal performance with flow structures, providing flow maps in Khandekar et al. (6). He also examined complementary operating parameters in collaboration with Groll (7) and studied the influence of nanofluids on thermal behavior (8).
- M. Marengo, together with collaborators such as M. Mameli, F. Bozzoli and S. Filippeschi, has examined a wide spectrum of PHP behavior. Their research covers zero-gravity cooling applications (9; 10; 11), analyses of fundamental operating mechanisms (12) and the impact of surface properties on performance (13).

The group of S.J. Kim has concentrated on micro-PHPs, with studies addressing a range of factors affecting performance. Examples include the role of geometric parameters (14), the influence of working-fluid selection (15), different manufacturing approaches (16) and investigations of the mechanisms governing micro-PHP operation (17).

V. Nikolayev has contributed extensively to the theoretical description of PHPs. His work includes the development of a dynamic film model for start-up and oscillation dynamics (18), simulations of orientation effects and nonlinear oscillations carried out with Nekrashevych (19) and more recent reviews that consolidate modeling approaches and stability criteria (20).

1.2 Current State of Knowledge on Cryogenic PHPs

When restricting the scope to pulsating heat pipes operating under cryogenic conditions, the number of active research groups is finite and their work can be described in detail. Compared to ambient conditions, interest in cryogenic PHPs has remained limited, largely because of the high entry cost: a laboratory must be equipped with a cryocooler, vacuum chamber and precise low-temperature instrumentation such as temperature and pressure sensors with minimal self-heating and calibration in cryogenic ranges. In addition, the

fabrication of PHPs for cryogenic use requires specialized techniques, including silver brazing of stainless-steel or copper heat interfaces, the use of high-RRR copper for thermal links and careful integration with cold stages, as demonstrated in the following works (21; 22; 23).

The main application that drives most of the international efforts is the cooling of superconducting magnets. Here, the objective is to ensure uniform heat removal and to avoid quenches, i.e., uncontrolled transitions from the superconducting to the normal resistive state, which have been investigated extensively in (24; 25; 26; 27). Other potential applications have been reported as well, including thermal links to cryopanels and cryopumps, as shown in the work of Liang et al. (28) and in a broader perspective, the cooling of cryogenic electronics, infrared detectors, or high-temperature superconducting (HTS) cables and joints subject to AC losses, as highlighted by Mito et al. (29).

At low temperatures, PHPs are therefore regarded as replacements or complements to conventional solutions based on liquid cryogens, including direct immersion, bath cooling, or exchanger-based systems, as well as to copper straps with high RRR values. While liquid cryogens are simple to use, they are logistically demanding and copper straps are heavy, costly and often less efficient in the potential operating ranges of PHPs. Although a wide range of operating principles and configurations has been explored, the number of research groups that have carried out systematic studies on cryogenic PHPs is small. A few laboratories have established continuity in this field, reporting both experimental and numerical results over many years. The most active centers include NIFS in Japan, CAS in China, CEA Saclay in France, and the University of Wisconsin–Madison in the USA. More recently, new contributions have been reported from the University of Zhejiang in China and from the SVNIT Surat in India. Their representative contributions and working fluids are summarized in Table 1.1.

Table 1.1: Cryogenic PHP studies grouped by laboratory, with working fluid, diameter and heat-load range.

Laboratory	Publication	Working fluids	Internal Diameters	Maximal Heat Load
	(23)	N_2	1.5 mm	25 W
	(30)	N_2	1.5 mm	20 W
CEA Society (Evence)	(31)	Ne	1.5 mm	50 W
CEA Saclay (France)	(32)	Ar, N_2 , Ne	1.5 mm	50 W
	(33)	Ne	1.0 mm	18 W
	(34)	Не	1.0 mm	$1.5~\mathrm{W}$
	(22)	N_2	0.5 mm	10 W
	(35)	N_2	0.5 mm	$4.5~\mathrm{W}$
University	(36)	Не	0.5 mm	1 W
Wisconsin–Madison (USA)	(37)	N_2	$1.08~\mathrm{mm}$	20 W
	(38)	Не	0.5 mm	$900~\mathrm{mW}$
	(39)	Не	$0.25,0.4~\mathrm{mm}$	$200~\mathrm{mW}$
	(24)	N_2 , Ne, H_2	1.65 mm	1.5 W
NIEC (Iaman)	(25)	N_2 , Ne, H_2	0.78, 1.58 mm	$1.5~\mathrm{W}$
NIFS (Japan)	(29)	N_2 , Ne, H_2	1.5 mm	10 W
	(40)	Ne	No info.	4 W
	(41)	Ne	0.9 mm	5 W
	(42)	Ne	1.0 mm	36 W
CAS (China)	(28)	N_2	1.0 mm	$12.24~\mathrm{W}$
	(43)	N_2	$1.65~\mathrm{mm}$	$380~\mathrm{W}$
	(44)	N_2	$0.9~\mathrm{mm}$	$32 \mathrm{W}$
	(45)	H_2	0.78, 1.58 mm	9 W
University of Theilers (Chine)	(46)	H_2	2.3 mm	$12 \mathrm{W}$
University of Zhejiang (China)	(47)	H_2	2.3 mm	14 W
	(48)	H_2	2.3 mm	10 W
	(49)	N_2	0.66 mm	300 W
CVNIT Curet (India)	(50)	N_2	1.3 mm	70 W
SVNIT Surat (India)	(51)	N_2	1.3 mm	60 W
	(52)	N_2	1.3 mm	70 W

1.3 Factors influencing on performance of PHP

The operation of pulsating heat pipes depends on a variety of design and operating parameters. In this section, the most relevant factors are reviewed with emphasis on their role under cryogenic conditions.

1.3.1 Working Fluid

The choice of working fluid has a direct and substantial impact on the operation and performance of PHPs. Thermophysical properties such as density, viscosity, surface tension and latent heat govern the oscillation behavior, phase-change dynamics and overall heat transfer efficiency (53). Differences in these parameters can lead to significant variations in oscillation frequency, flow regime stability and thermal resistance (54; 55; 56). Although several studies concerned the impact of individual fluid properties on PHP operation (57; 54), only a few works focused explicitly on cryogenic fluids. The first numerical study addressing cryogenic fluids was conducted by Han et al. (58), who simulated PHPs charged with nitrogen and hydrogen. Their results highlight fundamental differences in heat transfer and oscillation characteristics between cryogenic fluids and ambient-temperature fluids such as water. A second important contribution comes from Barba et al. (32), who examined the effects of thermophysical properties of various cryogenic fluids on the performance of a one-meter-long horizontal PHP. That work focused on argon, complemented by earlier studies on nitrogen (23) and neon (31). The results revealed notable differences in fluid behavior directly linked to their thermophysical characteristics. Neon exhibited dynamic circulation dominated by vapor, with heat transfer occurring mainly through sensible heat in the liquid phase. Nitrogen showed a stronger phase-change-driven heat transfer mechanism, requiring a higher filling ratio for optimal operation. Argon displayed intermediate behavior, with slower fluid motion and mixed heat transfer modes. Experimental studies directly comparing multiple cryogenic fluids under identical conditions are less common. Nevertheless, some works, such as those by Dixit et al. (33; 34), provide valuable insights by testing fluids such as neon and helium within the same PHP setup. These results further show that cryogenic fluids cannot be treated by direct analogy with ambient-condition fluids because they can operate beyond commonly used criterion limits such as critical diameter and therefore must be assessed within their specific operating ranges. In cryogenic applications, the choice of working fluid depends not only on thermal performance but also on the availability of fluids with suitable saturation curves for the target temperature range. Elevated saturation pressures at cryogenic temperatures impose mechanical restrictions on the PHP assembly, particularly on soldered or silver-brazed tube joints, which can hinder stable operation when the allowable internal pressure approaches joint strength or compromises leak tightness. Taking into account these pressure-temperature windows and practical availability, helium, hydrogen, neon, nitrogen, argon, and oxygen constitute the viable set of cryogenic working fluids. Figure 1.3 summarizes their saturation pressure as a function of temperature using REFPROP data (59). The plot reveals two temperature intervals without fluid coverage: between helium and hydrogen and between neon and nitrogen, indicating that, unlike ambient applications, the range of suitable cryogenic working fluids is comparatively narrow.

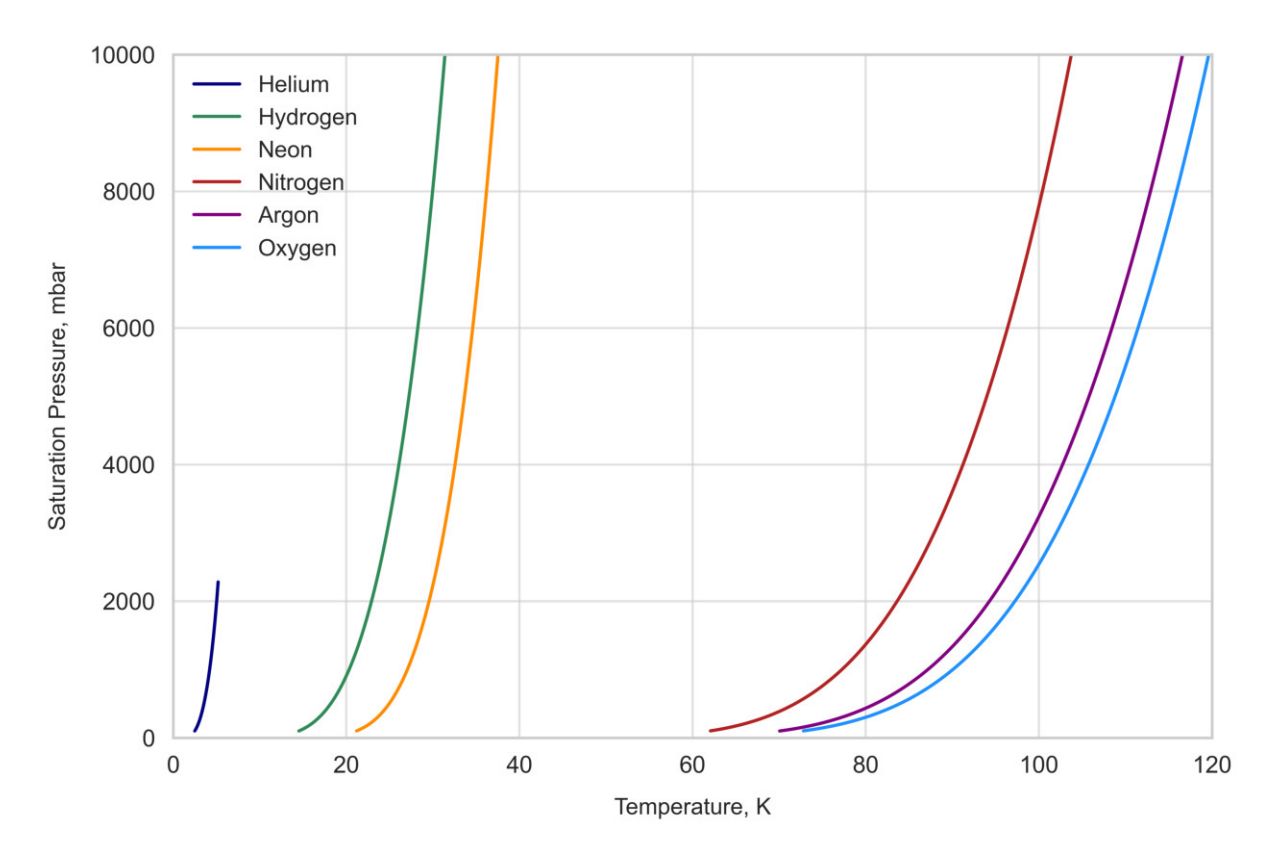


Figure 1.3: Saturation curves for selected cryogenic fluids commonly used in PHPs.

1.3.2 Number of Loops

Only a few studies consider the number of loops N_{loop} as a parameter in a controlled way and report their impact on start-up and sustained operation, especially in the horizontal orientation.

Charoensawan and Terdtoon (60) performed one of the earliest parametric campaigns on closed-loop oscillating heat pipes at ambient conditions, varying N_{loop} alongside working fluid and filling ratio. For horizontal operation, they reported that increasing N_{loop} widens the stable operating range and increases the maximum transportable heat. Following this study, very low turn counts led to intermittent or failed start-up, while higher counts enabled continuous oscillations. Authors conclude that N_{loop} threshold depends on fluid and the filling ratio.

Kammuang-lue et al. (61) examined vertical closed-loop systems with different meander counts and proposed correlations showing that additional turns increase the maximum heat flux and reduce thermal resistance. Although their configuration was not horizontal, the data show the benefit of larger $N_{\rm loop}$.

Noh et al. (62) performed a parametric sweep over N_{loop} and found that adding turns increases the number of active vapor-liquid interfaces where periodic evaporation and condensation couple pressure and volume changes $(p \, dV)$, which in their simulations facilitated the onset and persistence of oscillations and was accompanied by a reduced sensitivity to the chosen initial conditions.

Under cryogenic conditions, Sun et al. (47) compared 2-turn and 5-turn hydrogen PHPs. The 2-turn device showed only partial functionality near horizontal orientation, whereas the 5-turn version achieved stable functioning with lower thermal resistance and higher effective thermal conductivity. Results from Wisconsin (36; 37) on helium and nitrogen support the practical need for multiple turns to maintain oscillations near horizontal orientation, although those works did not sweep N_{loop} systematically.

Taken together, the available evidence indicates that there is no universal "magic number," but horizontal orientation operation generally requires substantially more turns than vertical orientation operation. A conservative design practice emerging from these studies is to avoid very low turn counts and to target higher N_{loop} once the working fluid, diameter and fill are fixed. The precise threshold remains system-dependent and is usually established experimentally, which strengthens the need for a good numerical model.

1.3.3 Condenser and Evaporator Design

Cooling designs based on PHPs vary, especially in the way heat is removed. At ambient temperatures, heat removal methods include Peltier elements (63; 64), natural convection (65), radiative cooling for space applications (66), or forced convection around the capillary (67). In cryogenic systems, the shape of the condenser usually depends on the chosen heat extraction method. An experimentally convenient and research-oriented method immerses the condenser in a liquid cryogen to enforce strong heat removal by pool boiling, as reported by Sagar et al. (68; 51), Jiao (43), and Li et al. (44). However, this approach is generally unsuitable for practical systems because it requires a cryogen supply. For cryogenic applications, however, such immersion essentially corresponds to batch cooling: since liquid cryogen is already required, it is usually more practical to cool the target system directly rather than through an intermediate PHP. In contrast, coupling the condenser to a cryocooler via high-RRR oxidized copper, as in (29; 31; 37), provides a more purposeful application of PHPs as a thermal link. Here, the PHP transfers heat from components that are spatially separated from the cryocooler cold head. This solution enables efficient cooling of distributed loads, reduces the need for bulky high-RRR copper straps and eliminates the operational complexity of handling liquid cryogens. Examples of condenser-heat sink connections and related design considerations, such as the importance of achieving homogeneous temperature across the condenser surface, appear in Dixit et al. (33; 34).

On the evaporator side, the priority is a heat-input interface that can adapt to varied heat-source geometries while enforcing well-posed thermal boundary conditions. Resistive heating wires are also common and Kapton heaters glued to the evaporator plates provide precise control of the evaporator wall temperature. The geometry of the evaporator can also be bent in a more circular form, as in the flower-shaped design proposed by Czajkowski et al. (69) for cooling rotary machines or the radial-rotating design by Jiang et al. (70). In cryogenics, Fonseca et al. (35) developed a configuration wound around a cylindrical surface. From the perspective of numerical modeling and code validation and given the need to simplify PHP to two dimensions, the most practical choice is to use flat plates with Kapton heaters to achieve conditions as close to uniform heating as possible.

1.3.4 Diameter

The inner diameter of a PHP affects flow resistance, capillary forces and the prevailing flow regimes. In cryogenic applications, maintaining a slug/plug flow regime is particularly challenging because of the lower surface tension and higher density ratio typical of cryogenic fluids (32). The Bond number, defined by

Bo =
$$D_i \sqrt{\frac{g(\rho_l - \rho_v)}{\sigma}}$$
 (1.1)

is commonly used to assess whether surface tension forces dominate over gravity. For a PHP to sustain oscillations in the slug/plug flow regime, the Bond number generally needs to remain below a threshold identified by Khandekar (7) (commonly reported as Bo < 4). However, in cryogenic PHPs the Bond number is not always a reliable indicator, as shown by Dixit et al. (33) for helium and Natsume et al. (25) for neon, thus constraining the maximum allowable PHP's diameter. In addition to this upper bound, the inner diameter must also satisfy a lower limit to avoid excessive frictional resistance. Qu et al. (71) proposed, based on experimental correlation, that the minimum critical diameter is governed by the balance between surface tension and inertial forces, expressed as

$$0.7\sqrt{\frac{\sigma}{(\rho_l - \rho_v)g}} \le D_i. \tag{1.2}$$

This relation defines the lower diameter limit, ensuring that viscous losses do not suppress oscillations. Together with the upper bound imposed by the Bond number, these constraints delimit the feasible diameter range for stable slug/plug flow. Within this range, the diameter strongly influences PHP performance. Smaller diameters enhance capillary confinement and stabilize liquid slugs, but increase viscous resistance and restrict nucleate boiling, which degrades thermal performance (72; 3). Larger diameters reduce flow resistance and facilitate circulation, yet weaken capillary action and promote liquid stratification under gravity, eventually suppressing the slug/plug regime (73). Experiments show that excessively small channels limit heat transfer capacity, whereas overly large ones lead to fluid accumulation and the loss of oscillations (57). In cryogenic PHPs, this optimization is even more delicate because density and surface tension vary sharply with temperature, shifting both the Bond number threshold and the viscous—capillary balance. As experimental data are often scarce or unavailable, diameter selection cannot rely solely on such correlations, showing the need for modeling, since the Bond number is not a reliable indicator under cryogenic conditions.

1.3.5 Gravity

Gravity is one of the primary factors influencing the operation of PHPs. It directly affects momentum exchange in the system by producing a pressure gradient that must overcome viscous forces and surface tension. Although the fluid mass inside the capillaries is relatively small, gravity assists in returning the condensate to the evaporator, thereby sustaining oscillatory motion, as shown by Gu et al. (74; 75). A higher number of loops often correlates with more reliable oscillations, partly because the system is less sensitive to gravity (10). The role of gravity also appears explicitly in the momentum conservation equation, discussed in Sections 2.4.4 and 2.4.7, where the body force term $\rho \mathbf{g}$ acts in the direction of gravity. At the same time, surface tension counteracts gravity by preventing gravitational draining of the liquid toward the bottom of the pipe, thereby preserving the slug/plug structure. Experimental studies confirm this theoretical influence. Many researchers have examined the impact of inclination on PHP performance (76; 77; 78; 79; 80) and Lyu et al. (81) extended these investigations to cryogenic temperatures. Changing the orientation from horizontal to vertical often reveals that gravity improves heat transfer by directing condensate more effectively toward the evaporator. Research under zero-gravity or microgravity conditions is much less common (82; 83; 84), but such experiments fundamentally differ from inclined setups by removing the gravitational body force. As a result, uneven liquid distribution and local film drying can occur, thereby reducing performance. To mitigate these effects, some investigators introduced check valves to maintain a preferred flow direction (83; 85; 86), stabilizing oscillations even at unfavorable orientations. Overall, the cited studies confirm the importance of gravity in sustaining oscillations and enhancing PHP performance.

1.3.6 Filling Ratio

The filling ratio (FR) is one of the main factors influencing how PHPs work. It is the fraction of the total pipe volume occupied by the liquid phase, with the remaining space filled by vapor. The formula defining the filling ratio is shown in Eq. (3.1):

$$FR = \frac{V_l}{V_t} \cdot 100\% \tag{1.3}$$

where V_l is the liquid volume and V_t is the total volume.

A too-small filling ratio leaves insufficient liquid to form stable slugs, reducing phase-change activity and thinning liquid films around vapor bubbles (72; 3). Too high a ratio restricts vapor space, weakens oscillations and lowers heat transfer capacity (72). In addition, the filling ratio directly influences the amount of enthalpy exchanged and thus the latent heat that can be effectively utilized during oscillations. No universal optimum exists, as the effect of FR depends strongly on geometry, fluid properties and operating conditions. Empirical correlations, such as that of Shafii et al. (87), are calibrated for the specific geometries and operating conditions of their experiments and thus have limited transferability beyond those set-ups. Numerous experimental studies in cryogenic working fluids, ranging from helium to argon (33; 25; 31; 23; 36; 37; 41; 42), consistently confirm the critical role of the filling ratio, while also showing that its optimal value is highly system-dependent. Despite this progress, thermal performance of PHPs cannot yet be predicted solely from FR. These observations motivate the present thesis, which will experimentally present the coupling between filling ratio, geometry and fluid properties in cryogenic PHPs within a defined configuration and operating window.

1.3.7 Limitations of Criterial Numbers

Although dimensionless numbers such as Bond, Jakob or Kutateladze provide physical intuition, their predictive power for PHP operation remains limited. Thresholds proposed in the literature (e.g., Bo < 4 (7; 88), Ku \approx 1 (89; 90)) are not universal and often fail under different working fluids or geometries. For instance, cryogenic studies report stable oscillations even when the Bond number exceeds the classical criterion (33; 34; 25), while small-diameter PHPs have shown contradictory lower bounds (71; 53). Similarly, Jakob

number trends can invert depending on whether sensible or latent heat dominates (91; 92) and Kutateladze-based predictions of dryout vary across configurations (93; 94). These inconsistencies indicate that no single criterial number can serve as a universal design rule. What remains informative is the qualitative balance between capillarity and gravity, between sensible and latent heat, and between applied and critical heat flux. However, any thresholds are strongly configuration-dependent and sensitive to geometry and filling ratio. Consequently, most existing correlations should be regarded as heuristic rather than predictive. The complexity of PHP dynamics instead calls for systematic experimental databases and validated numerical models to capture coupled effects beyond what single dimensionless numbers can provide (32).

1.4 Summary and Research Gap

The literature proves that PHPs represent a promising passive technology for thermal management in cryogenics. Their compactness, absence of moving parts and ability to operate without liquid cryogens make them suitable for applications ranging from superconducting magnets to cryogenic electronics. Despite these advantages, several limitations persist:

- The internal two-phase dynamics of PHPs remain poorly understood, particularly the coupling between oscillation regimes, filling ratio and geometry at cryogenic temperatures.
- Experimental investigations, though valuable, are restricted by the high entry cost of cryogenic infrastructure and the difficulty of ensuring reproducible operating conditions.
- Classical design criteria based on dimensionless numbers such as Bond, Jakob or Kutateladze are not universal under cryogenic conditions and often fail to predict operational thresholds.
- While some simplified models exist, no computational framework has been validated that consistently integrates cryogenic property variations, compressibility effects and phase-change dynamics in PHPs.
- Most published experiments concern medium- or large-scale PHPs. Multi-loop cryogenic PHPs, which would require limited computational resources and thus provide an accessible benchmark for model validation, are largely missing from the literature.

• There is no comprehensive dataset that jointly maps thermal performance against filling ratio, working fluid and channel diameter under identical conditions. Such systematic data would not only support the validation of the present model but could also serve as a reference for future numerical developments by other groups.

These gaps motivate the present dissertation. To address them, this work combines experiments on a dedicated multi-loop PHP with the development of a CFD framework for phase-change flows, specifically adapted to cryogenic conditions. The experimental results not only provide direct validation of the numerical predictions but also extend the database of cryogenic PHP performance. At the same time, the diversity and limitations of available experimental studies clearly indicate that systematic numerical modeling is indispensable for consolidating understanding and guiding design. The following chapter therefore reviews existing CFD approaches to PHPs, outlining the state of the art and positioning the present methodology within that context.

Chapter 2

Numerical Modeling

One of the main challenges when it comes to implementing PHP technology in complex cooling systems is the lack of understanding of fluid behavior inside PHP. Despite relatively well described know-how, including fluid selection, number of bends and dimensions, it is difficult to predict the overall performance that will be achieved. This makes PHP modeling highly demanded, as it allows for accurate performance predictions. Using various modeling approaches, the thermal performance of PHPs can be predicted, leading to more efficient and reliable designs. In modeling pulsating heat pipes, the approaches can essentially be divided into two branches, one-dimensional models and higher-dimensional models based on CFD techniques (20). To model the mechanisms of a pulsating heat pipe, it is necessary to mathematically describe the following physical phenomena: multiphase flow, evaporation, condensation, turbulence, heat transfer, and optionally conjugate energy transfer between the fluid and the solid.

2.1 What is CFD and What Topics Does it Cover

Computational Fluid Dynamics is a branch of fluid mechanics that uses numerical methods to analyze and simulate fluid flow and its interactions with the surrounding environment. The development of CFD as a scientific discipline is closely related to advances in computer technology. This connection stems from the fact that the description of fluid motion relies on the Navier-Stokes equations, which remain unsolved in their general analytical form. The greatest challenges in this field include accurately modeling turbulence and addressing the computational demands of large-scale domains, which require continuous improvements in computational power. A major milestone in the evolution of CFD was in the late 1980s, with the emergence of commercial software such as Flu-

ent, STAR-CD, and COMSOL. These tools made CFD more accessible to engineers and industries by integrating advanced numerical solvers into user-friendly platforms. The increasing availability of powerful computing resources further facilitated the adoption of CFD in various sectors. Today, CFD is commonly used as a design tool in industries such as aerospace, energy, and automotive engineering. It is used to optimize designs, enhance performance, and reduce energy consumption.

2.1.1 Available Numerical Methods

To describe the transport of momentum or energy, it is necessary to consider the underlying transport mechanisms. Whether transporting energy or momentum, the fundamental principles remain similar and are governed by two main processes, advection and diffusion. The equations describing these phenomena can be divided into two parts. The left-hand side represents the effects or outcomes of the transport mechanisms, while the right-hand side represents their sources. For the energy equation, the effects are typically expressed as changes in the temperature field, while the sources may arise from radiation, phase change, or heat generation. In the case of momentum transfer of fluids, sources include viscous interactions, pressure gradients, or surface tension effects. The generalized form of the advection equation is presented in Eq. (2.1).

$$\frac{\partial \theta_i}{\partial t} + \nabla \cdot (\theta_i \mathbf{u}) = \nabla \cdot (D_c \nabla \theta_i) + S$$
(2.1)

where θ_i is the transported quantity, **u** is the velocity vector, D_c is the diffusion coefficient, and S represents the source terms.

To solve the advection equation (2.1), it is necessary to discretize the spatial domain. Operations on field operators, such as gradient and divergence, require the spatial division of the domain to enable the discretization of conservation equations. One of the simplest methods for this purpose is the Finite Difference Method (FDM). This approach divides the computational domain into a grid of points, allowing derivatives to be approximated at these discrete locations. FDM is particularly well-suited for describing diffusive phenomena and one-dimensional problems. In such cases, flux continuity across cell boundaries is not a concern, as the method does not operate on cells but calculates values directly at points. For example, the advection equation on a structured grid in the x direction may be discretized using a central-difference scheme for the spatial terms together with a forward-Euler time integrator, as shown in Eq. (2.2).

$$\frac{\theta_i^{n+1} - \theta_i^n}{\Delta t} + \mathbf{u}_i \cdot \frac{\theta_{i+1}^n - \theta_{i-1}^n}{2\Delta x} = D_i \frac{\theta_{i+1}^n - 2\theta_i^n + \theta_{i-1}^n}{\Delta x^2} + S_i^n$$
 (2.2)

Another method for solving the advection equation is the Finite Element Method (FEM). In this approach, the balancing of the equation is performed at the mesh nodes. FEM approximates the finite element space of partial differential equations by interpolating the unknown function using a set of so-called basis functions. These functions are used to calculate derivatives and facilitate modeling of geometries and domains. FEM uses a weak form of the governing equations, with test functions w. The weak form of the advection equation is provided in Eq. (2.3) decomposing the computational domain, while the discrete algebraic system presented in (2.4) provides the basic input for the numerical solvers.

$$\int_{V} \frac{\partial \theta_{i}}{\partial t} w \, dV + \int_{V} (\theta_{i} \mathbf{u}) \cdot \nabla w \, dV = \int_{V} D_{i} (\nabla \theta_{i} \cdot \nabla w) \, dV + \int_{V} Sw \, dV \tag{2.3}$$

$$\mathbf{M}\frac{d\theta_{\mathbf{i}}}{dt} + \mathbf{K}_a \theta_{\mathbf{i}} = \mathbf{K}_d \theta_{\mathbf{i}} + \mathbf{F}, \tag{2.4}$$

where \mathbf{M} is the mass matrix, \mathbf{K}_a is the advection matrix, \mathbf{K}_d is the diffusion matrix and \mathbf{F} is the source vector.

The Finite Volume Method (FVM) is widely regarded as the most optimal and efficient approach for fluid dynamics simulations. In this method, scalar values are assigned to control volumes, while vector quantities are associated with the faces of these volumes. FVM is based on the integral form of the governing equations, ensuring the conservation of fluxes across the boundaries of each control volume. FVM leverages the divergence theorem, which transforms differential equations into their integral form as in Eq. (2.5).

$$\int_{V} \frac{\partial \theta_{i}}{\partial t} dV + \int_{\partial V} (\theta_{i} \mathbf{u}) \cdot \mathbf{n} dA = \int_{\partial V} D_{i} (\nabla \theta_{i} \cdot \mathbf{n}) dA + \int_{V} S dV$$
 (2.5)

The discretization of flux terms across the faces of control volumes yields the form expressed in Eq. (2.6)

$$\frac{\Delta V(\theta_i^{n+1} - \theta_i^n)}{\Delta t} + \sum_f (\theta_{if} \mathbf{u}_f) \cdot \mathbf{n}_f A_f = \sum_f D_i (\nabla \theta_i)_f \cdot \mathbf{n}_f A_f + S \Delta V$$
 (2.6)

The mathematical advantage of FVM over methods such as FEM or FDM lies in its inherent conservation properties. FVM ensures that the flux leaving one control volume

enters the adjacent one, as expressed in Eq. (2.7). This property guaranties both global and local conservation more efficiently, making FVM the optimal tool for modeling flow phenomena. In contrast, FDM does not inherently ensure flux conservation, often leading to numerical artifacts in flow simulations.

$$\int_{\partial V_1} (\theta_i \mathbf{u}) \cdot \mathbf{n} \, dA + \int_{\partial V_2} (\theta_i \mathbf{u}) \cdot \mathbf{n} \, dA = 0$$
 (2.7)

2.1.2 Multiphase Flow Modeling

To model the flow inside a PHP, an algorithm that accounts for the two-phase flow is required. In two-phase flow terminology, the boundary between phases is referred to as the interface, which must be accurately captured. The four most commonly used methods for interface tracking in multiphase flow are the Lattice Boltzmann Method (LBM) (95), the Level Set Method (LSM) (96), the Euler-Euler Method (EE) (97), and, according to the Scopus database, the most widely adopted, the Volume of Fluid Method (VOF) (98).

The LBM differs fundamentally from classical continuum-based approaches as it relies on a kinetic model of particle transport on a discrete grid rather than directly solving the Navier-Stokes equations (99). Although LBM has been successfully applied to multiphase flow problems, it is not conventionally used for interface tracking simulations in capillary-driven flows due to difficulties in handling large density ratios and surface tension effects (100). Although some implementations exist in dedicated software such as Palabos and MOOSE, they are not natively supported in OpenFOAM, ANSYS Fluent, or CFX.

The EE model is used in cases where the exact shape of the interface is not required, such as in modeling dispersed flows, chemical reaction kinetics (101), or classical heat pipes (102). A distinctive feature of this method is the use of separate velocity fields for each phase, which are balanced independently in the mass conservation equation, as depicted by Eq. (2.8).

$$\frac{\partial(\alpha_k \rho_k)}{\partial t} + \nabla \cdot (\alpha_k \rho_k \mathbf{u}_k) = \dot{m}_k \tag{2.8}$$

Since EE methods do not explicitly resolve the phase boundary, additional closure models for interfacial forces and phase interactions are required (103). This limitation makes the approach less suitable for capturing capillary-driven flows, where precise interface tracking and liquid film dynamics are obligatory (104). Among the interface tracking methods,

the level set method (LSM) provides a smooth representation of the interface through a scalar level set function $\varphi(x, y, z, t)$ defined as the signed distance to the interface. The phase boundary is the zero level set, $\varphi = 0$, while by convention $\varphi > 0$ denotes liquid and $\varphi < 0$ denotes gas. The level-set field evolves according to the transport equation in Eq. (2.9).

$$\frac{\partial \varphi}{\partial t} + \mathbf{u} \cdot \nabla \varphi = 0 \tag{2.9}$$

A major drawback of the LS method is that it does not inherently conserve mass. The level-set function may become distorted as a result of numerical diffusion, leading to mass loss over time. To counteract this issue, a re-initialization procedure is employed as in Eq. (2.10).

$$\frac{\partial \varphi}{\partial \tau} + \operatorname{sgn}(\varphi_0) \left(|\nabla \varphi| - 1 \right) = 0 \tag{2.10}$$

where τ is an artificial time variable introduced solely for the correction of φ (105). This additional step increases the computational cost of the method and requires a fine grid resolution to maintain interface accuracy. In complex geometries, this requirement poses significant challenges for the application of the LS method to PHP simulations (106).

The VOF method represents a compromise between the interface resolution provided by the LS method and the computational cost of EE. It describes phase motion using a volume fraction function, sometimes referred to as a color function. As in previous methods, phase transport follows the advection equation as depicted in Eq. (2.11).

$$\frac{\partial \alpha}{\partial t} + \nabla \cdot (\alpha \mathbf{u}) = 0 \tag{2.11}$$

Unlike the LS method, where the interface is implicitly defined by a level-set function, the VOF method interpolates the phase boundary, which is conventionally identified at $\alpha = 0.5$. Here, $\alpha = 0$ corresponds to the liquid phase, while $\alpha = 1$ represents the gas phase or another immiscible fluid. A key advantage of the VOF method is that it strictly enforces mass conservation, in contrast to the LS method, which suffers from volume loss due to numerical diffusion (107). However, the VOF method relies on interface reconstruction algorithms, such as Piecewise Linear Interface Calculation (PLIC), to improve the sharpness of the interface, which introduces additional numerical complexity (98). In the context of PHP modeling, the VOF method is preferred over the LS method due to its mass-conserving capacity and its ability to handle complex

interfacial deformations. However, the VOF method also has limitations. High-interface curvature regions are prone to numerical diffusion, which can affect the accuracy of phase distribution and heat transfer predictions (108). Based on the trade-offs presented, the VOF method was chosen as a numerical model in this work.

2.2 Phase Change Modeling

Several approaches exist to describe the mass transfer between phases at the interface. One of the earliest and most fundamental formulations is the Hertz-Knudsen model, derived from kinetic gas theory. This model comes from the work of Hertz (109) and Knudsen (110), who studied the rate of evaporation and condensation in rarefied gasses. It expresses the net mass flux at the interface as a function of local vapor pressure differences, as presented in Eq. (2.12).

$$\dot{m} = \alpha \rho_v \sqrt{\frac{M}{2\pi R_g T_{\text{sat}}}} \left(p_{\text{sat}} - p_v \right) \tag{2.12}$$

Here, α represents the accommodation coefficient, which accounts for the fraction of vapor molecules that undergo a phase change upon collision with the liquid surface. The equation also includes the local vapor density ρ_v , the molar mass of the fluid M, and the gas constant R_g . The term $(p_{\text{sat}} - p_v)$ defines the driving force for phase change, where p_{sat} is the saturation pressure at the interface and p_v is the local vapor pressure.

The Hertz–Knudsen model (109; 110) provides an expression for interfacial mass transfer and is widely used in theoretical studies, particularly at very low pressures where gasphase collisions are infrequent and kinetic-theory assumptions remain valid. However, in practical applications, such as PHPs operating at higher pressures or temperatures, deviations from the behavior of ideal gasses often require empirical corrections. Building on this foundation, Schrage (111) further developed the formulation incorporating molecular backcollisions through the accommodation coefficient γ in conjunction with a kinetic-theory description of velocity distributions. This refinement improves the estimate of net mass flux by accounting for the probability that vapor molecules return to the interface. Eq. (2.13) exemplifies the net mass flux of the Schrage model,

$$\dot{m} = \frac{2\gamma}{2 - \gamma} \left(\frac{M}{2\pi R_g}\right)^{\frac{1}{2}} \rho_v h_{lv} \frac{T_{lv} - T_{\text{sat}}}{T_{\text{sat}}^{3/2}},\tag{2.13}$$

where γ is the accommodation coefficient, representing the fraction of vapor molecules that contribute to the phase change process, ρ_v is the local vapor density, h_{lv} is the latent heat of vaporization, T_{lv} is the temperature of the vapor phase near the interface and $T_{\rm sat}$ is the saturation temperature.

The Schrage model (111) is more complex and precise than the Hertz-Knudsen formulation (109; 110) because it accounts for molecular back-collisions and gas-phase velocity distributions. It is particularly relevant when the interfacial Knudsen number departs from the free-molecular limit under transitional or near-continuum conditions, rather than strictly at very low pressures. However, because it relies on kinetic theory assumptions, the Schrage model may require an empirical modification of the accommodation coefficient γ in real applications, such as PHPs. In such cases, additional correction factors or hybrid approaches that incorporate experimental data may be necessary to obtain realistic phase-change rates. In the context of VOF-based PHP modeling, these kinetic-theory closures guide interfacial mass transfer, where sharp phase boundaries and interface dynamics are resolved with high fidelity. Their direct implementation can be computationally costly, which motivates simplified engineering closures such as the Lee model (112) or semi-empirical formulations such as Tanasawa (113) to reduce costs while maintaining controllable accuracy. For practical engineering applications, simpler empirical models are often preferred due to their low computational cost, resulting from the absence of dense mesh requirements and their ease of implementation in CFD solvers. One of the most widely used formulations is the Lee model (112), which describes the mass transfer rate as linearly dependent on the temperature difference, as detailed in Eq. (2.14),

$$\dot{m} = \beta \rho_l \frac{T - T_{\text{sat}}}{T_{\text{sat}}},\tag{2.14}$$

where β is an empirical coefficient that controls the phase change rate. The Lee model (112) is particularly well-suited for numerical simulations involving large computational domains, as it ensures numerical stability while still capturing the overall thermal behavior of the system. However, because of its simplified nature, this model does not account for interfacial molecular dynamics which may introduce non-physical smearing of the phase boundary in cases where precise interface tracking is required and requires iterative tuning of the β parameter.

A modification of models based on the kinetic gas theory is the Tanasawa model (113), which introduces an empirical correction factor to improve agreement with the experimental data. The mass flux in the Tanasawa model is expressed in Eq. (2.15),

$$\dot{m} = \frac{2\gamma}{2 - \gamma} \frac{h_{fg}}{\sqrt{2\pi R}} \rho_v \frac{T_v - T_i}{T_v^{3/2}},\tag{2.15}$$

where γ is an empirical factor that represents the fraction of molecules that participate in phase change. The Tanasawa model (113) provides improved accuracy in boiling and film condensation, but requires experimental calibration to determine appropriate values for γ under different operating conditions.

For high-fidelity simulations where local temperature gradients and phase fraction variations significantly influence the dynamics, phase change models based on temperature gradients provide an improved representation of the slope of the thermophysical properties interface. One such approach is the Nichita-Thome model (114), which accounts for the interaction between temperature and volume fraction gradients as presented by the Eq. (2.16),

$$\dot{m} = -\frac{\nabla \alpha_l \cdot \nabla T}{h_{\text{evap}}} k_{\text{eff}}, \tag{2.16}$$

where $\nabla \alpha_l$ represents the gradient of the liquid volume fraction, and k_{eff} is the effective thermal conductivity. This model has been shown to enhance numerical stability and accuracy in VOF-based PHP simulations, particularly in cases where phase change occurs in a nonequilibrium regime with significant thermal gradients.

The selection of an appropriate phase change model in VOF-based PHP simulations depends on the required balance between physical accuracy and computational efficiency. Models derived from kinetic theory, such as Schrage (111) and Hertz-Knudsen (109; 110), provide a precise solution of the mass transfer mechanism at the phase interfaces. Empirical approaches, such as the Lee (112) or Tanasawa (113) models, offer a numerically improved alternative. Meanwhile, gradient-based models, such as the Nichita-Thome formulation (114), introduce additional physics that improve interface tracking and heat transfer prediction. In the context of PHPs, where phase change and interfacial dynamics drive the overall system behavior, the choice of model is particularly important. Models such as Schrage (111) and Hertz-Knudsen (109; 110) may be suitable for low-pressure conditions or simulations that employ dense meshes in simplified geometries. The Lee model (112) remains a practical choice for large-scale computations. However, the Tanasawa model (113) is the most appropriate for accurately capturing phase change dynamics under a wide range of thermal and pressure conditions. Its empirical formulation provides a balance between accuracy and computational feasibility, making it especially suitable for simulations where the modeling of mass transfer at the interface is highly demanded

under moderate mesh resolution, as encountered in PHP modeling.

2.3 State of the Numerical Art

2.3.1 General Approaches to PHP Modeling using CFD Methods

One of the first articles on CFD-based modeling of PHP was by J. Wang et al. (115; 116; 117; 118; 119). They used the VOF technique in ANSYS Fluent, implementing the Lee phase change model (112) with an incompressible flow assumption. Their research covered diverse geometries and operational parameters:

- Different ratios of evaporator to condenser lengths (115)
- Corrugated walls in the evaporator, adiabatic, and condenser regions, combined with varying fill ratios and heat loads (116)
- Three-dimensional single-loop PHPs with various bending configurations (117)
- Surfactant addition and the degree of wetting in the PHP (118; 119).

For validation, these studies referred to Saha et al. (120), whose simple and transparent single-loop setup facilitated flow visualization and quantitative comparison.

Pouryoussefi and Zhang (121; 122; 123) also used the VOF method with Lee's model in ANSYS Fluent to study closed-loop PHP filled with water and ethanol. Their focus was on chaotic flow behavior and finding operating parameters for optimal thermal efficiency. Of these works, (121) stands out for validating numerical results against experiments and performing error analysis. Vo et al. (124) extended this to multi-loop transparent PHPs. Despite using a relatively coarse mesh, they noted good convergence with experimental temperature data, endorsing the feasibility of 3D CFD for complex geometries.

Li et al. (125; 126) were similarly validated against Saha (120), examining microencapsulated materials for start-up improvements (125) and the impact of altering the lengths of the evaporator, condenser, and adiabatic part (126). Xie et al. (127) contrasted rightangle and semicircular bends, testing multi-heat source inputs that reportedly enhanced PHP stability. Blasiak and Opalski et al. (128; 67) explored the influence of several phase change models (Lee (112), Tanasawa (113), Xu (129), and Kafeel-Turan (130)) and highlighted the importance of conjugate heat transfer between fluid and solid walls. Their experiments used particle image velocimetry in a transparent section and focused on the analysis of the fluid structure inside with high convergence with their own experimental data.

Another category of research focuses on the influence of working fluids. W.-W. Wang et al. (131) tested nanofluids in a quartz-glass PHP, allowing full-flow visualization. W.-W. Wang et al. (131) reported a strong alignment between numerical simulations and experiments. Choi and Zhang (132) used OpenFOAM with a modified Lee model (130), analyzing asymmetric geometries, but without direct experimental validation in that particular work and with nonphysical temperature changes.

Meanwhile, the number of turns in PHP remains critical with regard to performance. Mucci et al. (133) explored the effect of loop count on stability, indicating that multiple loops can mitigate local dryouts. Dreiling et al. (134) investigated a transparent PHP with two turns from Mameli's experiment (135), examining the sensitivity of flow patterns to phase-change relaxation coefficients in the Lee model (112). D. Zhang et al. (136) studied PHPs with five loops of varying diameters, examining how filling ratio affected the start-up behavior. Although their numerical velocity-field comparisons were qualitative due to an opaque test section, they noted that assuming laminar flow may elevate temperature peaks in the model.

2.3.2 Cryogenic PHP Modeling

Cryogenic PHPs pose additional complexity due to large variations in fluid properties, potential compressibility, density changes, and complex and expensive lab benches. Sagar et al. (137; 50) pioneered the CFD analysis of a cryogenic PHP, focusing on the role of the filling ratio. Their simulations used ANSYS Fluent, accompanied by power spectral density and autocorrelation function analyzes. However, they validated against Pouryoussefi et al. (122), who studied PHPs at room temperature. Singh et al. (138) instead referred to cryogenic data for validation by comparing their results with the experiments of Sagar (68). However, this comparison was limited to very low heat inputs 1–4 W, where the system had not even reached a steady state regime, putting into question the consistency of the claimed agreement.

Yang et al. (139) modeled a five-loop hydrogen PHP following Sun et al. (47) and reported a mean absolute percentage error of approximately 5% for thermal resistance and about 20% for the pressure over time averaged under matched heat loads. Reporting quantitative errors for both thermal and pressure quantities in a single study is uncommon, as most validations focus on thermal performance or present pressure only qualitatively.

However, Yang et al. did not clarify the computation of hydrogen properties or non-saturated states. Bu et al. (140) focused on nitrogen flow structures for about 10 seconds, comparing them qualitatively to Shi et al. (141). B. Singh and Atrey (142) extended Mameli's 1D model (135), showing close alignment with Fonseca's cryogenic experiments (35), albeit for a single test scenario. Such studies underscore the potential of cryogenic modeling but also highlight gaps, such as short simulation times, limited validation conditions, and reliance on ambient data for verification.

From a broader perspective, experiments with straightforward geometries are favored for model calibration and validation in cryogenic PHPs. Simple or single-loop designs reduce computational overhead and permit finer spatial resolution across the capillary width, which is beneficial for capturing swift temperature and phase transitions. Sagar et al. (51; 52) and Shi et al. (141) are examples of such efforts. The former approach includes thermal performance metrics, while the latter emphasizes flow visualization.

Although many researchers adopt ANSYS Fluent for PHP simulations, open-source platforms like OpenFOAM offer several advantages, including transparent source code and direct access to numerical routines. Choi and Zhang (132) showed that OpenFOAM can handle complex phase change modifications, while Blasiak and Opalski (128; 67; 143) used it effectively for PHPs at room temperature with multiple phase change models. However, there has been limited attention to cryogenic conditions in OpenFOAM, which can involve compressibility and large property gradients. To fill this gap, a fully compressible solver adapted to cryogenic environments was created.

2.4 Model description

The model is developed based on OpenFOAMv2106. Its earlier versions were developed and described in the work of Opalski and Błasiak (128; 67). Initially, the model was adapted to ambient conditions and allowed the prediction of flow behavior in systems where the thermophysical properties of the liquid exhibited minor variations between the evaporator and the condenser. Subsequently, the model was extended to fully account for compressibility, as discussed in (143), and the Lee phase change model was enriched with an adaptive coefficient. In that version, the phase-change rate was coupled to temperature-dependent thermophysical properties via an adaptive time scale, without explicit kinetic dependence on the pressure departure from saturation or on the interfacial area. Although this formulation is computationally efficient, it remains physically simplified because the interfacial mass flux is not derived from a kinetic relation. Therefore, in the present work, a physically consistent formulation based on the Tanasawa

approach (113) is employed, in line with recent trends in boiling modeling proposed by Scheufler and Roenby (144) and by Municchi et al. (145; 146). The model relies on the VOF method, which distinguishes three types of volumetric cells in the computational domain: vapor, liquid, and interface cells. In the case of a PHP, these correspond to gas-filled segments, liquid slugs, and interfacial regions that separate them. A graphical representation of this concept is shown in Fig. 2.1.

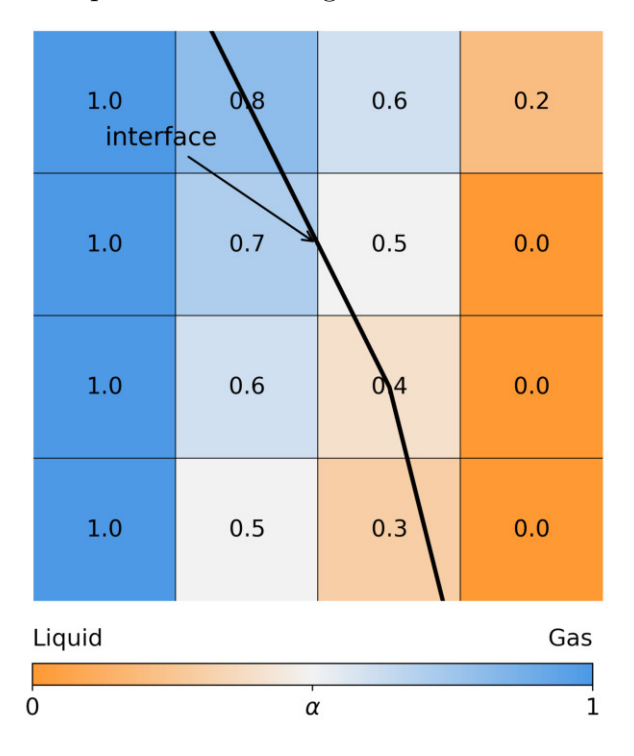


Figure 2.1: Schematic representation of phase distribution in the Volume of Fluid method applied to a pulsating heat pipe.

The main limitation of the quoted models is that they do not account for partial local condensation in subcooled liquid regions, as discussed, for example, in (147). The frameworks developed by Scheufler and Roenby (144), as well as Municchi et al. (145; 146), consider only evaporation processes. This effect is explicitly addressed in the present implementation through localized modeling. The general structure of the numerical algorithm is illustrated in Fig. 2.2, and each branch of the flowchart is explained in detail in the subsequent sections of this work.

The algorithm begins with field initialization. Data types include volScalarField for spatial scalar fields such as temperature, pressure or density, scalar for uniform scalar quantities such as time or model coefficients, volVectorField for volumetric vector fields such as velocity, and surfaceScalarField for surface-interpolated fluxes such as ϕ , representing the volumetric flow rate across cell faces. The createFields routine also includes a block to update the thermophysical properties.

Immediately after initialization, temperature-dependent volScalarField values are as-

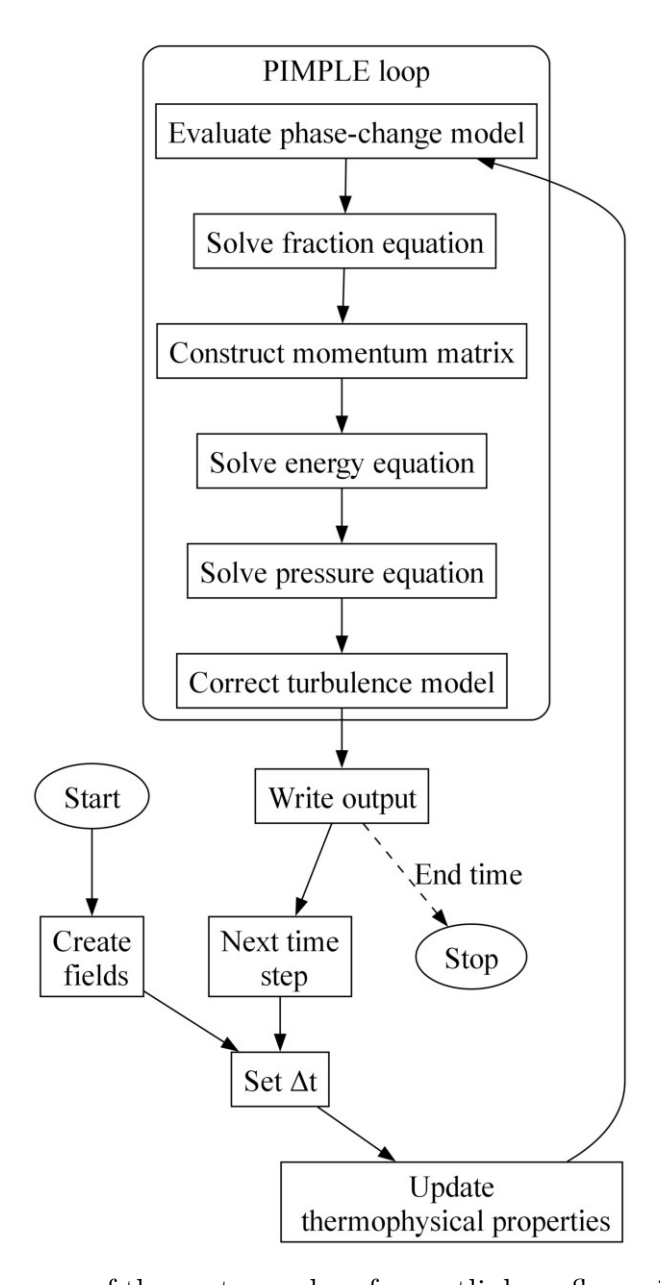


Figure 2.2: Block diagram of the custom solver for mutliphase flow with the phase change

signed to various thermodynamic properties, including phase fraction, pressure, and temperature. All properties are computed using third-order polynomial fits based on data retrieved from the REFPROP database (148). A notable feature of the model is the introduction of compressibility ψ to describe the sensitivity of density to pressure and temperature variations. The compressibility is formally defined by Eq. (2.17)

$$\psi = \frac{1}{\rho} \frac{\partial \rho}{\partial p} \bigg|_{T}. \tag{2.17}$$

Under dynamic conditions, where pressure varies with time, the density evolution for each phase i is

$$\frac{\mathrm{d}\rho_i}{\mathrm{d}t} = \rho_i \psi_i \frac{\mathrm{d}p}{\mathrm{d}t}.\tag{2.18}$$

Since the system operates not only along the saturation line but also in the regions of superheated vapor and subcooled liquid, the description must be correspondingly extended. The complete implementation of compressibility in the momentum equation, which includes the thermal response of density expressed through compressibility, is presented later in Eq. (2.63). However, in the case of the phase-fraction equation, the resulting density is based on the updated mixture density, computed using the volume-fraction-weighted interpolation, as shown in Eq. (2.19),

$$\rho = \alpha_1 \rho_1 + \alpha_2 \rho_2. \tag{2.19}$$

To illustrate the necessity of including compressibility effects, a comparison between the compressibility of liquid nitrogen, as a representative cryogenic fluid and liquid water is presented in Fig. 2.3. This approach was chosen because, unlike under ambient conditions, where liquids are often assumed to be incompressible, cryogenic fluids exhibit significantly higher compressibility even in the liquid phase. Moreover, cryogenic gasses substantially deviate from ideal gas behavior, as evidenced by the nonlinear shape of the density curve shown in Fig. 2.3. Therefore, neglecting compressibility in the evolution of density would lead to significant errors in terms of momentum and mass conservation.

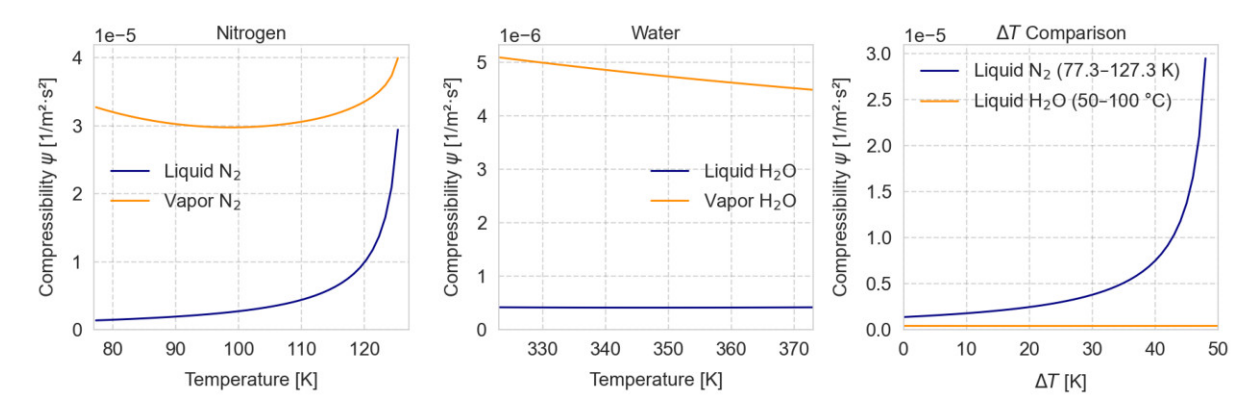


Figure 2.3: Comparison of the compressibility of nitrogen and water (59). Left: compressibility of nitrogen, middle: compressibility of water, right: comparison of compressibility of liquids in function of temperature gradient.

Correct modeling of PHP requires a clear assumption of the saturation state and the ability to handle local saturation conditions that vary in space. In the current model, the local saturation pressure $p_{\rm sat}$ is calculated based on the local temperature field using a third-order polynomial fit. In contrast, the saturation temperature $T_{\rm sat}$ is determined from the local pressure field via the inversion of the same polynomial relationship. This

dual approach allows for the definition of sub-cooled liquid and superheated vapor regions within the domain while maintaining flexibility with respect to non-equilibrium effects. The phase-change source terms are therefore driven by the deviation from local saturation conditions, without assuming immediate thermodynamic equilibrium. All temperature-dependent properties are evaluated locally based on the phase-specific values and the local volume fraction. For example, the interpolation of density across the phases is given by Eq. (2.19). The only exception to this interpolation scheme is the specific heat capacity at constant pressure, c_p , which must preserve the consistency of enthalpy across the mixture. It is thus computed using a mass-weighted formulation:

$$c_p = \frac{c_{p_1}\rho_1\alpha_1 + c_{p_2}\rho_2\alpha_2}{\rho_1\alpha_1 + \rho_2\alpha_2}. (2.20)$$

2.4.1 Determination of Time Step

The time step Δt is determined based on two complementary stability criteria, the classical Courant (Co) condition and the Galusinski-Vigneaux (GV) condition (149). The Courant number quantifies the ratio between the numerical and physical domains of dependence. Its maximum value across the domain is calculated using Eq. (2.21),

$$Co_{\max} = \frac{1}{2} \cdot \max\left(\frac{|\phi_i|}{V_i}\right) \cdot \Delta t, \tag{2.21}$$

where ϕ_i is the volumetric flux across face i, V_i is the volume of the associated control volume, and Δt is the time step. The mean Courant number is defined analogously as

$$Co_{mean} = \frac{1}{2} \cdot \frac{\sum_{i} |\phi_{i}|}{\sum_{i} V_{i}} \cdot \Delta t.$$
 (2.22)

Although the Courant number accounts for advective transport, it does not capture surface-tension-driven dynamics that are present in two-phase flows. To address this, the Galusinski–Vigneaux (GV) criterion introduces two timescales:

$$\tau_{\mu} = \frac{\mu \cdot \Delta x}{\sigma}, \quad \tau_{\rho} = \sqrt{\frac{\rho \cdot \Delta x^3}{\sigma}},$$
(2.23)

where μ is the dynamic viscosity, σ is the surface tension, and Δx is the local mesh size. These timescales represent the characteristic viscous and capillary response times of the interface. The resulting GV time step restriction is given by Eq. (2.24).

$$\Delta t \le \left[\frac{1}{0.5 \left(C_2 \tau_\mu + \sqrt{(C_2 \tau_\mu)^2 + 4C_1 \tau_\rho^2} \right)} \right], \tag{2.24}$$

where $C_1 = 0.01$ and $C_2 = 10.0$ are the empirical constants of the Galusinski-Vigneaux criterion (149), chosen following the recommendations of (150).

Compared to the Courant condition alone, the GV criterion offers enhanced stability control in two-phase simulations. By explicitly incorporating viscous and capillary effects at the phase interface, the dynamic adjustment of the time step is facilitated in regions where surface tension is strongest. This prevents the onset of interfacial instabilities that would otherwise go undetected by purely advective criteria. This approach has been used mainly among CFD researchers who develop their own numerical code (151; 152). The final time step is selected as the most restrictive of the two conditions, providing numerical stability with respect to both convective transport and surface-tension-dominated interfacial dynamics under the following assumption:

$$\Delta t = \min\left(\frac{\text{Co}_{\text{target}}}{\text{Co}_{\text{max}}}, \frac{1}{\text{GV}_{\text{max}}}\right).$$
 (2.25)

2.4.2 Phase Change Modeling

Phase-change mass transfer is implemented using a two-stage approach. In the first stage, raw source terms are evaluated based on the physical expression derived from the Tanasawa formulation (113). In the second stage, these raw sources are redistributed using the Hardt-Wondra method (153) to improve spatial localization and enhance numerical stability near the phase interface. The net interfacial mass flux is expressed as a function of local deviations from saturation conditions and is proportional to the magnitude of the phase-fraction gradient, which serves as an approximation of the interfacial area per unit volume. To account for asymmetries in the spatial distribution of liquid and vapor, two normalization coefficients, N_l and N_v , are used. In the implemented code, these coefficients correspond to the contributions of the liquid side and the vapor side to the total interfacial area. They are defined in Eq. (2.26),

$$N_{l} = \frac{\int |\nabla \alpha_{1}| \, dV}{\int |\nabla \alpha_{1}| \, \alpha_{1} \, dV}, \qquad N_{v} = \frac{\int |\nabla \alpha_{1}| \, dV}{\int |\nabla \alpha_{1}| \, (1 - \alpha_{1}) \, dV}. \tag{2.26}$$

In Eq. (2.26), $|\nabla \alpha_1|$ is used to approximate the density of the local interfacial area. In the VOF method, the liquid-vapor interface is not sharply resolved but is instead diffused

over several computational cells. Within this diffuse region, the phase fraction $\alpha_1 \in [0, 1]$ and the gradient $\nabla \alpha_1$ point normally to the interface. Consequently, its magnitude is non-zero only in interfacial cells and provides a consistent measure of the surface area distribution (153; 154). This allows the mass-source terms to dynamically adapt to the evolving topology of the two-phase boundary. The resulting raw mass source from the modified Tanasawa (113) derivation for evaporation (2.27) and condensation (2.28) is then given below.

$$\dot{m}_{\text{evap}} = \frac{2\gamma}{2 - \gamma} \cdot \frac{h_{\text{evap}}\rho_2}{\sqrt{2\pi R T_{\text{sat}}}} \cdot \frac{T - T_{\text{sat}}}{T_{\text{sat}}} \cdot \Theta(T - T_{\text{sat}}) \cdot \Theta(p_{\text{sat}} - p) \tag{2.27}$$

$$\dot{m}_{\rm cond} = \frac{2\gamma}{2 - \gamma} \cdot \frac{h_{\rm evap}\rho_2}{\sqrt{2\pi R T_{\rm sat}}} \cdot \frac{T - T_{\rm sat}}{T_{\rm sat}} \cdot \Theta(T_{\rm sat} - T) \cdot \Theta(p - p_{\rm sat}) \tag{2.28}$$

Here, $T_{\rm sat}$ and $p_{\rm sat}$ are the local saturation values, $h_{\rm evap}$ is the local latent heat of vaporization, and $\gamma = \Delta t$ represents the value of the dimensionless time step, commonly described as the accommodation coefficient.

To enhance numerical stability and suppress spurious currents, the raw source terms are diffused using the Hardt-Wondra method. This is achieved by solving a Poisson-type equation (Eq. (2.29)) for an auxiliary smoothed field ψ_{HW} :

$$\psi_{HW} - \nabla \cdot (D_{\psi} \nabla \psi_{HW}) = \dot{m}_{\text{evap}} + \dot{m}_{\text{cond}},$$
 (2.29)

where D_{ψ} is a diffusion coefficient that controls the extent of the smoothing region, with a value of $1 \times 10^{-10} \,\mathrm{m}^2$ as applied by Kunkelmann and Stephan (154). The resulting field ψ_{HW} is then reprojected onto the interfacial region using the phase fraction α_1 and a predefined cutoff threshold of the void fraction ϵ , yielding the final expression for the applied source term in (2.30).

$$\dot{m}_{HW} = \begin{cases} -N_v (1 - \alpha_1) \psi_{HW} & \text{if } \alpha_1 < \epsilon \\ +N_l \alpha_1 \psi_{HW} & \text{if } \alpha_1 > 1 - \epsilon \\ 0 & \text{otherwise} \end{cases}$$
 (2.30)

This two-step formulation preserves the physical structure of the phase-change model while eliminating spurious numerical peaks in the vicinity of the interface. The diffusion step regularizes sharp gradients in the raw mass source terms, which could otherwise destabilize the solution or distort the interface geometry.

2.4.3 Transport Equation For Void Fraction

In order to calculate the distribution of the phases, the proposed algorithm solves a transport equation for the liquid volume fraction α_1 , discretized as a conservative scalar advection equation extended with an interface compression term and volumetric phase-change source terms (150). The convective fluxes are constructed using the volumetric field ϕ , and interface compression is applied using a supplementary flux ϕ_r , which acts in the direction normal to the phase interface. This additional compression term counteracts numerical diffusion and improves interface sharpness in the diffuse VOF formulation. It is expressed in Eq. (2.31),

$$\phi_r = \phi_c \left(\vec{S}_f \cdot \hat{n}_f \right), \tag{2.31}$$

where \vec{S}_f is the face area vector, and \hat{n}_f is the unit normal vector to the interface, computed from the normalized gradient of the phase fraction field in Eq. (2.32):

$$\hat{n}_f = \frac{\nabla \alpha_1}{|\nabla \alpha_1|}\Big|_{\text{face}}.$$
(2.32)

The compression coefficient ϕ_c used in Eq. (2.31) is defined in Eq. (2.33),

$$\phi_c = c_\alpha \cdot |\vec{U} \cdot \hat{n}_f|,\tag{2.33}$$

where c_{α} is a user-defined scalar constant and \vec{U} is the velocity field. The total volumetric flux used in the advection of the phase fraction is then:

$$\phi_{\alpha} = \phi + \phi_r. \tag{2.34}$$

In practical simulations, the sharpness and stability of the interface are controlled by a set of user-defined parameters. These include the compression coefficient c_{α} , the number of correction steps for the phase-fraction equation, the number of subcycling steps per time step, and the number of iterations used in the nonlinear flux limiter. The value of c_{α} must be chosen as a trade-off between interface sharpness and computational efficiency. A too large value may lead to spurious oscillations or unbounded solutions, while a too

small value can result in excessive smearing of the interface. The numerical values used in this work are summarized in the section on numerical setup. In the phase conservation equation, volumetric source terms are defined based on the net mass exchange due to evaporation and condensation, as expressed in Eq. (2.35),

$$\dot{v}_{\text{net}} = \dot{v}_{\text{evap}} - \dot{v}_{\text{cond}}, \quad \text{with units } [1/s].$$
 (2.35)

Calculated volumetric fluxes are considered as additive sources. The resulting discretized transport equation for α_1 is given by Eq. (2.36),

$$\frac{\partial \alpha_1}{\partial t} + \nabla \cdot (\phi \alpha_1) + \nabla \cdot (\phi_r \alpha_1) = \dot{v}_{\text{net}}.$$
 (2.36)

To enforce the physical constraint $\alpha_1 \in [0,1]$ and preserve phase volumes in the presence of steep gradients, the MULES algorithm (Multidimensional Universal Limiter for Explicit Solutions) is applied (155). MULES is an iterative flux-corrected transport scheme that solves a non-linear boundedness constraint at each time step by modifying the phase-fraction advection term. Unlike classical high-resolution advection schemes that apply slope limiters to reconstructed face values (such as total variation diminishing schemes (156)), MULES operates by directly adjusting the volumetric face fluxes. MULES allows us to simultaneously enforce local boundedness and global mass conservation, even in the presence of strong gradients and sharp interfaces. The core of the algorithm consists of solving the transport equation (2.37) for α_1 as the modified form of equation (2.36),

$$\frac{\partial \alpha_1}{\partial t} + \nabla \cdot (\phi_\alpha \, \alpha_1) = \dot{v}_{\text{net}},\tag{2.37}$$

with ϕ_{α} pre-defined in (2.34). This is followed by a correction step that ensures the fraction remains within physical bounds. During each correction cycle, the fluxes on the cell faces are limited such that the updated value of α_1 remains between 0 and 1 in all cells. This is achieved by solving a set of local inequalities for the limited face fluxes using an iterative nonlinear algorithm.

The implementation uses a van Leer-type limiter to interpolate α_1 onto the faces during the advection step, but the boundedness guarantee arises from the nonlinear flux correction, not from the limiter itself. The algorithm distinction is that MULES modifies the face fluxes ϕ_{α} in a conservative manner while satisfying a global mass constraint and a local maximum principle (157). The final corrected flux $\phi_{\alpha}^{\text{lim}}$ replaces the convective term

in the discretized equation:

$$\frac{\partial \alpha_1}{\partial t} + \nabla \cdot \left(\phi_{\alpha}^{\lim}\right) = \dot{v}_{\text{net}}.$$
 (2.38)

After each correction cycle, the complementary phase field $\alpha_2 = 1 - \alpha_1$ is updated and interface-related quantities are reconstructed. The corrected convective flux ϕ_{α} is then used to evaluate the mixture mass flux $\rho\phi$, based on phase-wise densities, as:

$$\rho\phi = \alpha_1 \cdot (\rho_1 - \rho_2) \cdot \phi_\alpha + \rho_2 \cdot \phi_\alpha. \tag{2.39}$$

2.4.4 Momentum Matrix and Momentum Predictor

To determine the momentum field and consequently the velocity distribution along with the internal force balance within the computational domain, the first step of the algorithm is the construction of the momentum matrix in conservative form. This matrix includes inertial and diffusive terms, represents the advection form previously explained in Eq. (2.1), and is defined in code as a finite-volume matrix (fvMatrix<vector>) by Eq. (2.40).

$$\underbrace{\frac{\partial(\rho \mathbf{U})}{\partial t}}_{\text{transient term}} + \underbrace{\nabla \cdot (\rho \mathbf{U} \otimes \mathbf{U})}_{\text{convective transport}} + \underbrace{\nabla \cdot \tau}_{\text{viscous stresses}} - \underbrace{\left(\frac{\partial \rho}{\partial t} + \nabla \cdot (\rho \mathbf{U})\right) \mathbf{U}}_{\text{conservative correction}} = \mathbf{0}$$
 (2.40)

Equation (2.40) is a conservative formulation, where the momentum flux is expressed entirely in divergence form. The last term represents a conservative correction that compensates for the non-linearity introduced by the time and space-dependent density field, ensuring that momentum remains conservative even when $\rho = \rho(\alpha, T)$. Neglecting this term leads to the generation or loss of artificial momentum within the domain of compressible flows (158; 150). This correction term is specific to variable-density formulations and vanishes in the incompressible approach. At this stage, the constructed matrix operator $A(\mathbf{U})$ contains only inertial, convective, and viscous terms and remains decoupled from pressure and body forces. To obtain a preliminary estimate of the velocity field required by the energy equation prior to the pressure correction step, the momentum predictor is executed. In this context, the velocity field \mathbf{U}^* denotes the predicted velocity, computed using known pressure and interface forces, without enforcing the divergence-free constraint. This field is used for transporting scalar quantities, provides an initial estimate for pressure-velocity coupling within the PIMPLE loop. The governing relation for

the predicted velocity is explicitly given by Eq. (2.41).

$$A(\mathbf{U}) \cdot \mathbf{U}^* = \mathbf{F}_{\sigma} - \rho \nabla g h - \nabla p_{\text{rgh}}$$
 (2.41)

The right-hand side of Eq. (2.41) is evaluated explicitly on the cell faces. The surface tension force \mathbf{F}_{σ} , the hydrostatic correction $\rho \nabla g h$, and the pressure gradient $\nabla p_{\rm rgh}$ are calculated as vector fields centered on the face and multiplied by the corresponding vectors of the area of the face \mathbf{S}_f . Since the velocity field \mathbf{U}^* is stored in cell centers, the forces integrated with the face are projected back into the computational cells. In Open-FOAM, the operation of (fvc::reconstruct) is performed mathematically by summing the normal fluxes of the face around each cell, normalized by the volume of the cell V, as shown in Eq. (2.42):

$$(\mathbf{F})_c = \frac{1}{|V|} \sum_{f \in \partial V} (\mathbf{F}_f \cdot \mathbf{S}_f). \tag{2.42}$$

This operation ensures compatibility between the driving forces centered on the face and the momentum equation centered on the cell. Explicitly, the reconstructed volumetric force term on the right-hand side of Eq. (2.41) is expressed by Eq. (2.43),

$$A(\mathbf{U}) \cdot \mathbf{U}^* = \frac{1}{|V|} \sum_{f \in \partial V} \left[(\mathbf{F}_{\sigma} - \rho \nabla g h - \nabla p_{\text{rgh}})_f \cdot \mathbf{S}_f \right]. \tag{2.43}$$

The resulting linear algebraic system defined in Eq. (2.43) is solved iteratively using a preconditioned solver of the diagonal incomplete Cholesky (DIC) (159). The predicted velocity field obtained U^* is subsequently used in the energy equation to compute the temperature distribution and serves as an initial velocity field for the pressure—velocity coupling during the current outer iteration of the PIMPLE algorithm.

2.4.5 Energy Equation

In order to calculate the temperature, the distribution within the domain is divided into fluid and solid phases and calculated simultaneously. In fluid, the solution is determined by solving the energy equation in a conservative form. This equation accounts for transient, advective, diffusive, and phase-change source terms. Initially, it is expressed in continuous mathematical form in Eq. 2.44,

$$\frac{\partial(\rho c_p T)}{\partial t} + \nabla \cdot (\rho c_p \mathbf{U} T) - \left(\frac{\partial(\rho c_p)}{\partial t} + \nabla \cdot (\rho c_p \mathbf{U})\right) T - \nabla \cdot (\kappa_{\text{eff}} \nabla T) = \dot{q}_{\text{pc}}.$$
 (2.44)

In the above formulation ρ and c_p are defined in cell centers, and **U** is the cell-centered velocity field obtained from the solution of the momentum equation derived from the solution of predictor (2.41). However, for discretization and numerical implementation in the FVM used in the proposed algorithm, convective terms are solved using face-normal fluxes. Hence, Eq. (2.44) is discretized by replacing the velocity vector field **U** with the volumetric face flux ϕ attached to the cell wall, as expressed in Eq. (2.45),

$$\phi_f = (\mathbf{U}_f \cdot \mathbf{S}_f). \tag{2.45}$$

The use of ϕ facilitates conservative discretization and ensures a more precise mass and energy balance between cell boundaries compared to simpler FDM solutions. Thus, the discretized energy equation is expressed in Eq. (2.46).

$$\frac{\partial(\rho c_p T)}{\partial t} + \nabla \cdot (\phi_f c_{p,f} T_f) - \left(\frac{\partial(\rho c_p)}{\partial t} + \nabla \cdot (\phi_f c_{p,f})\right) T - \nabla \cdot (\kappa_{\text{eff}} \nabla T) = \dot{q}_{\text{pc}}$$
 (2.46)

In Eq. (2.46), scalar quantities such as density, specific heat, and temperature, originally defined at the centers of control volumes, are interpolated to the cell faces to ensure continuity of diffusive and convective fluxes across adjacent cells. This operation is required by the finite-volume formulation, where fluxes are naturally evaluated at the boundaries of control volumes. OpenFOAM provides a dedicated interpolation operator fvc::interpolate for this purpose, which transfers scalar field information from cell centers to faces across general unstructured meshes. The interpolation scheme corresponds to the same discretization strategy used in the momentum equation (2.42). The interpolated face value ψ_f of an arbitrary scalar field ψ is obtained using a convex combination of the values in the adjacent cells:

$$\psi_f = (1 - \lambda_f)\psi_P + \lambda_f \psi_N, \quad \text{where} \quad \lambda_f = \frac{|\delta_{P,f}|}{|\delta_{P,N}|}$$
 (2.47)

In this expression, the indices P and N refer to the centers of the two neighboring cells adjacent to the face f, $\delta_{P,f}$ is the distance vector from cell P to face f, and $\delta_{P,N}$ is the distance between the cell centers. The interpolation factor $\lambda_f \in [0,1]$ reflects the relative geometric position of the face between the two centers of the cells. In the case of uniform

orthogonal meshes, this expression simplifies to the arithmetic mean. This interpolation is applied consistently to all scalar fields that appear in the discretized energy equation, including ρ , c_p , and T, as part of the evaluation of face-based fluxes. The volumetric enthalpy flux term $\rho c_p \phi T$, constructed on the faces of control volumes, is thereby evaluated using the interpolated values of these fields. The third term in Eq. (2.46) represents a conservative correction ensuring energy conservation in the presence of spatially and temporally variable fluid properties. The effective thermal conductivity, κ_{eff} , responsible for the intensity of diffusion, combines the molecular thermal conductivity (k_f) and turbulent heat diffusivity in Eq. (2.48),

$$\kappa_{\text{eff}} = k_f + \rho c_p \frac{\nu_t}{\Pr_t}.$$
 (2.48)

In the formula for effective thermal conductivity, ν_t is the turbulent viscosity and \Pr_t is the turbulent Prandtl number set to default value of 0.85 (160). The phase change source term $\dot{q}_{\rm pc}$ appearing on the right-hand side of Eq. (2.46) accounts for latent heat exchange associated with evaporation and condensation. These processes are governed by the mass transfer rates $\dot{m}_{\rm evap}$ and $\dot{m}_{\rm cond}$, as defined in Eqs (2.30), and are driven by a local thermodynamic imbalance near the liquid–vapor interface. To ensure numerical stability while preserving physical consistency, the term latent heat source is linearized around the local saturation temperature $T_{\rm sat}$ and decomposed into implicit and explicit parts in the following formula (2.49),

$$\dot{q}_{\rm pc} = \underbrace{\left(\frac{\dot{m}_{\rm cond} - \dot{m}_{\rm evap}}{T_{\rm sat}}\right) h_{\rm evap} T}_{\text{implicit contribution}} - \underbrace{\left(\dot{m}_{\rm cond} - \dot{m}_{\rm evap}\right) h_{\rm evap}}_{\text{explicit contribution}}.$$
(2.49)

This formulation effectively captures the influence of local thermal differences over the interface through the temperature ratio $T/T_{\rm sat}$, which approximates the magnitude and direction of the driving force for phase change. Although the latent heat of vaporization $h_{\rm evap}$ is a thermodynamic property evaluated at equilibrium, the actual rate of energy release or absorption depends on the deviation of the local temperature from $T_{\rm sat}$. This approach ensures that the source term is activated only when a nonzero temperature difference is present across the interface. The implicit term, proportional to the unknown local temperature T, contributes to the diagonal of the discretized matrix system, thus improving the convergence of the energy equation. The explicit component, computed from values in the previous time step or iteration, enters the system as a fixed source. This semi-implicit treatment stabilizes the coupling between temperature evolution and phase change dynamics. The resulting algebraic system derived from Eq. (2.46) is solved

iteratively to obtain the updated temperature distribution for the fluid domain. Analogously, the temperature field in the solid region is governed by the transient conduction equation, simplified by the absence of convective terms and expressed by Eq. (2.50),

$$\frac{\partial(\rho_s c_{p,s} T_s)}{\partial t} - \nabla \cdot (\kappa_s \nabla T_s) = 0. \tag{2.50}$$

Here, ρ_s , $c_{p,s}$, and κ_s denote the local density, the specific heat capacity, and thermal conductivity of the solid material, all of which can vary significantly with temperature under cryogenic conditions. The formulation accounts for these variations by applying the time derivative to the full enthalpy term $\rho_s c_{p,s} T_s$ and including the temperature-dependent conductivity term within the divergence operator. This captures the effect of spatial gradients in thermal properties in order to accurately model heat transport in solids with strongly non-linear thermophysical behavior.

2.4.6 Conjugate Heat Transfer and Turbulence

In pulsating heat pipes, the flow regime is characterized by strong unsteady motions and significant spatial variations in velocity and Reynolds number. Preliminary analyzes of velocity structures and local Reynolds numbers, as described in (161; 162; 128), demonstrate the necessity of incorporating turbulence modeling. Although the inclusion of turbulence models increases computational resource requirements, it enables more accurate predictions of both fluid dynamics and heat transfer. These effects are previously included in the momentum and energy equations (2.40), (2.44). In the present thesis, turbulence is modeled using the standard k- ϵ approach (163), which is suitable for meshes characterized by $y^+ > 30$. This model introduces two additional scalar fields, the turbulent kinetic energy k and the turbulent dissipation rate ϵ . Their distributions are governed by the transport equations, the same way as in the momentum (Eq. (2.51)) or energy equation (Eq. (2.52)).

$$\frac{\partial(\rho k)}{\partial t} + \nabla \cdot (\rho k \mathbf{U}) = \nabla \cdot \left[\left(\mu + \frac{\mu_t}{\sigma_k} \right) \nabla k \right] + P_k - \rho \epsilon \tag{2.51}$$

$$\frac{\partial(\rho\epsilon)}{\partial t} + \nabla \cdot (\rho\epsilon \mathbf{U}) = \nabla \cdot \left[\left(\mu + \frac{\mu_t}{\sigma_{\epsilon}} \right) \nabla \epsilon \right] + C_{1\epsilon} \frac{\epsilon}{k} P_k - C_{2\epsilon} \rho \frac{\epsilon^2}{k}$$
 (2.52)

The model coefficients $C_{1\epsilon}$ and $C_{2\epsilon}$ are assigned their standard values, which are commonly used in engineering turbulence modeling (164). The turbulent viscosity μ_t is determined

by the Boussinesq approximation and resolved by Eq (2.53),

$$\mu_t = C_\mu \frac{\rho k^2}{\epsilon}.\tag{2.53}$$

The computed turbulent viscosity μ_t modifies both momentum and heat transfer, enhancing the effective viscosity and the effective thermal conductivity. In the energy equation (2.46), this leads to the expression for the effective thermal conductivity in Eq. (2.48) and in the momentum equation, it influences the viscous stress tensor in Eq. (2.40).

The conjugate heat transfer between the fluid and solid regions is modeled by enforcing the continuity of temperature and heat flux across the interface. The starting point is Fourier's law of heat conduction applied separately to each side.

$$\mathbf{q}_f = -\kappa_{\text{eff}} \nabla T_f, \tag{2.54}$$

$$\mathbf{q}_s = -k_s \nabla T_s,\tag{2.55}$$

At the fluid-solid interface, to meet continuity conditions, the following assumptions are imposed in (2.56),

$$T_f = T_s \qquad \mathbf{q}_f \cdot \mathbf{n} = \mathbf{q}_s \cdot \mathbf{n},$$
 (2.56)

where \mathbf{n} is the normal vector directed from the fluid to the solid. The first condition ensures thermal equilibrium at the interface, while the second guarantees conservation of energy flux. Unlike the classical OpenFOAM implementation, where the interfacial heat flux is approximated by direct interpolation between neighboring temperatures without explicit calculation of thermal resistances, the present model constructs the total thermal resistance as a sum of contributions from the fluid and solid sides. On the fluid side, resistance is associated with turbulent and molecular conduction and is proportional to the thickness of the fluid layer near the wall and inversely proportional to the effective thermal conductivity κ_{eff} , which incorporates the effects of turbulence and varies with temperature:

$$R_f = \frac{\delta_f}{\kappa_{\text{eff}}}. (2.57)$$

On the solid side, the resistance accounts for pure molecular conduction across a temperature-dependent solid thermal conductivity κ_s :

$$R_s = \frac{d_s}{\kappa_s}. (2.58)$$

The total thermal resistance $R_{\rm th}$ at the fluid-solid interface is thus given by:

$$R_{\rm th} = R_f + R_s = \frac{\delta_f}{\kappa_{\rm eff}} + \frac{d_s}{\kappa_s}.$$
 (2.59)

The normal heat flux q_n exchanged across the interface is then computed consistently from the local temperature jump divided by the total resistance,

$$q_n = \frac{T_f - T_s}{R_{\rm th}}. (2.60)$$

This resistance-based formulation accounts for turbulent heat transfer in the fluid, conduction in the solid, and temperature-dependent variations in material properties. By using spatially resolved thermophysical fields on both sides of the interface, the model offers a physically consistent description of conjugate heat transfer, especially in regimes with strong temperature dependence, such as cryogenics. Graphical description of the heat transfer between the solid and fluid is presented in Fig. 2.4.

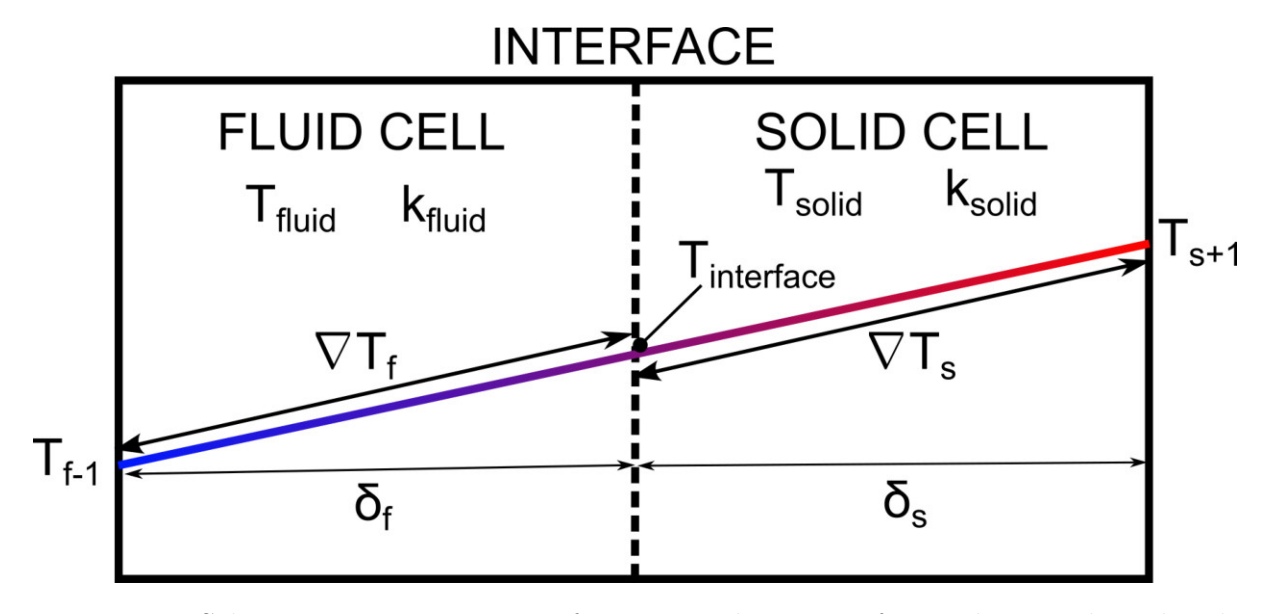


Figure 2.4: Schematic representation of conjugate heat transfer implemented to the algorithm at the interface.

2.4.7 Momentum Conservation and Pressure Correction

In order to ensure mass conservation and maintain a consistent force balance, it is necessary to correct the preliminary momentum field obtained from the predictor step defined in Eq. (2.41). The intermediate velocity field U*, resulting from the initial solution of the momentum equation, generally does not satisfy the continuity equation—particularly under compressible flow conditions with phase change. Therefore, a pressure correction step is introduced to enforce mass conservation. The corrected velocity field is expressed as,

$$\mathbf{U} = \mathbf{U}^* + rAU\nabla p_{\rm rgh},\tag{2.61}$$

where $rAU = 1/\text{diag}(A(\mathbf{U}))$ is the reciprocal of the diagonal elements of the discretized momentum matrix $A(\mathbf{U})$, and serves as an approximate inverse operator.

To derive the corresponding pressure correction equation, the corrected velocity field must be substituted into the governing mass continuity equation. This equation accounts for density variations due to pressure, temperature, phase change and forms the foundation for computing a consistent pressure field under transient, compressible flow conditions. The governing mass continuity equation, including phase-change-induced mass transfer, is given by Eq (2.62),

$$\frac{\partial \rho}{\partial t} + \nabla \cdot (\rho \mathbf{U}) = \dot{m}_{pc}. \tag{2.62}$$

To consistently expand the temporal density derivative in Eq. (2.62), it is connected to variations in pressure and temperature by employing a thermodynamic identity in Eq. (2.63),

$$\frac{\partial \rho}{\partial t} = \left(\frac{\partial \rho}{\partial p}\right)_T \frac{\partial p}{\partial t} + \left(\frac{\partial \rho}{\partial T}\right)_T \frac{\partial T}{\partial t}.$$
 (2.63)

This formulation is fully compatible with the compressibility-based approach adopted in the model. As previously introduced in Eq. (2.17), with isothermal compressibility ψ is defined as the sensitivity of density to pressure changes,

$$\psi = \frac{1}{\rho} \frac{\partial \rho}{\partial p} \bigg|_{T}. \tag{2.64}$$

Analogously, the isobaric thermal expansion coefficient quantifies the sensitivity of density

to temperature,

$$\beta_T = -\frac{1}{\rho} \left(\frac{\partial \rho}{\partial T} \right)_p. \tag{2.65}$$

Substituting these definitions into Eq. (2.63) leads to the following expression for the local density evolution as depicted by Eq. (2.66),

$$\frac{\partial \rho}{\partial t} = \psi \frac{\partial p}{\partial t} - \rho \beta_T \frac{\partial T}{\partial t}.$$
 (2.66)

Subsequently substituting the expression (2.66) into Eq. (2.62) and applying the corrected velocity formulation from Eq. (2.61) it follows Eq. (2.67):

$$\nabla \cdot \mathbf{U}^* + \nabla \cdot (rAU\nabla p_{\text{rgh}}) = \psi \frac{\partial p_{\text{rgh}}}{\partial t} - \rho \beta_T \frac{\partial T}{\partial t} + \dot{v}_{\text{pc}}.$$
 (2.67)

The divergence of the predicted velocity field $\nabla \cdot \mathbf{U}^*$ is approximated numerically by the divergence of the interpolated volumetric flux ϕ^* , scaled by the local compressibility as (2.68),

$$\nabla \cdot \mathbf{U}^* = \nabla \cdot \left(\frac{\psi}{\rho} \phi^*\right),\tag{2.68}$$

where ϕ^* is the face flux computed from \mathbf{U}^* .

Substituting Eq. (2.68) into Eq. (2.67) yields the scalar pressure correction equation (2.69) consistent with FVM method,

$$\psi \frac{\partial p_{\text{rgh}}}{\partial t} + \nabla \cdot \left(\frac{\psi}{\rho} \phi^*\right) - \nabla \cdot (rAU\nabla p_{\text{rgh}}) + \dot{v}_{\text{pc}} + \rho \beta_T \frac{\partial T}{\partial t} = 0.$$
 (2.69)

Once the pressure correction $p_{\rm rgh}$ is obtained from Eq. (2.69), the velocity is updated using Eq. (2.61), and the absolute pressure is reconstructed as

$$p = p_{\rm rgh} + \rho g h, \tag{2.70}$$

incorporating both dynamic and hydrostatic components.

2.5 Model Validation through Benchmarks

2.5.1 Stefan Problem

Validation of the new CFD model involves comparing numerical results with benchmarks. That approach provides a reference for assessing the accuracy of a solution based on data from simple experiments or analytically solvable problems. In the case of the solver under development, which extends the interFOAM family of algorithms to include phase-change phenomena, newly implemented features require a suitable benchmark. A fundamental benchmark in this field is the Stefan problem (165). The phenomenon involves a moving boundary between two phases, gas and liquid, under heat transfer. Analytical solutions exist for the one-dimensional version, enabling the direct validation of numerical models that incorporate phase change. The assumptions of the Stefan problem benchmark are depicted in Fig. 2.5.

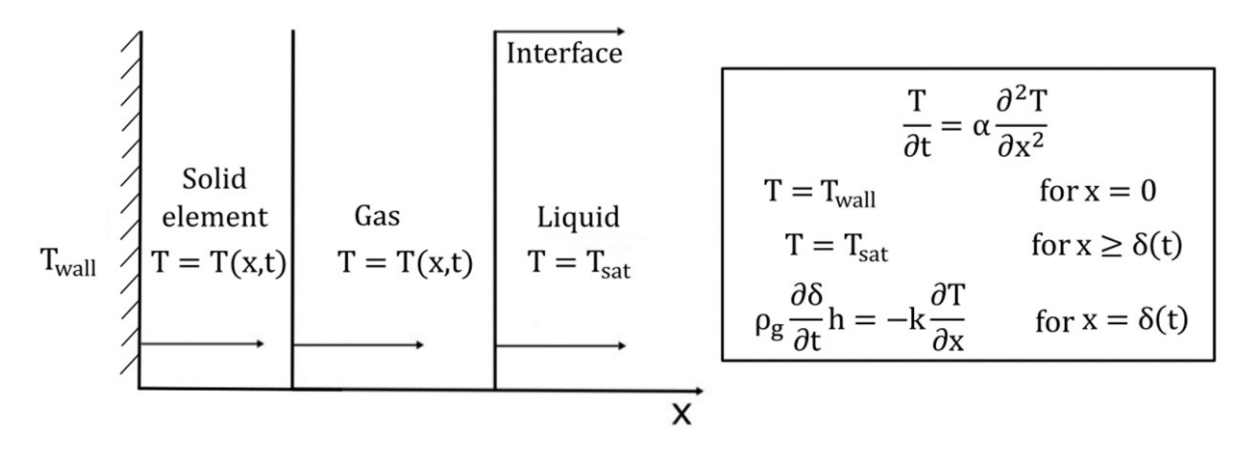


Figure 2.5: Boundary conditions and assumptions of Stefan problem solved analytically.

To describe the motion of the interface over time and implement the Stefan problem, the one-dimensional heat conduction equation governing the diffusion of heat is employed and expressed as (2.71),

$$\frac{\partial T}{\partial t} = \frac{k}{\rho c_p} \frac{\partial^2 T}{\partial x^2}.$$
 (2.71)

The positions of the phase interface are described by Stefan's condition, which is expressed in Eq.(2.72),

$$\rho_g h \frac{d\delta}{dt} = -k \frac{\partial T}{\partial x} \bigg|_{x=\delta(t)}.$$
(2.72)

In order to solve the energy equation (2.71) based on Stefan's condition (2.72), a dimensionless coefficient ζ is used, which allows one to reduce the equation to a transcendental form expressed in Eq. (2.73). This expression of the equation links the thermophysical properties of the system with the motion of the phase-change interface,

$$\zeta e^{\zeta^2} \int_0^{\zeta} e^{-C^2} dC = \frac{c_p(T_{\text{wall}} - T_{\text{sat}})}{\sqrt{\pi}L},$$
(2.73)

where C does not represent a physical property such as position, time, or temperature; instead, it simplifies the computation of the integral. Equation (2.73) is solved using the Newton-Raphson method. Once ζ is determined, the position of the interface is calculated using Eq.(2.74),

$$\delta(t) = 2\zeta \sqrt{\frac{k}{\rho c_p} t}. (2.74)$$

The temperature distribution is described by Eq.(2.75), where the liquid temperature corresponds to the saturation temperature, while the gas temperature is determined using the derived formula,

$$T(x,t) = \begin{cases} T_{\text{sat}}, & \text{for } x \ge \delta(t), \\ T_{\text{wall}} - \frac{(T_{\text{wall}} - T_{\text{sat}})}{2\sqrt{\pi} \int_{0}^{\zeta} e^{-C^{2}} dC} \cdot \frac{2}{\sqrt{\pi}} \int_{0}^{2\sqrt{\frac{k}{\rho c_{p}} t}} e^{-C^{2}} dC, & \text{for } x < \delta(t). \end{cases}$$
(2.75)

The Stefan moving interface simulations were conducted for liquid nitrogen. Constant thermodynamic parameter values were assumed in the model to ensure consistency with the analytical solution, where fixed fluid parameter values are also used. An example of the results is shown in Fig. 2.6, which presents the numerically obtained temperature and fraction contours after 1 s of simulation. A comparison of the analytical results with the numerically obtained data is plotted in Fig. 2.6.

2.5.2 Scriven Single Bubble Growth

A more complex approach to validate the model and ensure the correct implementation of phase change processes is to simulate the growth of a single vapor bubble. Similar to the Stefan problem, this case can also be solved analytically. Scriven in (166), proposed an analytical solution describing the growth of the radius of a single vapor bubble. Scriven's

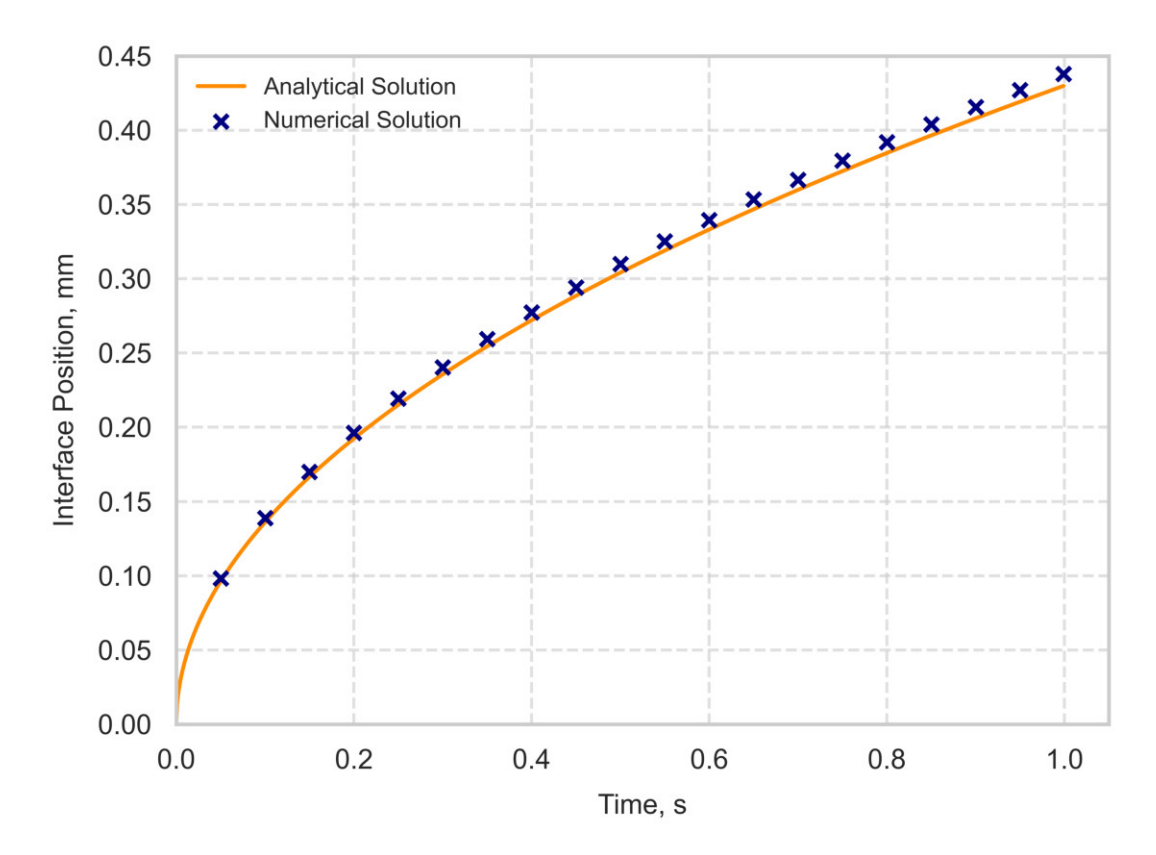


Figure 2.6: Temperature and fraction contour of 1-D numerically obtained visualization of Stefan problem.

relationship is expressed in equation (2.76):

$$R(t) = 2\beta \sqrt{Dt}. (2.76)$$

The use of a benchmark based on an analytical solution is one of the approaches proposed in the literature. It has been used by Georgoulas et al. (167), Magnini in his doctoral dissertation (168), and Kunkelmann and Stephan in (154). The mesh parameters and thermodynamic values were set in a way similar to those in the work of Georgoulas et al. (167). Unlike the previous benchmark, the validation was performed under ambient conditions due to the lack of precisely determined β values available in the literature for cryogenic liquids.

Under specific assumptions, the Scivern solution can be accurately reproduced, requiring an initial temperature profile as a key starting condition. These assumptions, thoroughly discussed by Magnini (168), are described using equation (2.77). To obtain a parabolic temperature distribution instead of a linear one, the original setup was modified. The adjustments made are reflected in Eq. (2.78). Fig. 2.7 illustrates the differences between linear and parabolic temperature profiles.

The linear temperature distribution in the thermal layer is

$$T(r) = \frac{\delta - 0.99 \cdot (T_{\infty} - T_{sat}) + R_0}{r} + T_{sat}, \tag{2.77}$$

and the parabolic temperature distribution in the thermal layer is,

$$T(r) = T_{\infty} - \left(\frac{\delta_r - (r - R_0)}{\delta_r}\right)^2 \cdot (T_{\infty} - T_{sat})$$
 (2.78)

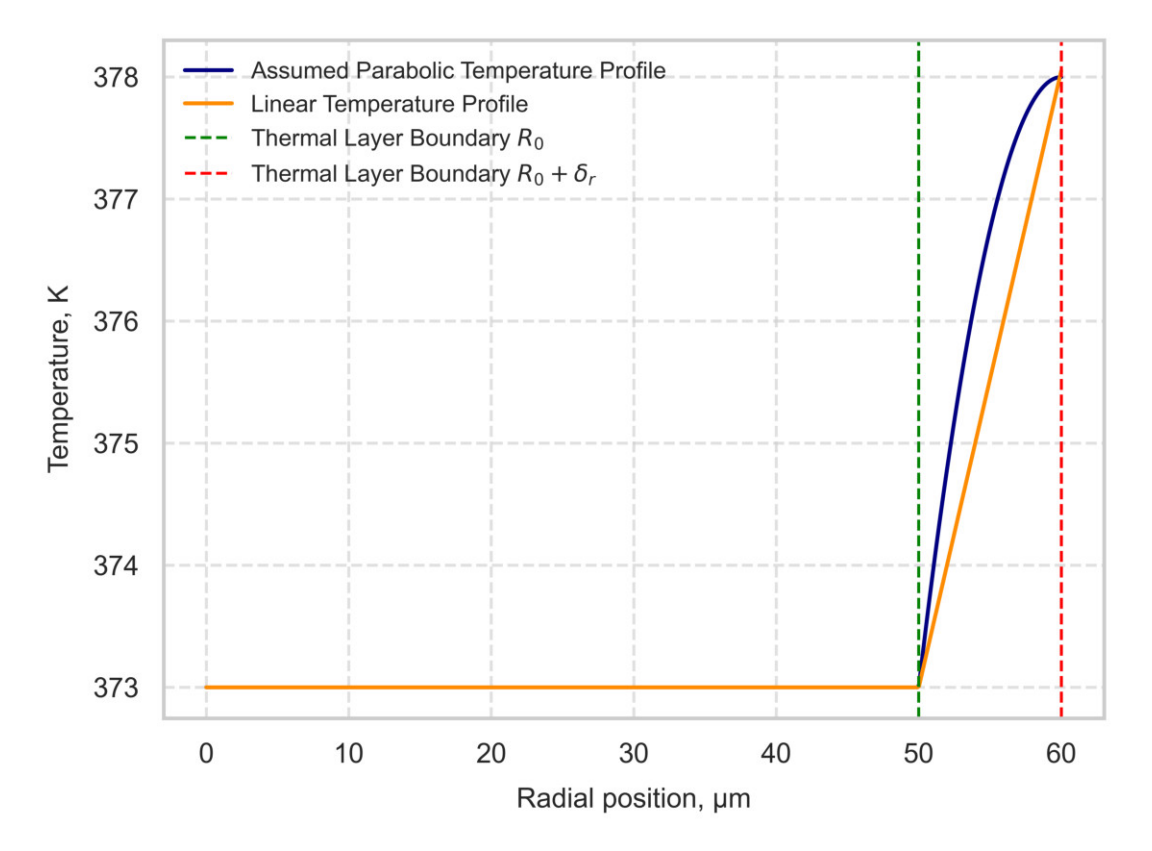


Figure 2.7: Assumed temperature distribution with comparison with linear assumption

Georgoulas et al. (167) introduced a critical refinement to the model by limiting phase change processes to occur exclusively within interface cells. Specifically, this method allows phase change only in regions where α lies between 0.05 and 0.95, effectively suppressing it elsewhere. This control strategy, integrated into the algorithm, has been adopted in the present study. The benchmark's schematic and underlying assumptions are shown in Fig. 2.8.

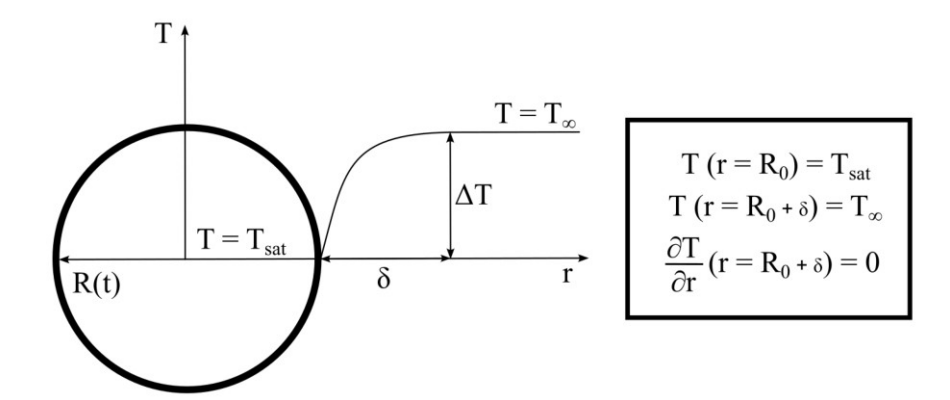


Figure 2.8: Schematic and assumptions for the bubble growth case proposed by Scriven (166).

The results of the numerical analysis, as well as the evolution of the vapor bubble, are shown in Fig. 2.9.

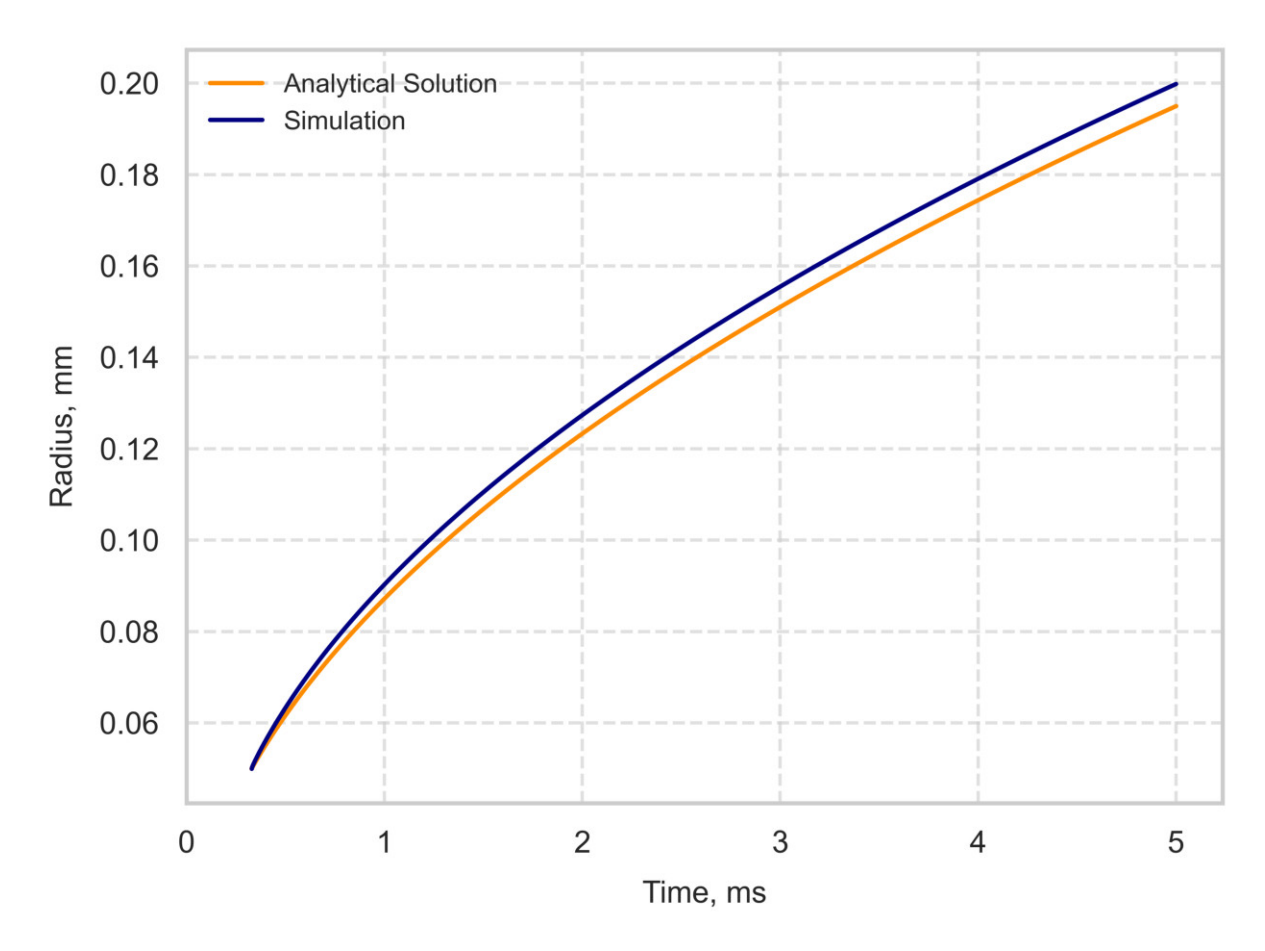


Figure 2.9: Graph of the evolution of the radius of the vapor bubble compared to the analytical solution.

The numerical results of Scriven bubble growth are compared in Fig. 2.10. The graph illustrates the shifted evolution of a bubble such that the numerically derived values,

marked by red crosses, start at the instance of the analytical solution for an initial radius of 0.1 mm.

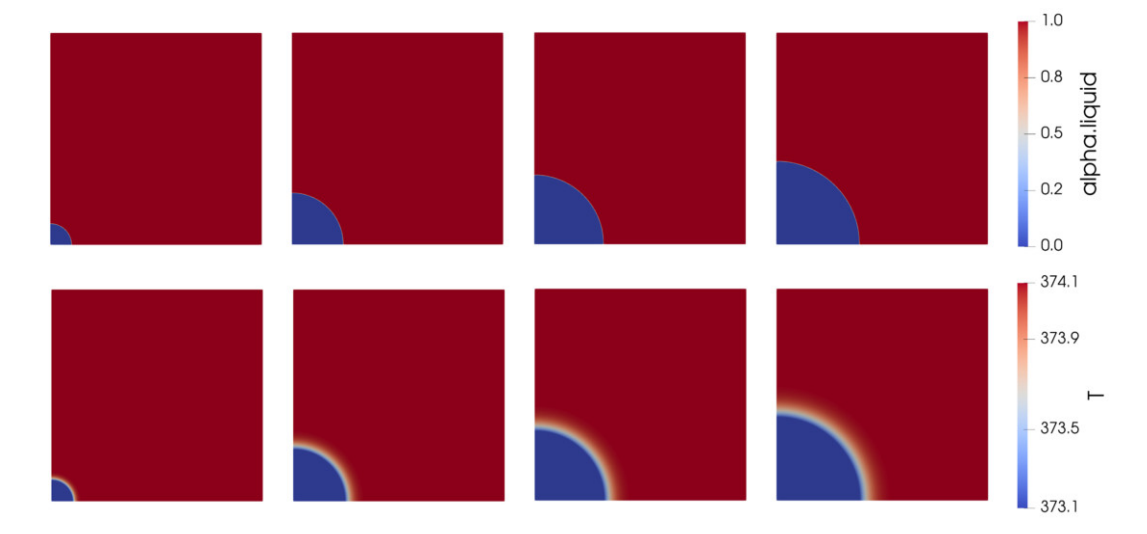


Figure 2.10: Evolution of fraction and temperature development of Scriven bubble growth.

The compliance of the solver with analytical solutions to the Stefan problem and the growth of Scriven bubbles are shown in Figures 2.6 and 2.9, with errors below 5%. These benchmarks verify the core phase change and transport mechanisms under controlled analytical conditions and quantify the accuracy of the baseline. They establish the reference upon which the subsequent PHP-specific studies are built.

Chapter 3

Experimental Test Facility

This experimental study aims to characterize the thermo-hydraulic behavior of small cryogenic PHPs. The objective is to investigate how the capillary pipe geometry (particularly the diameter), working fluid and filling ratio affect the thermal performance. The measured data will be used to validate the numerical model described in section 2.4. The experimental system is based on a closed-cycle two-stage cryocooler that serves as the cold source without the need for liquid cryogens. The PHP was connected to the cryocooler cold stage through a custom-designed thermal interface. The term 'small' refers to the geometry of the PHP optimized for computational modeling. The total pipe length and number of turns have been selected to preserve the pulsating mechanism while reducing the computational domain to a computationally tractable mesh size. The sections in this chapter provide a detailed overview of the cryocooling principle, working fluid selection criteria, geometric constraints, component manufacturing, and the measurement and control systems used in the experiment.

3.1 Design Principles in Cryogenics

Thermal system design at cryogenic temperatures differs substantially from conventional engineering practice under ambient conditions. The primary challenge lies in the nonlinear temperature dependence of material properties such as density, specific heat capacity and thermal conductivity. These parameters may vary by an order of magnitude depending upon the operating temperature ranges and their gradients must be taken into account during both mechanical design and thermal optimization. This often requires the use of oxygen-free copper or specialized alloys, which are costly and difficult to process. In this thesis, the primary role of the designed PHP is to provide controlled and

reproducible data to validate the numerical model, but is also intended to serve as an efficient thermal link. Achieving high thermal efficiency requires minimizing the temperature drop between the evaporator and condenser sections. The interface was developed to ensure uniform temperature distribution and minimal thermal resistance while preserving mechanical integrity. From a modeling perspective, the uniformity of heat removal from the condenser is requisite for reliable numerical validation. Any spatial variation in temperature along the condenser surface introduces non-uniform boundary conditions, which reduce the reliability of fixed-temperature assumptions. To mitigate this, design measures were implemented to maximize temperature uniformity, such as the use of highconductivity interface materials and symmetrical mounting geometries. The geometrical size and configuration of the PHP are typically governed by two main constraints: the available cooling power of the cryocooler and the physical dimensions of the cryostat. Since the cryocooler is the most expensive component of the system, the overall PHP layout is usually tailored to match its thermal performance. An exception to this approach arises in the application oriented PHP designs, where the objective is to transfer a specified amount of heat with predefined performance. In such cases, the cryocooler is selected accordingly, and the overall system cost becomes a secondary concern. In summary, cryogenic design demands high-conductivity interfaces to reach strictly uniform boundary conditions so that measured responses can be attributed to PHP geometry, working fluid, and fill ratio rather than uncontrolled thermal biases.

3.2 Cryocooling and Operating Ranges

A cryocooler is a mechanical refrigerator operating on a closed thermodynamic cycle to provide continuous cooling at cryogenic temperatures. Unlike dewars supplied with liquid helium or nitrogen, it operates without consumable cryogens. Early regenerative designs were developed in the early 1960s by Gifford and McMahon (169). In this experiment, the two-stage CH-208L cryocooler (Sumitomo SHI Cryogenics Group (170)) have been used. As a Gifford–McMahon (GM) unit, it employs an external compressor and a rotary valve to alternate high- and low-pressure helium through a regenerator and displacer in the cold head. A photo of the cryocooler, along with the thermomechanical interface to the first and second stages, is shown in Fig. 3.1. The cryocooler consists of two cooling stages. The first stage operates at intermediate temperatures, providing precooling near 70 K with a cooling capacity of up to 28 W, according to the CH-208L manufacturer specifications. The second stage is designed to reach 20 K, offering a cooling power of 8 W. Its operation follows a standard two-stage GM regenerative cycle in which an external compressor and rotary valve shuttle helium between high and low pressure through a

regenerator—displacer cold head. For PHP experiments, a two-stage GM cryocooler is preferred because it maintains stable cold-head temperatures under varying heat loads and enables thermal partitioning: a radiation shield anchored to stage 1 intercepts room-temperature radiation and parasitic conduction through supports and wiring, increasing the cooling capacity available at stage 2 for the PHP condenser and supporting uniform boundary conditions.

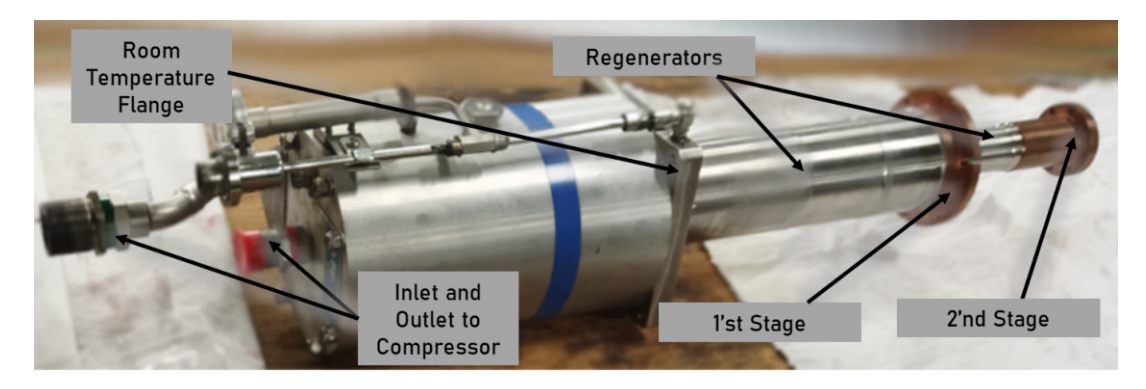


Figure 3.1: Cryocooler CH-208L with customized connection to the 1'st and 2'nd stage used in the experiment

The design of the experimental system is primarily constrained by three factors. The first is the cooling performance and operational range of the cryocooler, and the second is the boiling temperature of the working fluid within the accessible range. The manufacturer provides a performance map of the CH-208L cryocooler under no-load conditions, as shown in Fig. 3.2. Based on this data, realistic operating temperatures are approximately 30 K and above for systems thermally connected to the first stage, and above 10 K for components at the second stage (170).

The design of the experimental system is constrained by three factors. The first is the cooling performance and operating range of the cryocooler, and the second is the boiling temperature of the working fluid within the accessible range. The manufacturer's performance map for the CH-208L under no-load conditions is shown in Fig. 3.2. Based on these data, realistic operating temperatures are approximately 30 K and above for systems thermally connected to the first stage, and above 10 K for components at the second stage (170).

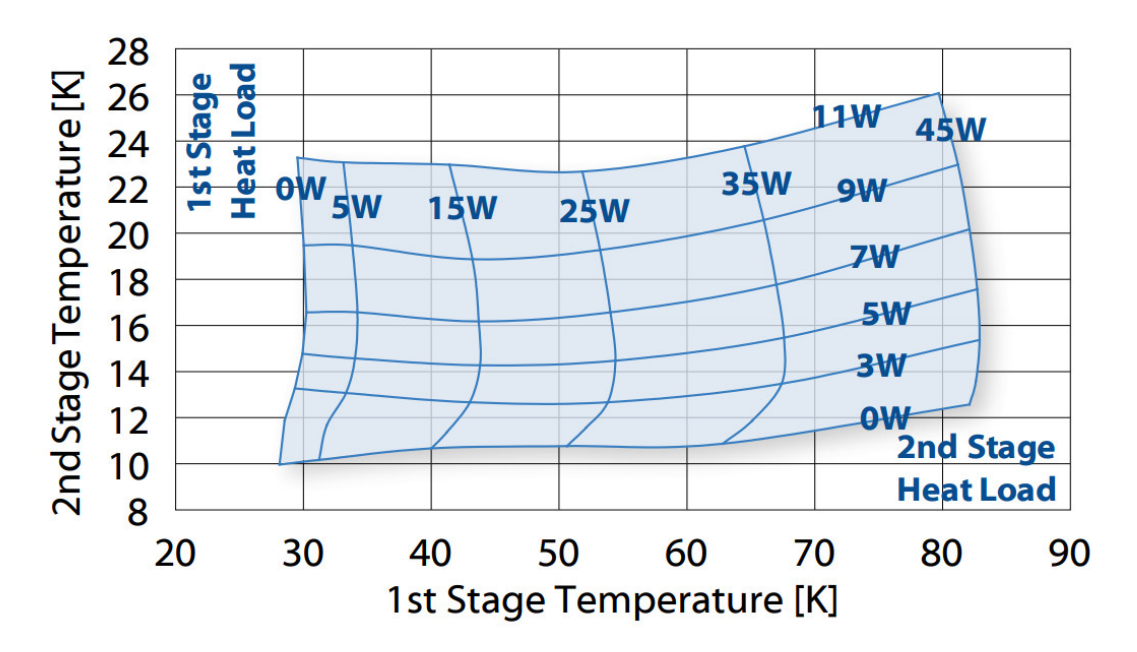


Figure 3.2: Performance map of the two-stage CH-208L cryocooler at 50 Hz, provided by SHI Cryogenics Group (170).

The third limitation is the allowable operating pressure. The filling-line connection and the pressure safeguards used in this study are described in Section 3.3.1. A relief valve set to 4.5 bar defines the maximum working pressure used throughout the experiments. The operating ranges are shown on the modified saturation diagram in Fig. 3.3. The diagram includes argon, nitrogen, neon, oxygen, and hydrogen to delineate the practical envelope of cryogenic fluids within the temperature and pressure window relevant to this setup. The experimental campaign is conducted on both stages of the cryocooler to cover the available temperature range. For the present work, the selected working fluids are argon, nitrogen, and neon to meet safety and handling requirements.

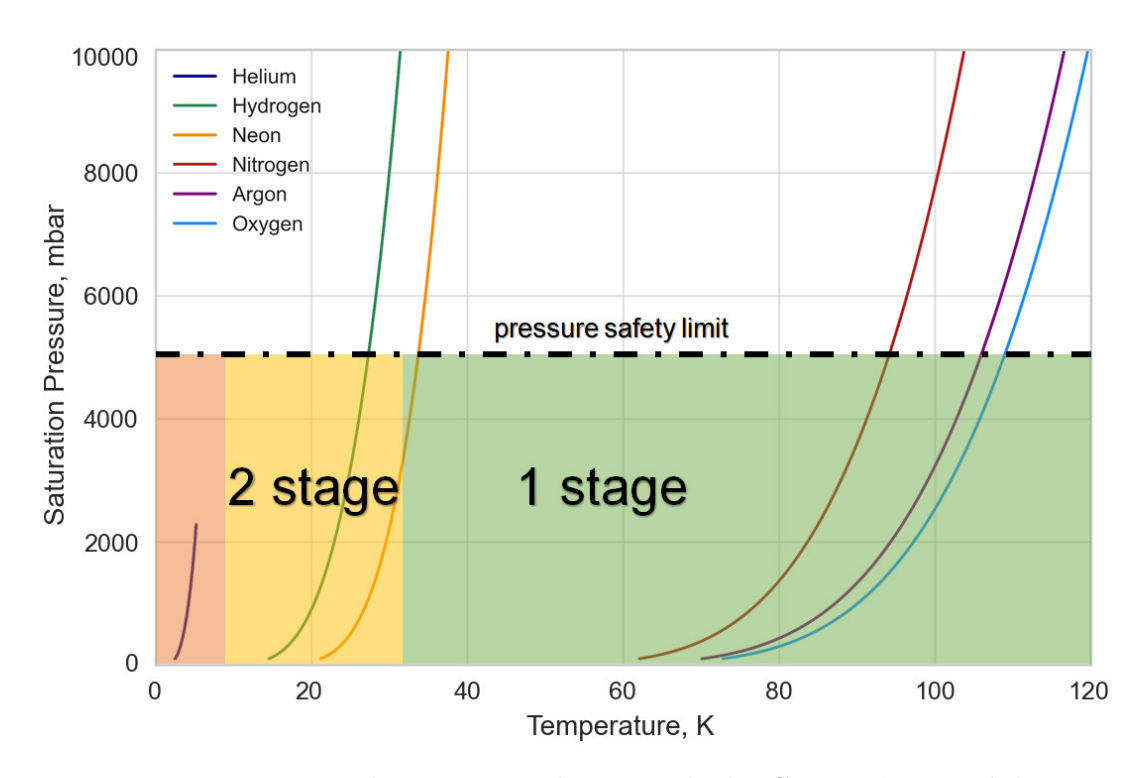


Figure 3.3: Potential experimental area with the Cryocooler capability

3.3 Design of the Experiment

The experiment begins by defining the operating window for the selected working fluids and the condenser temperature range. These choices guide the capillary geometry, the routing and bending strategy, and the connection to the filling and pressure control system. The thermal interfaces are sized to match the expected heat input and the available cooling capacity, and the assembly is integrated in a high-vacuum cryostat with a radiation shield to minimize parasitic loads. This framework establishes the layout and control strategy developed in the following subsections.

3.3.1 PHP design

One of the most commonly used indicators for selecting the internal diameter of a pulsating heat pipe is the Bond number criterion, discussed in Sections 1.3.4 and 1.3.7. Despite its limited predictive capability, the Bond number remains a useful first-order guide to delineating the viable operating range of PHPs. In the classical formulation, the admissible range is generally taken as $0.7 \le Bo \le 4.0$ (7; 71). Within this interval, one can infer, for a specified inner diameter, the condenser operating temperature at which the system satisfies the oscillatory-flow condition. From a performance standpoint, it is generally

advantageous to choose the largest diameter that still meets this criterion because it increases the liquid hold-up and enhances heat transport. Figure 3.4 reports the computed Bond numbers for several inner diameters and highlights the corresponding admissible ranges.

Based on the trends in Fig. 3.4, using thermophysical properties at saturation, two inner diameters, 1.3 and 1.7 mm, were selected. For nitrogen and argon, these choices keep the Bond number below the upper bound Bo = 4 over the relevant condenser temperature range, while for neon the same geometry crosses into Bo > 4. This enables a controlled comparison across the classical threshold: operation within the admissible window for N_2/Ar and deliberate probing of the supercritical regime Bo > 4 for Ne. In particular, recent cryogenic studies (e.g., Dixit et al. (34)) have shown that self-excited oscillations may persist even beyond the canonical interval Bo > 4, motivating the inclusion of both sides of the threshold in the present design.

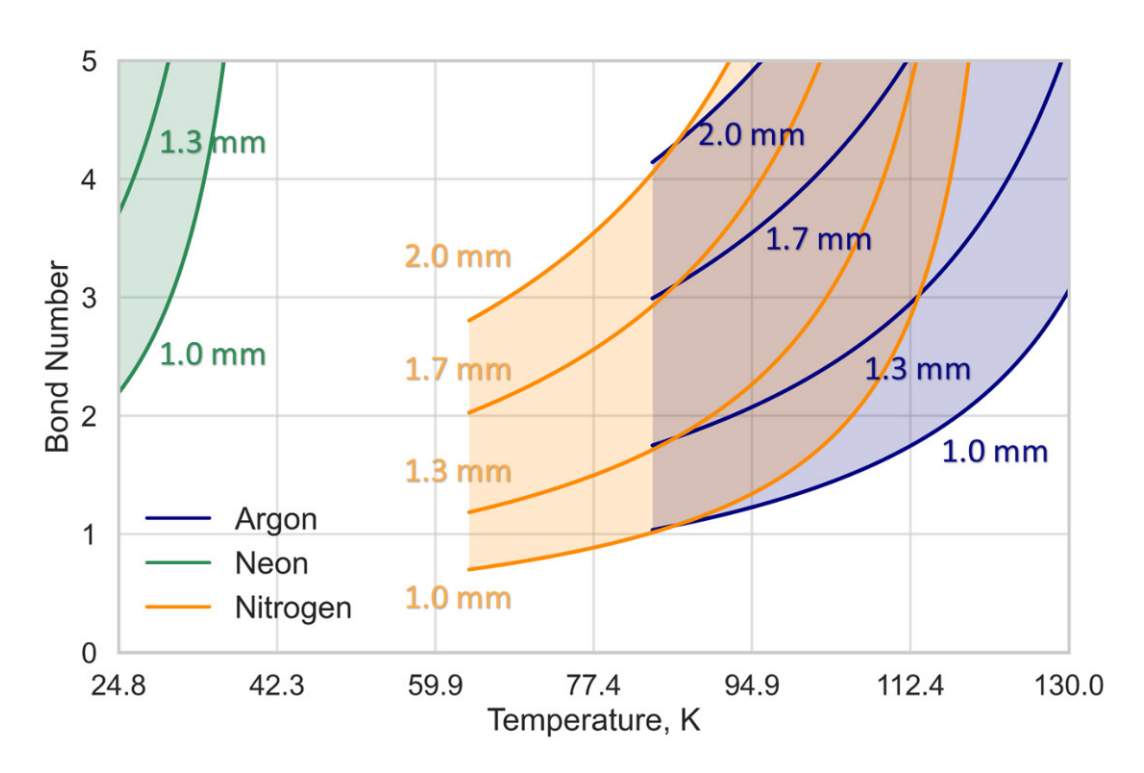


Figure 3.4: Bond number as a function of operating temperature for selected internal diameters.

This experiment investigates the influence of geometry on the performance of a PHP filled with argon, nitrogen, and neon. All capillaries share a fixed outer diameter of 2.5 mm for interchangeability and are fabricated from stainless steel 316L. The main rationale for stainless steel is to minimize axial heat leak so the adiabatic section remains nearly adiabatic under vacuum. Its low thermal conductivity limits the coupling between the evaporator and the condenser and allows a thermal-switch mode when the working fluid

is absent. A secondary rationale concerns the fidelity of the formation, as 316L maintains the inner diameter during tight bends better than softer metals such as copper. The common outer diameter unifies the mechanical and thermal interfaces and simplifies the swapping between variants with different inner diameters.

The first fabrication step involved bending a single continuous capillary tube into the PHP structure using a custom-made bender plate. The most challenging part of the process was preserving the internal channel cross-section during bending, which primarily limits the minimum achievable bending radius and the achievable in-plane vertical bend packing density. In this setup, a fixed bending radius of 5 mm was manufactured, with a loop pitch of 170 mm with the total length of 1977.08 mm. Consistent spacing between bends was required to ensure proper alignment within the condenser and evaporator plates. Notably, no welding was used, the entire PHP was formed from a single capillary tube. After bending, the capillary was mounted on custom-designed copper plates shown in Fig. 3.5 and tightened evenly with screws. The outer holes are used to interface with the cryocooler, while auxiliary holes are used to fix the plates together. The plates are made from high-purity copper with a RRR of 80. Screw placement ensures good thermal contact across the entire surface. This mitigates local overheating by distributing heat more uniformly. Each plate includes a central hole for mounting cylindrical Cernox® sensors. The plate dimensions are 50 mm ×107.5 mm.

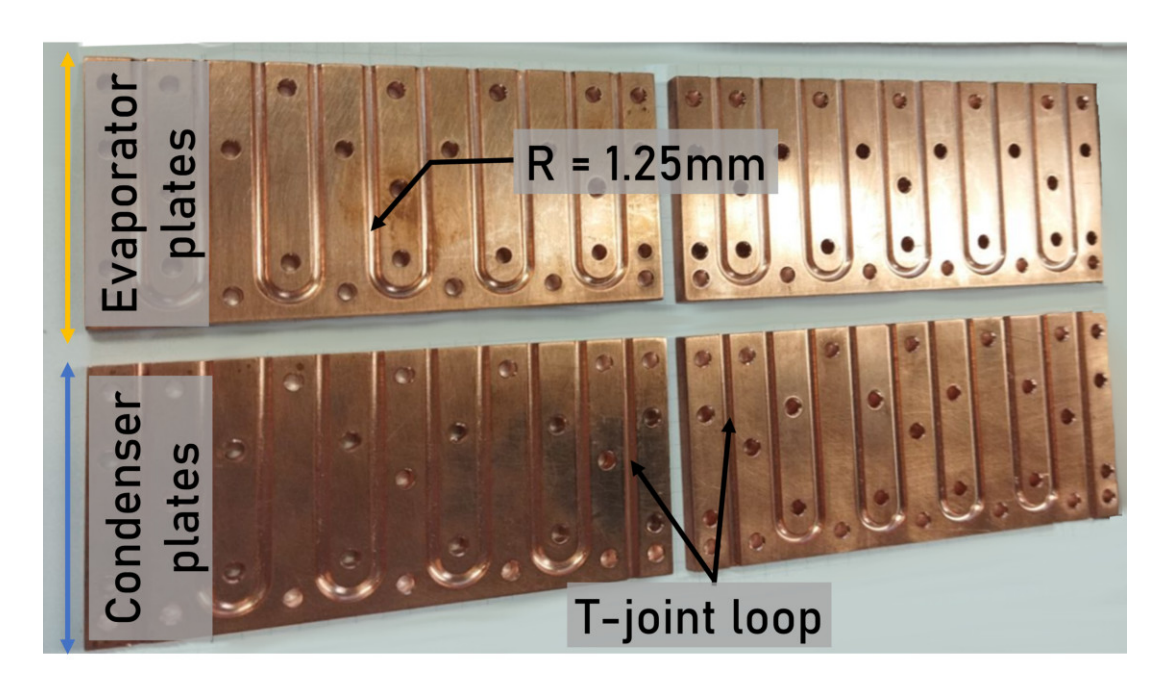


Figure 3.5: Copper plates for evaporator and condenser mounting

The complete assembly, shown in Fig. 3.6-A, includes 3D-printed holders to stabilize the adiabatic section and prevent mechanical deformation. Figure 3.6-B displays a silver-

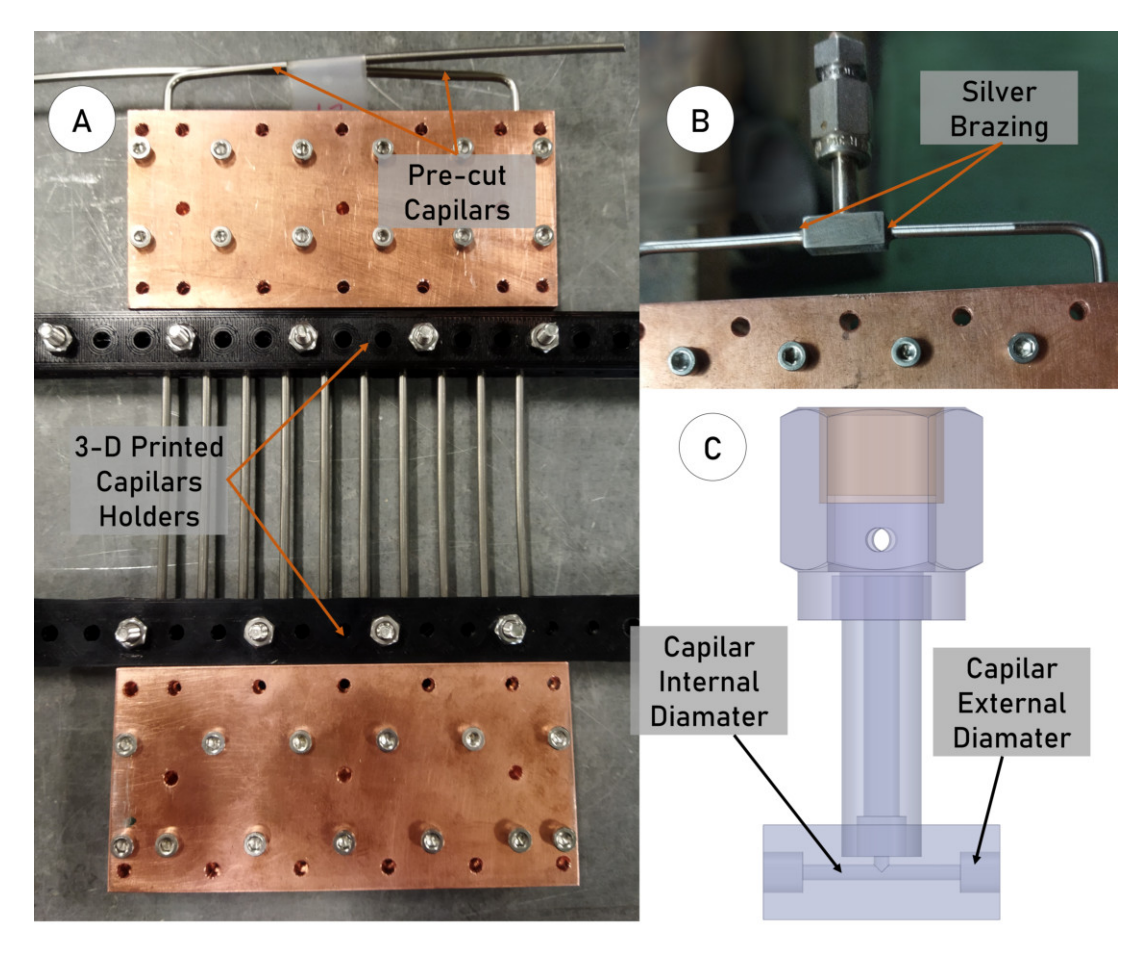


Figure 3.6: (A) Fully assembled PHP mounted with copper plates and 3D-printed holders, (B) silver-brazed T-joint connecting the capillary to the filling line, (C) CAD model of the T-joint geometry

brazed T-joint used to connect the capillary to the filling system. The CAD model of this joint is shown in Fig. 3.6-C. This junction is structurally sensitive due to mechanical stress during high-pressure operation and the potential for contamination during brazing. Each connection was hand-brazed with a thermal sink to draw heat away and protect the previously made bond on the opposite branch of the T-jont. The internal diameter matches precisely that of the capillary to prevent flow constriction or expansion, whereas the outer diameter is slightly larger than that of the pipe to seal it with silver.

The final stage in PHP fabrication involves verifying the mechanical integrity of the T-joint connections under thermal and high pressure cycling. The primary indicator of successful assembly is helium leak test, which confirms both the structural robustness and the quality of the brazed joints. Leak testing was performed using a PHOENIX Quadro helium leak detector (Leybold), with a detection sensitivity down to 1×10^{-12} mbar · l/s. Prior to leak detection, each PHP sample was subjected to repeated thermal cycling to simulate cryogenic fatigue stress. As illustrated in Fig. 3.7-A, the PHPs were immersed in liquid nitrogen and then returned to ambient temperature three times over the span

of several hours. Following thermal fatigue, a pressure test was conducted by filling the PHPs with nitrogen gas at 7 bar. The system was held at this pressure for several hours in the set-up as shown in Fig. 3.7-A, to confirm the mechanical endurance of the joints under internal pressurization. No decrease in pressure was were observed. Subsequently, helium leak detection was carried out on 1.3 and 1.7 mm PHPs. All PHPs passed the test, confirming that the T-joints remained sealed and mechanically sound, even after undergoing combined thermal and pressure cycling.

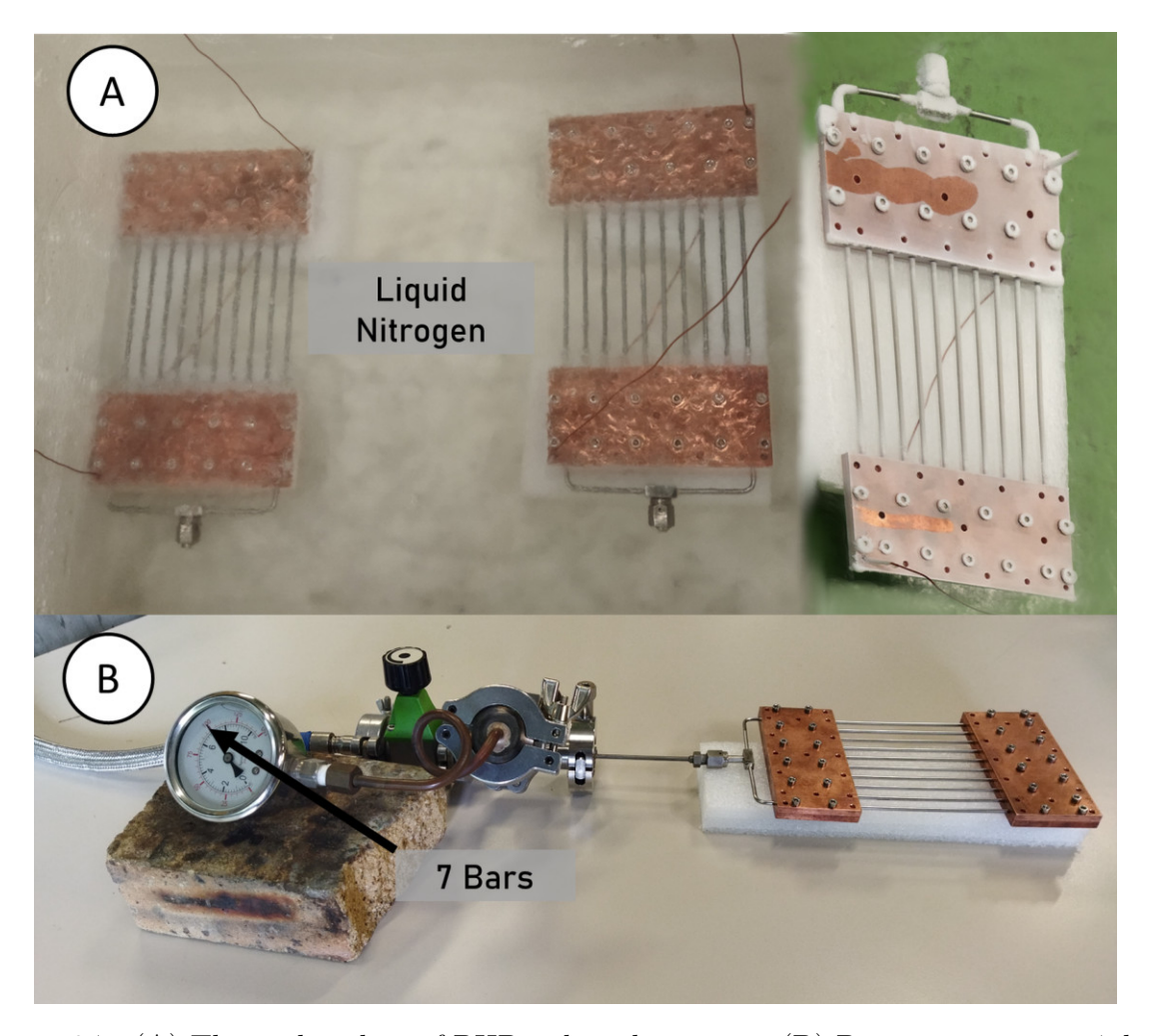


Figure 3.7: (A) Thermal cycling of PHP in liquid nitrogen, (B) Pressure testing at 7 bar.

3.3.2 Cryocooler Connection and Radiation Shield Design

The PHP module and its thermal interfaces were designed around a two-stage cryocooler. The cryostat is a vacuum enclosure adapted to house the cryocooler and the PHP assembly and is shown in Fig. 3.8. The geometry of the cryostat defines the envelope and port layout of the assembly, and the maintained high vacuum suppresses gas conduction and convection, thus reducing parasitic heat loads from the environment to the radiation

shield and cold stages. Within these spatial constraints, the first stage of the cryocooler serves as the primary thermal anchor for the nitrogen and argon PHPs and supports the radiation shield, while the second stage is dedicated to low-temperature operation with neon. The corresponding saturation temperatures at atmospheric pressure are 77.3 K for nitrogen, 87.3 K for argon and 27.1 K for neon.

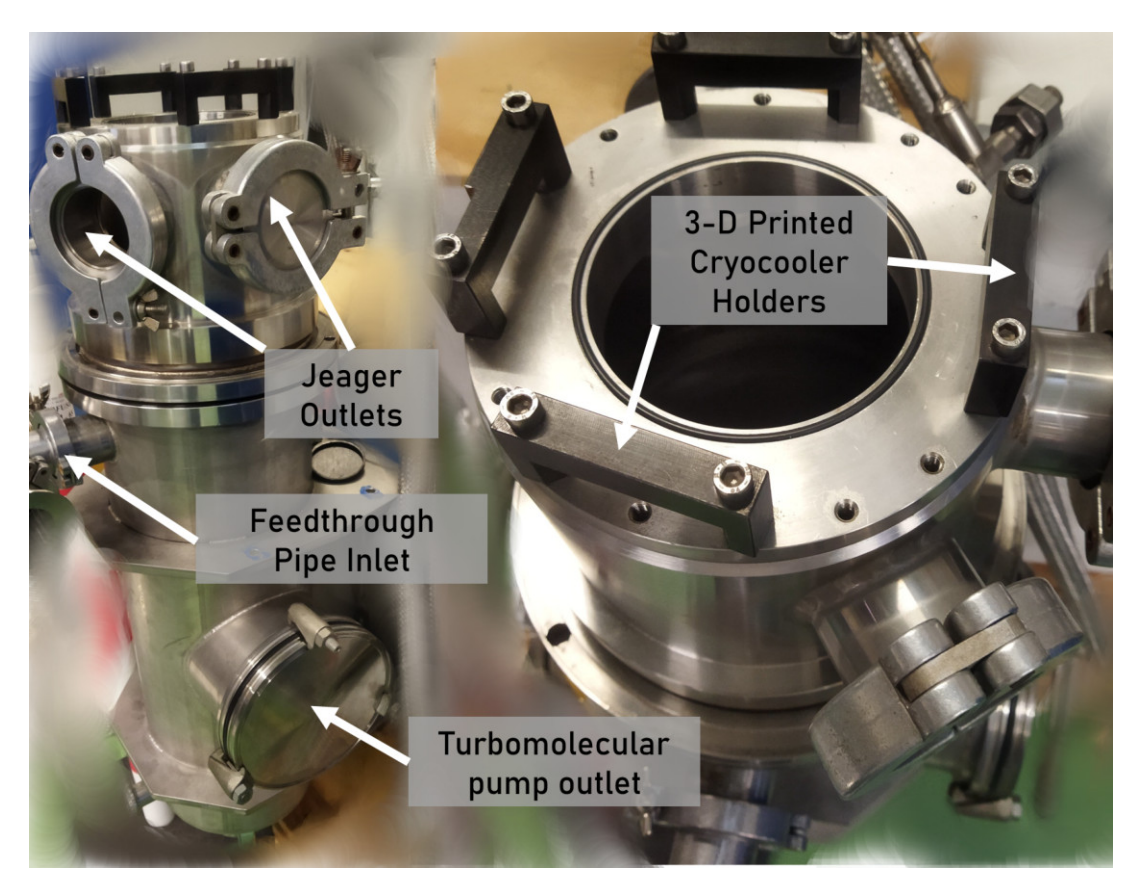


Figure 3.8: Photographs of the cryostat used in the experimental setup

The primary design goal was to minimize the temperature difference across the thermal interfaces while limiting the amount of copper used. This is consistent with good cryogenic practice: minimizing thermal resistances at interfaces while controlling mass reduces static and dynamic heat loads and eases cooldown. Designing the thermal connector also required balancing multiple constraints, including the fixed dimensions of the PHP module discussed earlier and the limited internal volume of the cryostat. In practice, a compact and well-matched cryostat is advantageous because it helps maintain high vacuum conditions and reduces external heat exchange to the radiation shield and cold stages. These considerations informed the finite element optimization carried out in ANSYS Mechanical, and the temperature-dependent copper data used in the FEM model are shown in Fig. 3.9.

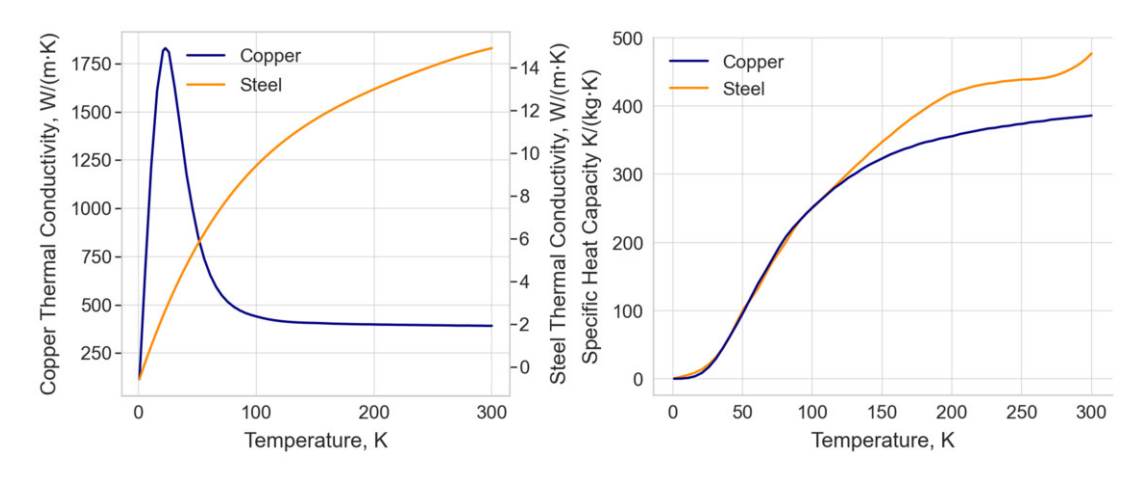


Figure 3.9: Temperature-dependent properties of copper used in FEM optimization

Due to the cylindrical geometry of the cryocooler stages (Fig. 3.1), the connectors were shaped to maximize the real contact area and to provide a smooth circular to rectangular transition, thus lowering contact resistance while remaining within the cryostat envelope. The length and profile of the transition were determined via a parametric FEM study under cryostat clearance constraints. The selected variant is the shortest geometry that satisfied the overall thermal and mechanical objectives. Numerical simulations were performed with boundary temperatures of 77.3 K for the first stage and 27.1 K for the second stage. Fixed thermal loads of 36 W and 10 W, respectively, were applied at the connector interfaces. On the outer surfaces of the condenser plates, a uniform heat flux was imposed to represent the thermal load transported toward the heat sink. The resulting temperature fields are presented in Figs. 3.10 and 3.11, which illustrate the thermal distribution across both the connector and condenser plates for each stage.

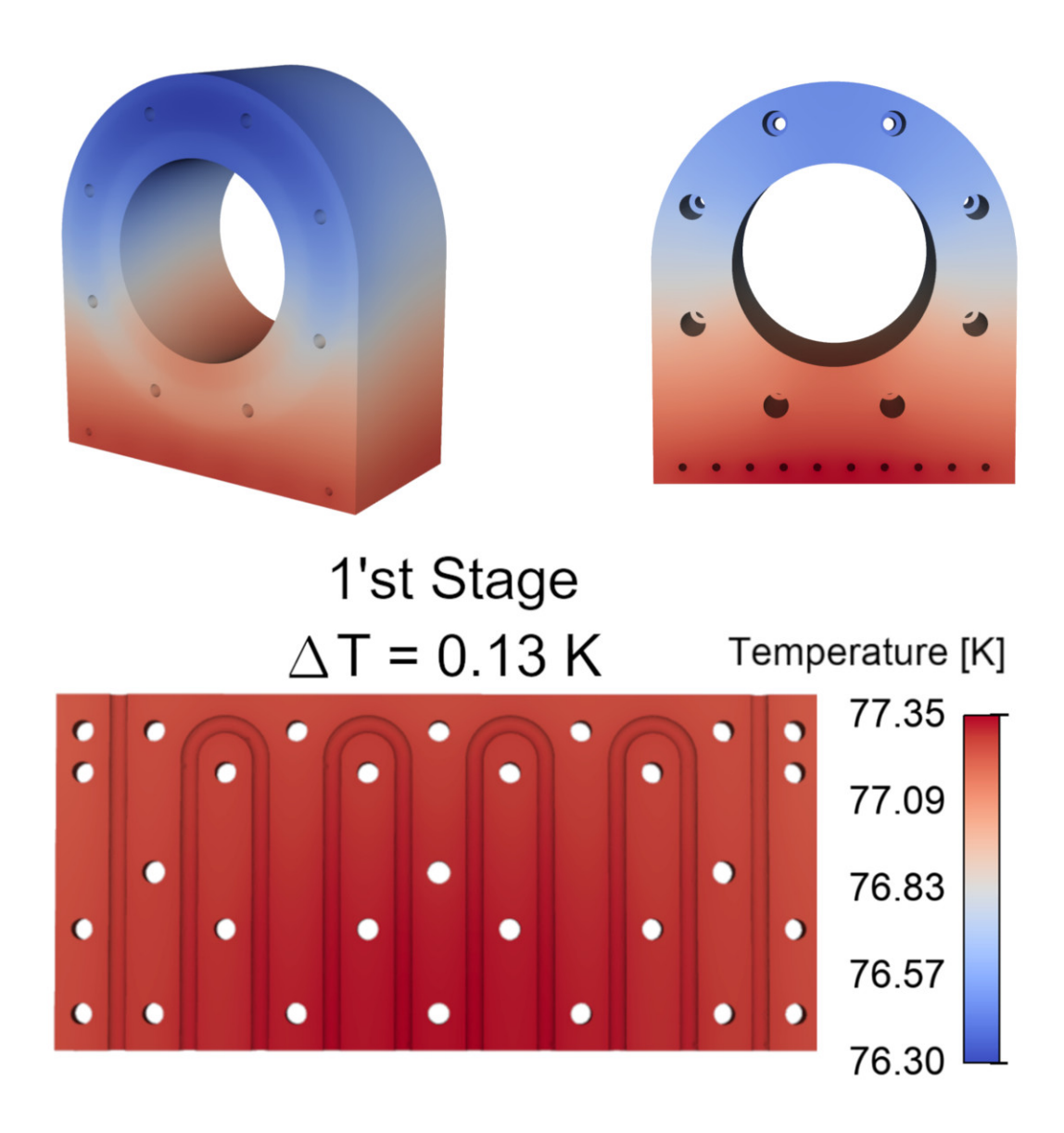


Figure 3.10: Simulated temperature distribution across the thermal connector and condenser plate attached to the first stage of the cryocooler.

The maximum temperature difference observed on the condenser surface was 0.13 K for the first stage and 0.02 K for the second stage. In steady-state operation, the lateral temperature spread on the condenser can be smaller than in the isolated FEM case, even though the effective cryocooler capacity integrated in the system is lower than the manufacturer capacity without an attached cold mass. The mechanical connection to the second cryocooler stage is shown in Fig. 3.12. Position 2-B is a through screw that engages in the stepped mounting hole of the thermal interface. Position 2-A is the washer on the opposite side that closes the joint. For the evaporator plate, full depth screws 1-A are used, corresponding to a 10 mm plate thickness. The condenser uses inner screws that clamp the condenser and evaporator plates together and outer screws 2-B that connect

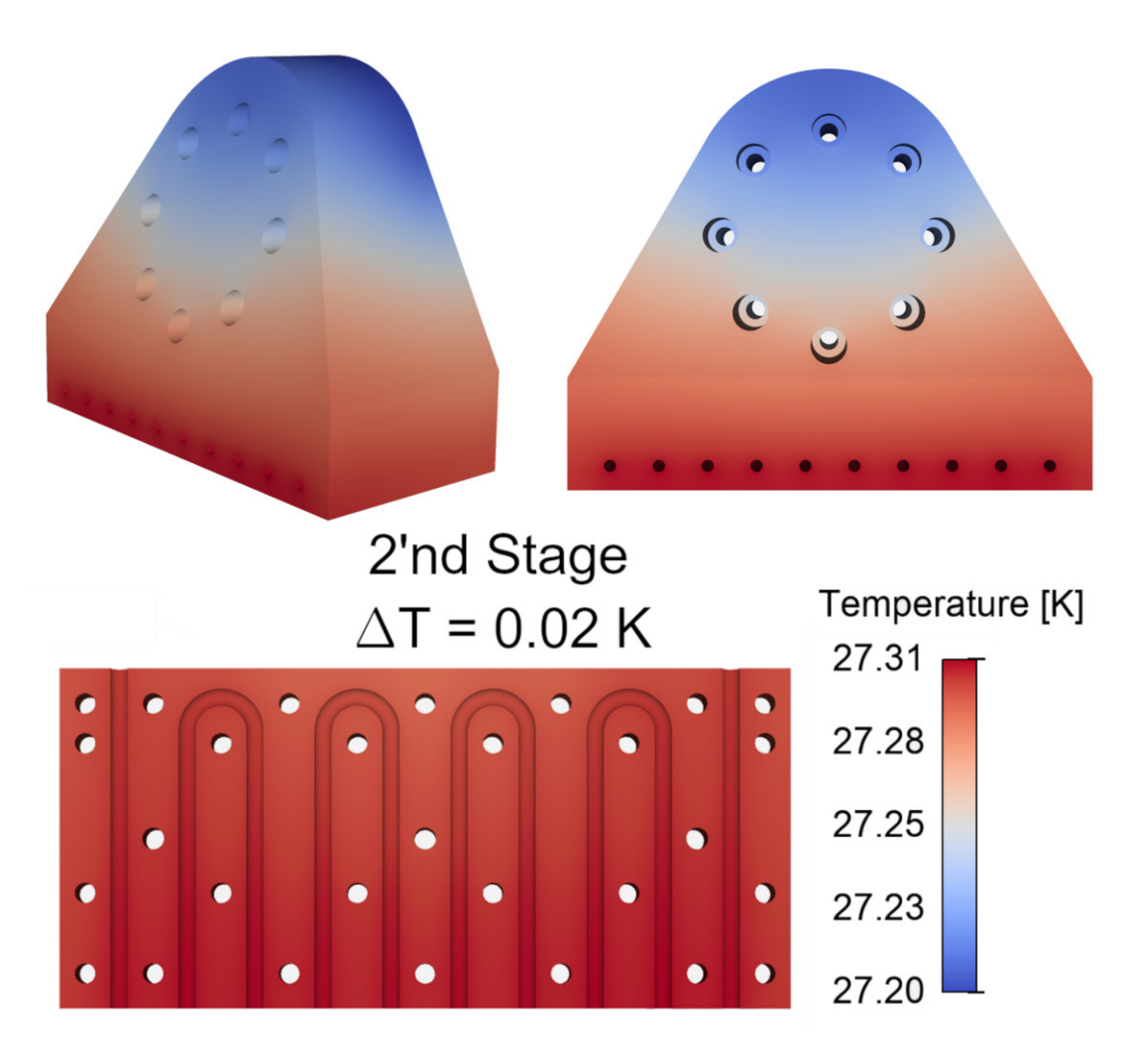


Figure 3.11: Simulated temperature distribution across the thermal connector and condenser plate attached to the second stage of the cryocooler.

the plates to the thermal interface. Label 3-A denotes the T-joint connection to the filling tube.

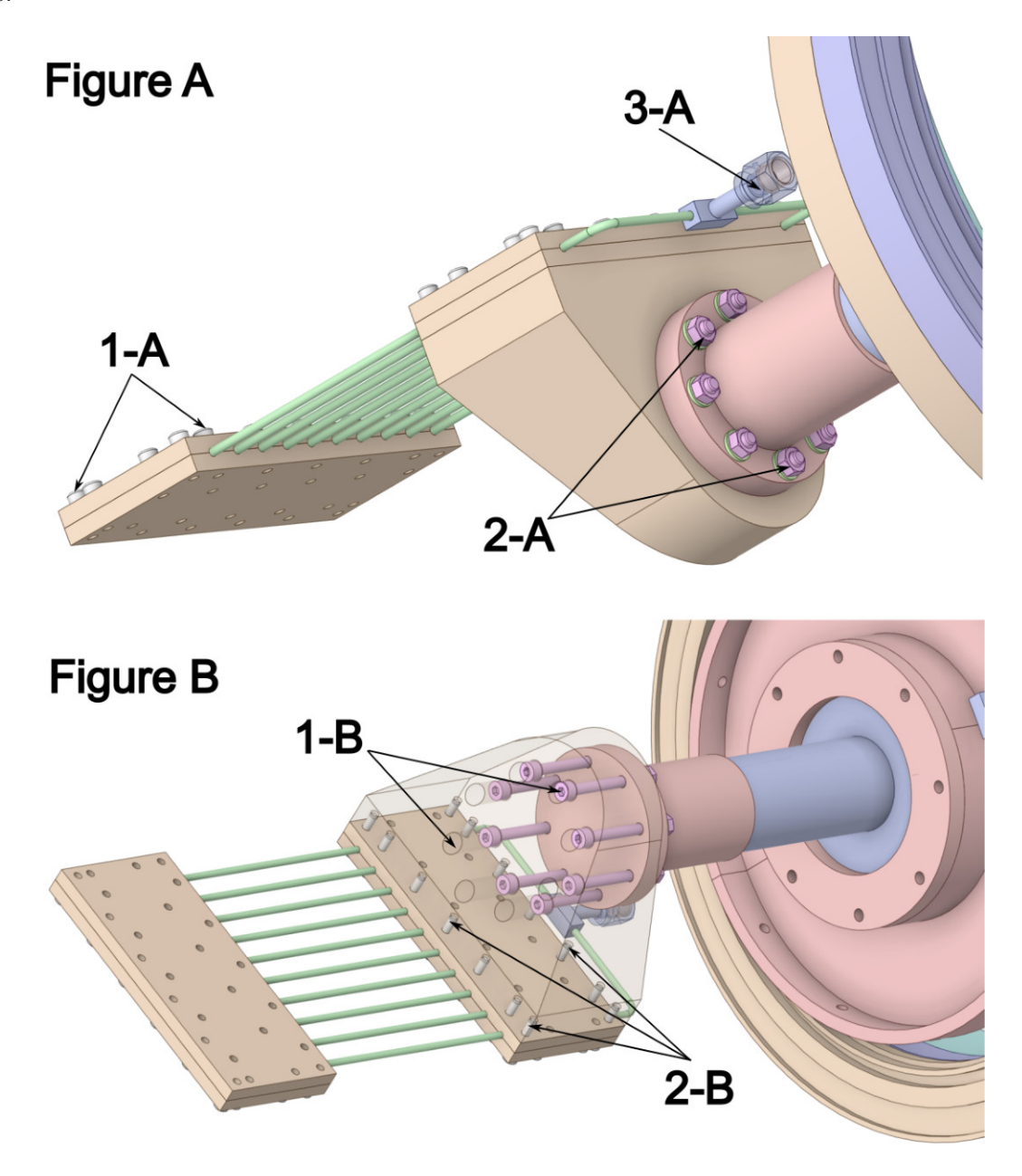


Figure 3.12: Mechanical connection of the PHP interface to the second cryocooler stage. Labels: 2-A—locking nut and washer, 2-B—cryocooler interface screw, 1-A—evaporator mounting screw, 3-A—T-joint with feedthrough pipe connection.

The upper flange at C-2 and D-4 in Fig. 3.13 provide thermal contact with the upper part of the cold head (D-3), as well as a mechanical interface for attaching the PHP via the mounting points D-1. The label C-1 enables the filling tube to pass through which connects the PHP T-joint with the external gas supply system. The radiation shield, fabricated from high-purity copper, is attached to the connector using screws at the D-2 locations. The complete assembly, including the PHP interface and the thermal

connection to the second stage, is shown in Fig. 3.14.

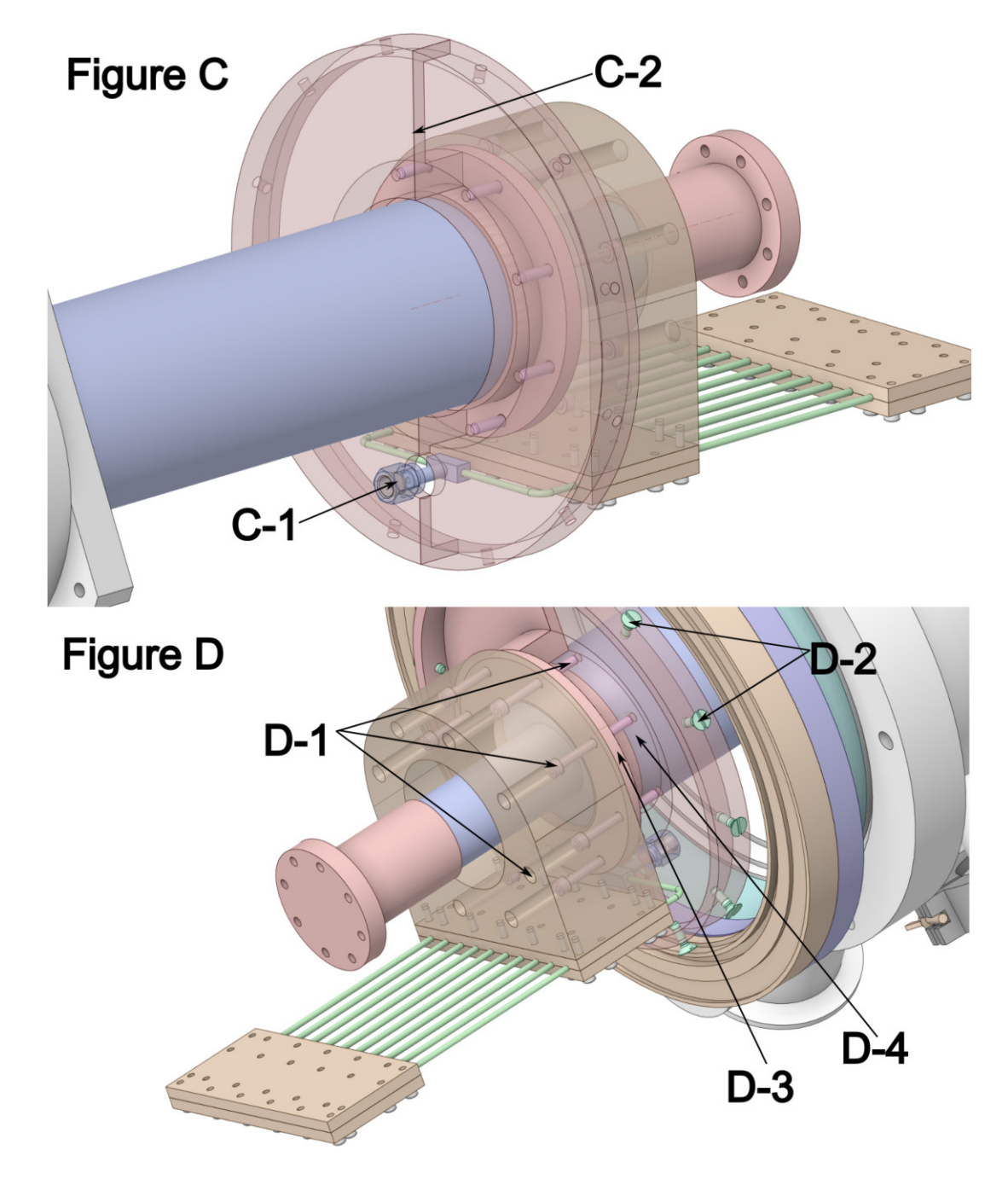


Figure 3.13: CAD rendering of the thermal connector and radiation shield assembly. Labels: C-2 and D-4—connector elements, D-3—cold head interface, D-1—PHP mounting points, C-1—cutout for the T-joint extension.

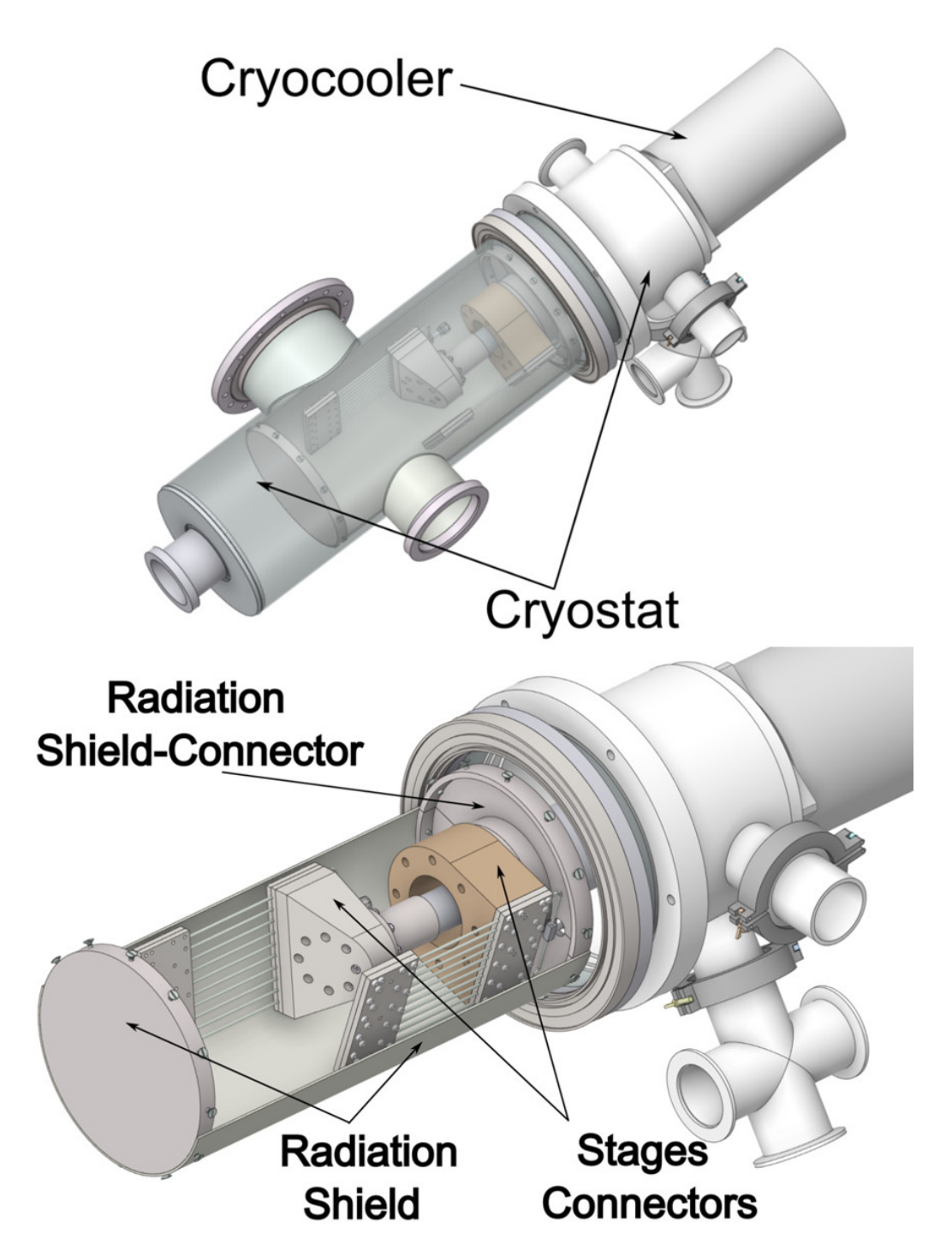


Figure 3.14: Exploded view showing the PHP mounting structure and radiation shield with the connection to the second stage of the cryocooler.

A radiation shield is commonly used in cryogenic systems to reduce parasitic heat load via thermal radiation. Since the interior of the cryostat is evacuated using a turbomolecular pump and maintained at a vacuum range of 10^{-6} mbar, convective and conductive heat transfer are effectively suppressed leaving radiation as the dominant mode of energy transport. Radiative heat exchange can be minimized in two main ways: by lowering the surface emissivity or by reducing the temperature difference between radiating surfaces.

The first method is achieved by wrapping the cylindrical radiation shield in multi-layer insulation (MLI), consisting of 15 layers of aluminum sheets separated by polyester spacer nets, where stacked low-emissivity foils create multiple reflections that reduce the effective emissivity and the net radiative heat load. The second approach involves thermally anchoring the shield to the first stage of the cryocooler. Thermal anchoring of the shield to the first stage acts as an intermediate temperature sink that pulls the shield temperature toward the first-stage level, reducing the temperature difference between radiating surfaces rather than increasing the cryocooler's intrinsic cooling power. As a result, the net radiative exchange between the inner wall of the shield and the test object (in this case, the PHP) becomes negligible (< 1 mW) due to the T^4 dependence in the Stefan-Boltzmann law. This arrangement also minimizes external thermal disturbances at the evaporator and condenser surfaces, thereby improving the quality of temperature measurements. The radiation shield mounting is shown in Figure 3.15. On the left, the MLI wrapped around the copper rad-shield is presented. The insulation is locally held waxed polyester thread to enhance mechanical stiffness and minimize the risk of contact with the cryostat walls or accidental suction of insulation material during vacuum pump initial launching. The central part of the figure displays the radiation shield made of high purity copper without the MLI. The mechanical joint and the bottom lid of the radiation shield are visible. In its operational orientation, the lid faces downward in alignment with the gravitational vector. The assembly is secured using flat-head screws. On the right, the interface component connecting the radiation shield to the top part of the cryocooler is shown. The holes labeled as the top part also serve to hold the connector between the condenser and the cryocooler. The entire structure is supported via threaded mounting holes, which align with recesses in the component labeled D-1 in Figure 3.13.

3.4 Selection of Sensors and Measurement Instruments

Two types of temperature sensors are used in the experimental setup: Cernox® thin film resistance temperature sensors and Pt100 platinum resistance thermometers. The Cernox® 1050 sensors, featuring a barrel-shaped ceramic encapsulation, are specifically designed for cryogenic applications. Their resistance increases as temperature decreases (negative temperature coefficient), making them highly sensitive and stable in cryogenic conditions. Six such sensors are embedded directly into dedicated holes in the evaporator and condenser plates, as shown in Fig. 3.16. Using three different sensors results in more reliable readings of averaged thermal resistance. Pt100 was used for auxiliary measurements. These sensors exhibit a nearly linear resistance—temperature relationship and a

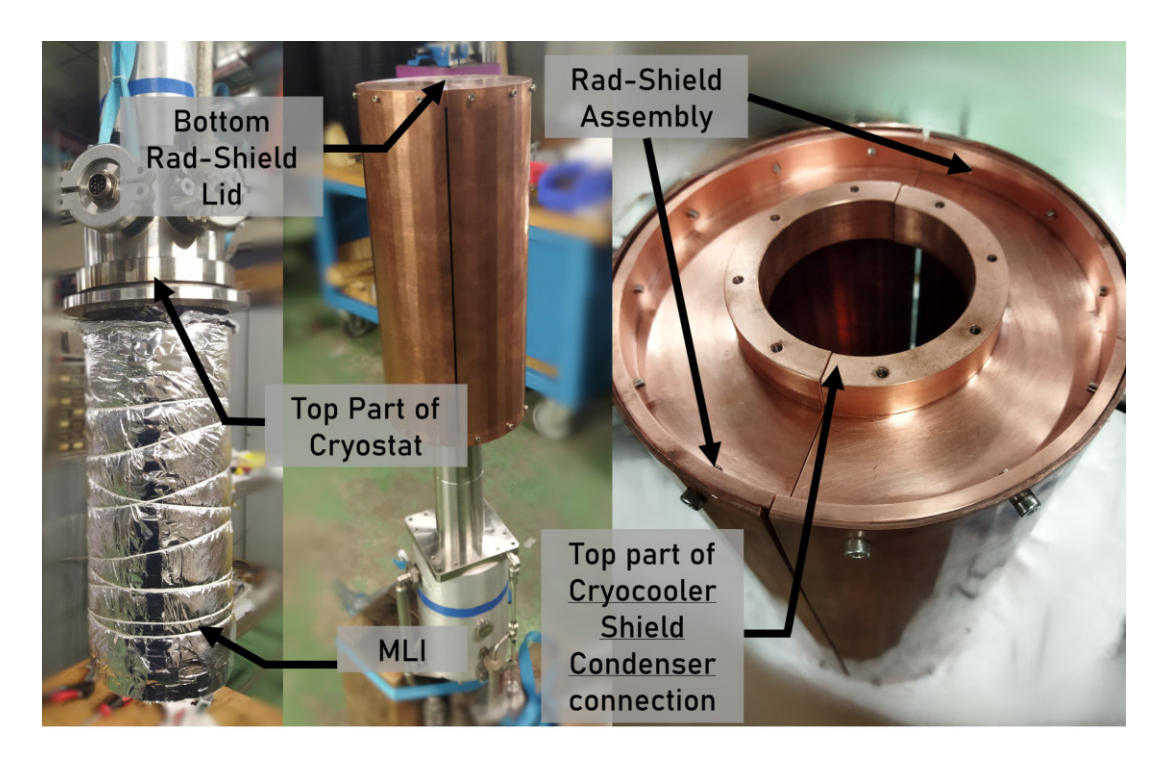


Figure 3.15: Radiation shield components and their assembly with cryocooler and thermal interfaces.

positive temperature coefficient, although their accuracy degrades in deep cryogenic conditions. In the present set-up, one Pt100 monitors the radiation shield to determine when steady state is reached, a second Pt100 on the feeding tube serves the same purpose by indicating stabilization of the fill line, and a third Pt100 tracks the buffer temperature during the filling procedure to improve the estimation of the filling ratio. For precision in measurements, all temperature sensors are connected using four wires. Current is supplied via copper wires, chosen for their low electrical resistance, while voltage is provided using manganin wires, which exhibit low thermal conductivity and temperature independent resistivity. This solution minimizes voltage drops caused by lead resistance and suppresses parasitic heat transfer along connections which are present in environments with a wide range of temperatures.

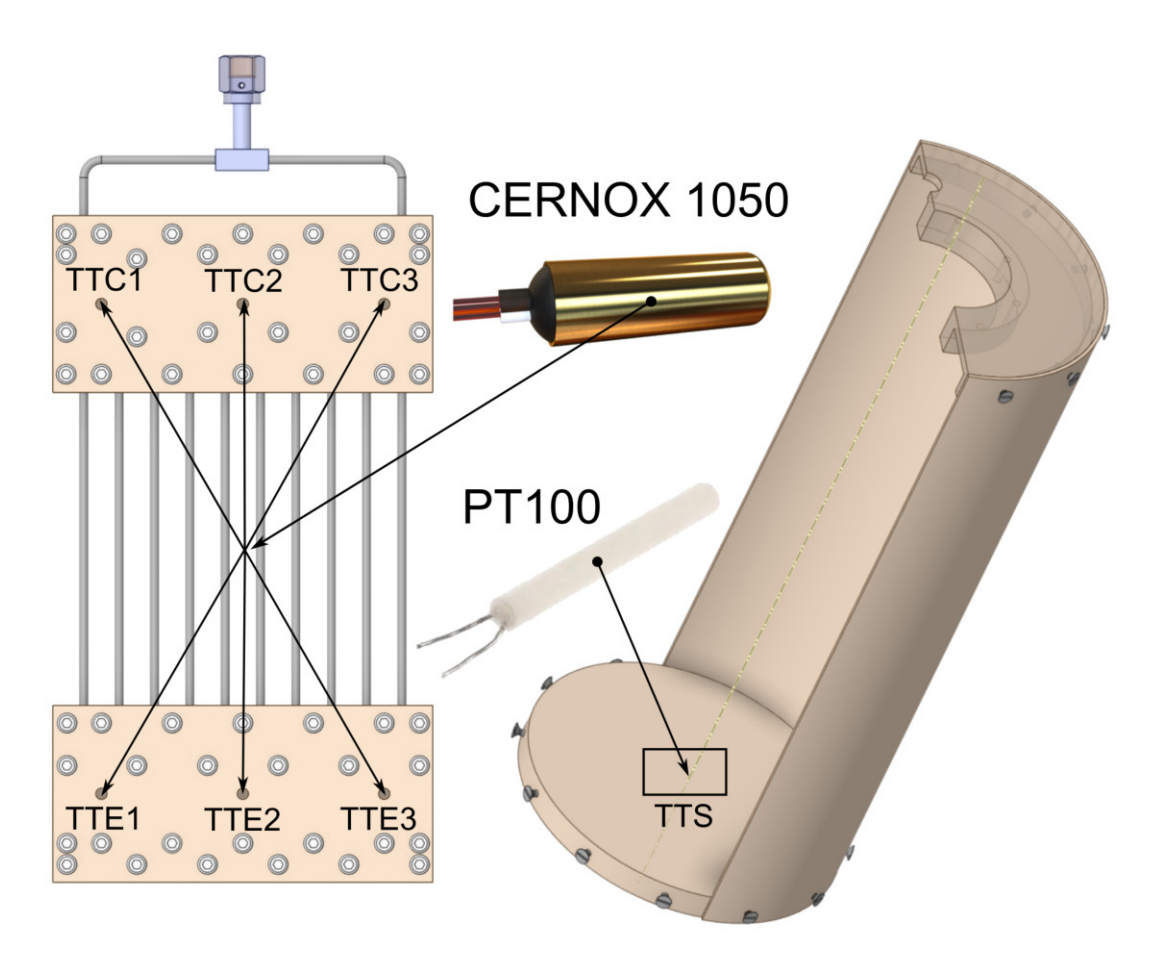


Figure 3.16: Cernox[®] placement at the PHP slots, and location of Pt100 on rad-shield

To further ensure accurate readings, thermalization of measurement cables was done at multiple points, as illustrated in Fig. 3.17. Thermalization refers to the process of gradually removing parasitic heat conducted along wires by thermally anchoring them to solids with relatively high internal energy like radiation shields or interfaces of cryocoolers. Without proper thermalization, heat from room temperature could reach the sensors and distort measurements. Copper plates, thermal interface parts and the shaft of the cryocooler were used to anchor the cables mechanically and thermally to colder structures.

In the present experiment, pressure is measured both to control initial conditions during the filling process and to track the dynamic behavior of the system during operation. Three MKS pressure transducers are used for this purpose, each assigned to a specific measurement point. The vacuum inside the cryostat is measured using an MKS QuadMag® 974B transducer. It combines three measurement principles depending on the pressure range: thermal conductivity at high pressure, ionization at intermediate vacuum, and membrane deflection at low pressure. This sensor is used to verify whether the turbomolecular pump achieves a sufficiently low pressure before initiating cooldown. The internal pressure of the PHP is measured using an MKS Baratron® 722B absolute

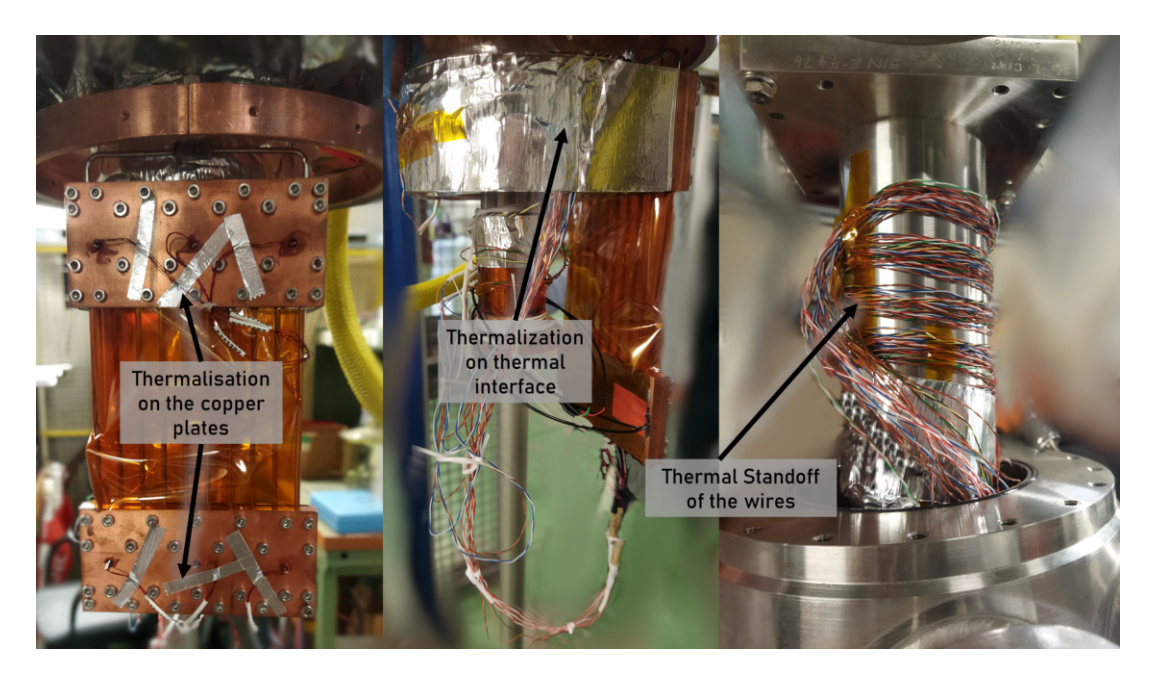


Figure 3.17: Thermalization of measurement cables. Left: connection to the plates and protection of condenser sensor from heat transfer from adiabatic part. Middle: anchoring to thermal interface using aluminum tape. Right: spiral wrapping of sensor cables on the cryocooler shaft.

capacitance manometer, connected externally to the PHP volume via a feedthrough line. The sensor measures the change in capacitance between an Inconel[®] diaphragm and a fixed electrode, providing accurate information on pressure evolution during PHP operation. A second MKS Baratron 722B sensor is installed on the buffer vessel, monitoring the absolute pressure during the filling procedure. Combined with temperature readings, this measurement is used to determine the PHP filling ratio. Placement of the pressure sensors is presented in a later section in Fig. 3.22.

3.5 Condenser Temperature Control

Temperature control at the condenser is used to regulate the system to a desired saturation temperature. For liquid nitrogen, the reference value corresponds to 77.3 K, which is the saturation temperature at 1 atm. In this setup, a PID controller (CTC-100) adjusts the heat input based on the temperature measured at point A (location of the CERNOX® sensor in 3.18). The heater power is regulated to match the cooling demand imposed by the cryocooler. Optimized parameter in the design is the positioning of the heater. Placing it close to the measurement point improves feedback response but may locally distort the temperature distribution near the condenser. Conversely, locating the heater farther from the sensing point reduces its influence on the temperature gradient along the condenser, at the cost of slower thermal response. Two configurations were

simulated: one with a single heater mounted on the radiation shield, and another with two heaters symmetrically placed on the thermal interface between the first cryocooler stage and the condenser plate. Mounting the heater directly on the cryocooler surface was not possible due to the geometry of the structural element labeled D-4. The applied boundary conditions are shown in Fig. 3.18.

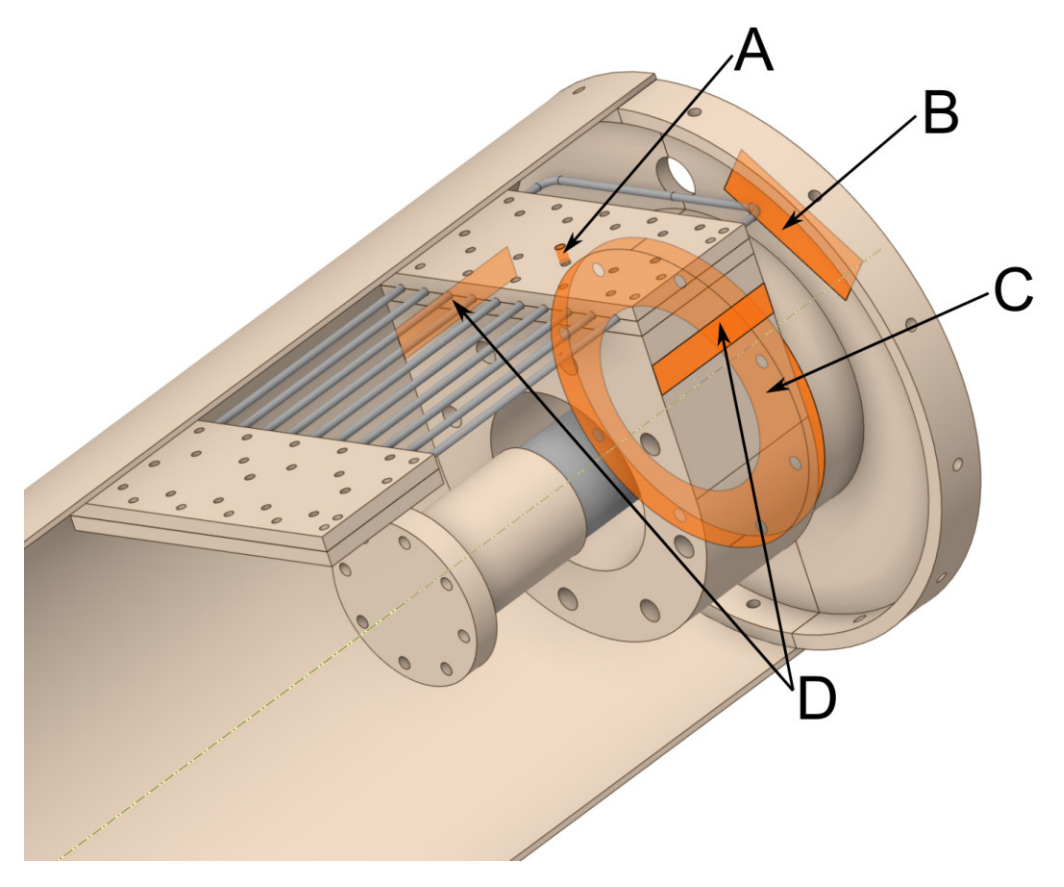


Figure 3.18: Boundary conditions applied to the simplified geometry used in the FEM thermal simulation. A - $CERNOX^{\oplus}$ sensor slot, B - single heater on radiation shield, C - heat extraction surface, D - dual symmetric heaters at the interface.

To compare both configurations, the system was initialized at 77.1 K, and a total heating power of Q = 50 W was applied. Simultaneously, the cryocooler was assumed to extract Q = 36 W at surface C. The resulting temperature distribution after 25 seconds is shown in Fig. 3.19.

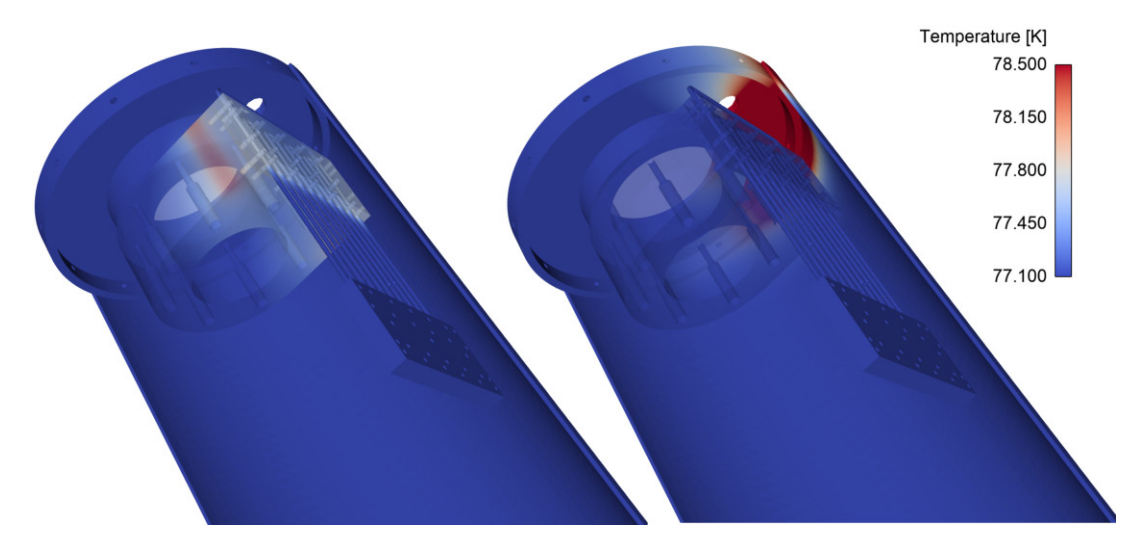


Figure 3.19: Temperature distribution at t=25 s. Configuration: dual heaters (B and D) supplying Q=50 W in total, cryocooler extracting Q=36 W at surface C. CERNOX® sensor positioned at point A.

In the case of the single heater, heat accumulates near the interface between the radiation shield and the cryocooler, with a limited effect on the condenser plate. In the dual-heater configuration, the thermal gradient is more uniform, and no local overheating is observed. The spatial distribution alone does not capture the system's temporal response. Figure 3.20 shows the temperature evolution at the CERNOX® sensor location. In the single-heater case (blue curve), the temperature initially decreases, indicating a delayed response. During this interval, the applied power is insufficient to immediately compensate for the extracted heat, which may interfere with regulation. In contrast, the dual-heater (orange curve) compensates for the cooling load promptly, without an initial temperature drop.

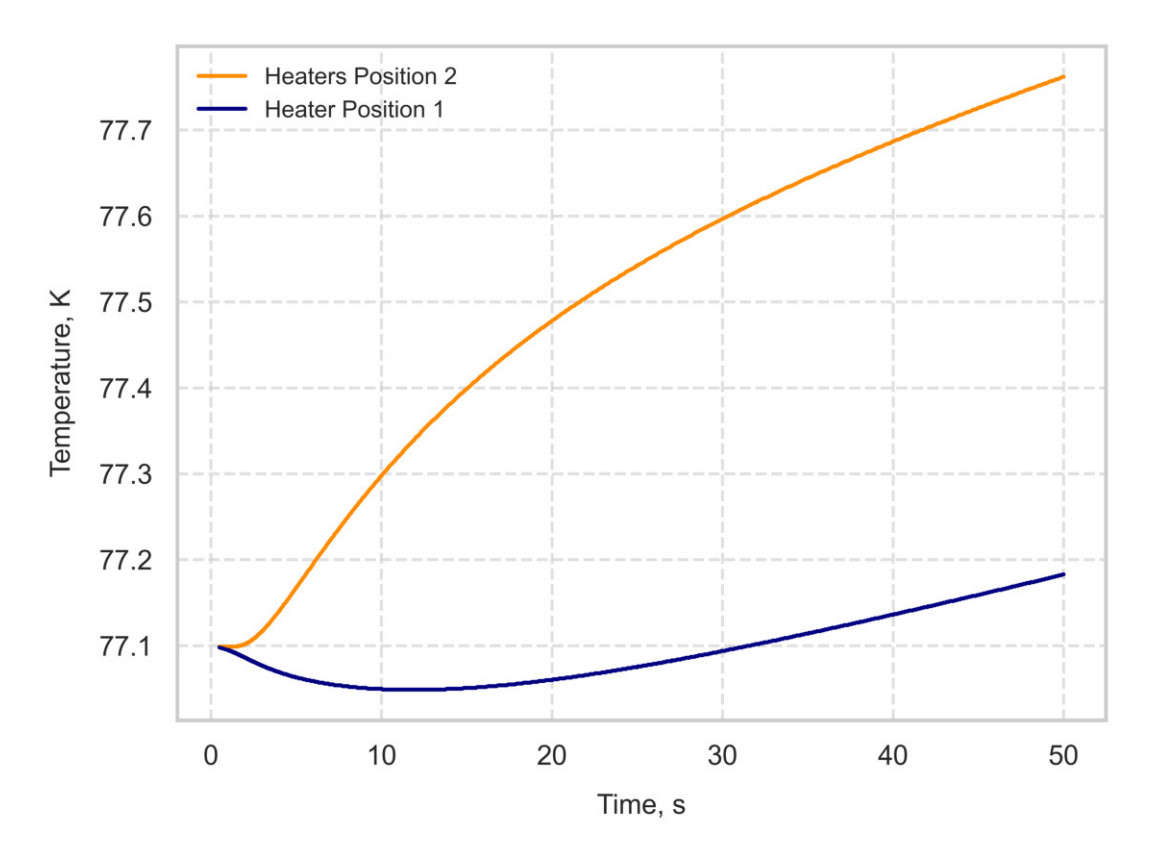


Figure 3.20: Temperature evolution at the CERNOX® sensor position. Blue: single heater 50 W, orange: dual heaters 2x25 W.

Based on the simulation results, two heaters (50 mm \times 10 mm each) were installed on opposite sides of the interface between the cold head and the condenser plate. Their mounting arrangement is shown in Fig. 3.21.



Figure 3.21: Final heater configuration adopted in the cryogenic setup.

3.6 Filling Process

Proper operation of the PHP requires high purity of the working fluid and accurate control of the filling ratio, both of which are obligatory for the correct reproduction of experimental results. This is particularly important in systems where the design process relies on prototype data. To meet these requirements, the filling system includes a high-purity gas source, a series of vacuum-compatible valves and fittings, and a dry scroll pump combined with a pressure measurement system. An overview of the filling setup is presented in Fig. 3.22.

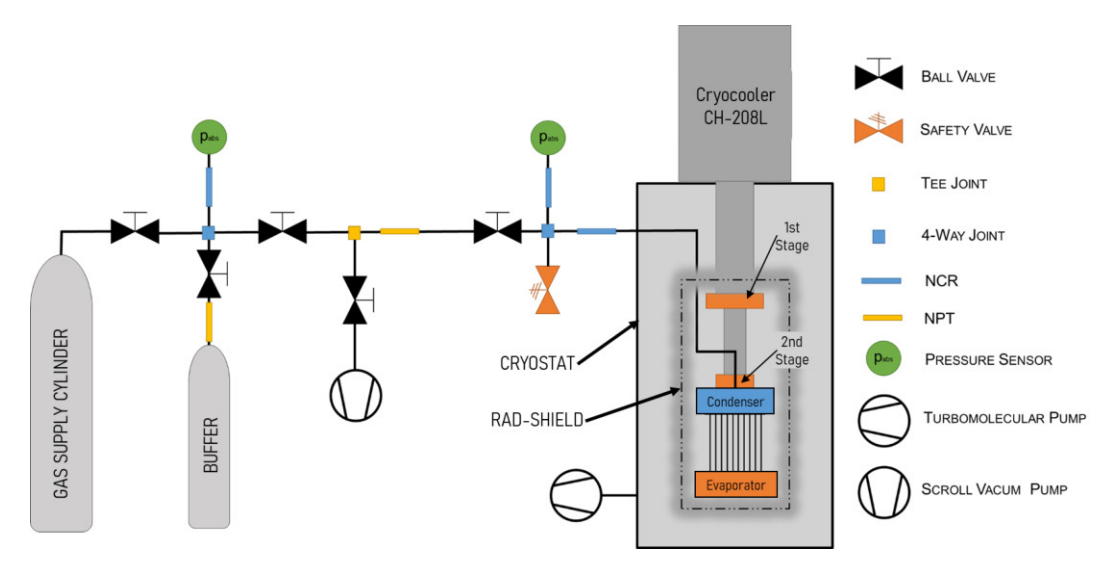


Figure 3.22: Schematic of the gas supply and filling system. All hydraulic components are Swagelok.

All hydraulic components used in the system are supplied by Swagelok. The design includes connections based on two thread types: NPT (National Pipe Tapered) and NCR (National Compression, Reduced). The dry scroll pump is responsible for evacuating both the PHP and the supply line. A 2.25-liter buffer reservoir is used as an intermediate storage vessel during the filling process. The full filling procedure consists of several steps, which may vary depending on whether the working fluid is being changed or the PHP unit has been replaced. The complete process consists of the following:

- 1. Initial pumping of the supply line, with the buffer and PHP isolated. This is required because the pressure regulators are not rated for vacuum on both sides. During this step, the buffer and PHP are kept closed to avoid potential contamination by dust particles or residual gas.
- 2. Flushing of the supply line using the working gas. This involves filling the volume with gas and then evacuating it multiple times to reduce contamination from

previous gases or air.

- 3. Pumping of the PHP and buffer sections with all valves closed on the supply side.
- 4. Flushing of the buffer and PHP sections. This step is critical for removing noncondensable gases and fine particles that cannot be eliminated under static vacuum conditions.
- 5. Charging the buffer with working gas to a pressure at least 0.5 bar above atmospheric pressure.
- 6. The actual filling is conducted by maintaining a constant low temperature at the condenser surface. The gas enters slowly from the buffer and condenses immediately upon contact with the cold surface. This ensures that the internal pressure in the PHP remains near saturation.
- 7. The amount of gas introduced into the PHP is determined from the definition of the FR, which is computed using:

$$FR = \frac{V_l}{V_l + V_g} \cdot 100\% \tag{3.1}$$

Here, V_l is the volume occupied by the liquid phase, and V_g is the volume of vapor, both referring to the internal volume of the PHP capillaries. The mass balance is performed by dividing the system into two control volumes.

3.7 Error Analsyis

Uncertainty analysis follows the GUM (Guide to the expression of uncertainty in measurement) framework (171), which classifies sources as Type A based on statistical analysis of repeated measurements and Type B based on prior knowledge, such as sensor calibration. Both types are combined using standard root-sum-square propagation.

3.7.1 Uncertainty in Thermal Resistance Measurement

The thermal resistance, being an indicator of thermal efficiency in the PHPs, is defined as Eq. (3.2).

$$R = \frac{T_e - T_c}{Q_{\text{evap}}} \tag{3.2}$$

Its uncertainty is computed using standard uncertainty propagation. The temperature uncertainty consists of a Type B component and a Type A component derived from the standard deviation of the measurement series. The combined uncertainties for the evaporator and condenser temperatures are calculated as:

$$u_{T_e} = \sqrt{u_{B,T}^2 + \frac{\sigma_{T_e}^2}{N}}, \quad u_{T_c} = \sqrt{u_{B,T}^2 + \frac{\sigma_{T_c}^2}{N}}$$
 (3.3)

where $u_{B,T}$ denotes the Type B uncertainty of the temperature sensor, σ_{T_e} and σ_{T_c} are the standard deviations of the measured temperatures at the evaporator and condenser, respectively, and N is the number of data points used in the averaging window. In this case, N corresponds to measurements acquired every 5 seconds over the final 15 minutes of each 45-minute power step, under the assumption that a quasi-steady state was reached during this period. The Type B uncertainties of the Cernox[®] temperature sensors are selected based on the target working fluid and corresponding operating temperature.

- Neon at 27.1 K: $u_{B,T} = 10 \text{ mK}$
- Nitrogen at 77.3 K: $u_{B,T} = 16 \text{ mK}$
- Argon at 87.3 K: $u_{B,T} = 16 \text{ mK}$

The heating power Q_{evap} is supplied by a Keithley[®] 2200 programmable power supply. Its uncertainty includes contributions from voltage and current readings. The manufacturer specifies the limits as $u_U = 0.03\% \cdot U$ and $u_I = 0.1\% \cdot I$. The uncertainty in power is provided in Eq. (3.4).

$$u_{Q_{\text{evap}}} = Q_{\text{evap}} \cdot \sqrt{\left(\frac{u_U}{U}\right)^2 + \left(\frac{u_I}{I}\right)^2}$$
(3.4)

The final expression for the combined uncertainty of thermal resistance is given by Eq. (3.5).

$$u_R = \sqrt{\left(\frac{u_{T_e}}{Q_{\text{evap}}}\right)^2 + \left(\frac{u_{T_c}}{Q_{\text{evap}}}\right)^2 + \left(\frac{(T_e - T_c) \cdot u_{Q_{\text{evap}}}}{Q_{\text{evap}}^2}\right)^2}$$
(3.5)

Additional parameter frequently used for quantitative assessment of the thermal performance of a PHP is the effective thermal conductivity expressed as Eq. (3.6), which characterizes the overall heat transport capability of the system. It is calculated based on the average thermal resistance and the geometric properties of the device.

$$K_{\text{eff}} = \frac{L_{\text{PHP}}}{A \cdot R} \tag{3.6}$$

The uncertainty for this quantity is directly obtained from the uncertainty in thermal resistance (Eq. (3.5)), using standard error propagation:

$$u_{K_{\text{eff}}} = \frac{L_{\text{PHP}}}{A \cdot R^2} \cdot u_R \tag{3.7}$$

where $L_{\text{PHP}} = \frac{1}{2}(l_e + l_c) + l_a$ is the effective conduction length, with $l_e = l_c = 45.75$ mm and $l_a = 88.5$ mm, resulting in $L_{\text{PHP}} = 132$ mm. The cross-sectional area is computed as $A = n \cdot \frac{\pi D_i^2}{4}$, with n = 5 capillaries and an internal diameter $D_i = 5$ of the capillary.

3.7.2 Uncertainty in Average Pressure Measurement

Pressure measurements were done using MKS Baratron® 722B absolute capacitance manometers. According to the manufacturer's datasheet, the accuracy of this sensor is better than 0.5% of the reading for the relevant range. The average pressure over the same 15 minutes, like in temperature, pressure is calculated as below.

$$\bar{p} = \frac{1}{N} \sum_{i=1}^{N} p_i \tag{3.8}$$

The measurement uncertainty for average pressure includes both instrument and statistical components in Eq.(3.9).

$$u_{\bar{p}} = \sqrt{\left(\frac{\sigma_p}{\sqrt{N}}\right)^2 + (0.5\% \cdot \bar{p})^2} \tag{3.9}$$

3.7.3 Filling Ratio Calculation Based on Mass Balance

The uncertainty in calculating the filling ratio arises from a combination of volume measurement errors, sensor inaccuracies, thermodynamic property uncertainties, and statistical deviations observed during the experiments. To clarify the derivation process, the experimental setup was segmented into two distinct parts, as shown in Fig. 3.23 with the supply section colored in orange, and the PHP section colored in blue.

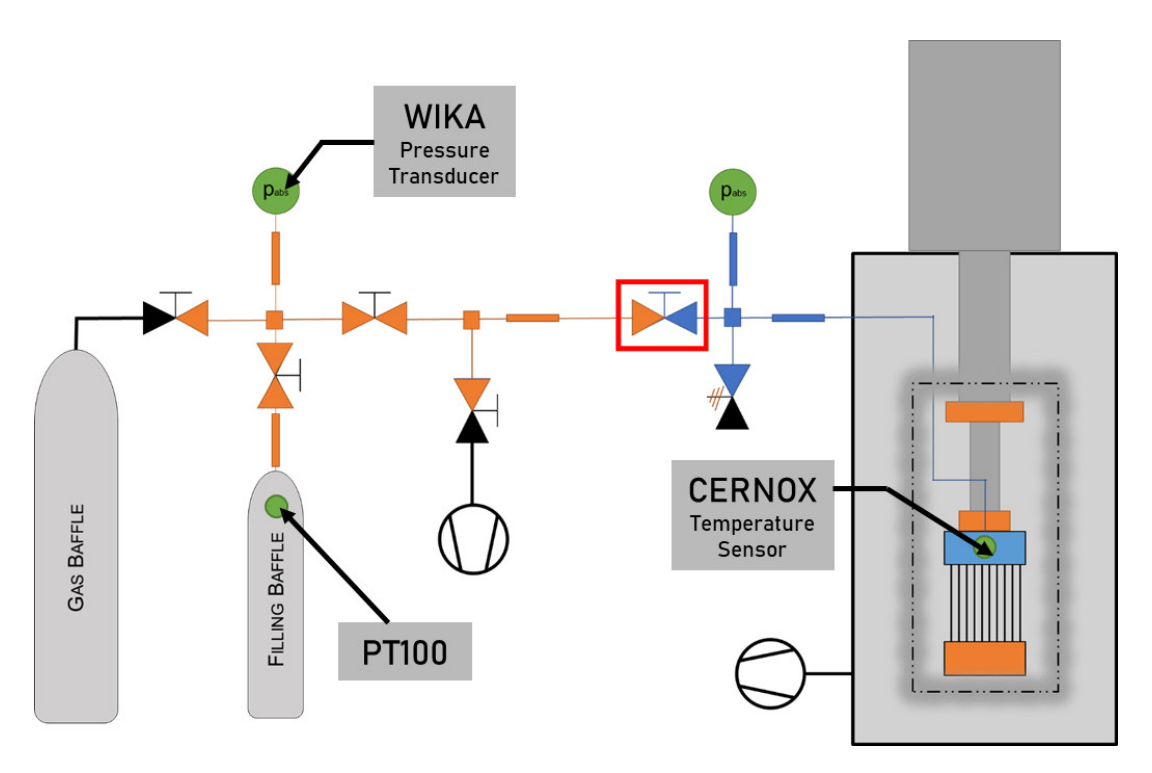


Figure 3.23: Segmentation of the system for filling ratio calculation with marked positions of the sensors. Orange: Supply section volume with gas at ambient temperature, Blue: Volume with gas and liquid inside of PHP.

The filling ratio, defined as the ratio of the liquid volume to the total PHP volume, is not directly measured but inferred via mass balance based on pressure and temperature readings. The gas mass displaced from the orange-marked supply section is assumed to be equal to the gas mass that accumulates in the blue-marked PHP section, which includes both the PHP itself and two segments of the filling line. This assumption forms the basis for the conservation relation in Eq. (3.10) used in the analysis.

$$m_{\text{orangeBefore}} - m_{\text{orangeAfter}} = m_{\text{blue}}$$
 (3.10)

The mass on the blue side is assumed to distribute between three regions:

1. Gas phase inside the PHP: assumed at condenser temperature T_{cond} , measured with a Cernox[®] sensor. The mass of this region is given by:

$$m_{\rm PHPg} = \rho_q(T_{\rm cond}) \cdot (V_{\rm PHP} - V_{\rm liquid})$$
 (3.11)

2. Filling tube inside the cryostat: this segment spans a linear temperature gradient from $T_{\rm cond}$ to ambient temperature $T_{\rm buffer}$. The gas mass is calculated via:

$$m_{\text{blueCryo}} = \int_{T_{\text{cond}}}^{T_{\text{buffer}}} \rho(T) \frac{dV}{dT} dT$$
 (3.12)

For uncertainty estimation, the density is approximated using the average temperature over the interval:

$$\rho_{\text{blueCryo}} \approx \rho \left(\frac{T_{\text{cond}} + T_{\text{buffer}}}{2} \right)$$

3. Filling tube outside the cryostat: assumed isothermal at averaged ambient temperature T_{buffer} , with gas mass:

$$m_{\text{blueOut}} = \rho(T_{\text{buffer}}) \cdot V_{\text{blueOut}}$$
 (3.13)

On the supply side, the change in gas mass due to the pressure drop in the buffer is expressed by:

$$\Delta m = \rho(T_0, p_0) \cdot V_{\text{orange}} - \rho(T', p') \cdot V_{\text{orange}}$$
(3.14)

Combining Eqs. (3.10)–(3.14), the mass balance becomes:

$$\rho(T_0, p_0)V_{\text{orange}} - \rho(T', p')V_{\text{orange}} = V_{\text{blueOut}} \cdot \rho(T') + V_{\text{blueCryo}} \cdot \rho_{\text{blueCryo}} + V_{\text{liquid}} \cdot \rho_l + (V_{\text{PHP}} - V_{\text{liquid}}) \cdot \rho_g$$
(3.15)

Rearranging the above to isolate V_{liquid} , and substituting $FR = \frac{V_{\text{liquid}}}{V_{\text{PHP}}}$, yields the final expression for the filling ratio:

$$FR = \frac{\rho(T_0, p_0)V_{\text{orange}} - \rho(T', p')V_{\text{orange}} - V_{\text{blueOut}} \cdot \rho(T') - V_{\text{blueCryo}} \cdot \rho_{\text{blueCryo}} - V_{\text{PHP}} \cdot \rho_g}{V_{\text{PHP}} \cdot (\rho_l - \rho_g)}$$
(3.16)

Uncertainty Estimation for Geometrically Determined Volumes

The internal volumes of the experimental setup, which include capillaries, filling lines, and buffer tanks, were estimated assuming ideal cylindrical geometry. The general formula for volume inside of capillary is:

$$V = \frac{\pi}{4}D_i^2 L \tag{3.17}$$

The corresponding uncertainty in volume, denoted as u_V , is computed via Gaussian error propagation under the assumption that the uncertainties in internal diameter D_i and length L are independent:

$$u_V = \sqrt{\left(\frac{\partial V}{\partial D_i} u_D\right)^2 + \left(\frac{\partial V}{\partial L} u_L\right)^2} = \sqrt{\left(\frac{\pi}{2} D_i L \cdot u_D\right)^2 + \left(\frac{\pi}{4} D_i^2 \cdot u_L\right)^2}$$
(3.18)

The length uncertainty u_L is determined by the usage of a ruler with ΔL of a millimeter. That means uncertainty came from ruler scale and is expressed by Eq. (3.19).

$$u_L = \frac{\Delta L}{\sqrt{3}} \tag{3.19}$$

with $\Delta L = 1$ mm. For the inner diameter uncertainty u_D , a tolerance of 0.01 mm was considered, based on manufacturer data (Interalloy AG (172)). Accordingly, the uncertainty in the volume of a capillary becomes:

$$u_{\text{capillary}} = \sqrt{\left(\pi \cdot \frac{D_i}{2} \cdot L \cdot u_{D_i}\right)^2 + \left(\pi \cdot \frac{D_i^2}{4} \cdot u_L\right)^2}$$
(3.20)

A relative uncertainty of 5% is assumed due to manufacturing tolerances and the lack of precise internal dimensional data.

The internal volume of the buffer tank with relative uncertainty of 5% provided by the manufacturer (Swagelok®) is therefore taken as:

$$V_{\text{buffer}} = 2.25 \pm 5\% \text{ L}$$
 (3.21)

Each valve contributes an internal volume, taken from CAD models from the Swagelok[®] catalog of:

$$V_{\text{valve}} = 8.168 \times 10^{-7} \text{ m}^3 \tag{3.22}$$

Although not propagated in the uncertainty analysis due to its minor contribution, valve

volume is included in the total side volumes:

$$V_{\text{blue}} = V_{\text{PHP}} + V_{\text{TPS}} + V_{\text{valve}} \tag{3.23}$$

$$V_{\text{orange}} = V_{\text{buffer}} + V_{\text{TBS}} + 3.5V_{\text{valve}}$$
 (3.24)

Consequently, the uncertainty of V_{orange} is provided in Eq. (3.25).

$$u_{V_{\text{orange}}} = \sqrt{u_{V_{\text{buffer}}}^2 + u_{V_{\text{TBS}}}^2} \tag{3.25}$$

Complete uncertainties table of each of the volume in the experiment is provided in Tab. 3.1.

Table 3.1: Volumes and associated uncertainties for PHP components

Volume Component	Symbol	Volume, m ³	Uncertainty, m ³	
PHP 1.3 mm	$V_{\mathrm{PHP,1.3mm}}$	2.62×10^{-6}	4.04×10^{-8}	
PHP 1.7 mm	$V_{\mathrm{PHP,1.7mm}}$	4.49×10^{-6}	5.28×10^{-8}	
Tubes Buffer Side	$V_{ m TBS}$	5.84×10^{-7}	6.12×10^{-9}	
Tubes PHP Side	$V_{ m TPS}$	2.22×10^{-6}	2.23×10^{-8}	
Buffer Tank	$V_{ m buffer}$	2.25×10^{-3}	1.125×10^{-4}	
Single Valve	$V_{ m valve}$	8.17×10^{-8}	_	

Uncertainty in Density and Mass Estimation

The fluid density is determined based on pressure and temperature measurements, using the REFPROP database (59) for thermophysical property evaluation. The gas pressure inside the buffer tank is measured using a WIKA® absolute pressure transducer and 3 bars were assumed as starting pressure, while the corresponding buffer temperature is recorded with an Omega® Pt100. In this calculation, maximal temperature change is assumed as 0.5 K starting from 293.15 K. At the condenser side, temperature is monitored using a Cernox® sensor mounted on PHPs plate. The total uncertainty in density arises from two main sources: sensor accuracy and the uncertainty of REFPROP (59) database described in (148) as 0.1%. For this analysis, the following terms are used to compute the total uncertainty in density:

$$u_p = \left(\frac{\partial \rho}{\partial p} \cdot \frac{p_0 + p'}{2}\right) \cdot u_{\text{WIKA}} \tag{3.26}$$

$$u_{p_{\text{REFPROP}}} = \left(\frac{\partial \rho}{\partial p} \cdot \frac{p_0 + p'}{2}\right) \cdot u_{\text{REFPROP}}$$
 (3.27)

$$u_{T_{\text{Pt}100}} = \frac{\partial \rho}{\partial T} \cdot u_{\text{Pt}100} \tag{3.28}$$

$$u_{T_{\text{Pt}100-\text{REFPROP}}} = \frac{\partial \rho}{\partial T} \cdot \frac{T_0 + T'}{2} \cdot u_{\text{REFPROP}}$$
 (3.29)

$$u_{T_{\text{Cernox}}} = \frac{\partial \rho}{\partial T} \cdot u_{\text{Cernox}} \tag{3.30}$$

$$u_{T_{\text{Cernox-REFPROP}}} = \frac{\partial \rho}{\partial T} \cdot \frac{T_0 + T'}{2} \cdot u_{\text{REFPROP}}$$
 (3.31)

Each of the above terms is added quadratically in the total uncertainty sum for $\rho(T, p)$. The values of $\frac{\partial \rho}{\partial T}$ and $\frac{\partial \rho}{\partial p}$ are computed from REFPROP (59) using differential values from the state after filling of the PHPs (T', p').

$$u_{\rho} = \sqrt{u_{p}^{2} + u_{p_{\text{REFPROP}}}^{2} + u_{T_{\text{Pt100}}}^{2} + u_{T_{\text{Pt100-REFPROP}}}^{2} + u_{T_{\text{Cernox}}}^{2} + u_{T_{\text{Cernox-REFPROP}}}^{2}}$$
(3.32)

Based on the above computation, density uncertainty (3.32) might be extended by volume (3.25) to total mass uncertainty in Eq. (3.33).

$$u_{\Delta m} = \sqrt{(u_{\rho} \cdot V_{\text{orange}})^2 + (u_{V_{\text{orange}}} \cdot \Delta \rho)^2}$$
(3.33)

By simplifying and merging components in Eq. (3.16), the filling ratio is defined by Eq. (3.34).

$$FR = \frac{\frac{\Delta m}{V_{\text{PHP}}} - \rho_g}{\rho_l - \rho_g} \tag{3.34}$$

To complete the uncertainty propagation in Eq. (3.34), the remaining missing components are the uncertainties of the liquid and vapor densities, ρ_l and ρ_g . These densities are obtained from the REFPROP (59) as a function of the temperature measured with a

Cernox[®] sensor located on the PHP surface. Therefore, their uncertainty arises from the temperature measurement uncertainty and the inherent sensitivity of the REFPROP (59) temperature—density relation. For the liquid phase, the density uncertainty is computed as:

$$u_{\rho_{\text{l-Cernox}}} = \frac{\Delta \rho_{\text{l}}}{\Delta T} \cdot u_{\text{Cernox}} \tag{3.35}$$

$$u_{\rho_{\text{I-REFPROP}}} = \frac{\Delta \rho_{\text{l}}}{\Delta T} \cdot \left(T_{\text{PHP}} + \frac{u_{\text{Cernox}}}{2} \right) \cdot u_{\text{REFPROP}}$$
 (3.36)

$$u_{\rho_l} = \sqrt{u_{\rho_{l\text{-Cernox}}}^2 + u_{\rho_{l\text{-REFPROP}}}^2}$$
 (3.37)

And for the vapor phase:

$$u_{\rho_{\text{g-Cernox}}} = \frac{\Delta \rho_{\text{g}}}{\Delta T} \cdot u_{\text{Cernox}}$$
 (3.38)

$$u_{\rho_{\text{g-REFPROP}}} = \frac{\Delta \rho_{\text{g}}}{\Delta T} \cdot \left(T_{\text{PHP}} + \frac{u_{\text{Cernox}}}{2} \right) \cdot u_{\text{REFPROP}}$$
 (3.39)

$$u_{\rho_g} = \sqrt{u_{\rho_{\text{g-Cernox}}}^2 + u_{\rho_{\text{g-REFPROP}}}^2} \tag{3.40}$$

The total uncertainty in FR is propagated by computing the partial derivatives with respect to each variable:

$$\frac{\partial FR}{\partial \Delta m} = \frac{1}{V_{\text{PHP}}(\rho_l - \rho_q)} \tag{3.41}$$

$$\frac{\partial FR}{\partial V_{\text{PHP}}} = \frac{-\Delta m}{V_{\text{PHP}}^2(\rho_l - \rho_q)} \tag{3.42}$$

$$\frac{\partial FR}{\partial \rho_l} = \frac{-(\frac{\Delta m}{V_{\text{PHP}}} - \rho_g)}{(\rho_l - \rho_g)^2}$$
(3.43)

$$\frac{\partial FR}{\partial \rho_g} = \frac{\frac{\Delta m}{V_{\text{PHP}}} - \rho_l}{(\rho_l - \rho_g)^2} \tag{3.44}$$

Finally, these terms are then combined to the total uncertainty and computed as in Eq. (3.45).

$$u_{FR} = \sqrt{\left(\frac{\partial FR}{\partial \Delta m} \cdot u_{\Delta m}\right)^2 + \left(\frac{\partial FR}{\partial V_{PHP}} \cdot u_{V_{PHP}}\right)^2 + \left(\frac{\partial FR}{\partial \rho_l} \cdot u_{\rho_l}\right)^2 + \left(\frac{\partial FR}{\partial \rho_g} \cdot u_{\rho_g}\right)^2}$$
(3.45)

The calculated values of the uncertainty of the filling ratio for different fluids and diameters used are listed in Table 3.2.

Table 3.2: Differential uncertainty u_{FR} (in $\pm\%$) for different fluids and diameters as a function of filling ratio.

FR, %	Argon		Nitrogen		Neon	
	1.3 mm	1.7 mm	1.3 mm	1.7 mm	1.3 mm	1.7 mm
10	± 1.707	± 1.078	± 2.057	± 1.266	± 1.093	± 0.774
20	± 1.974	± 1.418	± 2.274	± 1.561	± 1.429	± 1.192
30	± 2.388	± 1.866	± 2.635	± 1.975	± 1.862	± 1.668
40	± 2.886	± 2.360	± 3.089	± 2.446	± 2.339	± 2.163
50	± 3.431	± 2.878	± 3.602	± 2.948	± 2.838	± 2.668
60	± 4.005	± 3.408	± 4.151	± 3.468	± 3.349	± 3.177
70	± 4.596	± 3.946	± 4.725	± 3.998	± 3.867	± 3.689
80	± 5.198	± 4.488	± 5.314	± 4.535	± 4.390	± 4.202
90	± 5.809	± 5.034	± 5.915	± 5.077	± 4.916	± 4.717
100	± 6.426	± 5.582	± 6.524	± 5.622	± 5.445	± 5.233

3.8 Data Acquisition system

The actual laboratory setup contains all components together with the DAQ used to carry out the experiment, as shown in Fig. 3.24.

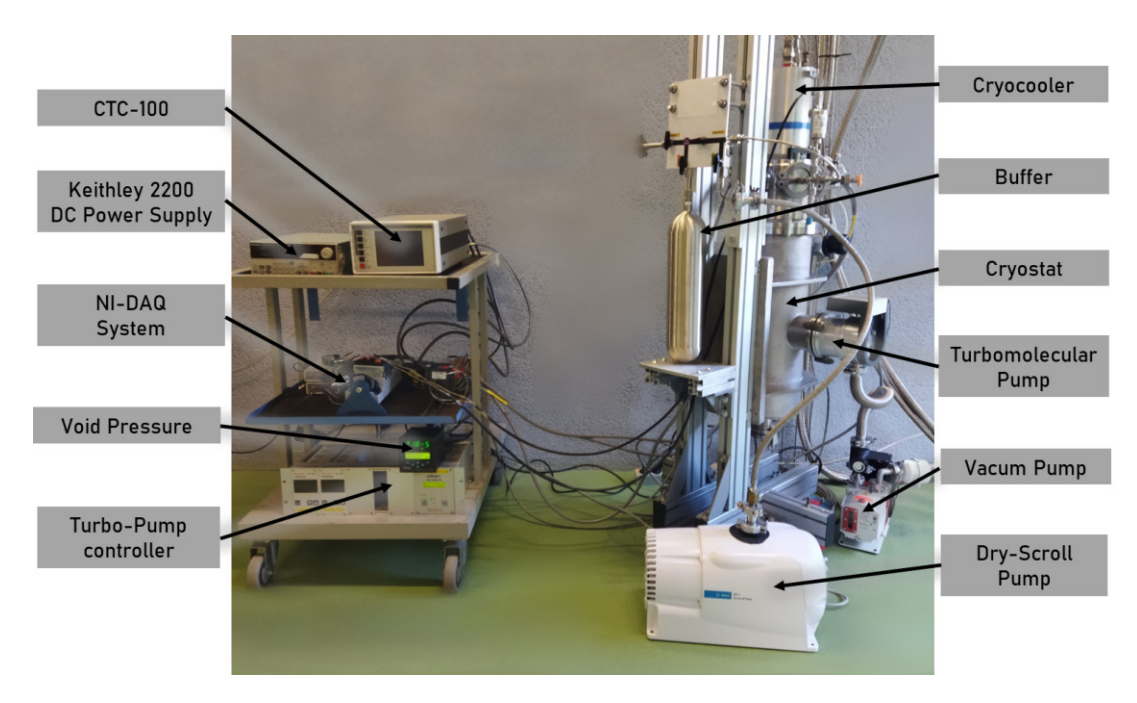


Figure 3.24: Experimental setup with all experimental components including DAQ, pumping system and outside construction.

All sensor signals were recorded using LabVIEW® software. The system integrates temperature, pressure and power measurement modules and continuously monitors and records all experimental parameters. An example user interface used during the neon measurements is shown in Fig. 3.25. The left column displays, from top to bottom, the condenser temperatures, system pressure, heating power applied to the evaporator, and the control heater power on the condenser side. The right column shows the evaporator temperatures, the temperature of the feedthrough line, and the calculated thermal resistance.

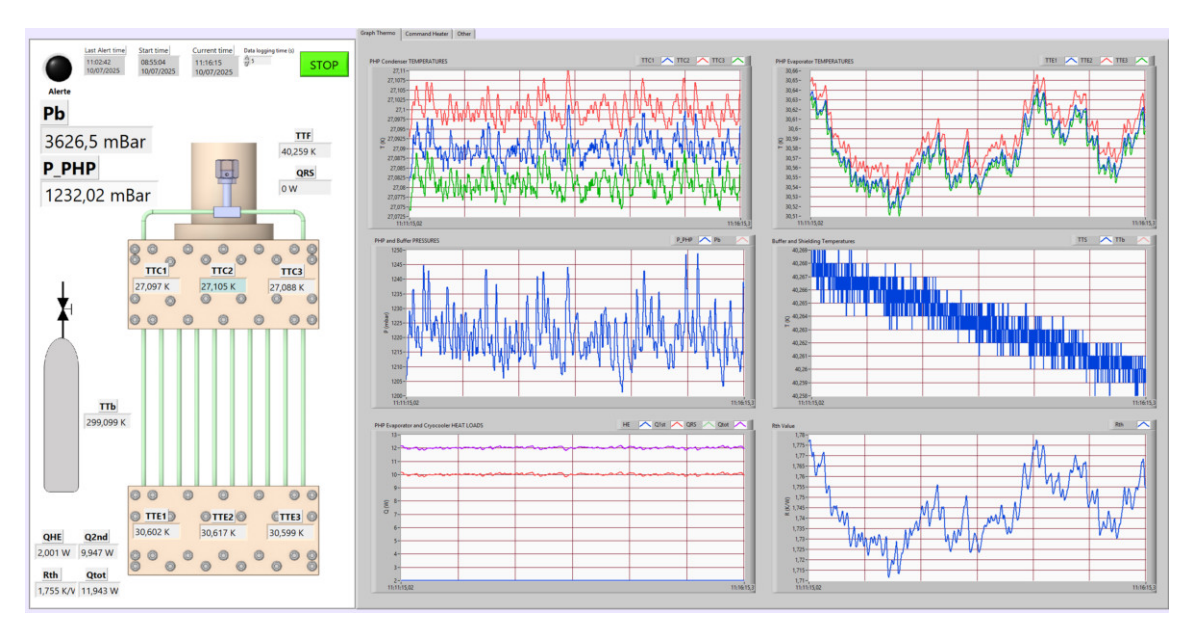


Figure 3.25: Example LabVIEW interface used during measurements with neon.

3.9 Cooling Process and Temperature Regulation

To initiate the experiment, the setup must be cooled down. This requires establishing vacuum conditions inside the cryostat. Lower residual pressure reduces parasitic heat losses and increases the operational range of the cryocooler. In the case of this experiment, it was pumped for at least 2 days. Before activating the temperature control system, the thermal performance limits of the cryocooler were characterized. The available cooling power decreases with increasing thermal load. To determine the behavior of the system, cooling was first performed without any heater-induced load. The minimum temperatures achievable under these conditions are used as reference limits. The cooling curves for both cryocooler stages are presented in Fig. 3.26. The first stage is marked in red, the second stage is marked in blue. The cooling rate of the first stage is lower due to the larger thermal mass it is responsible for, including the radiation shield (Fig. 3.15) and the thermal interface (Fig. 3.10). The second stage exhibits a faster temperature decrease due to reduced thermal inertia and a smaller interface area (Fig. 3.11).

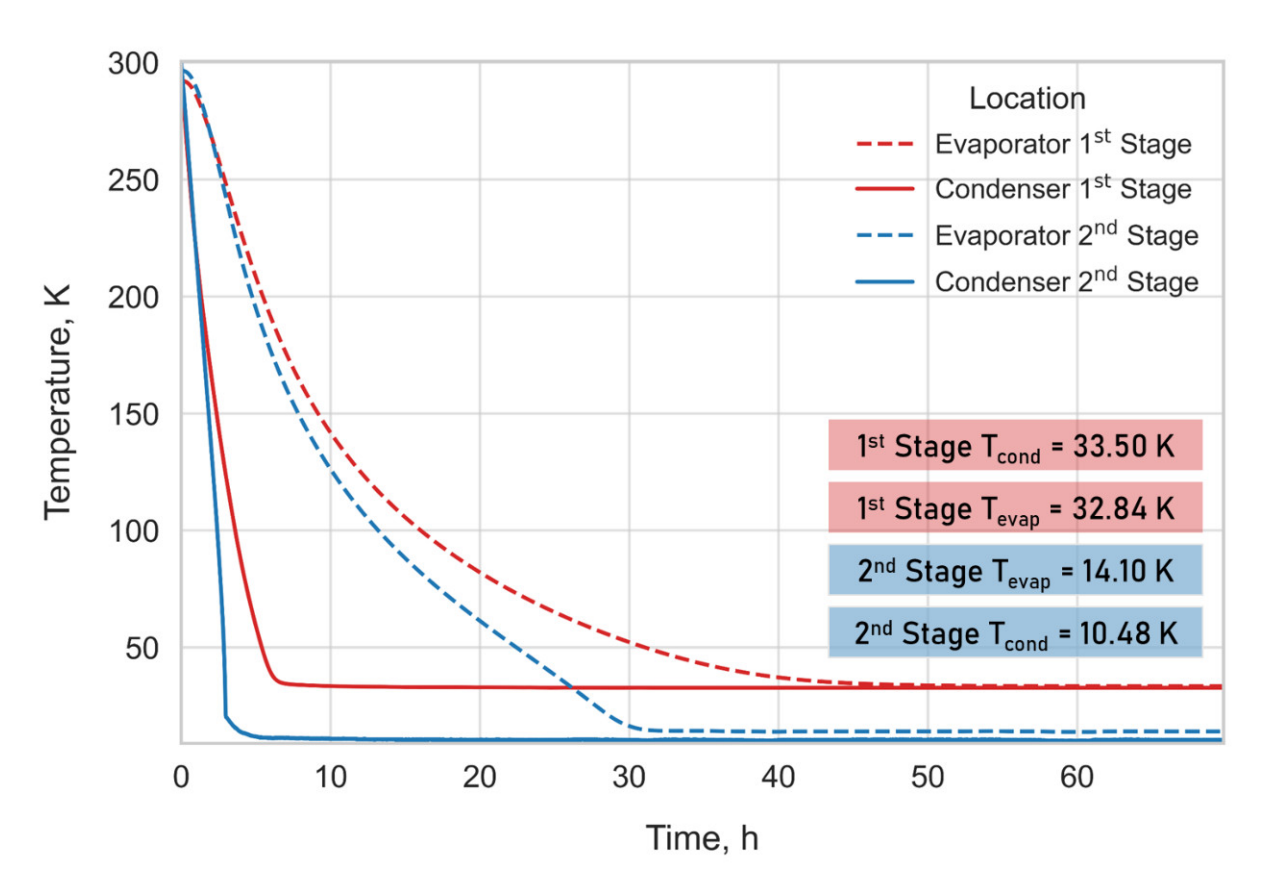


Figure 3.26: Cooling curves for the first and second stage of the cryocooler without fluid inside the capillaries. Cryocooler control limits are indicated by colored rectangles. The red curve corresponds to the first stage, the blue curve to the second.

A lower temperature is reached at the evaporator connected to the first stage compared

to the condenser. This results from radiative heat transfer toward the evaporator surface, despite the use of MLI designed to suppress this effect. In the second stage configuration (Fig. 3.27), higher evaporator temperatures are observed due to the geometry of the radiation shield, which receives heat from both directions. In contrast, the condenser on the first stage is exposed only on one side and is positioned closer to the external heat sink.

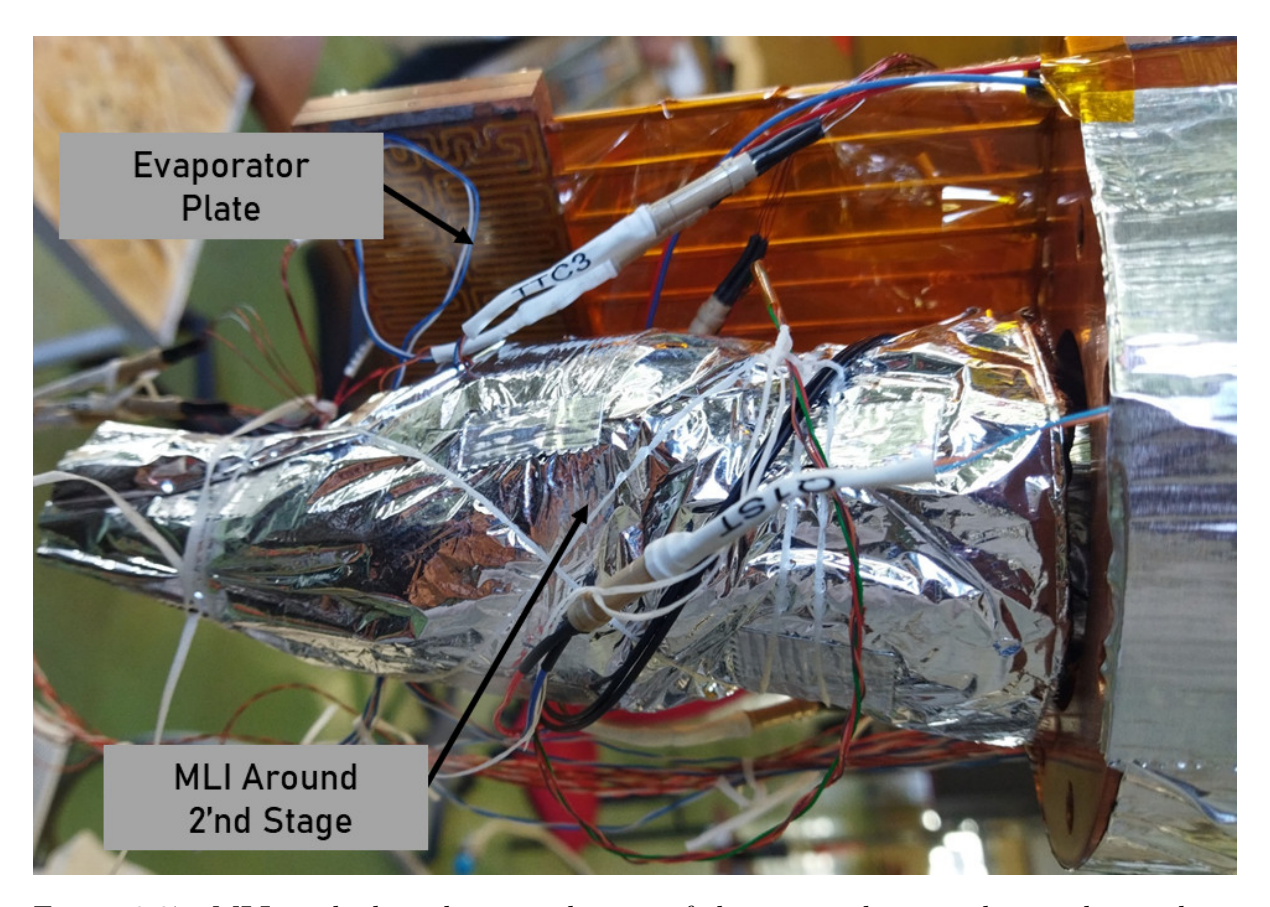


Figure 3.27: MLI applied to the second stage of the cryocooler to reduce radiative heat transfer between the evaporator and the heat sink.

Temperature Regulation and Cryocooler Capacity

Temperature control is managed by the CTC100 cryogenic temperature controller. The tuning process was initiated after the saturation temperature of each working fluid was reached, followed by activation of the internal auto-tuning routine. The final control parameters and the resulting cryocooler heat loads are summarized in the table below. The controller tuning was performed using the middle sensor mounted on the condenser and the heaters are located as in Fig. 3.21.

The resulting proportional-integral coefficients are as follows:

• Argon: $K_p = 79.75, K_i = 2.23$

• Nitrogen: $K_p = 111.4, K_i = 3.38$

• Neon: $K_p = 19.99, K_i = 1.43$

The steady-state heat loads of the cryocooler were estimated over a 6-hour operation period without any applied heating power on the evaporator. The reported uncertainties combine the standard deviation of the data with the instrumental resolution of the CTC100 controller, as specified in the user manual (173).

Q_{Ar} [W]	$Q_{\mathrm{N}_{2}}$ [W]	Q_{Ne} [W]
35.27 ± 0.15	29.68 ± 0.07	12.13 ± 0.05

Table 3.3: Cryocooler capacity for each working fluid \pm total uncertainty based on the controlling heater power.

Chapter 4

Experimental Analysis Results

This chapter reports the results of the cryogenic pulsating heat pipes experiments conducted with nitrogen, argon and neon as working fluids. The measurements were performed on five-loop PHPs with internal diameters of 1.3 and 1.7 mm. For each fluid and geometry, filling ratios between 10% and 90% were investigated with a 10% increment. All datasets include quantified uncertainties and are structured to allow direct comparison with the numerical model developed in this work. The analysis focuses on the effect of filling ratio, tube diameter and applied heat load on start-up, thermal resistance, effective thermal conductivity and pressure. Since experimental data on cryogenic PHPs, particularly with argon and neon, remain scarce, the present results constitute multi-loop datasets suitable for the validation of numerical simulations in this regime.

4.1 Experimental Results

Figures in this section summarize the PHP behavior across the tested fluids and diameters. Actual filling ratios determined after each charging procedure are listed in Table 4.1. deviations from the nominal targets arise mainly from ambient temperature fluctuations and the finite resolution of the separation valve between the filling system and the internal volume. In all plots of pressure and temperature, the real filling ratios are indicated, while performance indicators (thermal resistance and effective conductivity) were evaluated using rounded values. The adopted maximum safe operating pressures were 3750 mbar for nitrogen, 4000 mbar for argon and 4500 mbar for neon.

Table 4.1: Target and actual filling ratios (%) for all fluids and diameters.

FR target [%]	N_2		Ar		Ne	
	1.3 mm	1.7 mm	1.3 mm	1.7 mm	1.3 mm	1.7 mm
10	10.39	10.07	9.89	9.94	10.18	10.07
20	19.87	20.07	20.13	19.99	20.13	20.05
30	29.94	29.97	30.10	30.01	29.97	30.07
40	40.27	40.00	39.86	40.00	40.16	40.05
50	50.16	50.01	50.14	50.46	50.10	50.10
60	59.97	60.08	60.29	60.00	60.07	63.37
70	70.03	70.16	69.93	70.35	70.17	70.03
80	80.13	80.12	80.20	79.89	80.01	79.98
90	90.04	90.15	90.06	90.05	90.07	90.02

4.1.1 Nitrogen

The experiment with nitrogen was carried out as part of the campaign. Next, repeatability tests were performed to confirm the stability of the system and the reliability of the filling procedure. After filling the PHP with the working fluid, the system was left for at least one hour to allow the evaporator temperature to stabilize. This was necessary because the fluid needs to cool down to a temperature close to that imposed by the condenser plate. The system was subjected to gradually increasing heat loads, from 0 W to 25 W, applied in regular time intervals of 1800 s for 0 W and 2700 s for the rest.

Internal Diameter of 1.3 mm

Figure 4.1 shows the temperature evolution of the evaporator and condenser over time for a nitrogen-filled PHP with an internal diameter of 1.3 mm. Each curve corresponds to a different filling ratio, ranging from 10% to 90%.

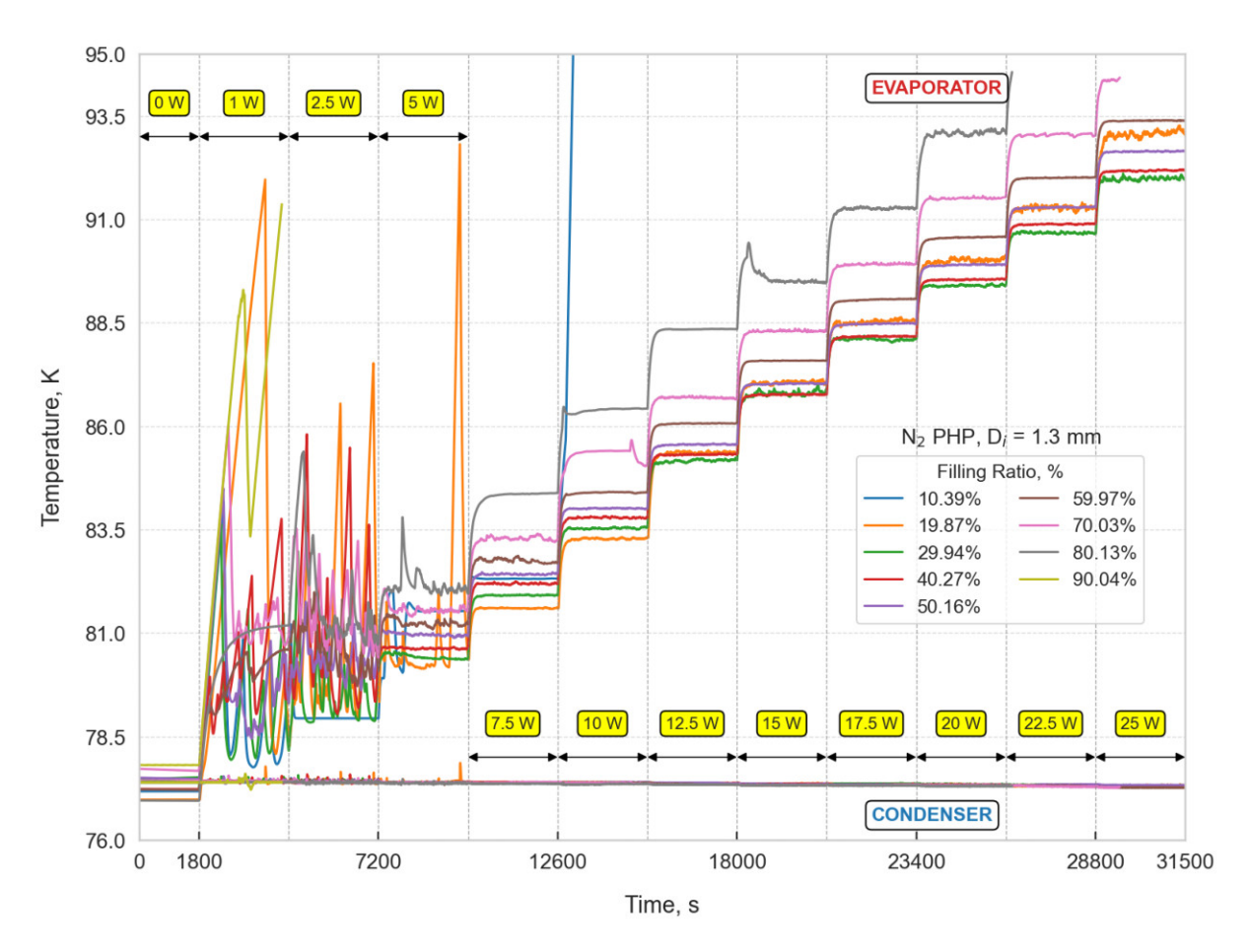


Figure 4.1: Temperature evolution in a 1.3 mm diameter PHP filled with nitrogen, under heat loads ranging from 0 to 25 W and filling ratios from 10% to 90%.

In the low heating power range (0-5 W), the system exhibits strong temperature instability. Large-amplitude, irregular oscillations indicate weak evaporation-condensation to sustain two-phase circulation. At this stage, the evaporator reaches local dryout conditions, which limits its ability to transfer heat. As a result, the delivered energy is insufficient to sustain oscillations, as the pressure differences are too small. A transition to a quasi-steady regime is observed at a power of about 7.5 W, where the curves flatten and stabilize, indicating the onset of stable oscillations and improved heat transfer performance. An exception is observed for the 10% filling ratio, where only 2.5 W was sufficient to maintain stable oscillatory behavior. Above 10 W, a clear separation appears between the temperature curves for different filling ratios. Configurations with fillings below 50% maintain the lowest evaporator temperatures. The data suggest that, at low heat loads ($Q \leq 10$), low filling ratios below 30% perform more efficiently. Nevertheless, for both FR of 70 and 80%, the experiment was interrupted at 22.5–25 W due to safety constraints. This safety limit entails a trade-off, while higher fill ratios generally improve heat transfer performance at elevated heat inputs, for example, 30–50% start to outperform 10-20% from 15 to 25 W, they also lead to increased operating pressures, thus reducing the safety margin and limiting the applicable power range. Additionally, for a filling ratio of 70% at 10 W and 80% at 15 W, an improvement in performance was observed compared to lower heat inputs. This may indicate a potential shift in the internal flow structure toward an annular regime, as suggested in the findings of Khandekar (174). However, this observation does not constitute a definitive evidence of the prevailing flow pattern, but rather suggests a possible change in the dominant flow structure within the PHP. A global dryout occurred at 10% filling at 10 W, evidenced by a rapid temperature increase and a simultaneous pressure drop (Fig. 4.4). This phenomenon results from flow stagnation and the loss of thermal connectivity between the condenser and the evaporator. In practical terms, it implies that the liquid remains trapped in the condenser under saturation pressure, with little or no return flow to the evaporator. Although this cannot be directly observed in the present setup due to the absence of visualization. A similar behavior associated with the onset of global dryout in nitrogen-based PHPs was also reported in Barba et al. (32). In contrast, for 90% filling, initiating oscillations would require exceeding the safety pressure, with peaks surpassing the acceptable limit. This is characteristic of overfilled systems, where the excess liquid reduces the available vapor volume and dampens the oscillation mechanism. To provide a quantitative assessment of the thermal performance, Fig. 4.2 presents two key indicators, the thermal resistance (Eq. (3.2)) and the effective thermal conductivity (Eq. (3.6)). Both parameters were plotted as functions of heating power and were calculated based on the averaged steadystate data from the last 15 minutes of measurements before the change in heat load. The left panel shows a rapid decline in thermal resistance up to approximately 7.5 W, beyond which the values tend to stabilize. This behavior corresponds to the transition from incomplete or no start-up conditions at low heat loads to a stable oscillating regime, where temperature fluctuations diminish and heat transfer becomes more efficient. Similar transient dynamics, often referred to as geyser pulsations, have been reported in visualization studies of start-up processes for water-based PHPs (73). Configurations with filling ratios of 20–40% achieve the lowest resistance, in the range of 0.6–0.65 K/W. In contrast, the 10% and 90% cases exhibit higher resistance across the heating power range, indicating less favorable heat transfer characteristics. The right panel illustrates the evolution of k_{eff} with increasing power. The effective thermal conductivity exceeds 30000 W/(m·K) for filling ratios between 20% and 60%, with a maximum surpassing 35000 W/(m·K), a performance superior to other five-loop nitrogen PHP configurations reported by Shi et al. (175) and nearly twice as effective compared to the results of Natsume et al. (25). Although the 70% and 80% filling cases also demonstrate high conductivity, their curves are truncated due to experimental pressure limit. The distinct behavior observed for the 10% case is attributable to local dryout or unstable flow regimes resulting from insufficient liquid return to the evaporator. Similar tendencies were reported by Fumoto and Ishii (176), who investigated a flat-plate PHP operating at ultra-low filling ratios of 5-10%. In their study, stable and highly efficient heat transport was achieved without dryout. The comparison suggests that in the present configuration, low filling ratios promote efficient operation at low heat loads but become increasingly prone to local dryout and performance degradation as the heat input increases.

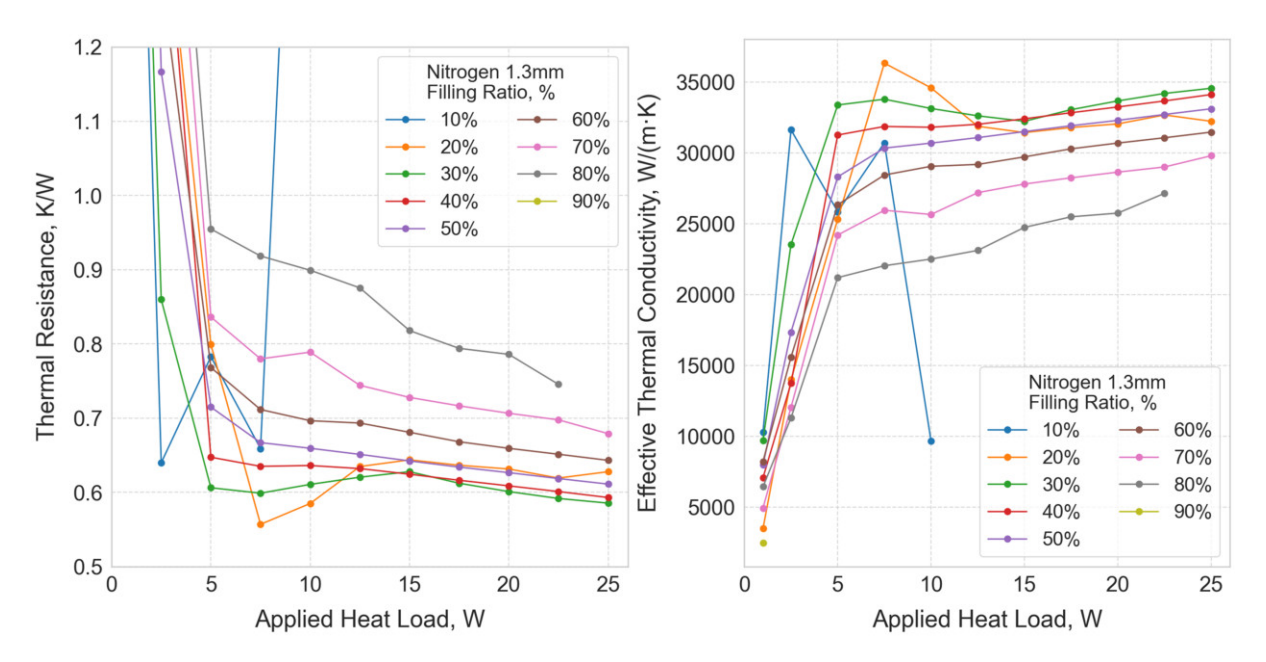


Figure 4.2: Averaged thermal resistance (left) and effective thermal conductivity (right) of 1.3 mm nitrogen PHPs, calculated for each heat load and filling ratio over the final 15 minutes of each operating period.

The uncertainty of the measurements based on the previously described methodology in Section 3.7 is shown in Fig. 4.3. Values of the statistical deviation were averaged from all data for each filling ratio. For both parameters, the highest values of uncertainty were observed for small heat loads.

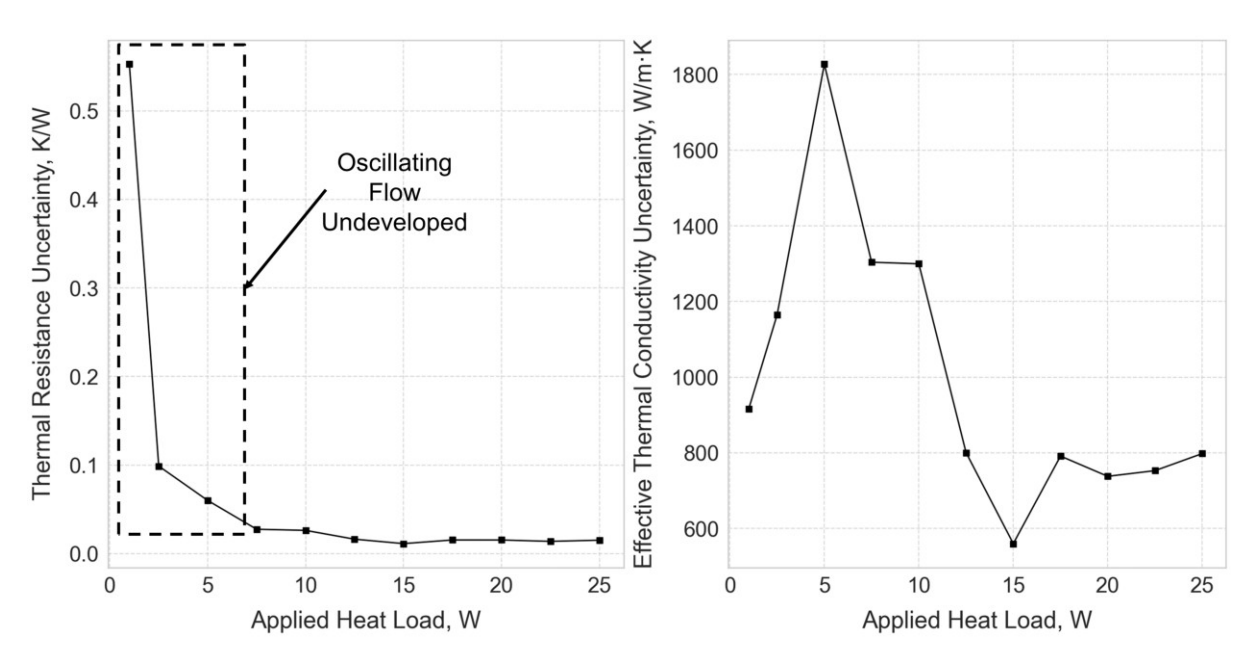


Figure 4.3: Uncertainty of the experimental thermal resistance (left) and effective thermal conductivity (right) of 1.3 mm nitrogen PHP.

Figure 4.4 presents the evolution of pressure. A characteristic feature of the PHP operation is the increase in pressure with the increasing filling ratio and evaporator heat load. In contrast to temperature behavior, lower pressures at lower filling ratios do not necessarily indicate better thermal performance. Instead, the pressure variations and oscillations are directly linked to the temperature stability at the evaporator: the larger the pressure oscillations, the more pronounced the temperature fluctuations. This trend is particularly evident at 20% and 30% filling ratios. The observed relation between increased oscillatory pressure amplitude and evaporator temperature aligns with findings reported for circular-type 6-loop nitrogen PHPs in Wang et al. (177). For the cases of 70% at 10 W and 80% at 15 W, a clear change in flow behavior can be observed. In these cases, the onset of pressure oscillations resulted in a noticeable temperature drop, as shown in Fig. 4.1.

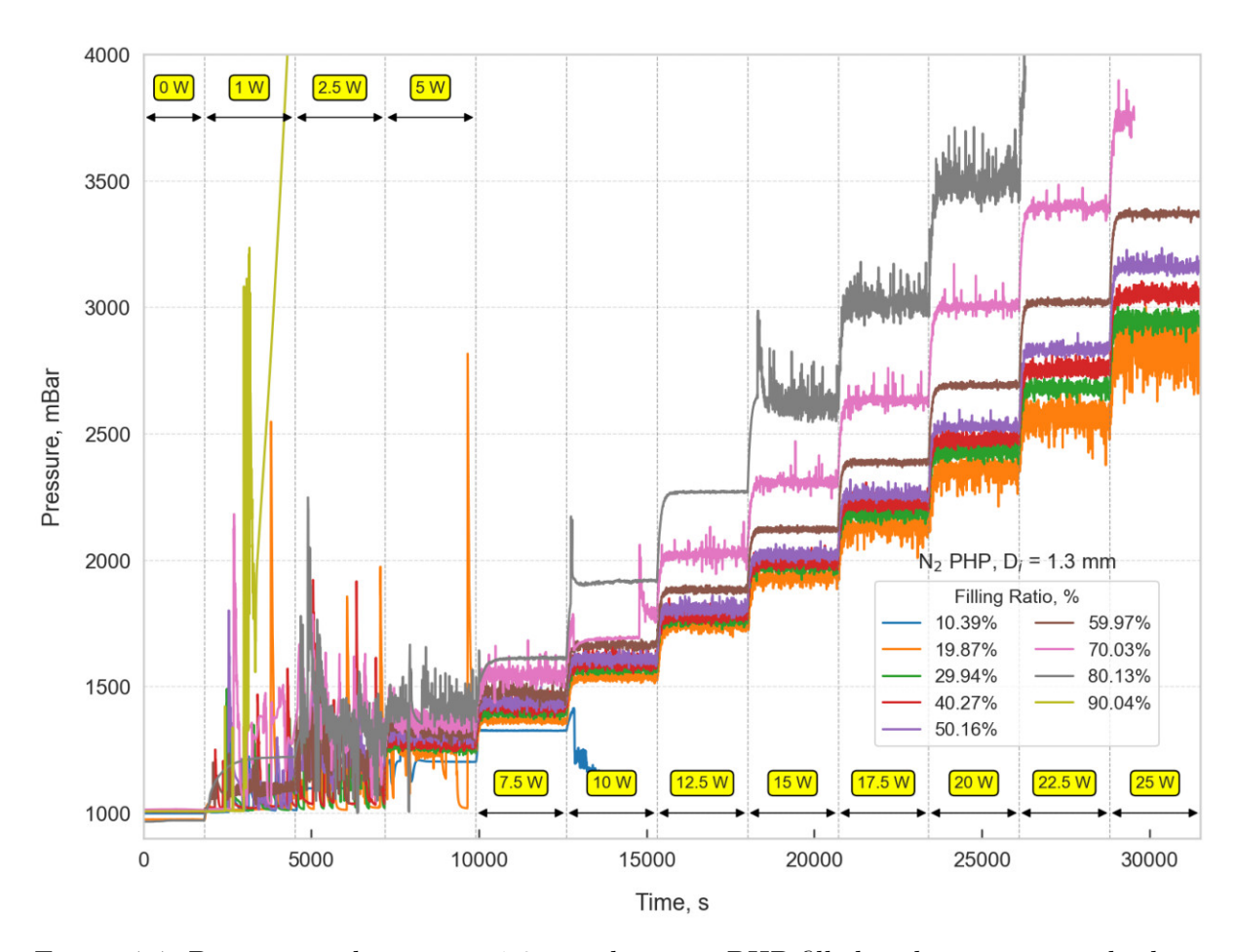


Figure 4.4: Pressure evolution in a 1.3 mm diameter PHP filled with nitrogen, under heat loads ranging from 0 to 25 W and filling ratios from 10% to 90%.

At 7.5–10 W the oscillations stabilize and the thermal resistance reaches its minimum, while at higher inputs the oscillations grow in amplitude and irregularity and the performance deteriorates. This evolution is consistent with a shear-driven transition. Zuber (178) related the increase in vapor velocity to the onset of interfacial instability and dryout once inertial forces overcome capillary stabilization. In pulsating heat pipes the corresponding threshold appears as the Kelvin-Helmholtz wave growth at the liquid-vapor interface when the interfacial shear exceeds the surface tension restoring force, as analyzed for PHP stability by Nikolayev et al. (179). Wave amplification promotes droplet entrainment and progressive stripping of the wall film, which reduces the active area for phase change and lowers the effective heat-transfer coefficient. Thome (180) showed that controlled thin film boiling reaches a maximum heat transfer rate at a critical film thickness and then declines as the film becomes too thin, which explains the deterioration observed above about 10 W. The consistency with this mechanism is reinforced by studies of annular two-phase flow, where the conditions of best heat transfer coincide with a continuously wetted but thin wall film. Hewitt and Hall-Taylor (181) reported that stronger interfacial waves increase droplet entrainment and thin the residual film, establishing a direct pathway from growing oscillations to loss of wetting. Zhang and Ding (182) quantified how the measured wave characteristics control the interfacial momentum exchange and provided criteria for the onset of film depletion, which align with the degradation observed once the pressure and temperature oscillations intensify at higher power. Higher FRs follow the complementary trend implied by this mechanism. A larger FR helps to maintain a thicker wall film and delays shear-induced depletion at elevated inputs, therefore, the heat-transfer performance improves as power rises. At the same time, the added liquid mass increases hydraulic damping and the start-up threshold at low power and the higher liquid content increases operating pressure. Consequently, intermediate fills between 30% and 60% provide the highest effective thermal conductivity in the present measurements because they balance the stability of the film at higher inputs with acceptable starting and pressure levels, while very low fills near 10% become prone to intermittent dryout as power increases and very high fills between 80% and 90% encounter pressure limits with damped oscillations.

Internal Diameter of 1.7 mm

The temperature evolution of nitrogen-based PHPs with a capillary diameter of 1.7 mm is presented in Fig. 4.5. Increasing the diameter relative to 1.3 mm reduces capillary confinement because the pressure difference that stabilizes the meniscus scales inversely with the radius of the tube. As a result, the flow becomes more inertia-dominated and the ability to sustain thin liquid films along the wall decreases. At the same time, the larger cross section accommodates a larger volume of working fluid, which increases the overall heat transport capacity and allows operation at higher filling ratios without exceeding the safety pressure threshold. Figure 4.5 shows the temperature profiles of the evaporator and condenser. The operating temperatures are slightly lower compared to those observed for the 1.3 mm diameter case in Fig. 4.1. For the larger diameter, none of the tested filling ratios exceeded the safety pressure limit. Moreover, the operational range is extended, as observed at the lowest filling ratio of 10%, stable operation is maintained up to 17.5 W, compared to dryout occurring at 10 W for the 1.3 mm configuration. A full operational range with distinct thermal stratification is again observed at 7.5 W, similar to the 1.3 mm case. It is evident that for filling ratios exceeding 60%, the temperatures increase significantly compared to other filling levels. For intermediate filling ratios (20–50%) under higher heat loads (> 20 W), the temperatures remain relatively close to each other. The condenser temperature, similar to the 1.3 mm case, diverges only at specific points of sudden pressure change (Fig. 4.8) and during startup. For low heat loads, such pressure fluctuations have also been reported by Wang et al. (65). However, they are typically not observed in PHP systems with limited capacity at the cryocooler stage and relatively high thermal inertia, such as the 1-meter-long PHP studied by Bruce et al. (23), or in experiments involving nitrogen pool cooling (52; 51).

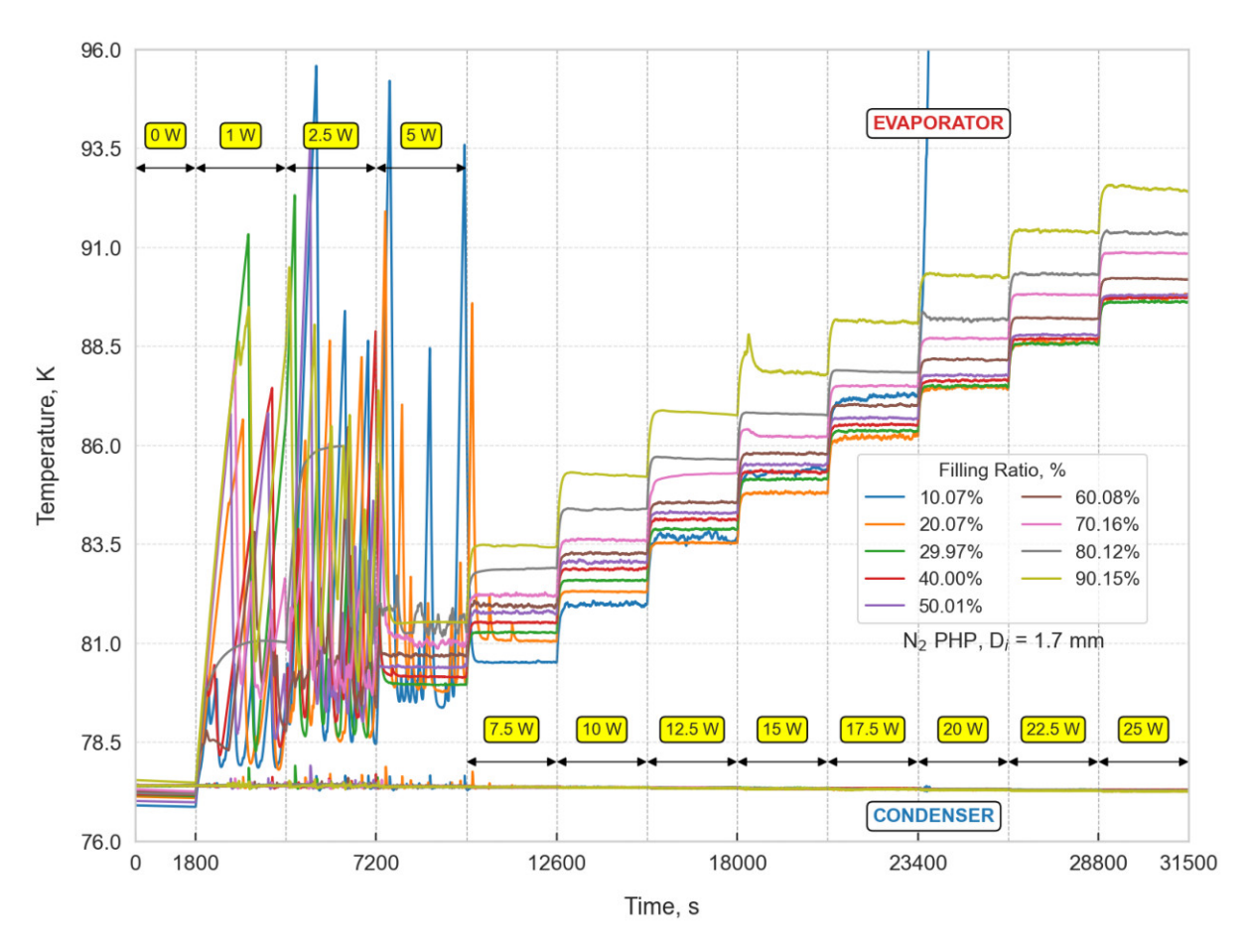


Figure 4.5: Temperature evolution in a 1.7 mm diameter PHP filled with nitrogen, under heat loads ranging from 0 to 25 W and filling ratios from 10% to 90%.

Figure 4.6 presents a comparison between thermal resistance and effective thermal conductivity. The lowest thermal resistances are observed for lower filling ratios, namely 10% and 20%, particularly under low heat loads. For higher heat fluxes (>20 W), the lowest resistances occur for intermediate fillings between 20% and 50%. The performance peak is achieved at the lowest filling ratio (10%) under a low thermal load of 7.5 W. The observed trend of decreasing thermal resistance with increasing heat input for all other filling ratios, except 20%, suggests that the cryocooler capacity limit significantly constrains the characterization of performance at potentially higher loads. The thermal resistance values for the 1.7 mm configuration fall below 0.5 K/W, which is lower than those recorded for the smaller diameter. However, the effective thermal conductivity is reduced, as expected from its geometric definition (Eq.(3.6)). While this parameter is often used as a performance indicator, it does not reliably reflect the real heat transfer capability at minimal temperature gradients like thermal resistance, which is more relevant in thermal link applications. Similar limitations of this indicator were noted by

Sagar et al. (51) and Shi (175), who showed that even with a similar range of thermal resistances varied significantly due to differences in geometry, particularly the adiabatic section length.

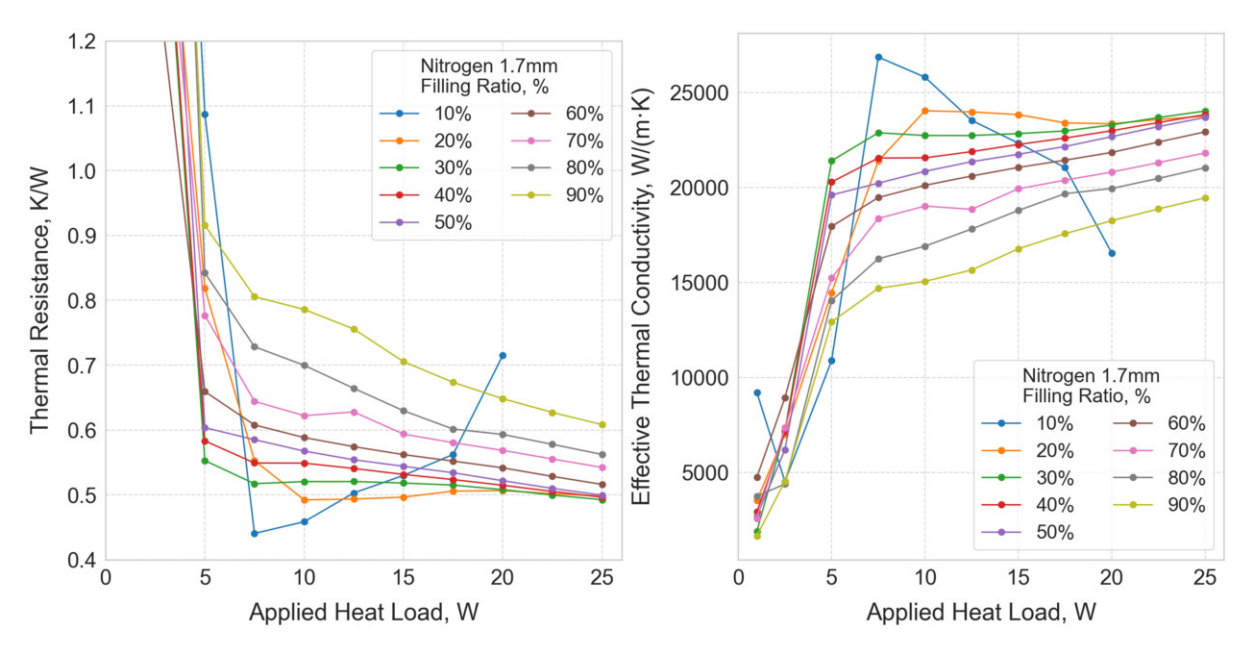


Figure 4.6: Averaged thermal resistance (left) and effective thermal conductivity (right) of 1.7 mm nitrogen PHPs, calculated for each heat load and filling ratio over the final 15 minutes of each operating period.

The uncertainty of the measurements is shown in Fig. 4.7. The main contributor to the larger error at low heat loads is the statistical uncertainty associated with strong temperature fluctuations in the evaporator. At higher heat loads, the measurement uncertainty is slightly greater compared to the 1.3 mm case, remaining relatively low due to a stable evaporator temperature.

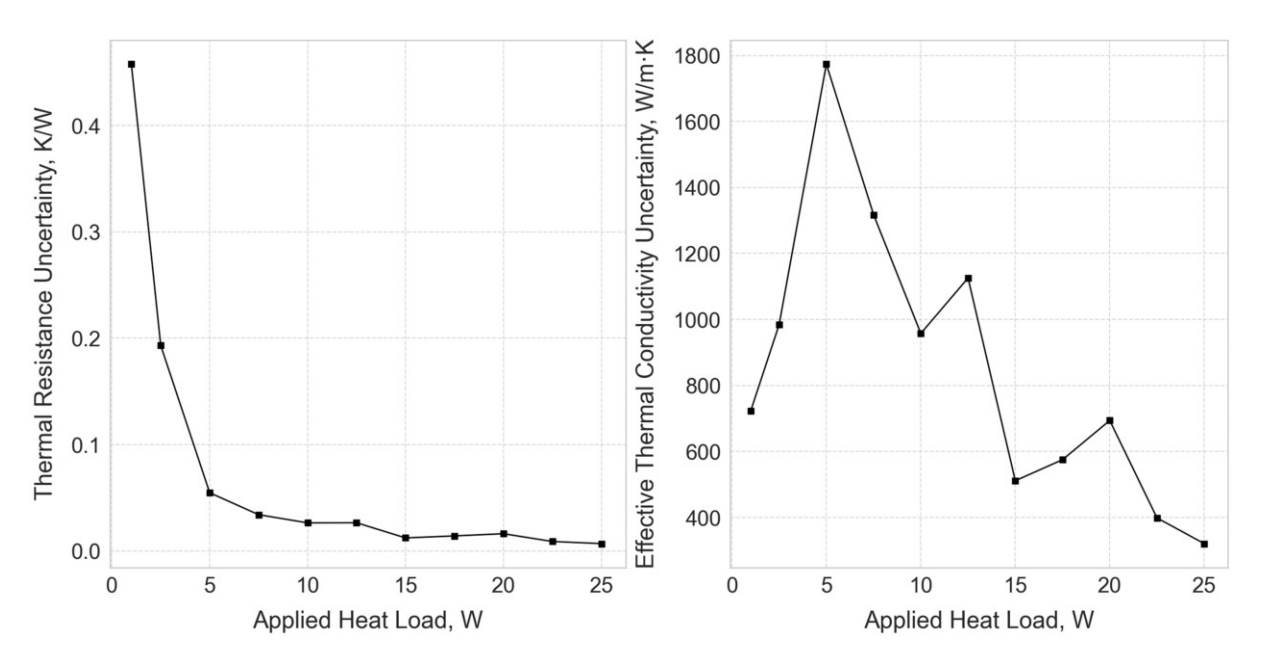


Figure 4.7: Uncertainty of the experimental thermal resistance (left) and effective thermal conductivity (right) of 1.7 mm nitrogen PHP.

The pressure evolution for the 1.7 mm nitrogen PHP is presented in Fig. 4.8. All cases, except for FR=90\%, remained below 3000 mbar, which is far from the safety limit. Assuming structural integrity as a key safety criterion, larger diameters tend to offer increased robustness against potential leakage or rupture, as shown by the lower operating pressure ranges. As in the 1.3 mm case (Fig. 4.1-4.4), pressure increases with the filling ratio. However, within the 30–50% range, the trend is less pronounced. Repeatability was assessed by rerunning at least half of the operating points and cases with questionable behavior were repeated until consistent pressure and temperature ranges were obtained. This agreement indicates that the pressure and temperature responses remain coherent near the saturation line as long as localized partial dryouts do not occur, which appear under higher heat loads together with altered internal flow structures. Similar behaviour was reported by Li et al. (183; 184), who associated intensified pressure oscillations with local dryout observed through high-speed visualization in nitrogen PHPs. Such behavior is also observed here in FR=90% at 15-25 W and 80% at 20-25 W, or for 20% in the 1.3 mm configuration within the 17.5–25 W range. In contrast, the phenomenon of global dryout, identified by a rapid increase in the evaporator temperature, leads to a sharp pressure drop inside the PHP as the evaporator and condenser regions decouple thermally and the vapor space expands. This behaviour is consistent with the interpretation proposed by Barba et al. (185), who reported that during dryout the system pressure relaxes toward the saturation value corresponding to the liquid confined within the condenser section.

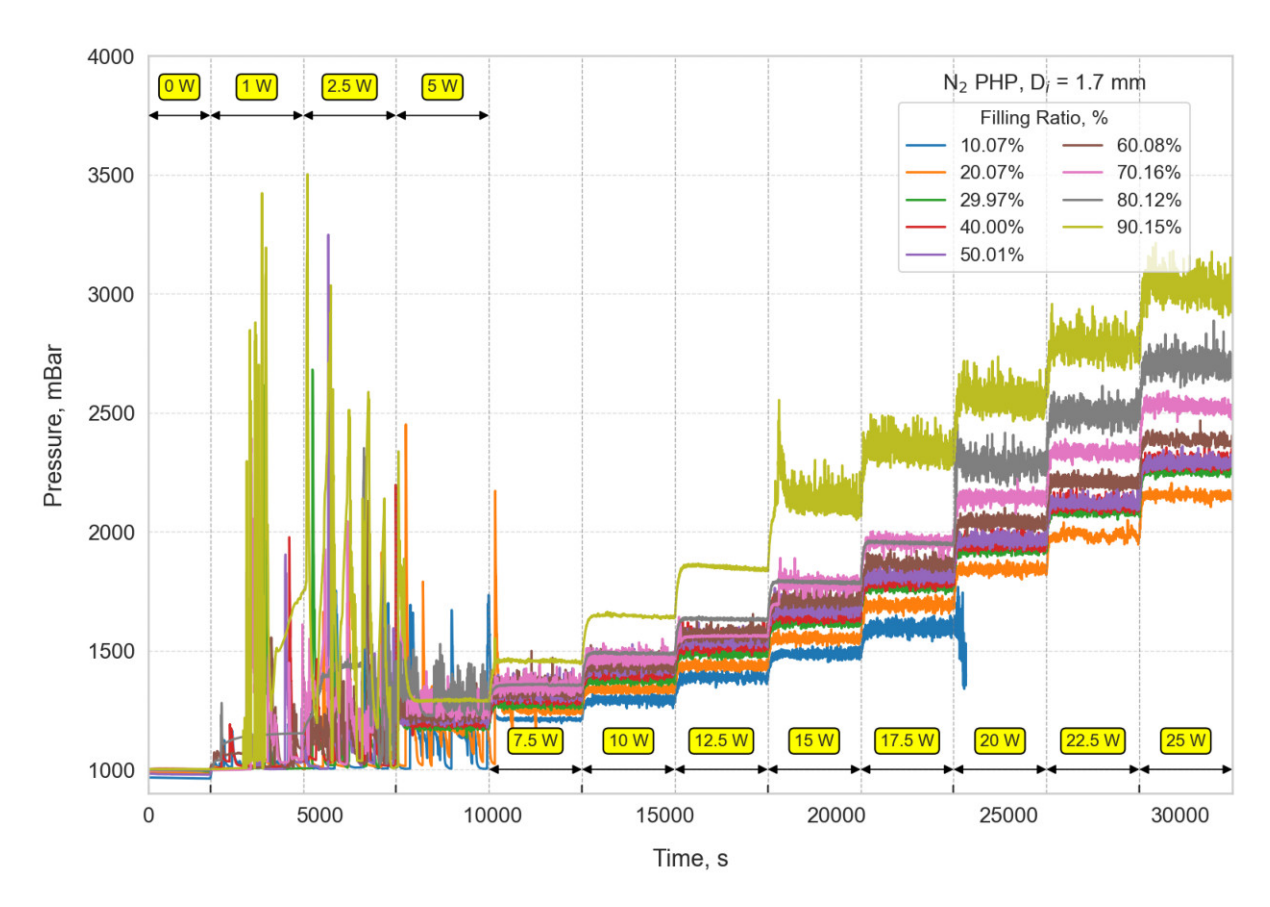


Figure 4.8: Pressure evolution in a 1.7 mm diameter PHP filled with nitrogen, under heat loads ranging from 0 to 25 W and filling ratios from 10% to 90%.

4.1.2 Argon

The experiment with argon was carried out following the same methodology as in the nitrogen-based analysis. To date, only limited experimental studies involving argon PHPs exist, with the notable exception of the work by Barba et al. (186; 32). As with the nitrogen case, repeatability tests were performed to verify the results. The main difference, apart from the condenser temperature, is the safety pressure limit, which was increased to 4000 mbar for argon. The experimental range was also modified due to the specific performance characteristics of the cryocooler, whose cooling power increases with the operating temperature of the stage. The measurements were conducted using the same time intervals: 1800 s for the zero-load and 2700 s for each heat load.

Internal Diameter of 1.3 mm

Figure 4.9 shows the temperature evolution of the condenser and evaporator for the 1.3 mm PHP filled with argon. The operating range for argon exceeds the cryocooler

capacity, as evidenced by the increase in condenser temperature at 32.5 W. Dryout occurred for the two lowest filling ratios: 10% at 10 W and 20% at 27.5 W. The experiment was interrupted in cases where the safety pressure limit was exceeded for filling ratios between 70% and 90%, despite otherwise stable operation. In contrast to the nitrogen-filled 1.3 mm PHP, the argon case does not exhibit clear evaporator temperature drops during the starting oscillatory behavior (e.g. for FR = 80% at 15 W and 70% at 10 W in the nitrogen case (Fig. 4.1)), apart from those occurring after steady operation is reached at heat loads above 7.5 W.

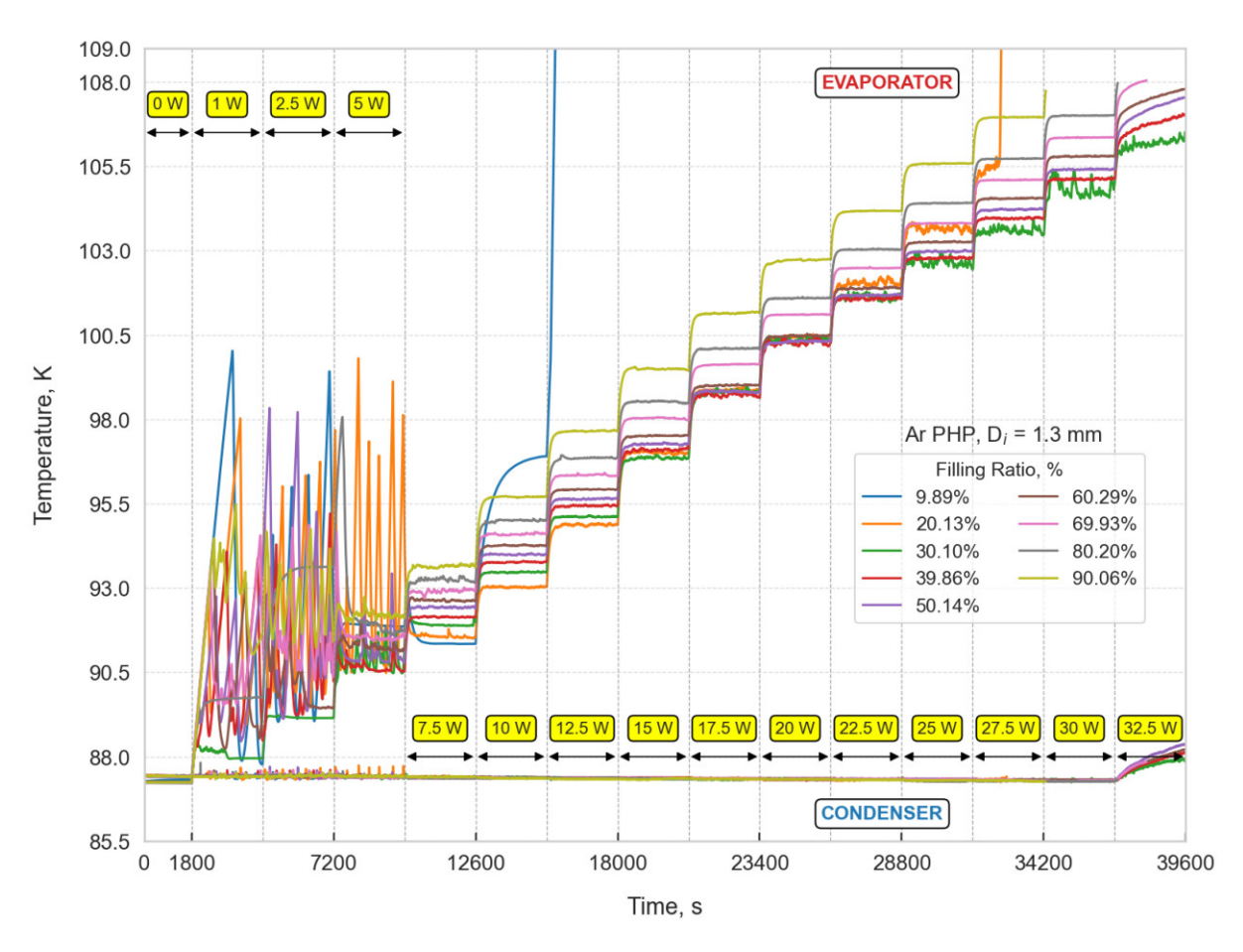


Figure 4.9: Temperature evolution in a 1.3 mm diameter PHP filled with argon, under heat loads ranging from 0 to 32.5 W and filling ratios from 10% to 90%.

From 7.5 W upward, the PHP operates stably and the amplitude of temperature oscillations decreases with increasing filling ratio. At the lowest heat loads (7.5–12.5 W), the 20% filling shows the best performance. Between 17.5 W and 20 W, the temperature responses converge for filling ratios in the range of 20–60%. Above 25 W, the 30% filling exhibits the most effective thermal performance. A summary of the calculated values is presented in Fig. 4.10 and the corresponding uncertainties are shown in Fig. 4.11. As in the previous cases, the uncertainties are primarily associated with statistical variations, particularly at lower heat loads. The error decreases progressively with increasing power

and reaches a minimum around 25 W, where a balance is achieved between system stability, the amplitude of temperature oscillations and the growing influence of heat flux uncertainty.

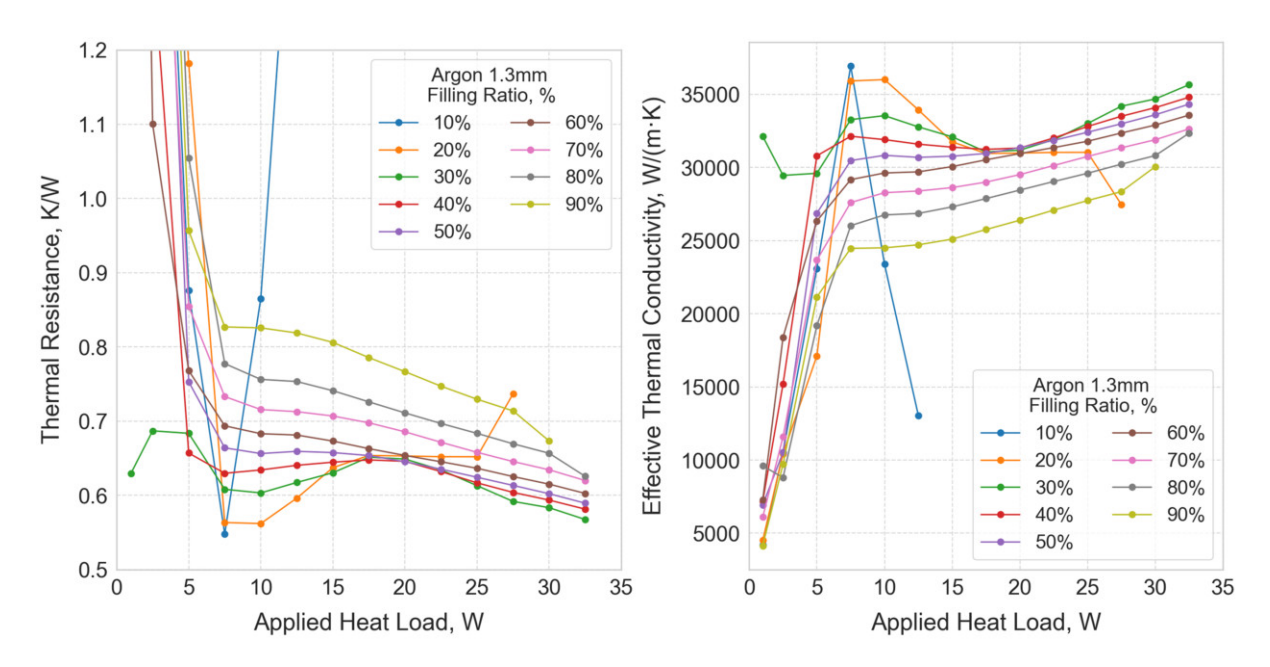


Figure 4.10: Averaged thermal resistance (left) and effective thermal conductivity (right) of 1.3 mm argon PHPs, calculated for each heat load and filling ratio over the final 15 minutes of each operating period.

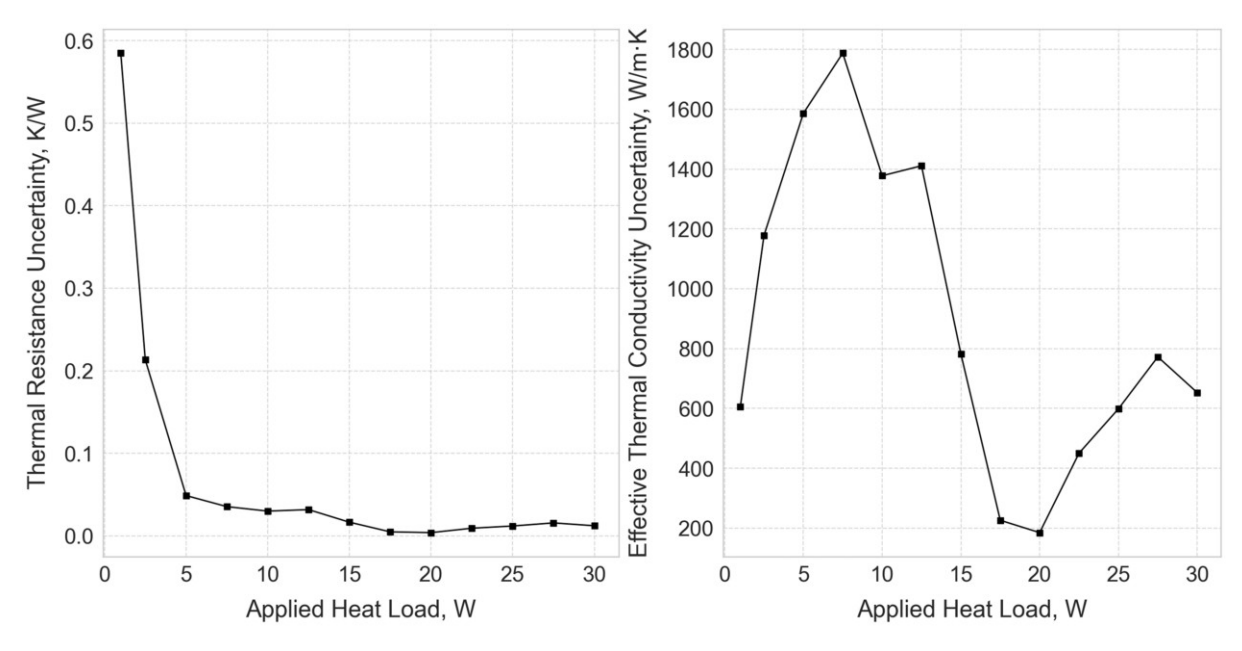


Figure 4.11: Uncertainty of the experimental thermal resistance (left) and effective thermal conductivity (right) of 1.3 mm argon PHP.

The pressure evolution for the 1.3 mm argon PHP is presented in Fig. 4.12. The moments when the safety pressure limit is exceeded for filling ratios of 70–90% are clearly visible in

the plot. The dryout behavior in terms of pressure differs significantly between the 10% and 20% cases. For 10%, dryout occurs after exceeding 12.5 W without any preceding pressure fluctuations. As the filling ratio increases, more distinct pressure changes are observed, particularly in the 30–50% range. Comparable pressure magnitudes are observed for similar power ranges: 12–22.5 W in this case and 20–25 W for the 1.7 mm nitrogen PHP (Figs. 4.5 and 4.8). In the nitrogen case, extending the experimental range was limited by the cryocooler capacity. Here, beyond 25 W, the pressure profiles for fillings between 30–60% begin to diverge significantly. The 80% (20–25 W) and 90% (10–12.5 W) cases exhibit isolated pressure peaks. However, these are not reflected in the temperature profiles shown in Fig. 4.9, indicating that these brief local overheating events do not result in observable thermal deviations and are suppressed by the high thermal inertia of the evaporator plates. Notable deviations begin to appear when pressure elevation is sustained for a longer duration, as observed in the broader pressure peak at 15 W for FR=90%, where subtle undulations can be seen in the temperature sensor signals.

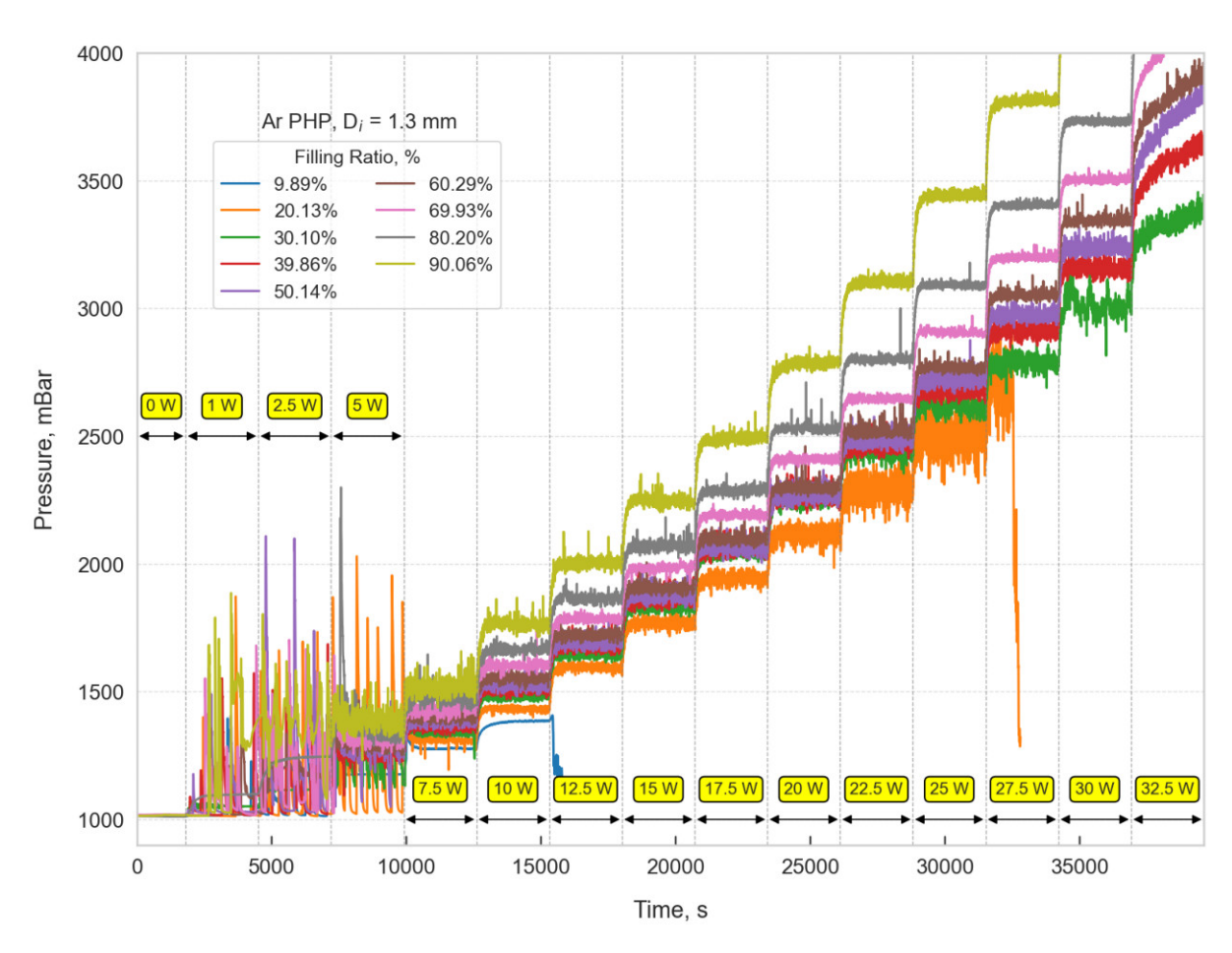


Figure 4.12: Pressure evolution in a 1.3 mm diameter PHP filled with argon, under heat loads ranging from 0 to 32.5 W and filling ratios from 10% to 90%.

Internal Diameter of 1.7 mm

The temperature evolution of argon-based PHPs with a capillary diameter of 1.7 mm is presented in Fig. 4.13. The experimental range was the same as in previous cases, covering heat loads from 0 to 32.5 W. Global dryout occurred only for the smallest filling ratio of 10%. In contrast to the 1.3 mm case (Figs. 4.9–4.12), dryout did not occur at 20% filling. A similar trend was observed for nitrogen: dryout shifted from the lowest filling (10%) in the 1.3 mm configuration (Figs. 4.1–4.4) to a higher filling in the 1.7 mm case (Figs. 4.5–4.8). Across the full operating range, the 20% filling exhibits the most favorable heat transfer performance. At lower heat loads (up to 12.5 W), significant temperature differences are observed between fillings from 20% to 70%. This trend changes beyond approximately 17.5 W, where variations in filling between 40–70% have minimal impact on PHP thermal behavior. This behavior is consistent with the smaller-diameter case (Figs. 4.9–4.12), though in that case it occurs over a smaller filling range (30–60%). A distinct deviation from the general trend is noted for the 20% filling at 7.5 W. Although other configurations exhibit clear signs of stable and oscilatory heat transfer, this case shows reduced performance due to temperature peaks despite demonstrating the highest thermal efficiency at higher heat loads (>10 W). This behavior is not unique to argon, as a similar response was identified in the 1.7 mm nitrogen case (Figs. 4.5), albeit with more pronounced temperature fluctuations. In contrast, no such effect was observed for either working fluid at 1.3 mm diameter. During the 0 W phase, evaporator temperatures vary depending on ambient conditions, particularly the temperature of the compressor and the cryocooler. On colder days, the evaporator temperature drops lower. Extreme filling ratios tend to reach higher steady-state temperatures in the absence of heating, which result from enhanced diffusive heat transport through the capillary due to the larger liquid volume.

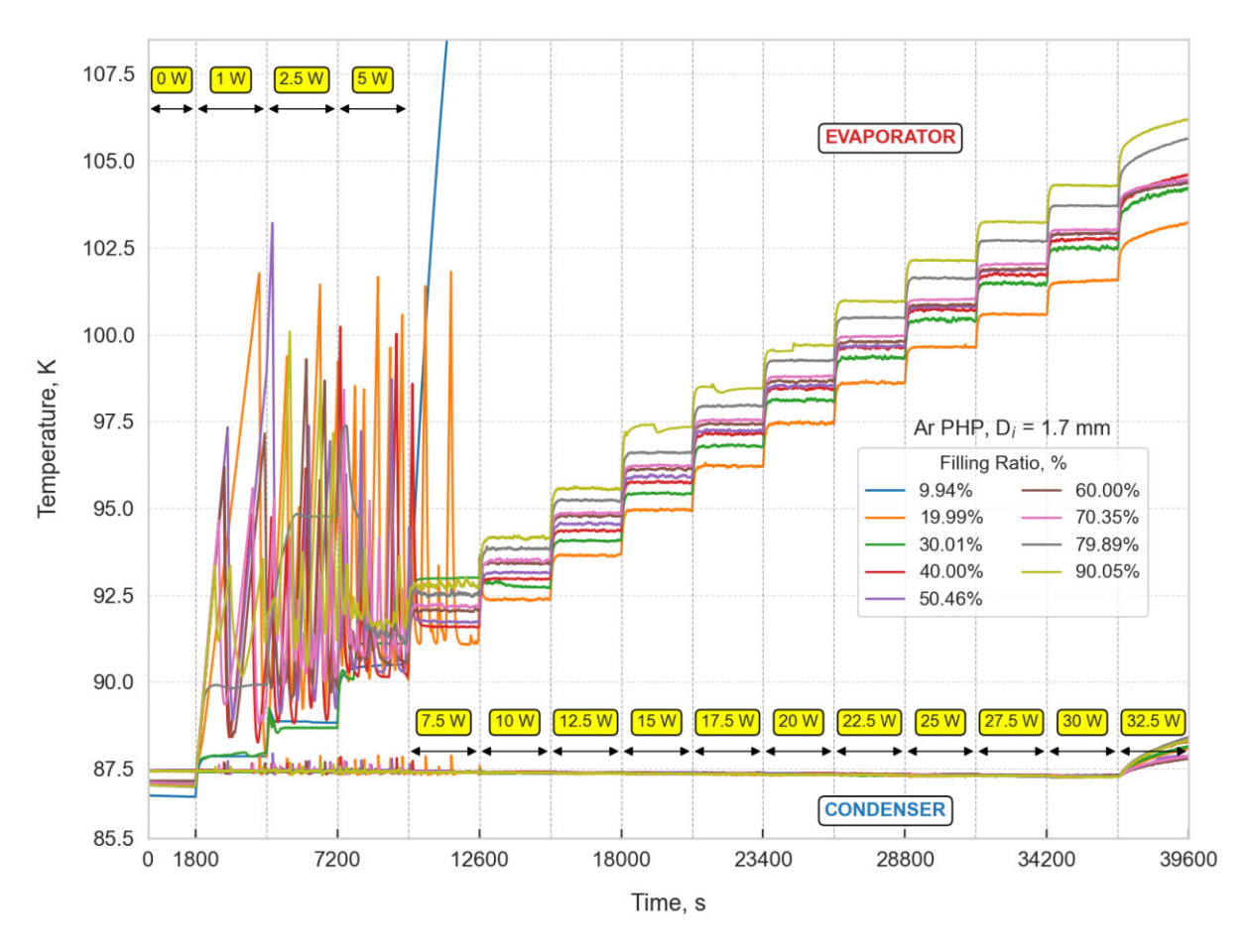


Figure 4.13: Temperature evolution in a 1.7 mm diameter PHP filled with argon, under heat loads ranging from 0 to 32.5 W and filling ratios from 10% to 90%.

Figure 4.14 presents a summary of thermal resistance and effective thermal conductivity for the 1.7 mm argon PHP. For this enlarged diameter, a lower thermal resistance is observed across all filling ratios compared to 1.3 mm. Thermal performance improves with increasing heat load for all cases except FR = 10%, where dryout occurred. An outlier appears at FR = 30%, where weak internal circulation and the absence of temperature peaks were recorded even at low input. This behavior reflects the well-documented fragility to initial conditions in PHPs, in which small differences in initial liquid distribution, nucleation availability and prior oscillation state select different operating modes under nominally identical set points, as shown experimentally by Song and Xu (187). To limit this sensitivity, each power step was held until a stationary regime was reached and only then were the last 15 minutes averaged, so the reported values correspond to a reproducible operating branch. Compared with previous argon studies by Barba et al. (186; 32), the present results indicate that layouts with a higher number of loops start-up sensitivity and improve performance by providing several parallel circulation paths and, as a result of 1 m length, a longer evaporation-condensation train that sustains phase exchange. This interpretation agrees with established influences of turn number and overall length on activation and stability in PHPs described in the Mameli et al. review (188). The corresponding measurement uncertainty for this configuration is presented in Fig. 4.15.

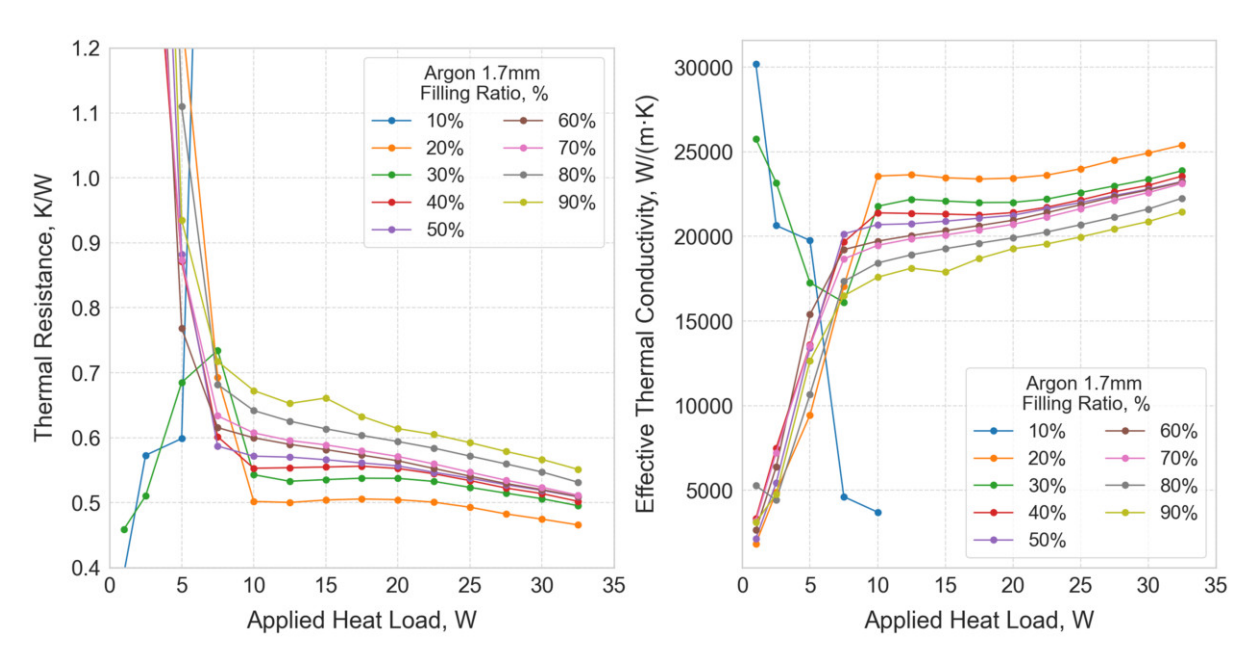


Figure 4.14: Averaged thermal resistance (left) and effective thermal conductivity (right) of 1.7 mm argon PHPs, calculated for each heat load and filling ratio over the final 15 minutes of each operating period.

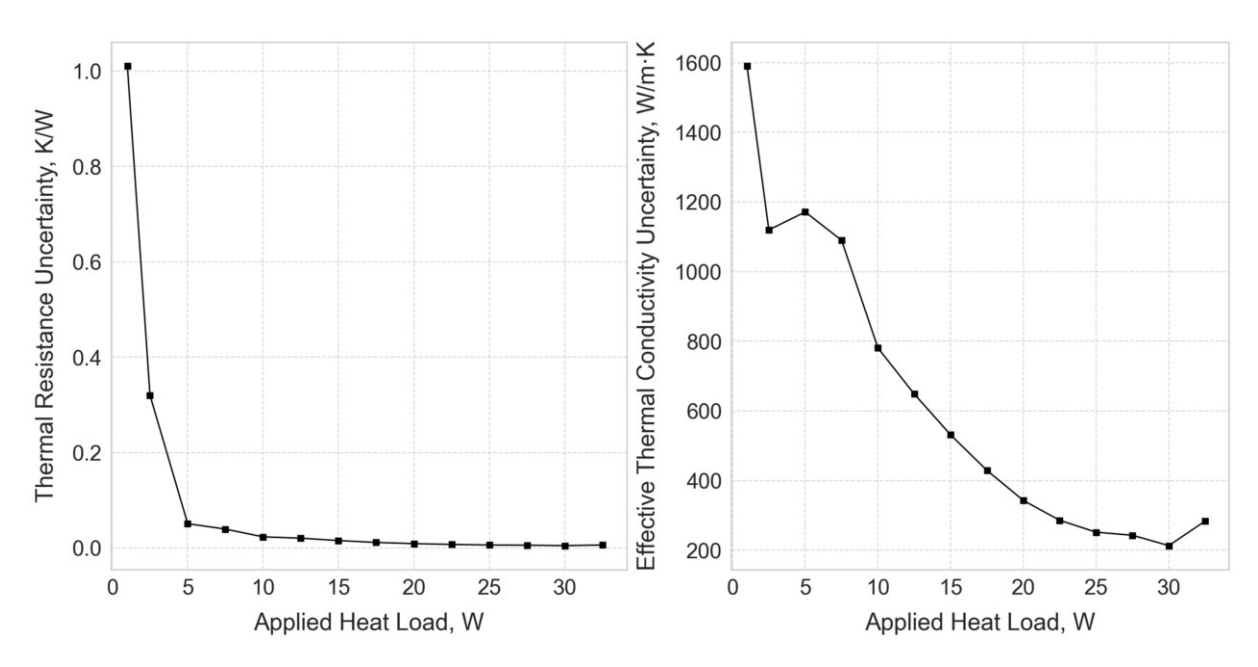


Figure 4.15: Uncertainty of the experimental thermal resistance (left) and effective thermal conductivity (right) of 1.7 mm argon PHP.

Figure 4.16 presents the pressure evolution in the 1.7 mm argon PHP. As in the previous configuration, pressure rise correlates with the filling ratio and remains below the upper safety threshold of 3500 mbar. The highest pressures (approaching 3000 mbar) were

recorded for the 70–90% filling cases, while the lowest values occurred for FR = 10-20%, with pressure remaining below 1800 mbar even at peak heat loads. An atypical behavior is observed for the 90% filling, where pressure does not consistently increase with the applied heat load. A distinct transition from a regime of low-amplitude pressure oscillations to a more pronounced oscillatory mode is visible between 15 and 20 W. Notably, the 90% case shows the largest pressure fluctuations, with amplitudes exceeding 100 mbar, while midrange fillings (30–60%) remain relatively stable, with variations confined below 50 mbar. In cases where short pressure spikes (lasting less than a minute) occur, a corresponding temperature drop is observed—suggesting enhanced internal circulation induced by these transient events. This behavior contrasts with the case at 20% filling, where a transition to sustained oscillations of approximately 50 mbar amplitude correlates with an increase in the steady-state temperature, indicating a distinct thermal regime. Another unusual feature is the presence of pressure drops rather than peaks. In earlier cases, such pressure decreases were typically associated with global dryout. Here, due to the combination of low filling ratio and relatively high heat load, these downward pressure spikes presents for FR = 20 \% in between 20 and 25 W are likely indicative of a pre-dryout state rather than complete flow cessation. Overall, the pressure behavior in the 1.7 mm argon PHP suggests a complex interplay between filling ratio and heat input. While higher filling ratios ($\geq 70\%$) lead to elevated steady-state pressures, they do not necessarily result in thermal performance deterioration—unless sustained peaks are observed. Mid-range filling ratios (30–60%) exhibit the onset of oscillatory pressure behavior at lower heat inputs (10–15 W), indicative of early activation of the PHP circulation. Compared to the 1.3 mm configuration, the 1.7 mm PHP exhibits a broader operational working heat with reduced susceptibility to abrupt dryout and smoother pressure evolution across most fillings.

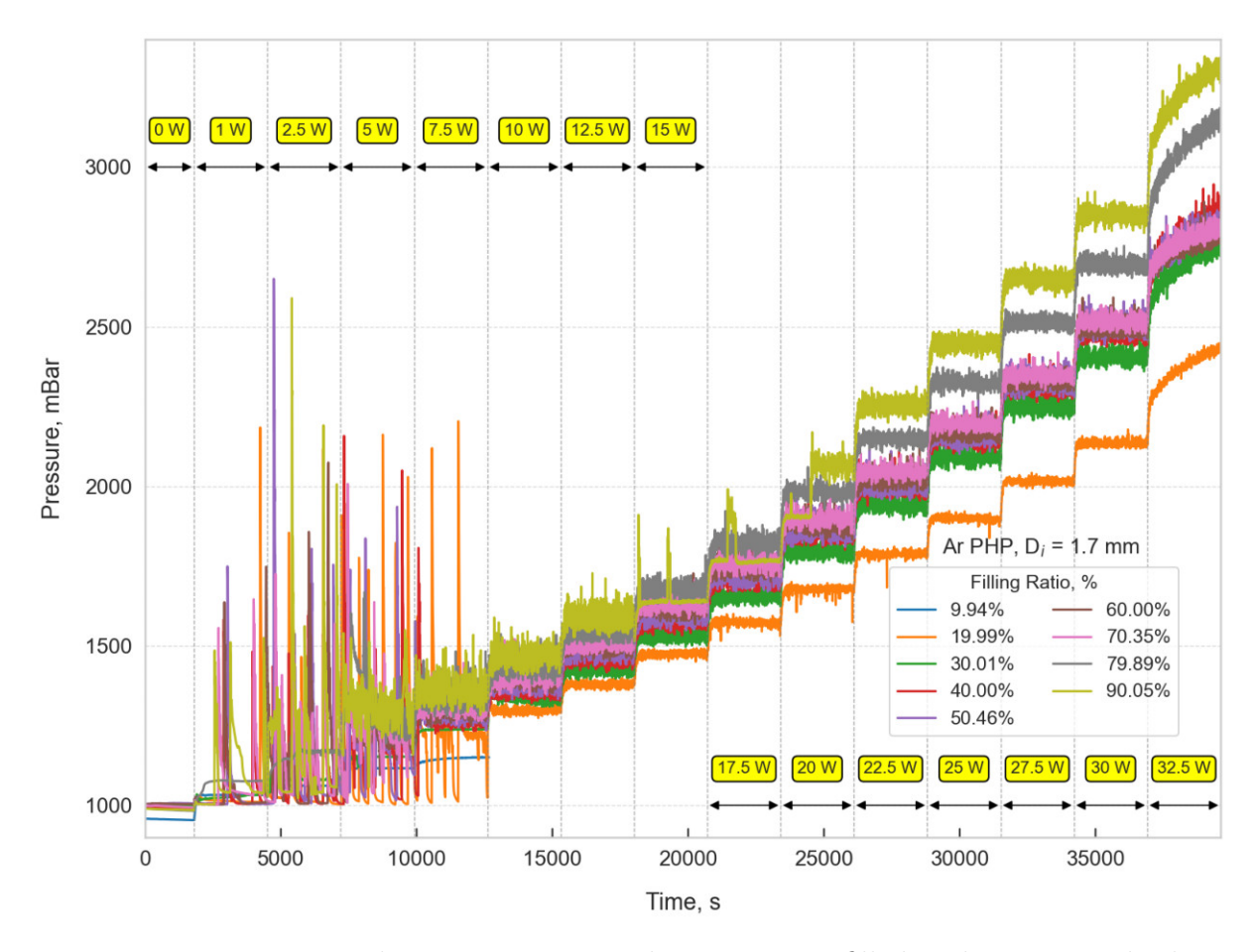


Figure 4.16: Pressure evolution in a 1.7 mm diameter PHP filled with argon, under heat loads ranging from 0 to 32.5 W and filling ratios from 10% to 90%.

4.1.3 Neon

The experiments with neon were carried out on the second stage of the cryocooler, which required replacement of the thermal interface. In contrast to the previous measurements, the temperature of the feeding tube was also monitored. In this case, each measurement was initiated only after the feeding tube temperature reached a steady state. This procedure involved operating the PHP for approximately one hour after the initially stable temperature had been reached. Once the PHP was switched off and a new steady state was established (after about another hour), the measurement sequences were started. Based on previous experience, the safety pressure limit was set to 4500 mbar.

Internal Diameter of 1.3 mm

Figure 4.17 presents the time evolution of evaporator temperatures for a 1.3 mm diameter PHP filled with neon, subjected to heat loads ranging from 0 to 10 W and FR between

10% and 90%. The first prominent observation is the high evaporator temperature for the case with FR = 90%. On the second cryocooler stage the condenser temperature is fixed by the cold head and the available cooling power is limited, so when transport is insufficient the evaporator stabilizes at a higher temperature than the condenser, unlike on the first stage (argon and nitrogen). A similar effect of elevated evaporator temperature at higher filling ratios, even in the absence of applied heating power, has been reported by Dixit et al. (33). The PHP begins to operate in a reasonably stable manner starting from 2 W of heating power. For low heat loads (2–5 W), a clear trend is observed: the higher the filling ratio, the higher the evaporator temperature. At 6 W, however, the lowest evaporator temperature occurs for FR = 20%, which most likely results from a transition of the flow regime into a locally partially dry structure reported by Li et al. (183; 184), who demonstrated that decreasing FR promotes annular flow structures at the expense of dry spots that degrade thermal performance. Maximum evaporator temperatures reached up to 35.5 K, limited by the safety pressure threshold. The PHP operated for all filling ratios up to 9 W, with dryout observed at FR = 10% under 9 W. With increasing heat load, oscillations and temperature peaks diminished, indicating more stable thermal behaviour.

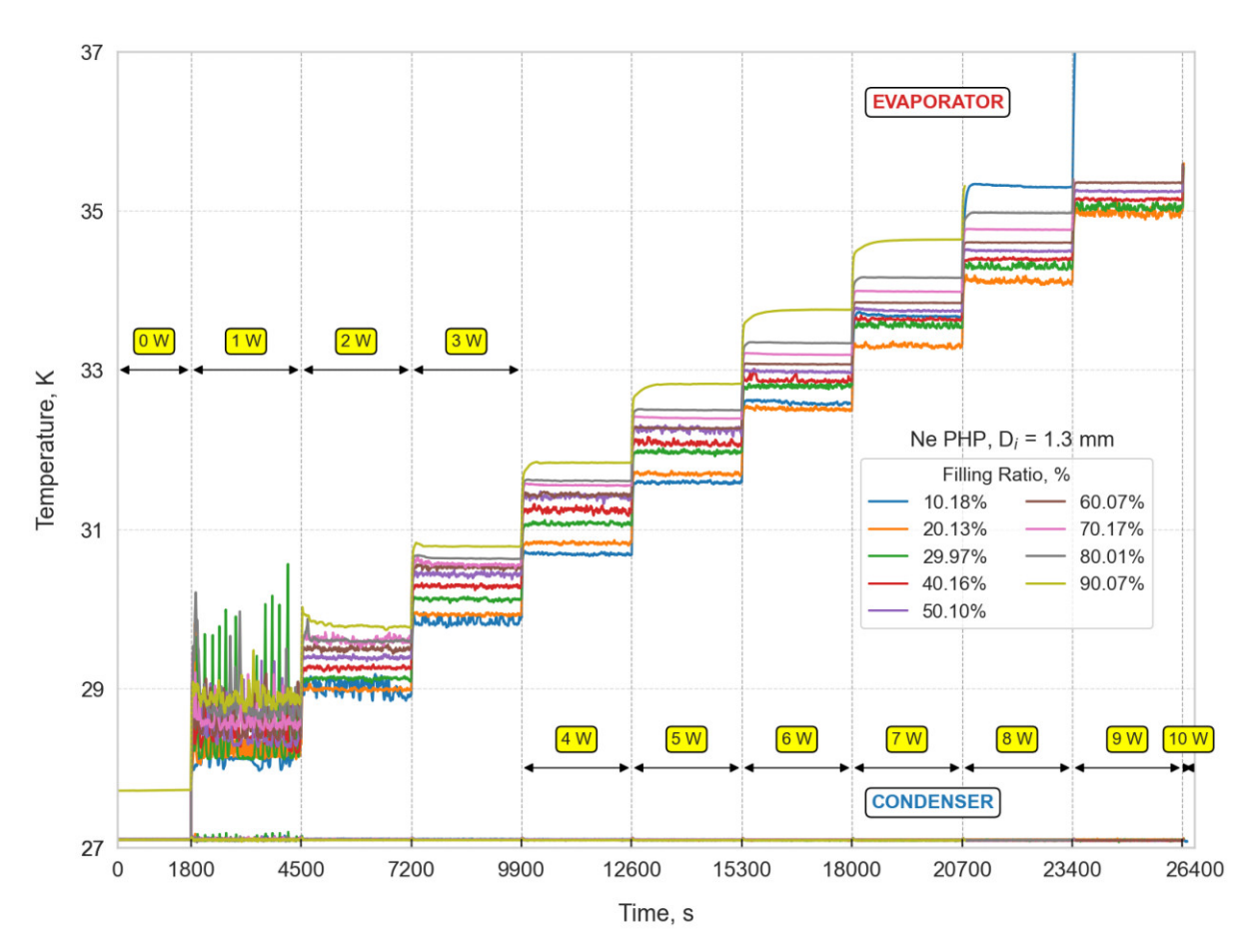


Figure 4.17: Temperature evolution in a 1.3 mm diameter PHP filled with neon, under heat loads ranging from 0 to 10 W and filling ratios from 10% to 90%.

Figure 4.18 summarizes the thermal performance results. The thermal resistance is significantly higher than for nitrogen or argon, exceeding 0.8 K/W. Once the heating power surpasses 3 W, the thermal resistance decreases for all cases except FR = 10%, where dryout occurs. A general tendency can be noted: lower filling ratios lead to lower thermal resistance, but at the expense of reduced heat capacity. For the given cryocooler capacity, operation across the full power range is possible provided that the safety pressure remains at 4.5 bar. In the range of 2–6 W, the thermal resistance decreases more steeply than in the 6–9 W interval, suggesting a possible transition to a different flow regime, as temperature plots in the latter range no longer exhibit strong oscillations. Nevertheless, the thermal performance remains considerably lower than in the setup reported by Dixit et al. (33), where resistances as low as 0.2 K/W were achieved. Their system, however, was approximately twice as large. Results for PHPs of similar dimensions and number of loops, such as those of Liang et al. (41; 42) or Natsume and Mito et al. (189; 24), are in closer agreement. It should also be noted that in those studies the effective thermal conductivity was calculated using a different formulation, based on the condenser length rather than the total PHP length, which led to significantly overestimated values of effective thermal conductivity.

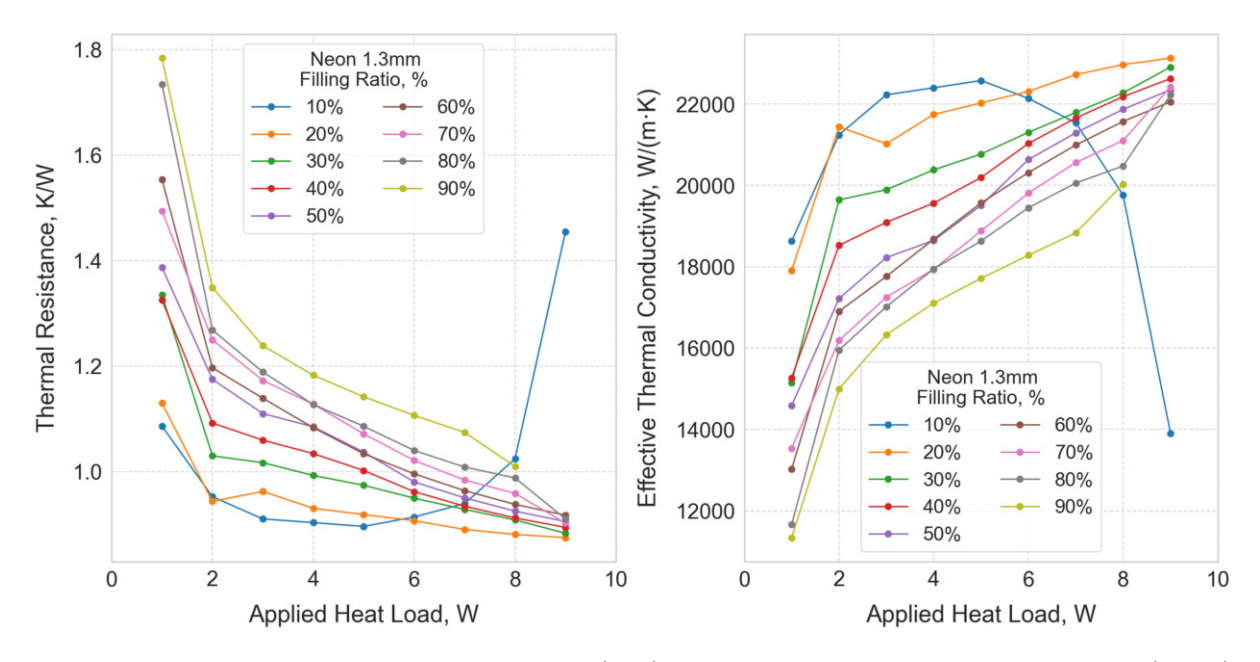


Figure 4.18: Averaged thermal resistance (left) and effective thermal conductivity (right) of 1.3 mm neon PHPs, calculated for each heat load and filling ratio over the final 15 minutes of each operating period.

Figure 4.19 presents the measurement uncertainties. With increasing heat load, temperature oscillations diminished, which led to a reduction in statistical uncertainty despite the higher applied power. An exception occurred at 8 W, where stronger fluctuations in temperature increased the statistical uncertainty. The case with FR = 90%, which

Effective Thermal Conductivity Uncertainty, W/m·K 1400 0.10 Thermal Resistance Uncertainty, K/W 1200 0.08 1000 0.06 800 0.04 600 400 0.02 0 2 8 10 2 8 10

showed the weakest stability, was therefore excluded from the analysis.

Applied Heat Load, W

Figure 4.19: Uncertainty of the experimental thermal resistance (left) and effective thermal conductivity (right) of 1.3 mm neon PHP.

Applied Heat Load, W

Figure 4.20 presents the evolution of the operating pressure in a 1.3 mm diameter PHP filled with neon, for FR ranging from 10% to 90% and heat loads from 0 to 10 W. Similar to the temperature behavior described earlier, a clear tendency is observed: higher FR values correspond to higher operating pressures, which in turn lead to higher working temperatures. The largest discrepancy in pressure occurs between FR = 10% and FR =20%, where a distinct step change in pressure levels is visible. For FR = 10%, dryout is observed upon reaching 10 W, manifested by a pressure drop, analogous to the behavior reported for nitrogen (Fig. 4.4, Fig. 4.8) and argon (Fig. 4.12). Flow regime transitions are also evident in this dataset. For example, at FR = 70%, the transition between 3 W and 5 W is marked by a progressive damping of pressure oscillations until they nearly vanish. A similar phenomenon occurs between 4 W and 5 W for FR = 60%. Such regime changes resemble the behaviour observed for nitrogen in the 1.7 mm PHP (Fig. 4.8), where low heat loads are characterised by oscillatory pressure signals that subsequently stabilise into damped oscillations. Only beyond a certain heat flux threshold do renewed oscillations appear. In the case of neon, however, the operating range is too narrow to capture such re-emergence of oscillations. For FR = 10\%, oscillations do not increase with applied power and only collapse upon the onset of dryout. Conversely, at very high filling ratios (above 80%), pressure characteristics are consistent with the observations of Dixit et al. (33), where high FR values led to elevated operating pressures and reduced oscillatory dynamics. The curves for intermediate filling ratios (30–50%) largely overlap, indicating that the liquid inventory in this range is sufficient to maintain a stable flow

structure. Despite differences in liquid quantity, the flow regimes established at these FR values exhibit similar pressure characteristics.

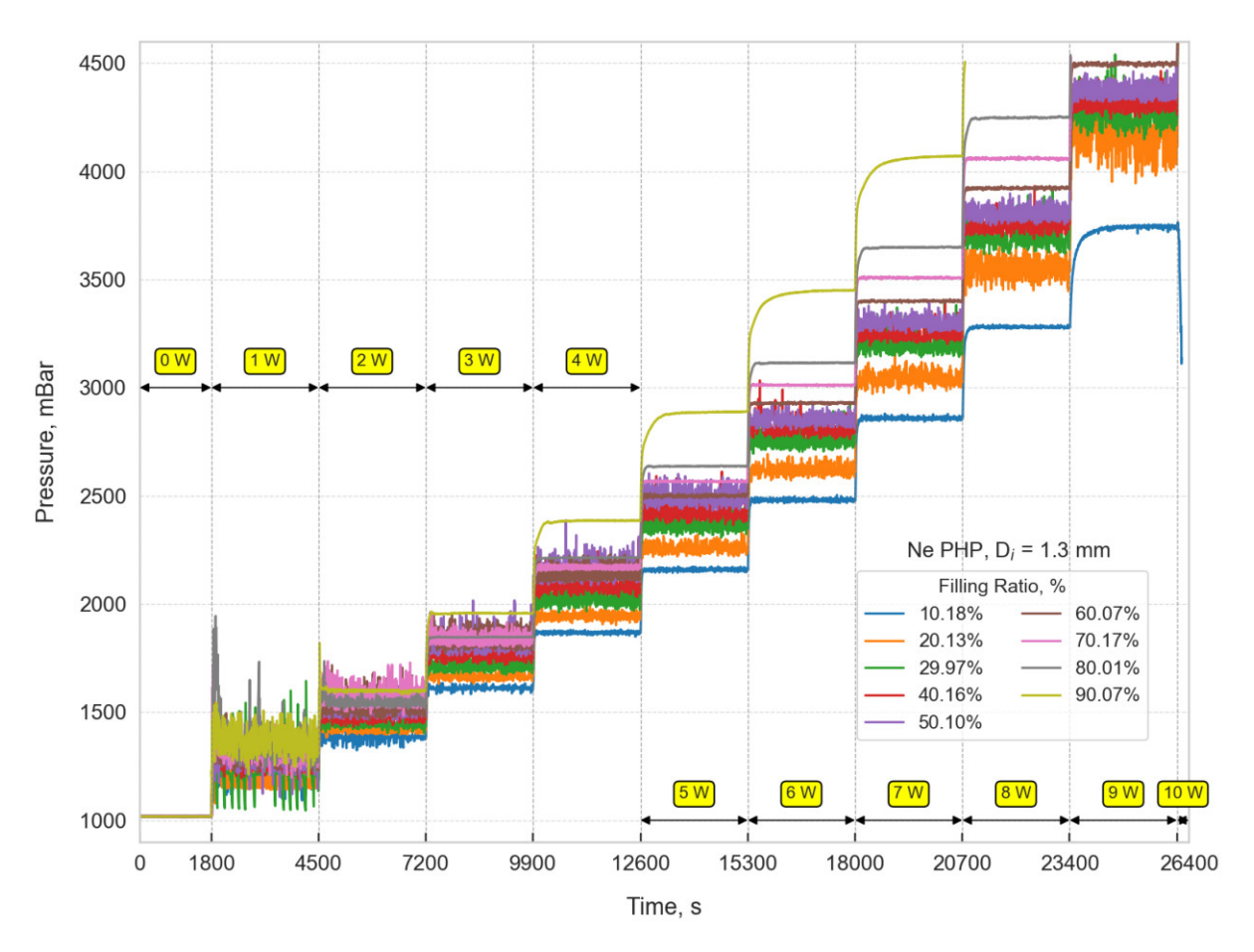


Figure 4.20: Pressure evolution in a 1.3 mm diameter PHP filled with neon, under heat loads ranging from 0 to 10 W and filling ratios from 10% to 90%.

Internal Diameter of 1.7 mm

Figures 4.21–4.24 present the results obtained for neon with an internal diameter of 1.7 mm. The experiments were performed well above the Bond criterion, with a value of 7.09 calculated for a condenser temperature of 27.1 K. Owing to the larger diameter, the safety pressure of 4500 mbar enabled measurements up to the performance limit of the cryocooler, slightly below 12 W. This represents one of the few cases where the limitation was not the safety pressure but the cooling capacity of the cryocooler, particularly for filling ratios of 10 and 20%. The effect was accompanied by a rise and subsequent stabilization of the condenser temperature, consistent with the increase in cryocooler efficiency at higher operating temperatures. Differences between filling ratios became increasingly pronounced as the applied heat load increased. The amplitude of thermal oscillations decreased with higher input power. The largest fluctuations occurred at 1–3 W, whereas

at higher loads the system evolved toward a more stable regime. This trend was observed consistently for both low filling ratios (10–20%) and high filling ratios (70–90%). Two distinct groups of behavior can be identified. At low filling ratios (10–20%) and at high filling ratios (70–90%), the evaporator exhibited smaller temperature oscillation amplitudes compared to the intermediate range (30–60%). Nevertheless, a general trend is evident across all cases that the average evaporator temperature rises with increasing filling ratio. The lowest temperatures were obtained at 10%, while higher filling ratios systematically shifted the operating point toward elevated temperature levels. The condenser temperature remained nearly constant up to the maximum tested load, with a noticeable increase only in the final stage of the experiment, when the cryocooler capacity was reached.

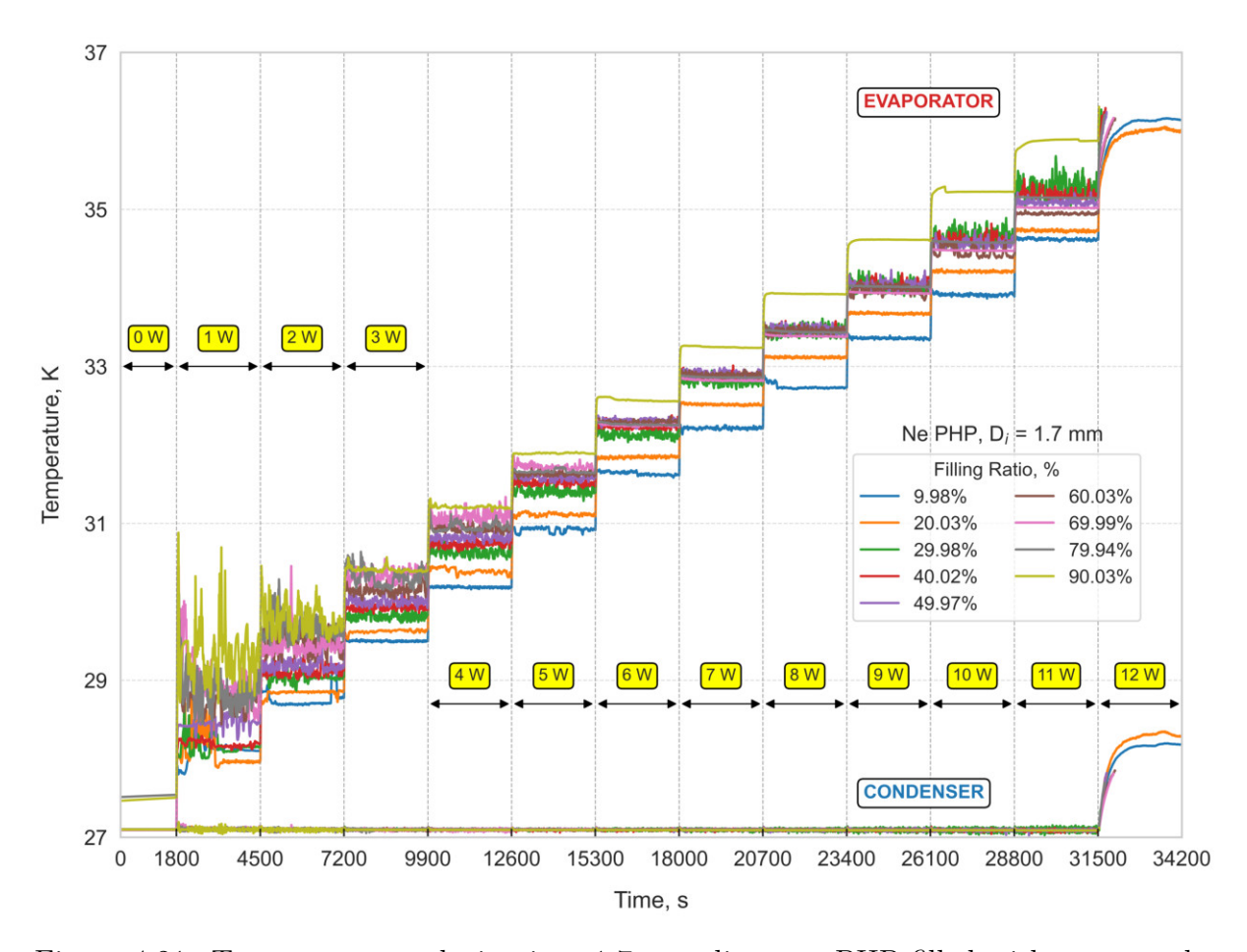


Figure 4.21: Temperature evolution in a 1.7 mm diameter PHP filled with neon, under heat loads ranging from 0 to 12 W and filling ratios from 10% to 90%.

Figure 4.22 summarizes the thermal resistance and effective thermal conductivity for the case of neon with an internal diameter of 1.7 mm. As in the previous analyses, the thermal resistance decreases with increasing heat load and no dry-out condition was observed. The largest reduction in thermal resistance occurs at low heat inputs, which corresponds to the onset of oscillations and the transition into the pulsating operation mode. In terms

of thermal performance, the 1.7 mm PHP consistently outperforms the 1.3 mm configuration, for which the Bond number calculated at the condenser temperature equals 4.14. Based on the conventional guidelines, such a trend is expected. However, in cryogenic conditions, the applicability of the Bond criterion becomes increasingly questionable, as also demonstrated in the study of Dixit et al. (34). The achieved performance is still far from the high-conductivity PHPs reported by Dixit et al. (33). Nevertheless, for PHPs of comparable dimensions, the present configuration shows lower thermal resistance than in other studies (41; 42; 189; 24). The associated uncertainties are presented in Fig. 4.23. These results indicate that the effective thermal conductivity of neon PHPs increases significantly with the number of loops. In this case, the dominant contribution to the uncertainty originates from statistical effects, since despite the increase in applied heat load, the main influence arises from the amplitude of temperature oscillations.

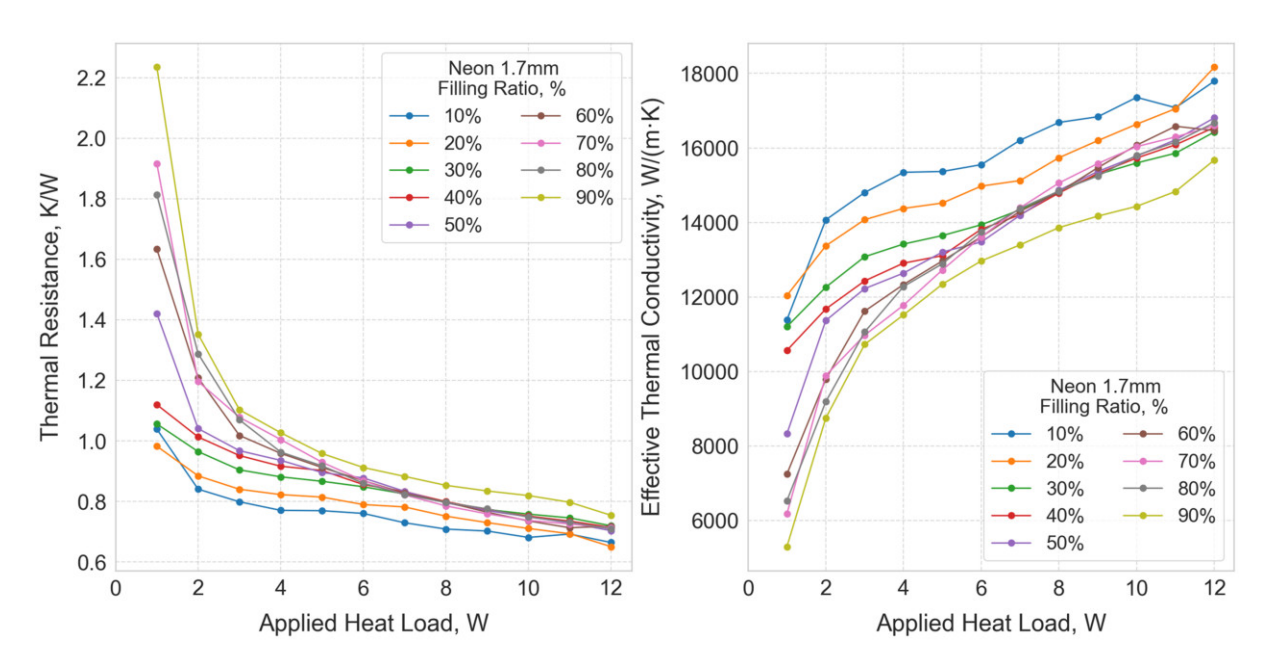


Figure 4.22: Averaged thermal resistance (left) and effective thermal conductivity (right) of 1.7 mm neon PHPs, calculated for each heat load and filling ratio over the final 15 minutes of each operating period.

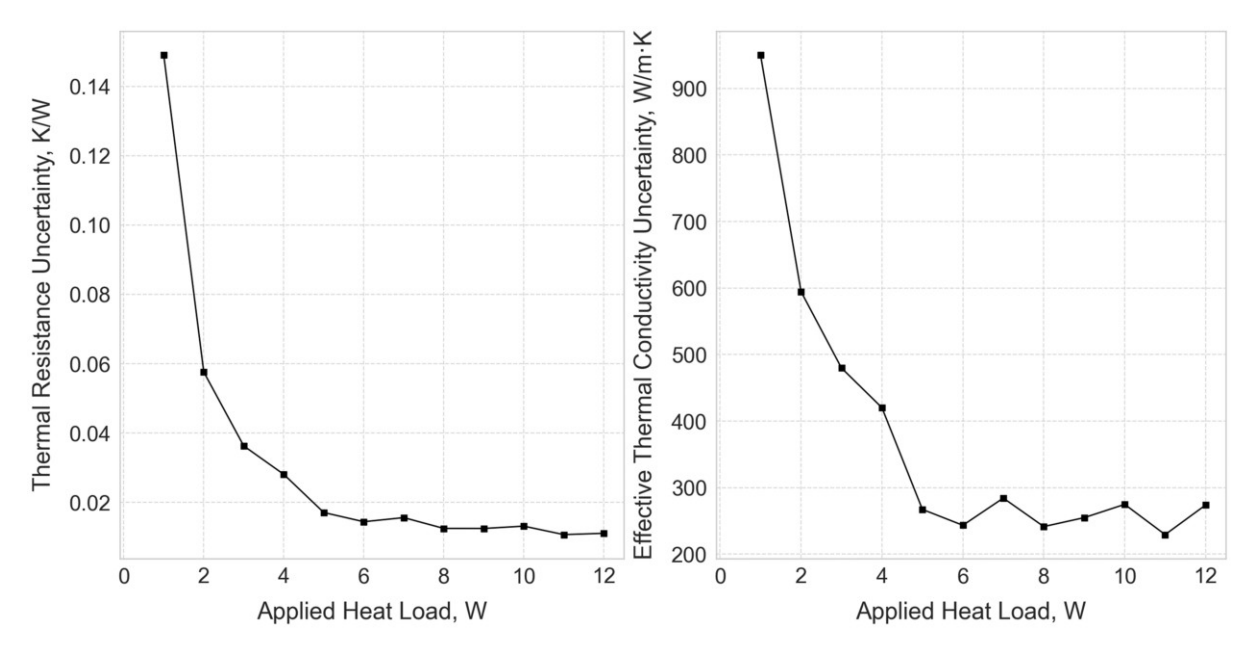


Figure 4.23: Uncertainty of the experimental thermal resistance (left) and effective thermal conductivity (right) of 1.7 mm neon PHP.

Figure 4.24 shows the pressure evolution over time for the PHP with an inner diameter of $D_i = 1.7$ mm filled with neon. In all cases, the average pressure increases monotonically with the applied heating power, which reflects the rise of the saturation pressure, independent of the changing flow characteristics and oscillation amplitude. The curves corresponding to filling ratios of 30–50% are the closest to each other, while the extreme cases (10% and 90%) show more pronounced deviations. In this test, a particularly interesting observation is that the increase in average pressure does not correlate directly with the increase in filling ratio. Distinct flow regime transitions are evident: at low heat loads (1–3 W) the pressure profiles exhibit strong oscillations, which is consistent with the previous tests, which then become significantly smoothed at higher heating powers. A similar effect is observed for filling ratios of 70–80%, where the pressure profile gradually stabilizes with increasing heat input. These smoothed profiles tend to exhibit smaller oscillation amplitudes compared to the lower filling ratio cases, especially in the range of 30–60%. Such behavior is not typical for standard PHP operation and most often occurs in cases with a high Bond number, where capillary forces are less dominant factor governing the flow dynamics. A similar phenomenon was reported by Dixit et al. (34) for helium PHPs, where the average pressure did not increase with higher filling ratios due to a change in the flow regime. For neon, the current state of the literature does not provide other examples of PHPs investigated in such detail.

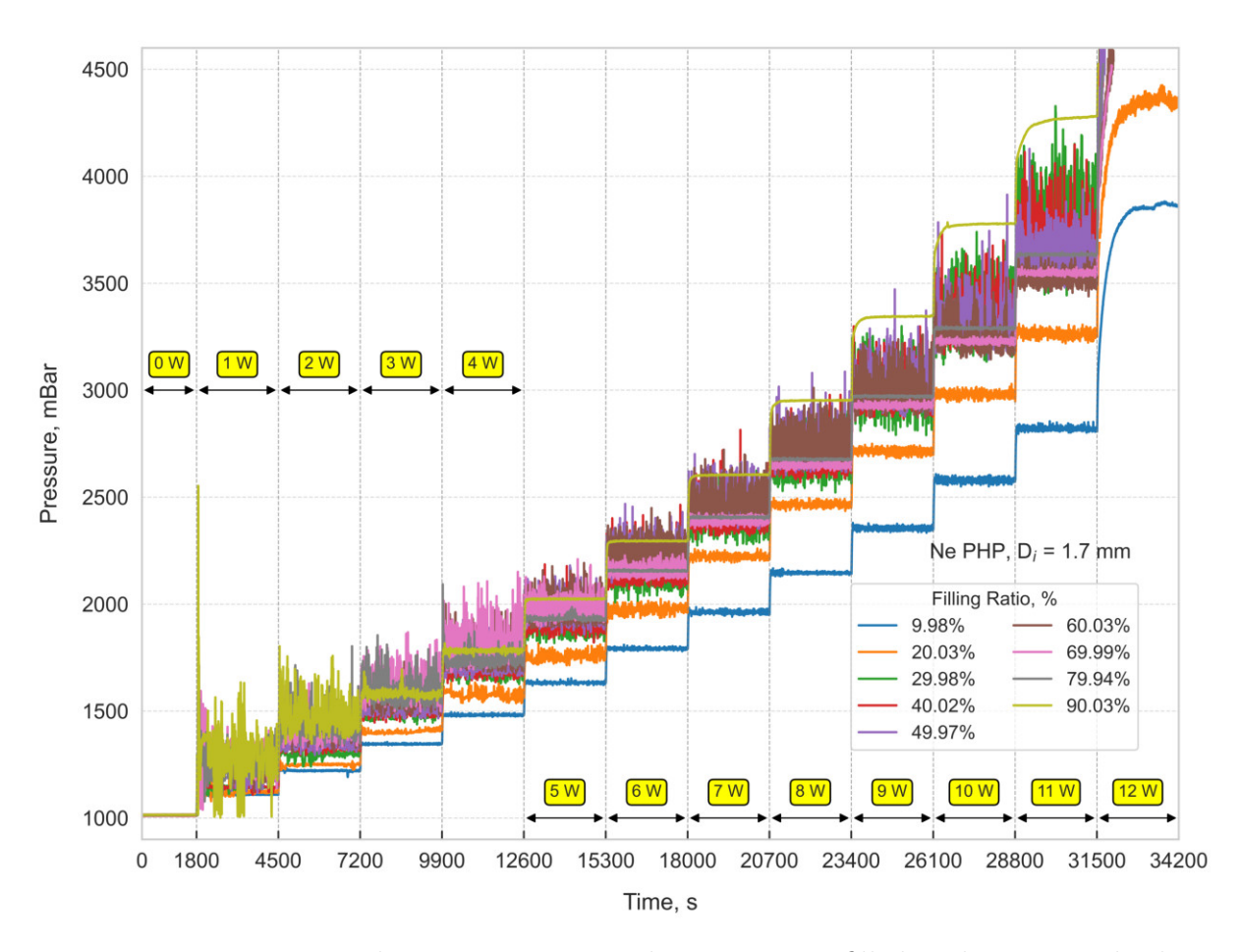


Figure 4.24: Pressure evolution in a 1.7 mm diameter PHP filled with neon, under heat loads ranging from 0 to 12 W and filling ratios from 10% to 90%.

4.2 Summary of Experiment and Parametric Analysis

Figure 4.25 compiles, for each heat input Q, the minimum thermal resistance obtained across filling ratios ranging from 10% to 90%. The color of each marker identifies which filling ratio gives the lowest value at that Q. When a point is rendered with two colors, it indicates that two filling ratios have achieved a minimum that is close to the same value, enhancing the readability of the chart. The curves show that the 1.7 mm PHPs maintain lower thermal resistance than the 1.3 mm PHPs over the entire range and the difference is on the order of a few tenths of K/W, except for Argon 1.7 mm at 7.5 W where heat was insufficient to maintain stable operation. Argon and nitrogen form the lowest band, with minima approaching about $0.5 \, \text{K/W}$ at the upper end of their heat loads. Neon remains at higher levels above about $0.75 \, \text{K/W}$ and its operating range is narrower. The narrower temperature range for neon originates from the steeper saturation curve. The pronounced drop in performance at the maximum heat load for Ne 1.7 mm makes it clear

that, because the fluids operate over different temperature—pressure ranges, a direct crossfluid performance ranking is not meaningful and that only trends and diameter effects can be inferred. This cannot be concluded without interpretation through thermophysical properties and dimensionless indicators, which will be introduced next. Local peaks of the best thermal resistance for the given FR and Q are particularly visible for neon; for example, between 5-6 W for the 1.3 mm or 11-12 W for the 1.7 mm, they indicate a decreasing performance of low filling ratios as the applied heat increases. Based on the available knowledge of flow regime transitions, after a peak, the lowest thermal resistance is reached for a given filling ratio, the incidence of localized liquid-film dryout increases, and thermal performance shifts in favor of higher filling ratios. This is consistent with the regime maps proposed by Khandekar (6), Saha et al. (120) and has been shown statistically with cryo-PHP by Li et al. (183). Near-linear decreases in thermal resistance are observed for Neon at 1.3 mm and 6 to 9 W, for Argon at 27.5 to 32.5 W for both diameters and for Nitrogen at 1.3 mm and 17.5 to 25 W. This behavior indicates a velocity-driven enhancement or an annular-type shift consistent with the flow-boiling characteristics described in the review of Thome (180) within the same filling ratio. Meanwhile, the rise of thermal resistance between 4 and 5 W for neon 1.7 mm and a rise between 5 and 6 W at 1.3 mm and then a consistent decrease, may further suggest a transition from Taylor-bubble slug/plug structures toward churn and annular-like flow, as observed in the microchannel regime evolution by Harirchian and Garimella (190) and by Triplett et al. (191), with a statistical thermo-visual study of cryogenic PHP reported by Li et al. (183) supporting such an interpretation. A potential explanation is that, in churn flow, which being more chaotic and therefore exhibits horizontal velocity components, the wall liquid film is prone to rupture, which disturbs highly efficient liquid film heat transfer. This phenomenon also occurs for argon at 1.3 mm in the range of 15 to 22.5 W for a filling ratio of 40%. After reaching maximum performance at a low filling ratio, as with neon at 1.3 mm at 5 W or at 1.7 mm at 10 W, higher fillings become the most efficient. Similar behavior was reported by Iwata and Bozzoli (192), who, using an infrared camera, attributed the low-FR limit to evaporator-side localized dryout and superheated vapor, which reduce latent heat transfer and shift the process toward a sensible-heat-limited regime. For argon, the optimal filling ratio shifts from about 10% to 20% at low Q to about 30% to 50% as Q increases. For nitrogen, the optimum lies mainly between 20%and 30%. For neon, the best points remain at or below 30%. No optimal filling ratio appears above 50% because a high filling ratio increases viscous dissipation due to the higher viscosity of the liquid and reduces the relative contribution of capillarity from the interfacial area to the internal forces from higher content of mass, which weakens the oscillatory driving. A very low filling ratio of around 10% facilitates startup at small Q, but it becomes prone to drying out as Q grows and stable operation at this level has been confirmed only for neon. Lower heat-transport capacity for neon arises from the smaller

volumetric latent heat content for a given closed capillary volume compared to argon and nitrogen.

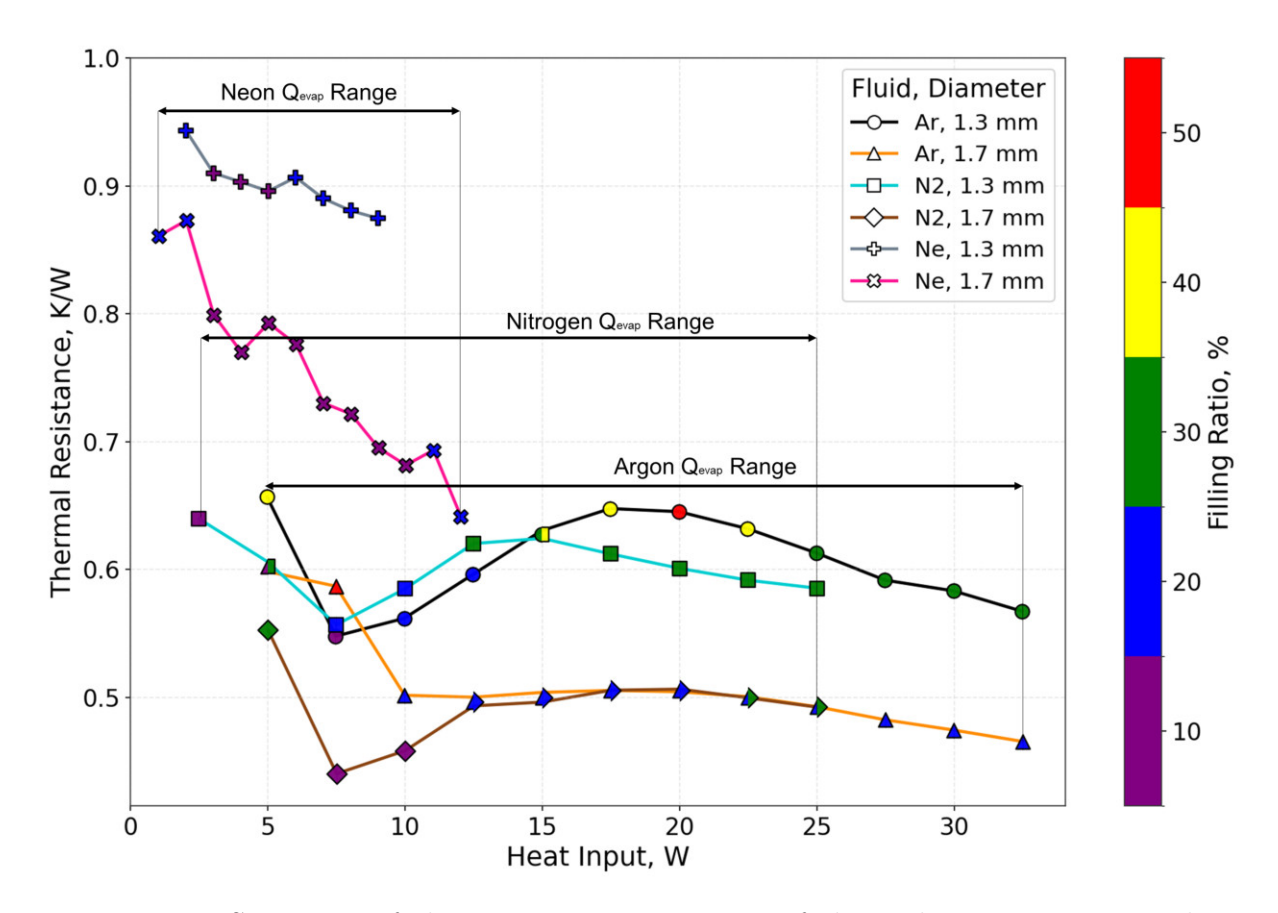


Figure 4.25: Summary of the experiments in terms of thermal resistance versus heat input for the tested fluids, diameters and filling ratios. The color on the right-hand side indicates the most efficient filling ratio for a given heat load. For each Q, the minimum $R_{\rm th}$ was selected from filling ratios in the range 10–90%.

To generalize the findings from Figure 4.25 and provide deeper physical insights into the controlling mechanisms, the data are re-evaluated within a dimensionless framework. The dimensionless number and thermophysical properties presented are calculated using the REFPROP database (148). All properties are evaluated at the average operating temperature, defined as $T_{\text{avg}} = (T_e + T_c)/2$, which is taken as an average value from the last 15 min of each measurement and assumed to be under saturation conditions. The common legend for the analysis in Figures 4.26–4.30 is detailed in Table 4.2.

Table 4.2: Legend for Figures 4.26, 4.27, 4.28, 4.29 and 4.30; arrows denote the change of X_i in response to an increase of heat input ΔQ for different working fluids and inner diameters D_i at FR = 50%.

Fluid	D_i [mm]	ΔT [K]	$\Delta Q \ [\mathbf{W}]$	Marker	Line
Ar	1.3	16.9	$7.5 \rightarrow 22.5$	•	
Ar	1.7	14.5	$7.5 \rightarrow 22.5$	×	
N_2	1.3	12.6	$7.5 \rightarrow 22.5$	•	
N_2	1.7	10.5	$7.5 \rightarrow 22.5$	×	
Ne	1.3	6.6	$3 \rightarrow 9$	•	
Ne	1.7	6.9	$3 \rightarrow 9$	×	

Legend: • and a solid line denote $D_i = 1.3 \,\mathrm{mm}$; × and a dashed line denote $D_i = 1.7 \,\mathrm{mm}$. Additionally, marker opacity corresponds to the filling ratio (FR), where higher opacity (darker markers) indicates a higher FR

The analysis begins with the Bond number (Bo), an indicator of the gravity-capillarity balance that is widely used in PHP studies. In PHPs, it reflects the competition between body-force effects under q and capillarity, which maintains slug-plug flow. A commonly cited value, $Bo \approx 4$, is often taken as an upper geometric limit beyond which gravitational effects dominate and oscillations are suppressed, as previously detailed in Section 1.3.7. Figure 4.26 shows the thermal resistance reorganized along this axis. Argon and nitrogen fall into the low-Bo range, where capillary forces remain sufficient to sustain thin films. The vertical reference lines, calculated at a common initial pressure of 1 bar, separate the two diameters and confirm that the $D_i = 1.7$ mm shifts to higher Bo due to the square of the diameter dependence while still achieving lower resistance because capillary-inertial balances remain favorable within the tested window. Neon forms a distinct band at higher Bo. Even though it exceeds the conventional $Bo \approx 4$ value for each diameter, stable oscillatory operation is observed, and R decreases with heating until the pressure limit is reached. This behavior results from simultaneous reductions in surface tension and density differences of the phases along the accessible saturation range, which increase Bo without decreasing the evaporation—condensation intensity. The arrows in Fig. 4.26, defined in Table 4.2, trace the response to increasing heat load at FR = 50%. For argon and nitrogen, the operating point shifts gently toward larger Bo as T_{evap} increases, following the monotonic decrease in $\sigma(T)$. For neon, the drift is steeper because both σ and $\Delta \rho$ vary more strongly with temperature. However, its predictive possibilities are limited when the amplitude and curvature of the directions depend on temperature and the shape of the saturation curve.

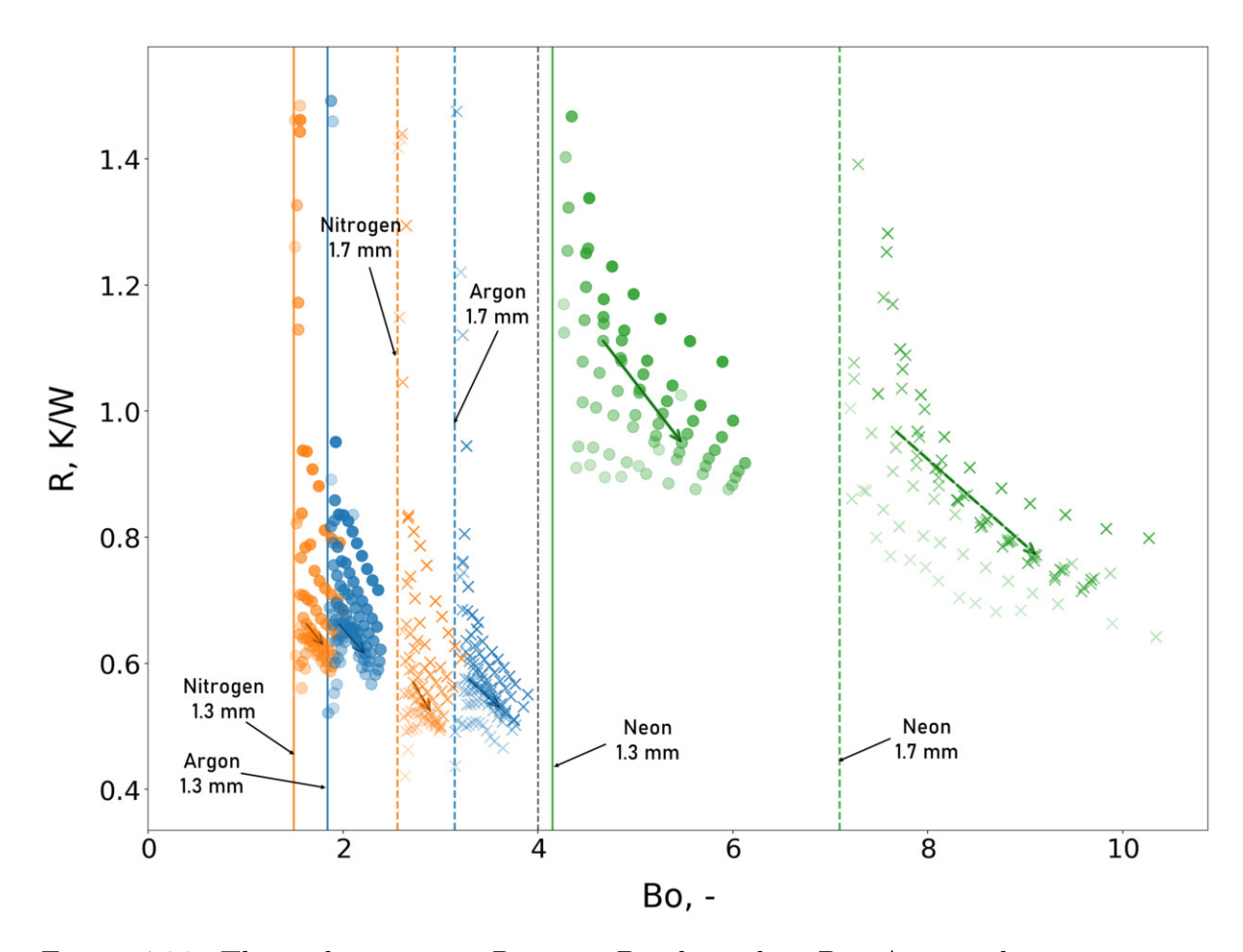


Figure 4.26: Thermal resistance R versus Bond number Bo. Arrows show trajectories with increasing Q at FR = 50%, legend in Table 4.2.

To relate the driving potential to the measured resistance, Fig. 4.27 plots the slope of the saturation curve, $dp/dT|_{\rm sat}$, against R. This derivative is the pressure rise per unit temperature difference. Neon occupies the highest range, exceeding $4\times10^4\,{\rm Pa}\,{\rm K}^{-1}$, while argon and nitrogen lie below $3\times10^4\,{\rm Pa}\,{\rm K}^{-1}$. Despite the stronger driving potential, neon exhibits the largest R. The reason is operational: a large $dp/dT|_{\rm sat}$ causes pressure to climb rapidly, even for small ΔT . Argon and nitrogen, with lower $dp/dT|_{\rm sat}$, can sustain larger ΔT and thus higher heat transfer potential. The arrows in Fig. 4.27 show that at FR=50% increasing Q increases $dp/dT|_{\rm sat}$ and reduces R until the pressure or cryocooler capacity limit is approached.

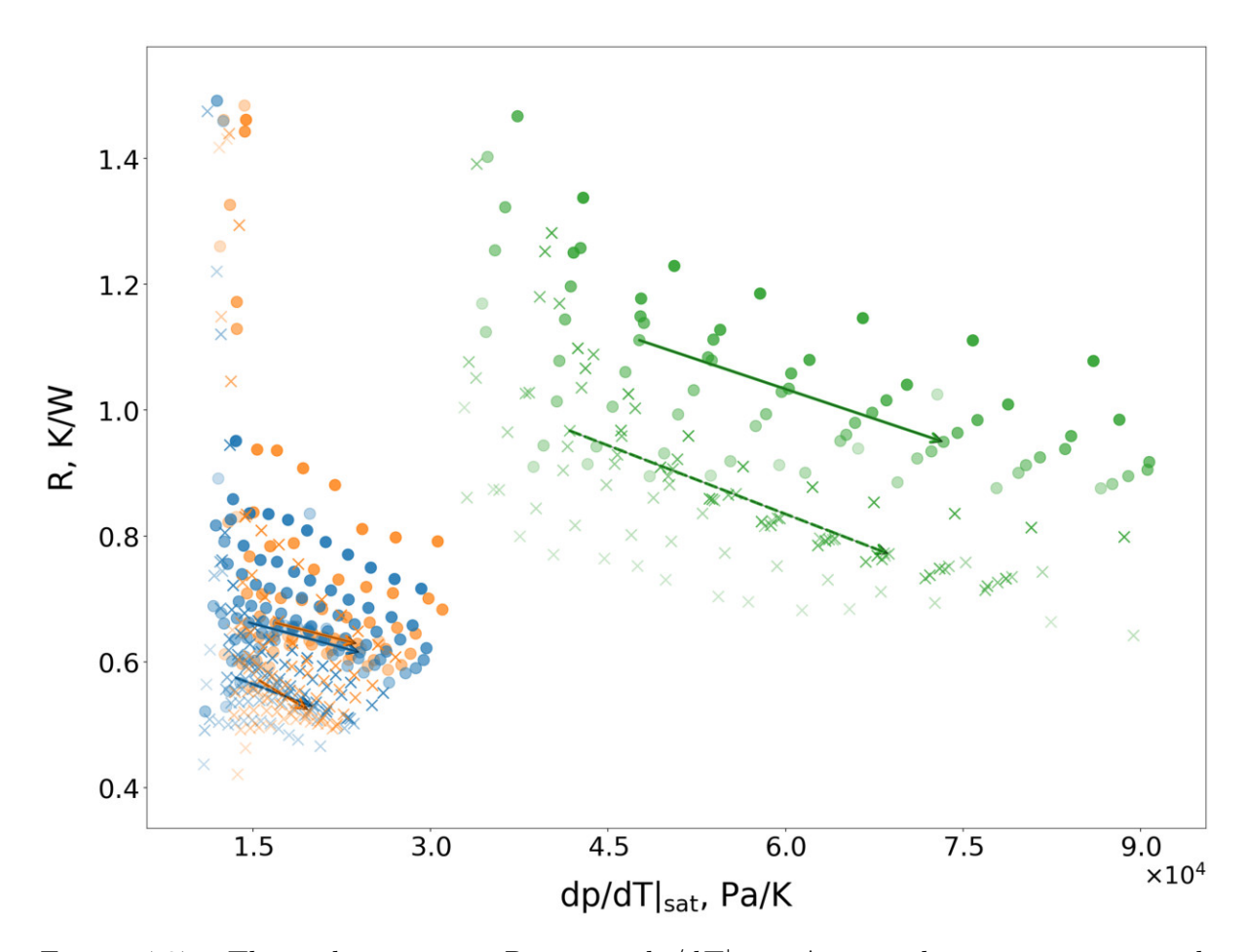


Figure 4.27: Thermal resistance R versus $\mathrm{d}p/\mathrm{d}T|_{\mathrm{sat}}$. Arrows show trajectories with increasing Q at FR=50%; legend in Table 4.2.

The role of viscous damping is examined using the Ohnesorge number $Oh = \frac{\mu}{\sqrt{\rho\sigma D_i}}$, which characterizes the relative contribution of liquid viscosity to inertial and capillary effects. Figure 4.28 plot R against Oh. A direct global interpretation is misleading: neon has the highest thermal resistance yet operates at the lowest Oh (primarily $Oh < 1.35 \times 10^{-3}$), whereas argon and nitrogen reach lower R at higher Oh values of up to 1.65×10^3 . This inverts the simple expectation that higher damping should correlate with higher resistance. The relevant physics are visible locally: as Q increases, temperature rises, the liquid viscosity μ_ℓ drops more rapidly than $\sqrt{\rho_\ell \sigma}$, so Oh decreases (left-pointing arrows) while R decreases (downward arrows). Reduced relative viscous damping facilitates stronger oscillations and film renewal, as described by Tessier-Poirier et al. (193), lowering R. Thus Oh acts as a local indicator of hydrodynamic damping, not as a global predictor across fluids. Neon performs poorly not because its viscous damping is high, but because its accessible operating window is reduced by its high $dp/dT|_{\rm sat}v$ in Fig. 4.27, preventing access to the high-Q, low-R regime.

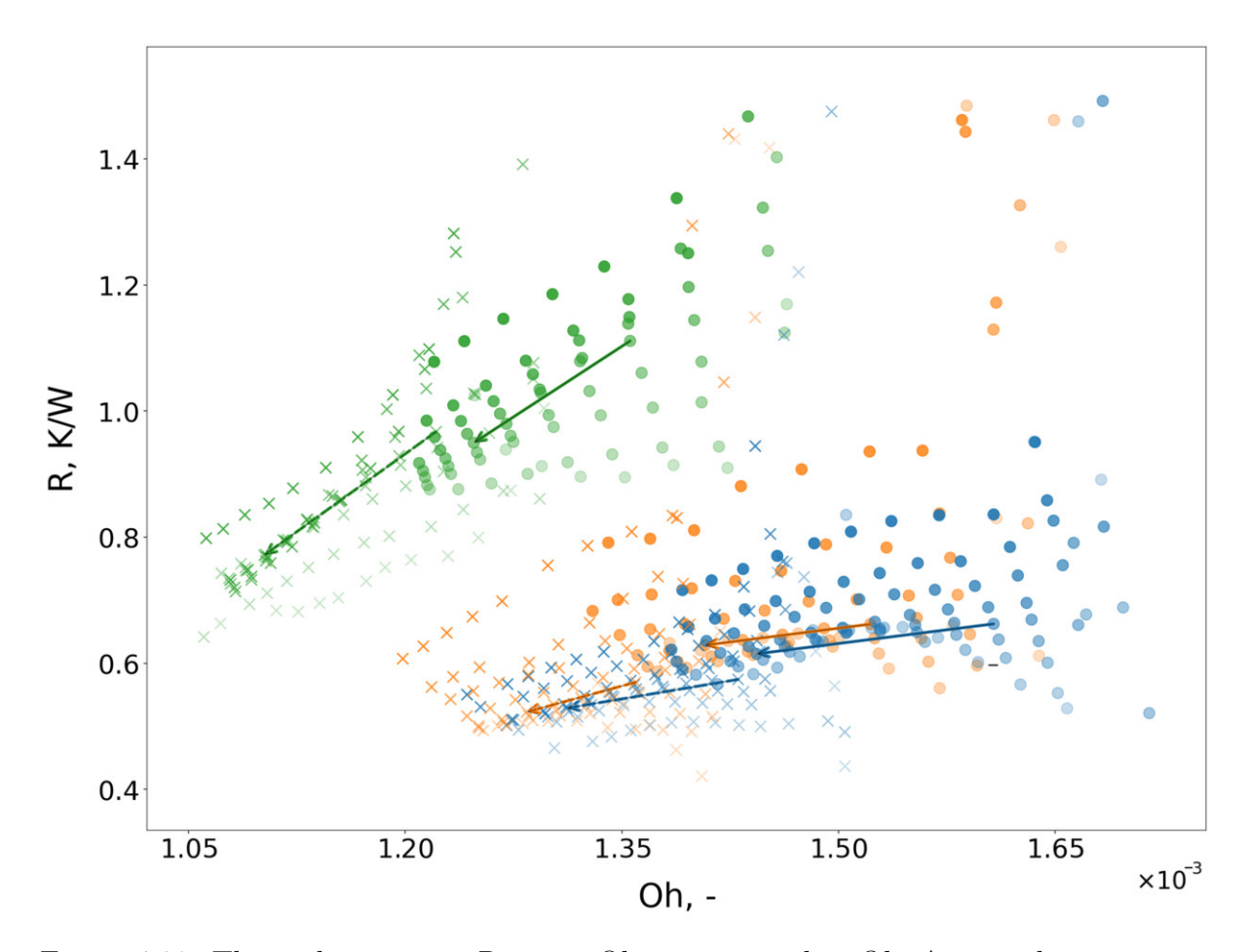


Figure 4.28: Thermal resistance R versus Ohnesorge number Oh. Arrows show trajectories with increasing Q at FR = 50%; legend in Table 4.2.

The thermal efficiency of the phase-change cycle is evaluated using the Jacob number $Ja = \frac{c_P (T_{\rm evap} - T_{\rm cond})}{h_{lv}}$ in Fig. 4.29, which represents the ratio of sensible heat absorbed by the liquid to the latent heat of vaporization. A low Ja is, in principle, favorable, as it implies that a larger fraction of heat input is converted into latent heat for driving the flow (194). Here Ja ranges of argon, nitrogen and neon partly overlap, so Ja alone does not determine the relative performance of different fluids. Argon and nitrogen cluster mainly at Ja < 0.12 and achieve the lowest R, whereas neon extends to higher Ja (up to 0.25) and generally exhibits higher R. Thus, Fig. 4.29 indicates that a larger Ja can be a contributing penalty, but it does not, by itself, explain why R remains highest for neon. The offset likely reflects the combined property set, such as latent heat per unit volume, rather than Ja alone. Locally (arrows at FR = 50%), R decreases as Ja increases. This does not contradict the global finding and shows that the performance gains from operating at higher temperatures simultaneously increase $dp/dT|_{\rm sat}$ (Fig. 4.27) and decrease Oh (Fig. 4.28), dominating the thermodynamic penalty of rising Ja.

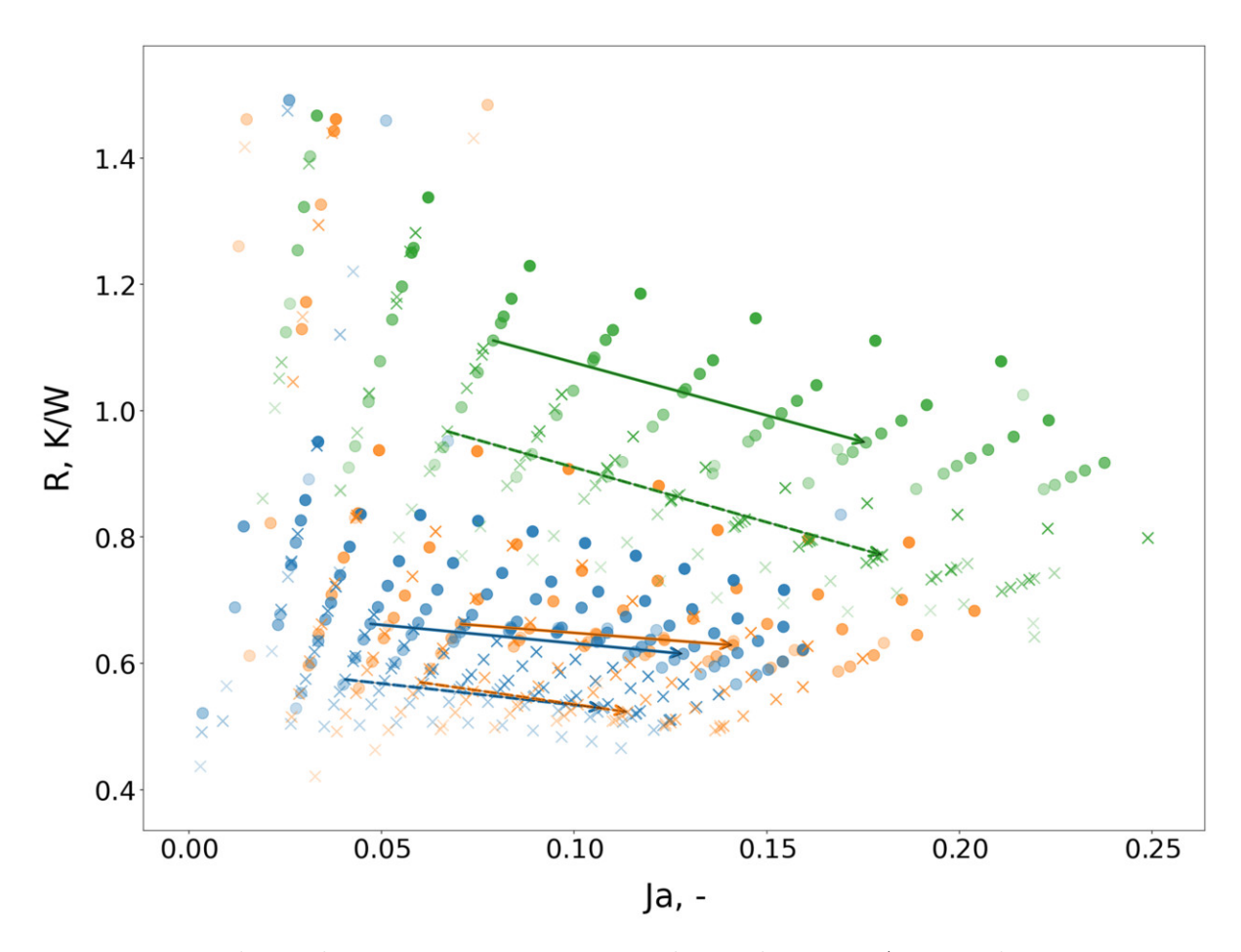


Figure 4.29: Thermal resistance R versus Jacob number Ja. Arrows show trajectories with increasing Q at FR = 50%; legend in Table 4.2.

The final analysis in Figure 4.30 organizes the data by fundamental properties. The left panel plots the latent heat h_{lv} and the right panel plots the surface tension σ . The h_{lv} plot shows a clear global relation in which thermal resistance R decreases with increasing latent heat. Argon $(h_{lv} \approx 1.8-2.0 \times 10^5 \,\mathrm{J\,kg^{-1}})$ and nitrogen $(\approx 1.5 \times 10^5 \,\mathrm{J\,kg^{-1}})$ achieve low R. Neon $(\approx 0.8 \times 10^5 \,\mathrm{J\,kg^{-1}})$ remains in the high $R \gtrsim 0.85 \,\mathrm{K\,W^{-1}}$ range. This confirms the conclusion from the Jacob-number analysis: h_{lv} is a primary indicator of baseline performance and sets the energy transport capacity. The global ordering shows neon at low σ and argon/nitrogen at higher σ , consistent with the Bo analysis. Locally, increasing Q raises the temperature and lowers σ , shifting the operating point to lower σ and downward by decreasing R.

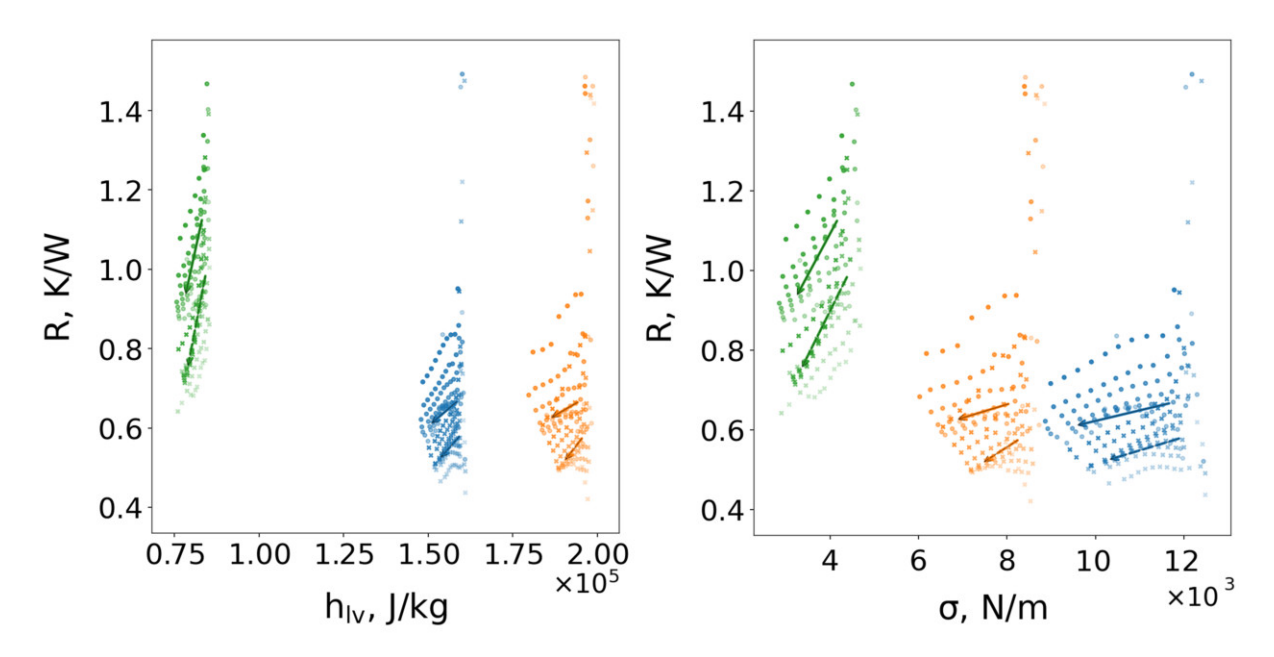


Figure 4.30: Thermal resistance R versus latent heat h_{lv} (left) and surface tension σ (right). Arrows show trajectories with increasing Q at FR = 50%; legend in Table 4.2.

Chapter 5

CFD Analysis Results

This chapter presents the capabilities of the numerical model, the generated flow structures and a comparison between the measured data and the simulation. Representative frames are shown to illustrate the internal dynamics of the PHP, together with averaged quantities and their agreement with experimental measurements. Analyses were carried out for all fluids examined experimentally and for two different internal diameters to demonstrate both the strengths and limitations of the proposed numerical approach.

Particular attention is devoted to the dynamics of vapor bubbles, which are the main manifestations of the model performance. Their shape, distribution and motion provide insight into the internal processes governing PHP operation.

5.1 Mesh Independence Study

The early shape and distribution of bubbles was also used as a criterion for mesh density selection. This approach was already applied in (143) and the same grid resolution is used here. That study analyzed how mesh density affects bubble nucleation, interface sharpness and heat input at the evaporator wall. The mesh independence study from that publication is briefly revisited below.

Three mesh variants are shown in Figure 5.1. The heating rate on the evaporator wall, expressed in K/s as the time derivative of the average temperature, was used as the primary measure of mesh sensitivity. Figure 5.2 illustrates the dependence of the heating rate on the density of the mesh. Mesh 2 was selected as it reproduces the heating rate of Mesh 3 with significantly lower computational cost.

However, thermal convergence in terms of the heating speed of evaporator alone is not sufficient. The initial phase distribution is also influenced by mesh resolution. To ensure consistent starting conditions, a random distribution based on the prescribed filling ratio was applied in all cases. Vapor structures at 1, 3 and 5 s were compared to assess bubble formation and interface resolution. The coarsest mesh (Mesh 1) fails to capture small vapor bubbles, while the smearing of the interface and the flow distortion are clearly visible. The black circles in Figure 5.3 highlight blurred regions and the squares indicate non-physical flow features.

By contrast, Mesh 2 and Mesh 3 both capture small bubbles, preserve the sharpness of phase interfaces and minimize numerical artifacts. Therefore, Mesh 2 provides the best compromise between accuracy and computational efficiency and is used in all subsequent simulations.

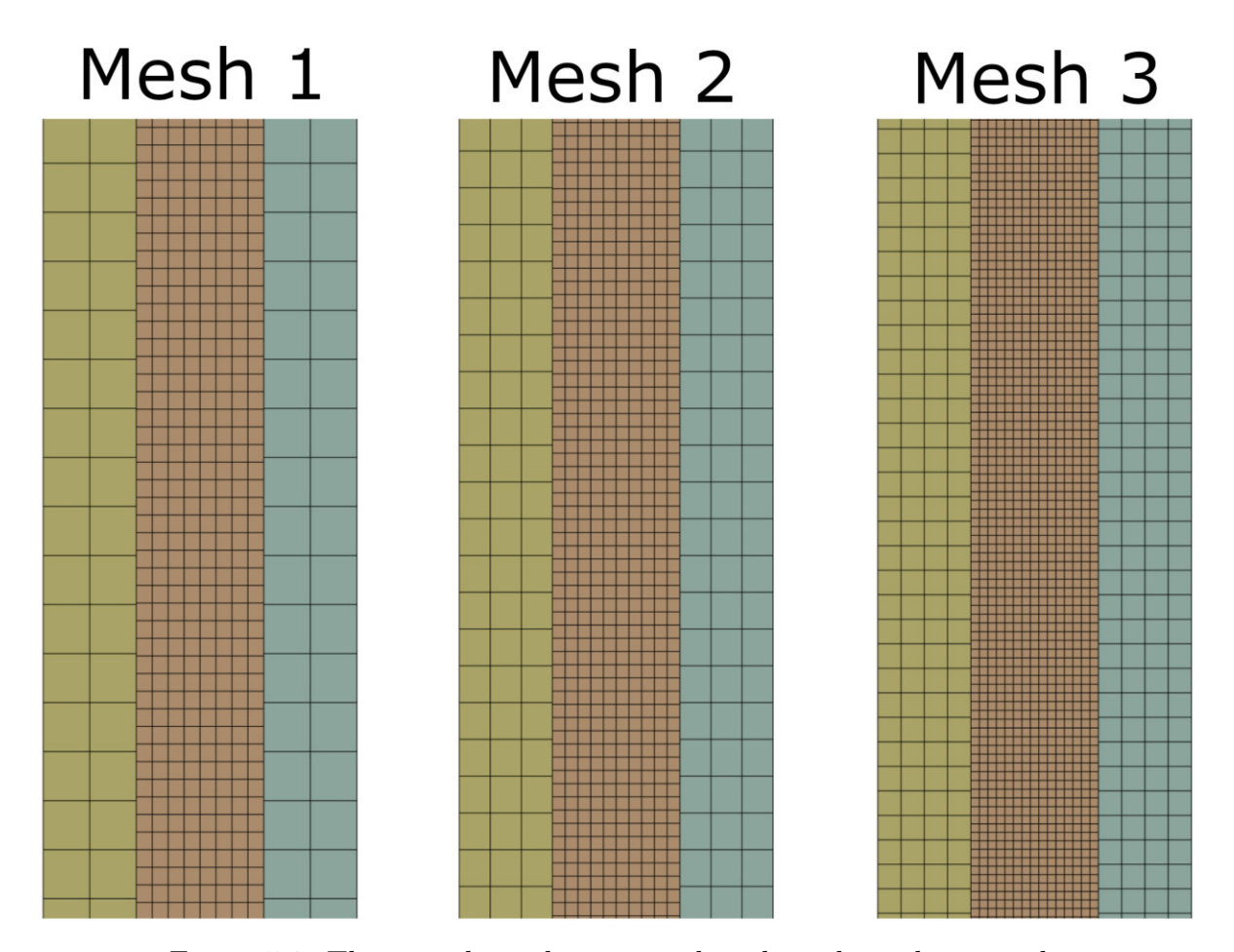


Figure 5.1: Three mesh resolutions used in the independence study.

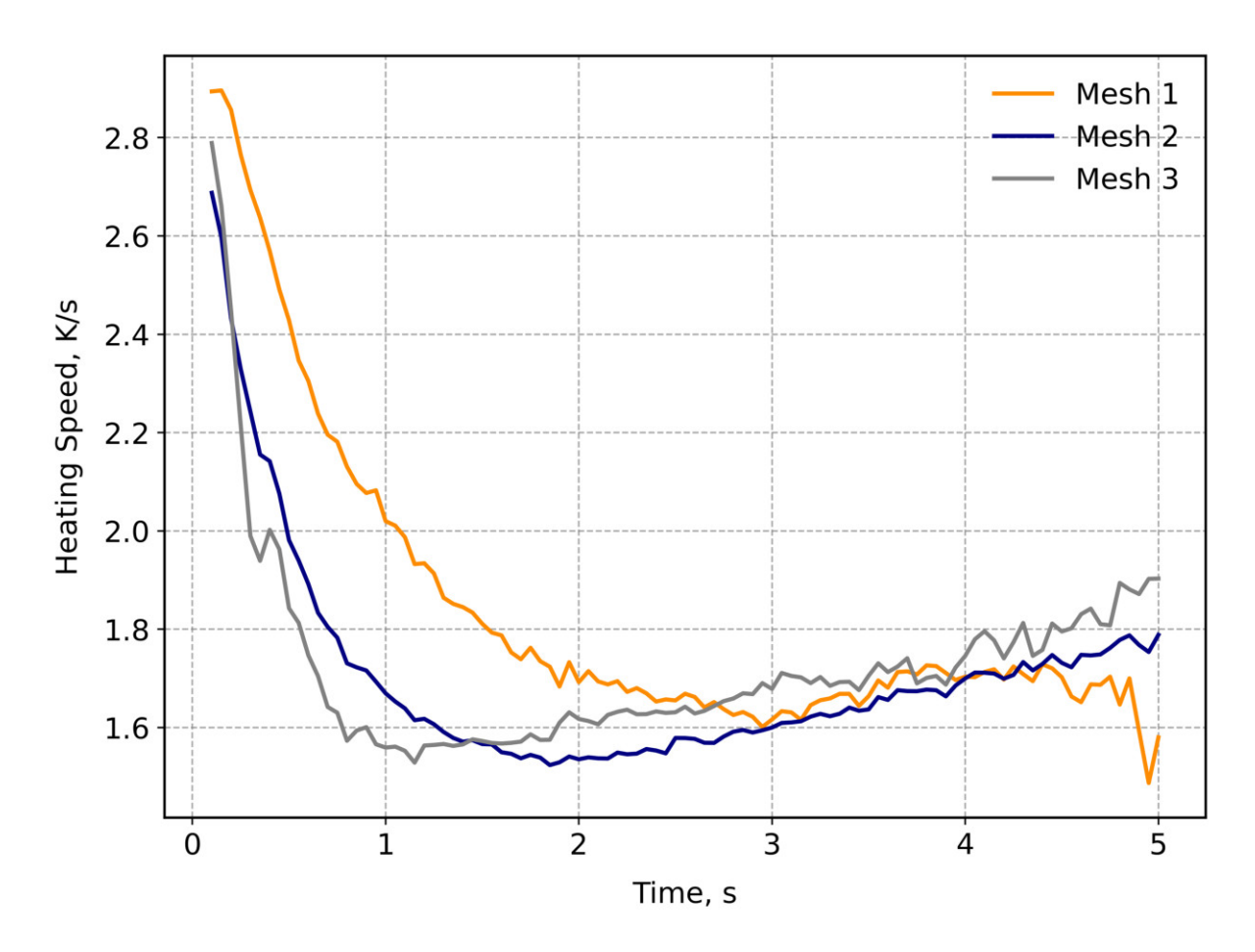


Figure 5.2: Heating rate of the evaporator wall for different mesh densities.

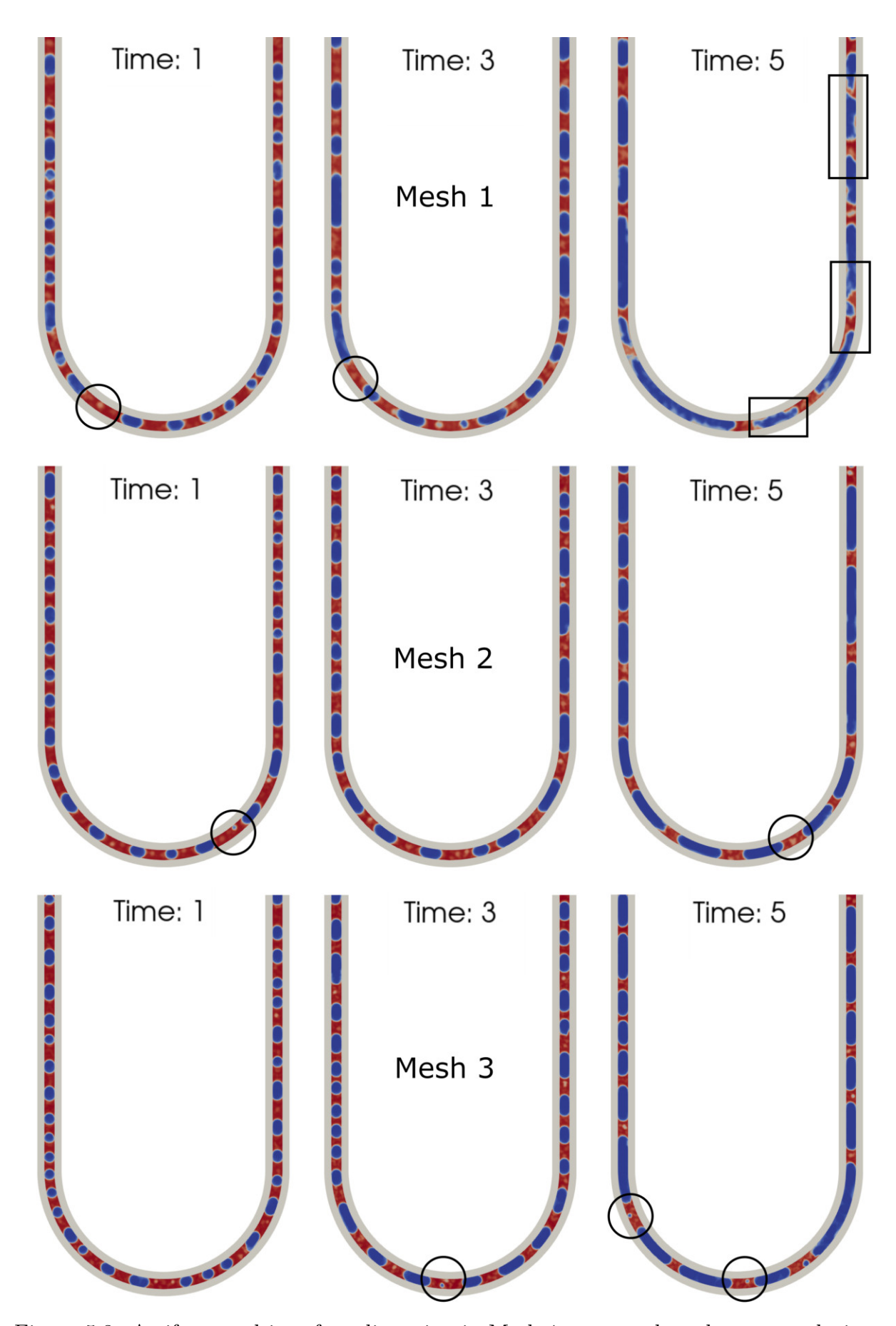


Figure 5.3: Artifacts and interface distortion in Mesh 1 compared to sharper resolution in Mesh 2 and Mesh 3.

The use of early bubble topology in addition to the heating rate criterion is consistent with best practices for VOF in capillary flows, where interface sharpness and meniscus curvature must be preserved to avoid artificial diffusion. The present choice of Mesh 2 therefore targets global thermal performance and plug—slug kinematics rather than microlayer physics, which would require a different refinement strategy (143).

5.2 Numerical Setup and Initialization

The numerical settings adopted in Table 5.1 were chosen as a compromise between accuracy, predictive capability and computational cost. Gradient and second-order accuracy interpolation schemes provide sufficient resolution, while van Leer-based divergence schemes with interface compression preserve sharp phase boundaries without introducing spurious oscillations (150). Corrected Laplacian and surface normal treatments mitigate errors due to mesh non-orthogonality in the U-bends. The PIMPLE configuration with three inner corrections was found sufficient for pressure-velocity coupling, supported by strict solver tolerances to ensure convergence in the closed domain. Relaxation factors of 0.8 were applied to all main fields to stabilize iterative convergence without noticeably affecting accuracy.

Table 5.1: Numerical schemes and solver settings used in the simulations.

Parameter	OpenFOAM Entry		
Time integration	Euler		
Gradient scheme	Gauss linear		
	div(phi,alpha): Gauss interfaceCompression vanLeer 1		
Divergence schemes	div(phirb,alpha): Gauss interfaceCompression vanLeer 1		
Divergence schemes	<pre>div(rhoPhi,U), div(phi,U): Gauss vanLeer</pre>		
	<pre>div(phi,T), div(phi,k), div(phi,p): Gauss vanLeer</pre>		
Laplacian scheme	Gauss linear corrected		
Interpolation scheme	linear		
Surface-normal gradient	corrected		
PIMPLE algorithm	nOuterCorrectors = 1, nCorrectors = 3		
Pressure solver	PCG with DIC, tolerance 10^{-9}		
Velocity and turbulence	PBiCG + DILU, tolerance 10^{-8}		
Phase-fraction solver (α)	MULES with nAlphaSubCycles = 3, cAlpha = 0.75		
Energy solver	PBiCG + DILU, tolerance 10^{-8}		
Relaxation factors	0.8 for all main fields		

Therefore, an interface compression option is used together with van Leer convection for α as listed above. It sharpens the interface and improves the curvature and normal

estimates, helping to control smearing and spurious currents in the sealed geometry, which was mentioned by Okagaki et al. (195).

In simulations of PHPs, the initial distribution of the liquid phase inside a sealed capillary is unknown and can only be observed in transparent pipes, which are rarely done under cryogenic conditions. Moreover, even under gravity, liquid redistribution does not necessarily align with the gravitational vector (73; 196) due to capillarity and surface tension. To represent this uncertainty, a random initialization of the volume fraction is applied. Each computational cell is assigned $\alpha = 1$ or $\alpha = 0$ according to a probability consistent with the prescribed filling ratio. This nondeterministic start relaxes over roughly one second as surface tension reorganizes the phase field into vapor bubbles and liquid slugs. After this short capillary relaxation, long-time statistics are insensitive to the specific random seed provided the filling ratio is preserved. The early restructuring of the phase distribution is shown in Figure 5.4.

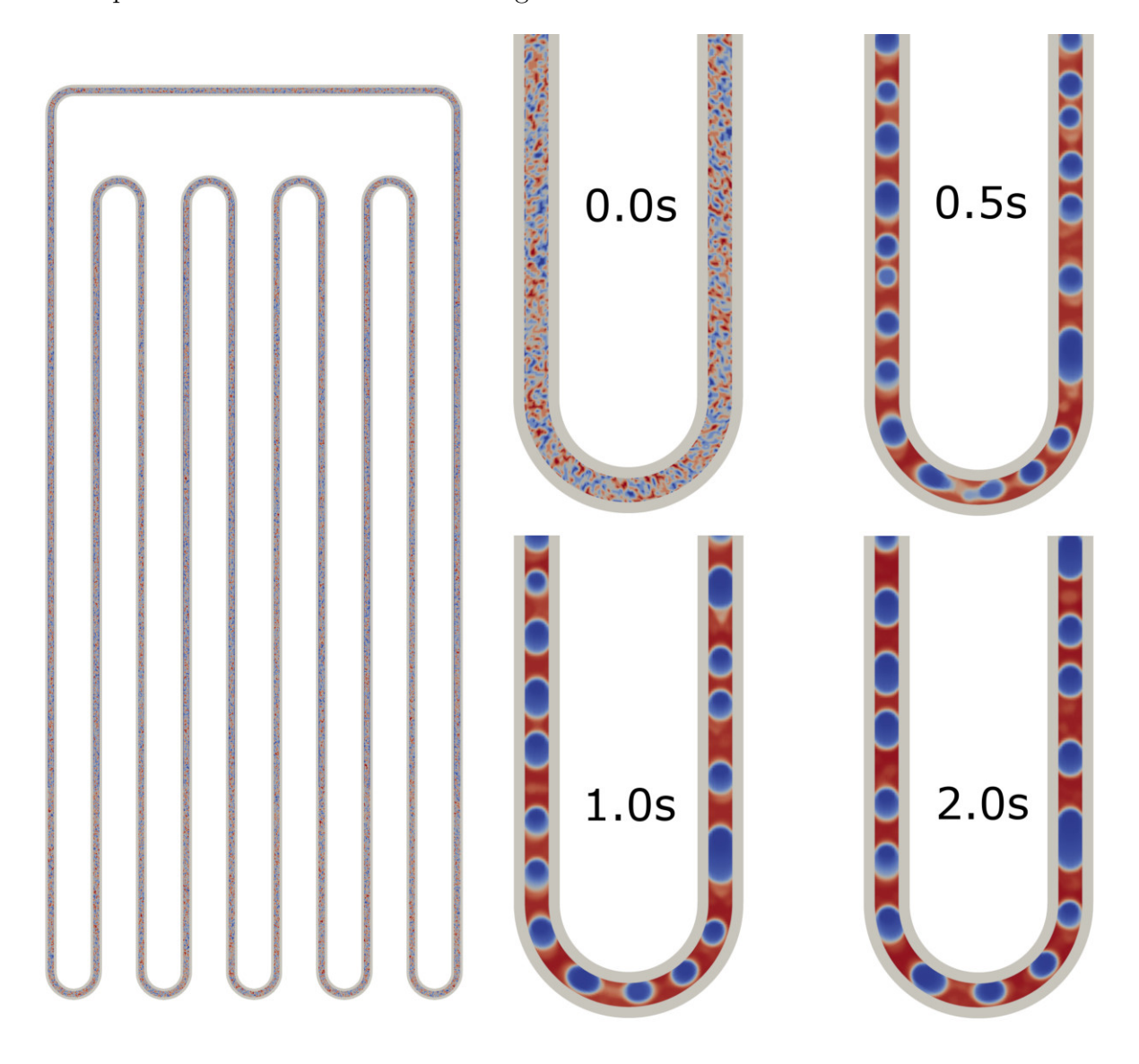


Figure 5.4: Early evolution of the phase field in the pulsating heat pipe after initialization.

Table 5.2 summarizes the boundary and initial conditions applied in the simulations for the three working fluids. The initial temperature was set equal to the condenser temperature of each fluid, while the initial pressure was fixed at 1000 mbar. All of the scalar are interpolated on walls with assigned boundary conditions using internalField. The quantities of turbulence were prescribed following the approach adopted in (143), with $k_{t=0}$ and $\epsilon_{t=0}$ assigned uniform internal fields. The condenser wall was maintained at a fixed value corresponding to the saturation temperature of the respective fluid at 1000 mbar and heat was supplied to the evaporator using the externalWallHeatFluxTemperature condition over the ranges indicated. Different filling ratios were considered depending on the fluid in order to examine the effect of filling ratio on PHPs behavior.

Table 5.2: Boundary conditions and properties for different working fluids

Working Fluid	ing Fluid Variable Boundary Condition		Value	Unit
	$T_{t=0}$	internalField	77.3	K
	$p_{t=0}$	internalField	1000	mbar
	$k_{t=0}$	internalField	0.05	m^2/s^2
	$\epsilon_{t=0}$	internalField	0.01185	$\mathrm{m}^2/\mathrm{s}^3$
Nitrogen	k	kqRWallFunction	internal Field	m^2/s^2
Mitrogen	ϵ	epsilonWallFunction	internal Field	$\mathrm{m}^2/\mathrm{s}^3$
	U	noSlip	0	m/s
	T_{cond}	fixedValue	77.3	K
	Power	external Wall Heat Flux Temperature	7.5 to 25	W
	Filling Ratio	alpha.liquid	30, 50, 70	%
	$T_{t=0}$	internalField	87.3	K
	$p_{t=0}$	internalField	1000	mbar
	$k_{t=0}$	internalField	0.05	$\mathrm{m}^2/\mathrm{s}^2$
	$\epsilon_{t=0}$	internalField	0.01185	$\mathrm{m}^2/\mathrm{s}^2$
Angon	k	kqRWallFunction	internal Field	$\mathrm{m}^2/\mathrm{s}^2$
Argon	ϵ	epsilonWallFunction	internal Field	$\mathrm{m}^2/\mathrm{s}^3$
	U	noSlip	0	m/s
	T_{cond}	fixedValue	87.3	K
	Power	external Wall Heat Flux Temperature	7.5 to 25	W
	Filling Ratio	alpha.liquid	50	%
	$T_{t=0}$	internalField	27.1	K
	$p_{t=0}$	internalField	1000	mbar
	$k_{t=0}$	internalField	0.05	$\mathrm{m}^2/\mathrm{s}^2$
	$\epsilon_{t=0}$	internalField	0.01185	$\mathrm{m}^2/\mathrm{s}^3$
Neon	k	kqRWallFunction	internal Field	$\mathrm{m}^2/\mathrm{s}^2$
reon	ϵ	${\it epsilonWallFunction}$	internal Field	$\mathrm{m}^2/\mathrm{s}^3$
	U	noSlip	0	m/s
	T_{cond}	fixedValue	27.1	K
	Power	external Wall Heat Flux Temperature	2 to 9	W
	Filling Ratio	alpha.liquid	50	%

5.3 Model Limitations

The model can quantify the overall thermal performance of PHPs, as already demonstrated for earlier versions of the solver (143; 197), yet several fundamental limitations remain. The first and most critical issue concerns the treatment of the mass. In most CFD formulations of phase change, strict mass conservation remains unresolved. In this work, the balance is maintained in part by linking density variations to compressibility instead of using polynomial fits, which alleviates long-term divergence but does not fully eliminate accumulated errors. Additional stabilization is introduced through two mechanisms. First, the Tanasawa (113) accommodation coefficient γ is modified. Ideally, this factor should remain close to unity, but on coarser meshes, it must be reduced to prevent local instabilities or energy spikes. Second, a proportional correction factor is applied to the phase-change source terms based on the ratio of the initial mass to the current system, m_0/m^{actual} . This term compensates for the cumulative imbalance over long simulations by scaling the evaporation and condensation rates. Both corrections improve numerical stability, but they shift the thermal balance toward latent heat transfer at the expense of sensible mechanisms. This challenge is less visible in configurations with natural outlets or conjugate domains, where mass imbalance can dissipate through boundary conditions, which explains why many studies report stable operation without explicit corrections (145; 198). However, in a sealed capillary, these mechanisms cannot operate, making strict conservation a persistent challenge. Small cumulative mass residuals perturb the density averaged in the domain and the void fraction field α , altering the compressibility. This can change the steady-state evaporator temperature and absolute pressure, change the start time, and move apparent thresholds for partial or global drying. Because the m_0/m^{actual} scale favors latent exchange, similar thermal resistances can arise from different α distributions and vapor generation, resistance trends are useful, while inferences from absolute mass partition or integrated vapor production should be treated as indicative.

The second limitation concerns mesh resolution. A detailed representation of the PHP dynamics would benefit from resolving microscale liquid films and maintaining wall units $y^+ \lesssim 1$. Such wall-normal refinement across multi-loop geometries is computationally impractical at present. Consequently, the grid prioritizes interface sharpness and numerical stability over fully resolved wall layers, consistent with previous multiloop studies that reported the same cost–accuracy trade-off (139; 133; 137). In the present work, each simulation consumed approximately one week on 20 cores of the Intel Xeon Platinum 8268 CPU of the BEM2 supercomputer in Wrocław. This constraint inevitably limited both the mesh density and the number of parametric cases, making the chosen grid a compromise between capturing bubble dynamics and suppressing numerical artifacts.

Limited wall resolution smooths curvature and underestimates capillary jumps, altering the shape and coalescence of the meniscus. The absence of subcell films underpredicts thin-film evaporation and overestimates near-wall sensible heat.

Another limitation concerns interfacial physics. The present model does not include the Marangoni thermocapillary stresses (166). Surface tension is modeled as a function of temperature, which does not fully represent Marangoni-driven stresses and wettability is introduced through a prescribed contact angle. For nitrogen, only approximate values are available (199), while for neon and argon, consistent data sets are lacking, in particular for the dynamic contact angle that numerical studies have linked to thermal resistance in PHPs (119). These uncertainties propagate to predictions of meniscus motion, bubble detachment and dewetting and thereby to film deposition and phase distribution. In the absence of dedicated cryogenic measurements for the present geometry, validation is therefore limited to global thermal metrics rather than local interfacial quantities.

A further limitation concerns the modeling of thin liquid films and film boiling, which has been recently addressed in interface—resolved studies (146). In PHPs, a significant part of heat transfer occurs through evaporation and condensation on films deposited by oscillating slugs. The present formulation does not resolve the microlayer near the contact line or includes a film thickness-based closure. Consequently, it cannot capture film-dominated regimes or the onset of film boiling. Recent analyses confirm that both film conduction and interfacial evaporation strongly influence the effective thermal resistance of PHPs (200; 201). Additional work on microlayer formation under nucleate boiling conditions (202) and direct numerical simulation of film boiling in cryogenic fluids (203) further emphasizes the importance of thin-film physics. Even parametric studies show that surface wettability modifies the flow pattern and global thermal performance (119) and reviews of current developments consistently identify film dynamics as a limiting factor for predictive models of oscillating heat pipes (204). Film-controlled heat transfer is underpredicted and the transition to film boiling cannot be captured. The minimum of thermal resistance at low loads may appear shallow, and the degradation of high loads may be delayed. The amplitudes of geyser-type pulses are not reliable. Quantities that depend on film thickness, such as depletion length or critical heat flux, are outside the fidelity of the model.

5.4 Numerical Results

The numerical simulations presented in this chapter are characterized by an extended computational time horizon not previously reported in CFD studies of pulsating heat

pipes. Yang et al. (139) investigated cryogenic PHPs with a similar five—loop geometry, but their simulations were restricted to about 50 s. Mucci et al. (133) performed ambient temperature simulations of multiloop PHPs, also limited to around 90 s. In contrast, the present work extends the simulated duration to 350 s, which makes it possible to capture sustained oscillatory regimes and to analyze both the initial formation of plugs and slugs, as well as their long—term evolution. The results are organized into three parts: contour plots of representative fields that are used to illustrate the spatial dynamics, averaged quantities that are presented together with their concordance with experimental data and the flow structure dynamics to understand more deeply the heat transfer mechanism in PHPs.

5.4.1 Contour Plots of Representative Fields

The following contour plots illustrate the instantaneous distributions of phase fraction, pressure and temperature, which together highlight the physical mechanisms governing plug-slug motion inside the PHP. Figure 5.5 shows three frames of the liquid volume fraction α_l for nitrogen in a 1.3 mm pipe at 50% filling and a heat load of 15 W, taken at t = 195 s, 200 s and 205 s. The distribution consists of alternating liquid plugs and vapor slugs, with loop-to-loop variations in length and spacing. This variability reflects the convective transport term $\nabla \cdot (\phi \alpha_l)$ in Eq. (2.36), which advects the phase fraction along the path. Near U-bends, the local increase in the interface curvature κ increases the Laplace pressure jump $\Delta p = \sigma \kappa$ and redistributes momentum between adjacent segments, which favors plug break-up or coalescence and modifies the thickness of the deposited film. These effects are consistent with classical results from capillary tubes linking interfacial curvature to pressure drop and film deposition around moving bubbles (205). Phase-change sources $\dot{v}_{\rm evap}$ and $\dot{v}_{\rm cond}$ (Eq. (2.35)) further redistribute the vapor content in the heated and cooled sections. A complementary 1D meniscusbased analysis by Nikolayev (179) shows that the coupling between capillary pressure and thermal forcing can destabilize the interface and sustain oscillations in a capillary, offering a physical analogue for perturbations induced near bends in pulsating heat pipes. Taken together, pressure and temperature fields show that advection, capillarity, and interphase mass transfer act jointly to produce the observed spatio-temporal pattern of the α_l .

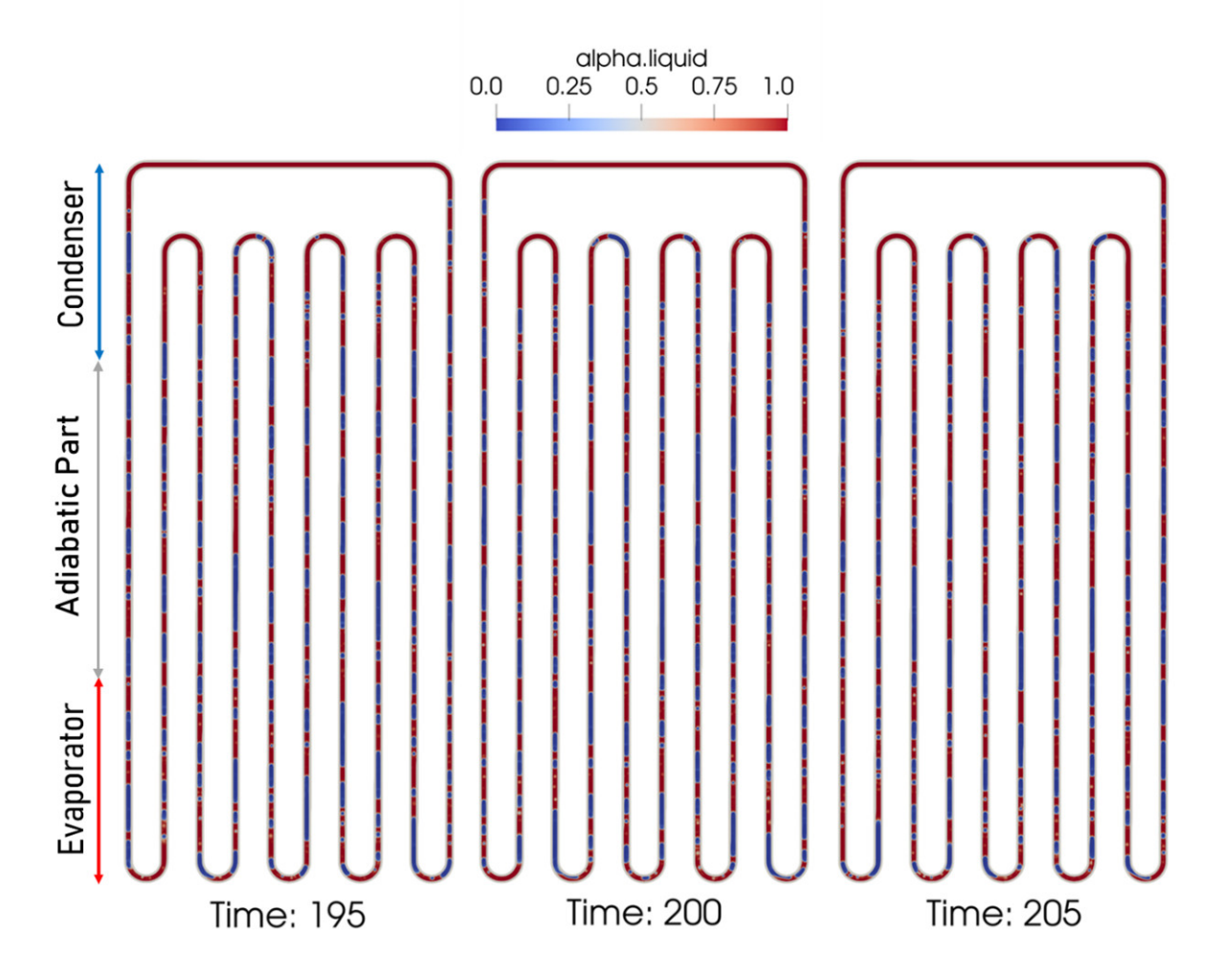


Figure 5.5: Liquid volume fraction α_l at three frames for nitrogen, D=1.3 mm, fill ratio 50% and Q=15 W. Snapshots at t=195 s, 200 s and 205 s.

The absolute pressure field (Fig. 5.6) mainly reflects the hydrostatic and compressibility components of the flow. Each frame uses its own color scale, which highlights local gradients, but should not be compared in absolute terms. The most pronounced differences occur at the U bends, where curvature enhances the capillary contribution \mathbf{F}_{σ} in momentum balance (Eq. (2.40)). In addition, the hydrostatic contribution ρgh together with the compressibility term ($\psi \partial p/\partial t$ in Eq. (2.67)) produces a systematic offset: pressures remain elevated in the lower part of the device and reduced near the top. as expected These mechanisms dominate the global structure of p and are consistent with the displacement of the plugs shown in Fig. 5.5.

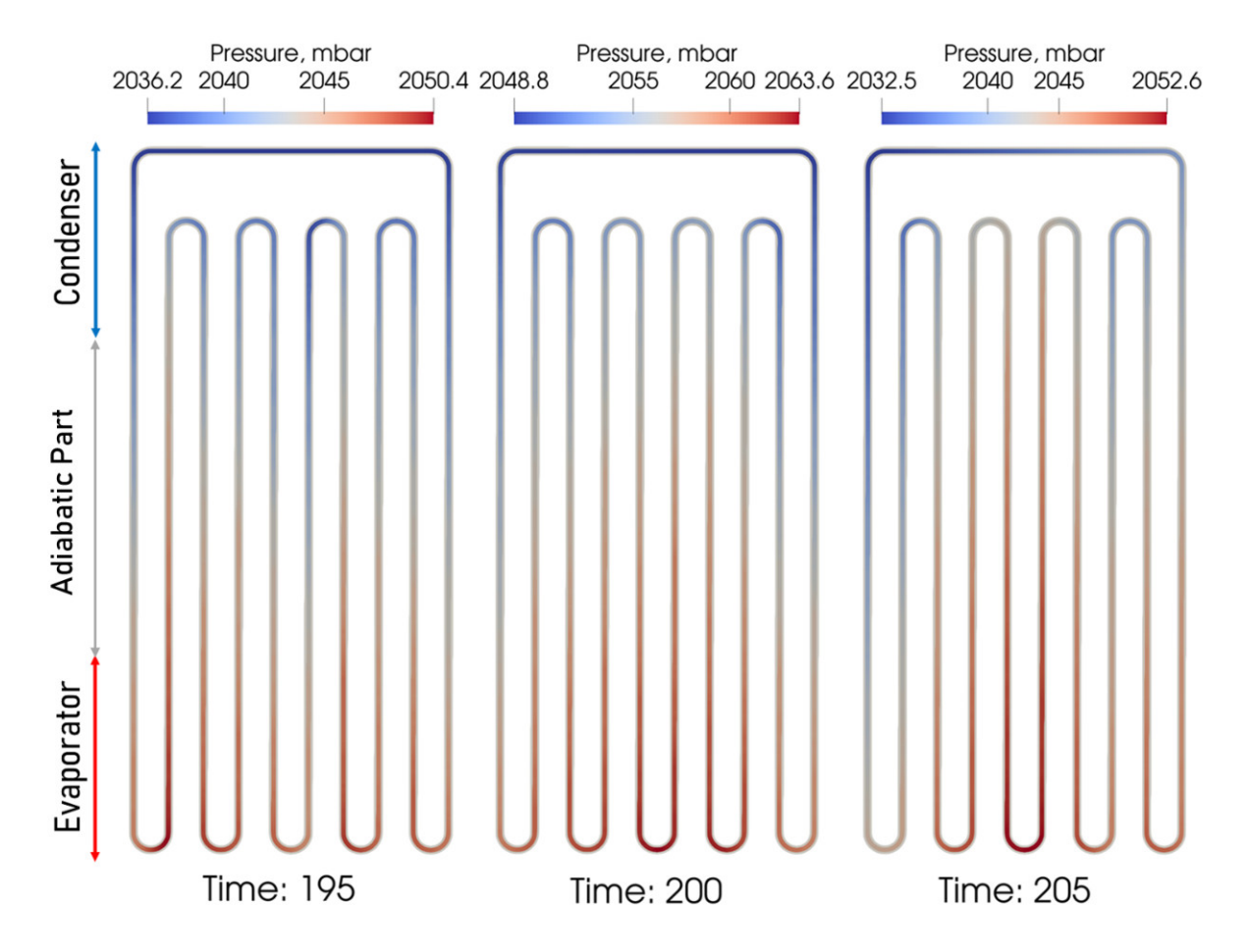


Figure 5.6: Absolute pressure distribution for nitrogen, D=1.3 mm, fill ratio 50% and Q=15 W at t=195 s, 200 s and 205 s. The legend is rescaled independently for each frame to highlight local variations.

A clearer picture of the dynamic behavior is obtained from the relative pressure field $p_{rgh} = p - \rho gh$ (Fig. 5.7), plotted using a common scale. Subtracting the hydrostatic component isolates the unstable part of the response governed by compressibility, inertia, and viscous diffusion. Viscous stresses smooth the pressure gradients within the liquid slugs, while inertial and unstable terms $\psi \partial p_{rgh}/\partial t$ and $\partial(\rho \mathbf{U})/\partial t + \nabla \cdot (\rho \mathbf{U} \otimes \mathbf{U})$ produce local pressure variations correlated with the motion of the vapor plugs. At t = 200 s, the region of high p_{rgh} extends over the evaporator section, coincident with significant displacement of slugs. At t = 195 s and 205 s, alternating pressure bands appear after coalescence events, showing the oscillatory nature of the flow.

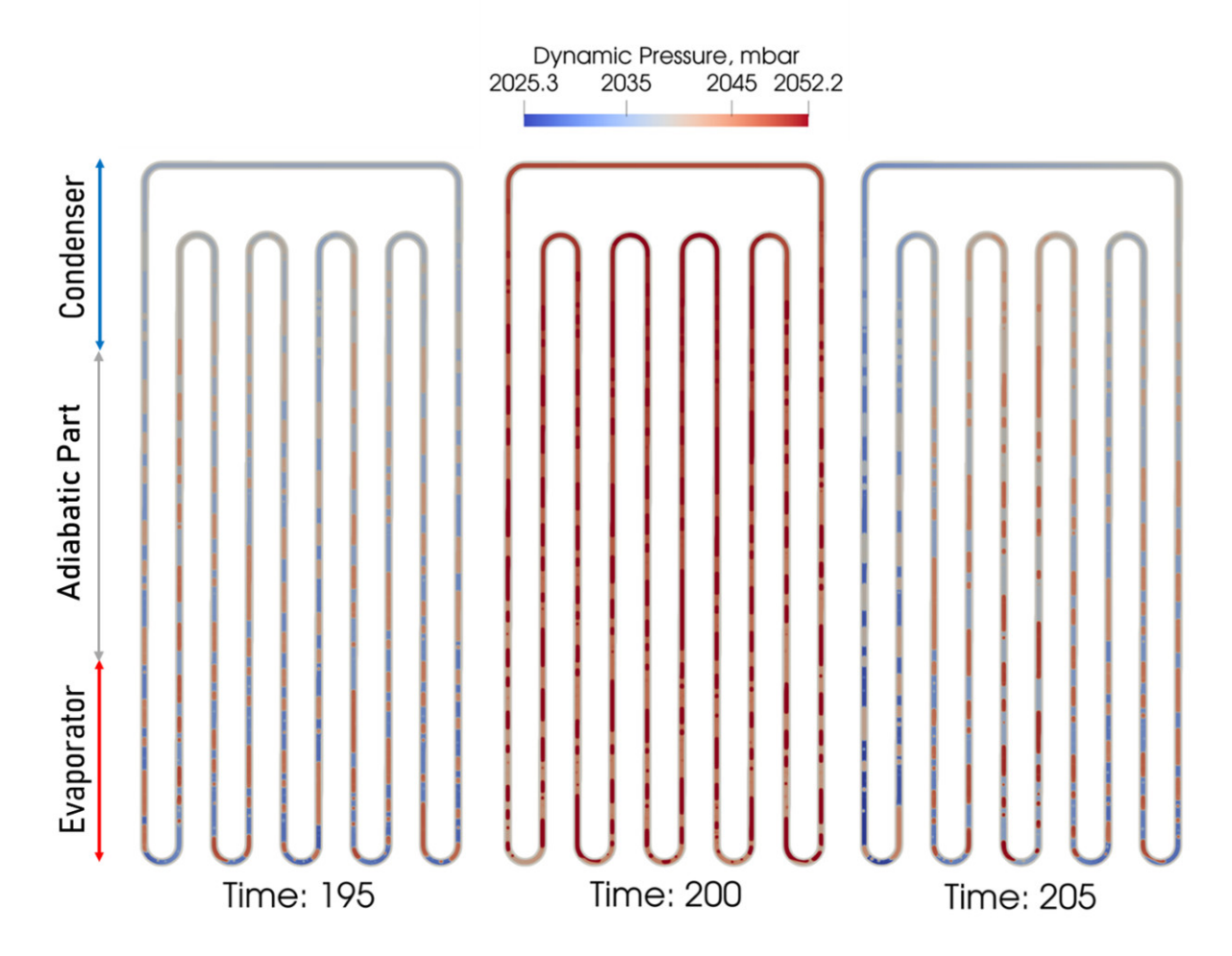


Figure 5.7: Relative pressure distribution $p_{rgh} = p - \rho gh$ for nitrogen, D = 1.3 mm, fill ratio 50% and Q = 15 W at t = 195 s, 200 s and 205 s. A single legend is used for all frames.

A direct correspondence emerges when the three fields are examined together. The liquid-vapor distribution (Fig. 5.5) is governed by the structure of the static and dynamic pressure fields (Figs. 5.65.7), which in turn shape the temperature distribution (Fig. 5.8). In the evaporator section, periodic vapor generation leads to locally increased wall temperatures as a result of reduced liquid contact and intermittent phase-change activity. In particular, the yellow fragments in the evaporator (seen in Fig. 5.8), which are distinct from the hottest zones, indicate strong local evaporation or a directional flow of liquid draining from the condenser. These zones coincide with the presence of vapor plugs in Fig. 5.5 and pressure gradients in Fig. 5.7, confirming the coupling between latent heat exchange and dynamic pressure response. Closer to the condenser, the flow becomes dominated by liquids, pressure gradients weaken, and the temperature field is nearly uniform as a result of the fixed boundary temperature. Although the interface positions of the fraction fluctuate over time, the overall pattern temperature remains periodic, indicating a quasi-steady oscillatory regime.

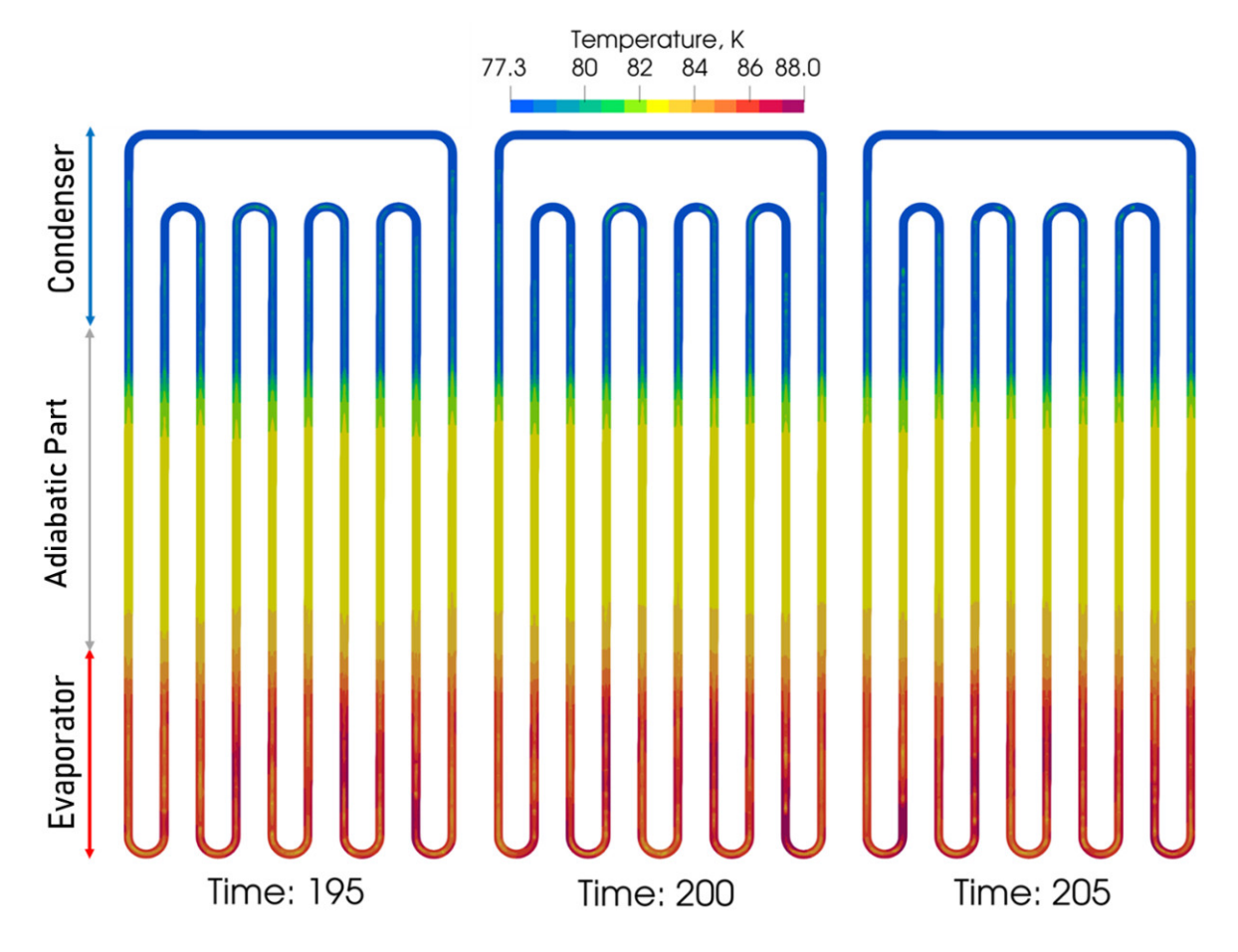


Figure 5.8: Temperature distribution for nitrogen, D=1.3 mm, fill ratio 50% and Q=15 W at t=195 s, 200 s and 205 s.

5.4.2 Quantitative Validation of the Numerical Model

In this subsection, a comparison between the experimental and numerical results is presented. The analysis includes the average evaporator temperature and the absolute pressure as a function of time. In the experiment, the average evaporator temperature was evaluated during the last 15 minutes of the heating process starting from the initial condition, while in the simulations the time window 250–350 s was considered. The computational campaign investigated the influence of the filling ratio as well as the tube diameter (1.3 and 1.7 mm). The comparison of temperatures and pressures enables the evaluation of the model accuracy in predicting thermo-hydraulic behavior. Figure 5.9 shows the temporal evolution of the average evaporator temperature for a 1.3 mm nitrogen PHP at a filling ratio of 50%. Most cases converge towards stationary values, with the exception of the lowest and the highest heat loads, where stabilization is slower and incomplete. The most pronounced temperature increase occurs at the beginning of the heating process, which results from the absence of established circulation in the domain

and the progressive development of internal flow until the mass and energy fluxes are balanced. In contrast to the experiment, the numerical model does not exhibit a distinct start-up phenomenon but rather a continuous growth of the global momentum of the liquid and vapor phases. A gradual accumulation of oscillations rather than a distinct start-up event is typical for interface-resolved CFD of multi-loop PHPs (133; 139).

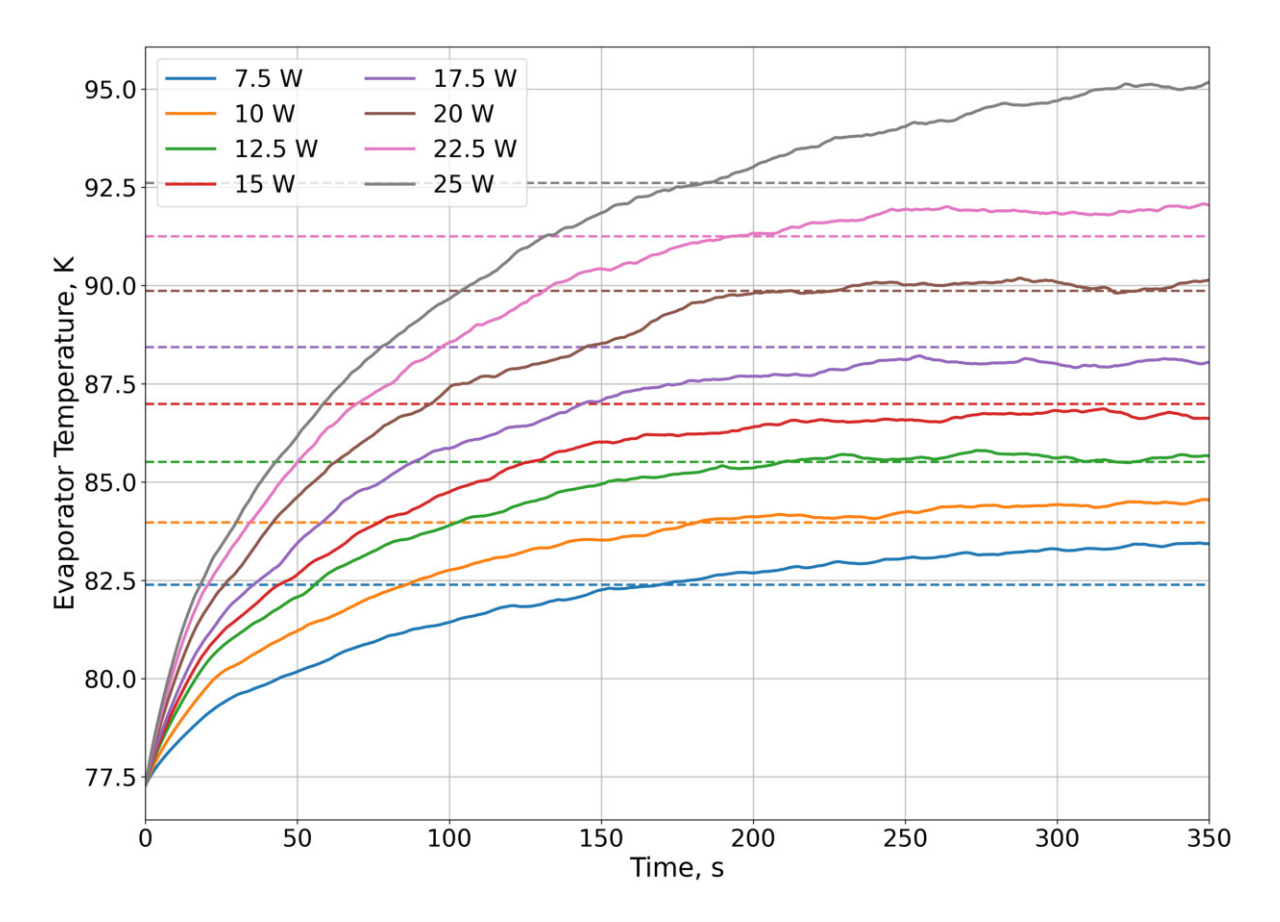


Figure 5.9: Simulated average evaporator temperature evolution in a 1.3 mm nitrogen PHP with a filling ratio of 50% under heat loads ranging from 7.5 to 25 W.

Figure 5.10 presents the evolution of the absolute pressure. In contrast to temperature, the pressure signal exhibits more pronounced oscillations throughout the simulation time. This behavior originates from the higher sensitivity of the hydrodynamics to perturbations and from the role of the thermal capacity of the fluid, which tends to smooth out temperature variations. In the experiment, the pressure fluctuations are expected to be smaller because the measurement is performed outside the cryostat in the external loop, which introduces damping. However, in the numerical results, a clear increase in the oscillation amplitude with the applied heat load can be observed. Differences in pressure amplitude are expected because measurement through an external line attenuates high-frequency components, as noted in experimental reviews (206).

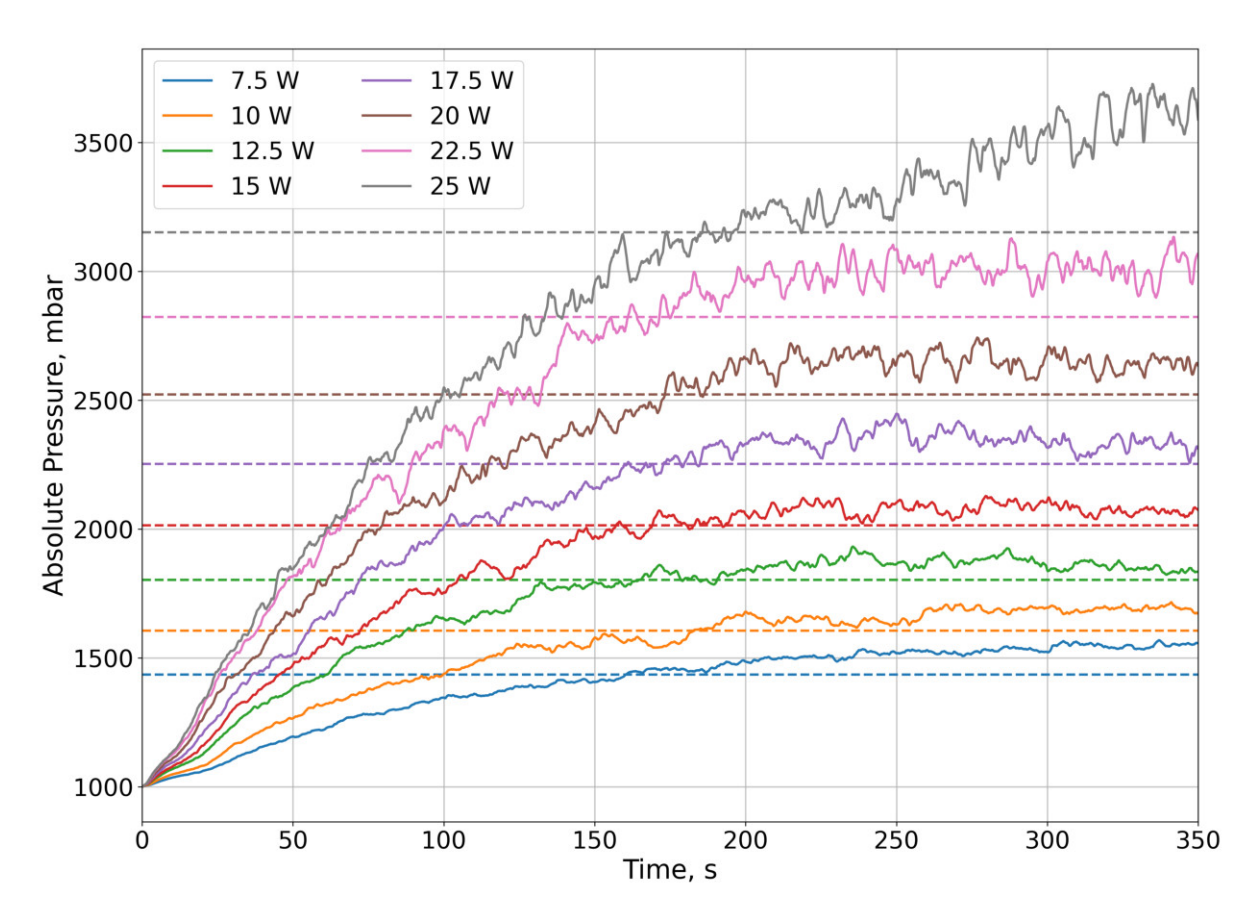


Figure 5.10: Simulated absolute pressure evolution in a 1.3 mm nitrogen PHP with a filling ratio of 50% under heat loads ranging from 7.5 to 25 W.

Figure 5.11 presents a direct comparison between the experimental and numerical results. A noticeable discrepancy can be observed in the growth trends of temperature and pressure. In the experiment, the temperature of the evaporator exhibits an almost linear increase with heat load, whereas in the simulations, the growth follows a more exponential trend, which is strongly correlated with the evolution of the pressure. Although the dynamic shape of the simulated pressure rise corresponds well to the experimental behavior, the magnitude of the deviation is more pronounced at higher heat loads. Quantitative analysis shows that the deviation in the evaporator temperature remains below 5% for the entire investigated range. For absolute pressure, the relative error does not exceed 8%, except for the highest heat load, where a larger overprediction is observed. This indicates that the numerical model captures the general thermohydraulic behavior of the system with a reasonable accuracy, while the main limitation arises from the nonlinear amplification of pressure at higher heat inputs.

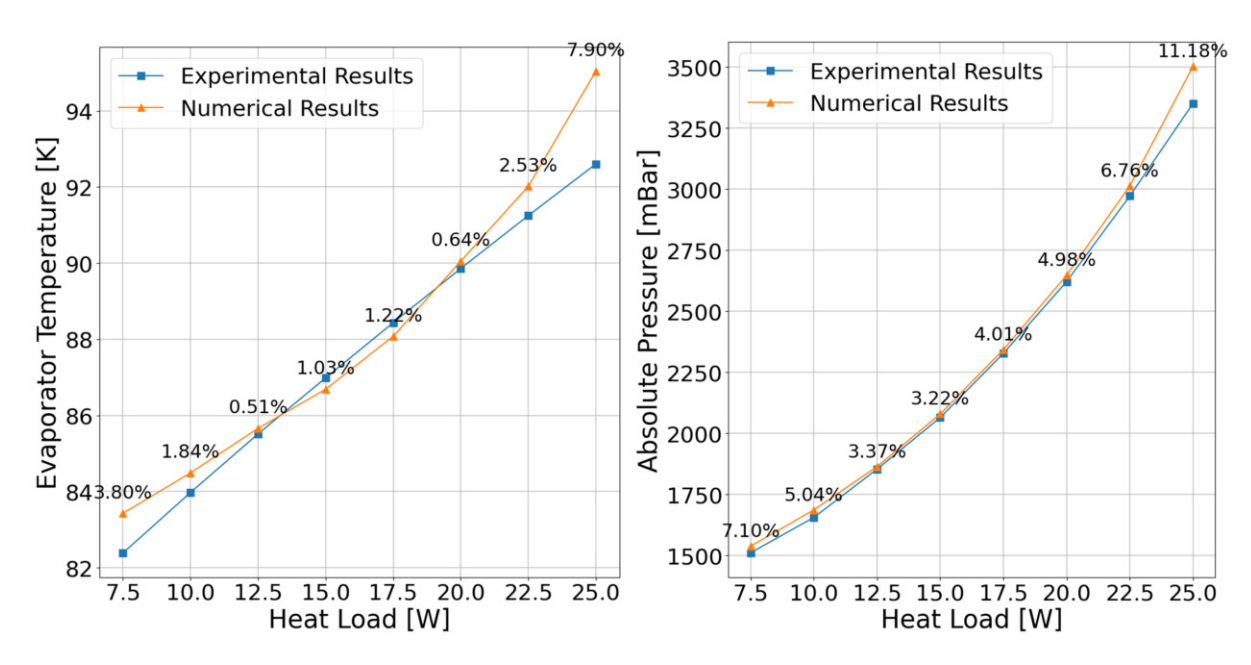


Figure 5.11: Comparison between experimental and simulated results for a 1.3 mm nitrogen PHP with 50% filling ratio under heat loads ranging from 7.5 to 25 W: (left) averaged evaporator temperature, (right) averaged absolute pressure. Percentage values indicate the relative deviation between simulations and experiments.

Figure 5.12 shows the temporal evolution of the averaged evaporator temperature for a 1.3 mm nitrogen PHP with a filling ratio of 30%. A faster attainment of the steady plateau can be observed compared to the case with 50% filling. This behavior results from the reduced liquid inventory, which decreases the damping of momentum transfer as a result of viscosity and thus accelerates the temperature rise. In this case, all temperature curves reached a stationary state, indicating that the system remains stable throughout the entire range of applied heat loads.

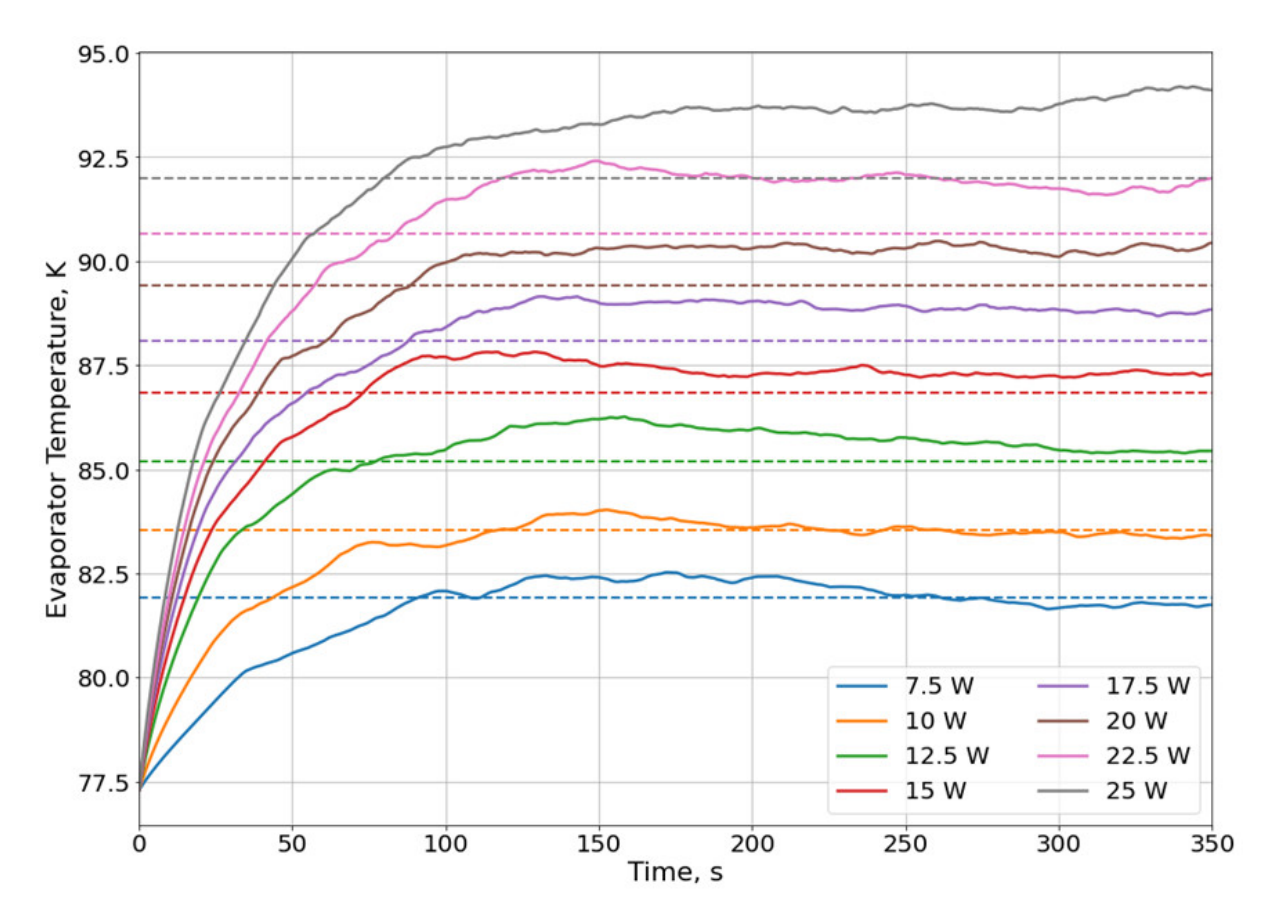


Figure 5.12: Simulated averaged evaporator temperature evolution in a 1.3 mm diameter PHP under heat loads ranging from 7.5 to 25 W with a filling ratio of 30%.

The corresponding absolute pressure evolution is presented in Figure 5.13. The results indicate a general overprediction of pressure compared to the experiment. The pressure curves follow the same trend as the temperature evolution and reach lower values than in the 50% filling case, which is consistent with the reduced liquid fraction in the system.

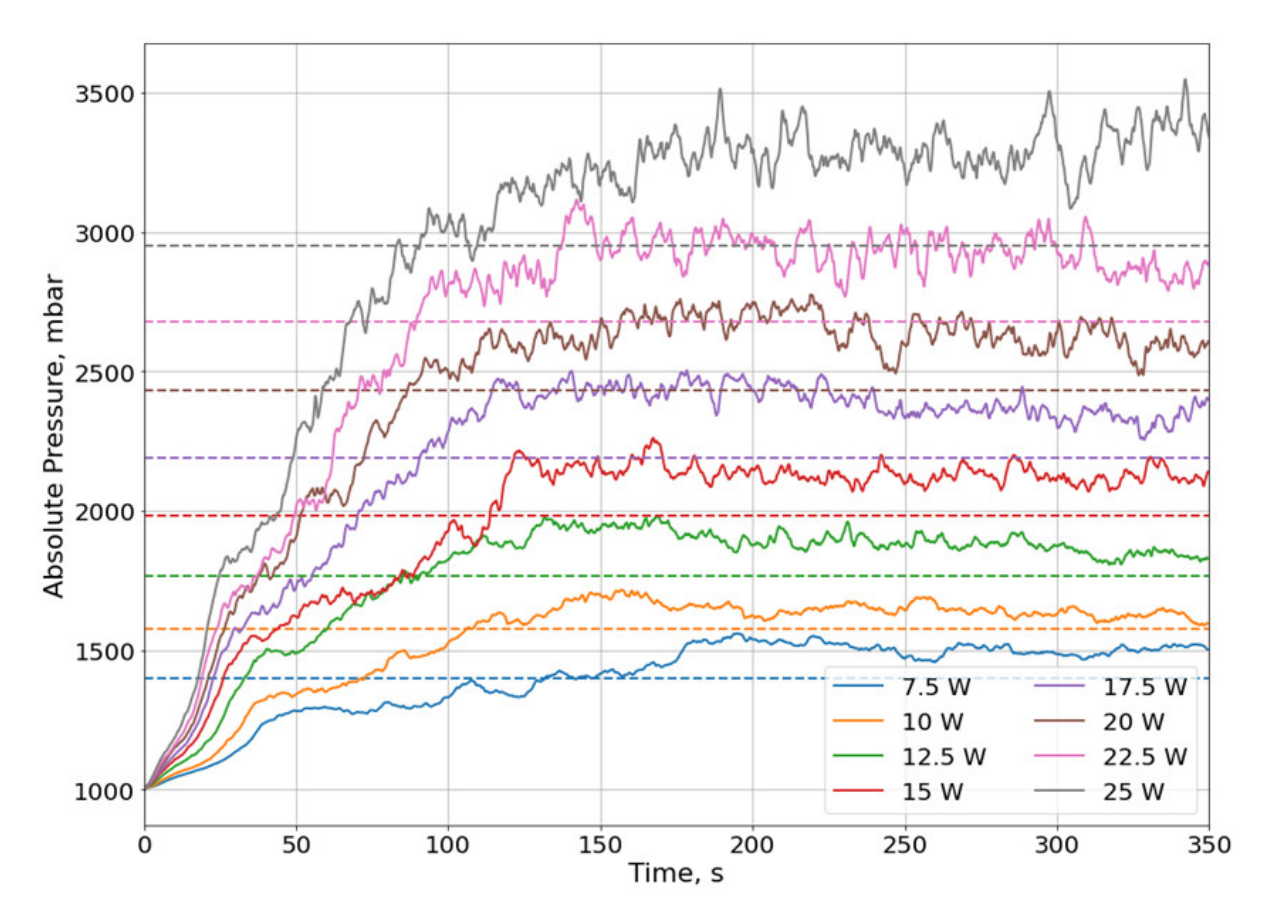


Figure 5.13: Simulated averaged pressure evolution in a 1.3 mm diameter PHP under heat loads ranging from 7.5 to 25 W with a filling ratio of 30%.

Figure 5.14 compares the experimental and numerical results. The evaporator temperature shows very good agreement with the measurements in all heat loads, while the pressure is consistently overestimated by the model. The largest discrepancy is observed at 25 W, similarly to the case with 50% FR, highlighting a reduced predictive precision of the model at the highest thermal loads. However, due to the full convergence of the temperature curves to steady state, the PHP remains in stable operation for the entire range of heat loads, in contrast to the 50% FR where stationary behavior was not achieved.

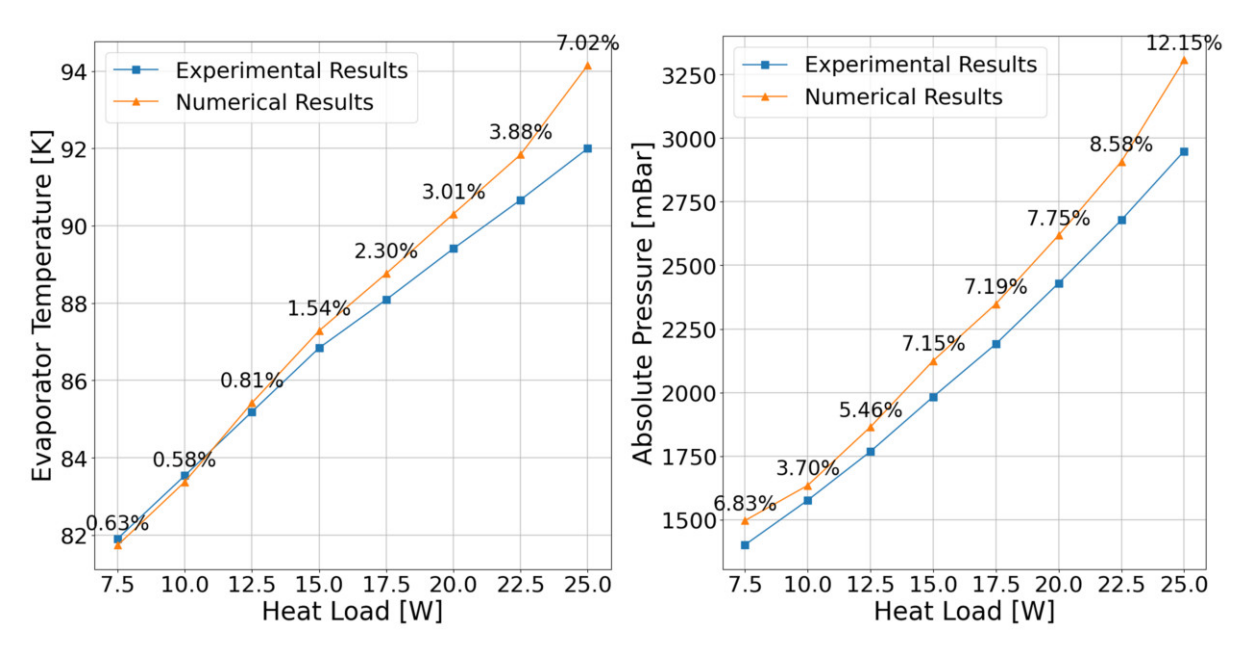


Figure 5.14: Comparison between experimental and simulated results for a 1.3 mm nitrogen PHP with 30% filling ratio under heat loads ranging from 7.5 to 25 W: (left) averaged evaporator temperature, (right) averaged absolute pressure. Percentage values indicate the relative deviation between simulations and experiments.

Figure 5.15 presents the evolution of the average temperature of the evaporator for a filling ratio of 70%. It can be observed that, with increasing heat load, the numerical results tend to diverge more strongly from the experimental data. The lack of convergence becomes evident already at 22.5 W, whereas for the 50% case this discrepancy appeared only at 25 W. Furthermore, at 25 W a dryout occurs, leading to overheating of the tube. During this process, the vapor fraction increases significantly and in the simulations the evaporator temperature rises to very high values until numerical instabilities appear due to interpolation errors, ultimately resulting in floating point exceptions.

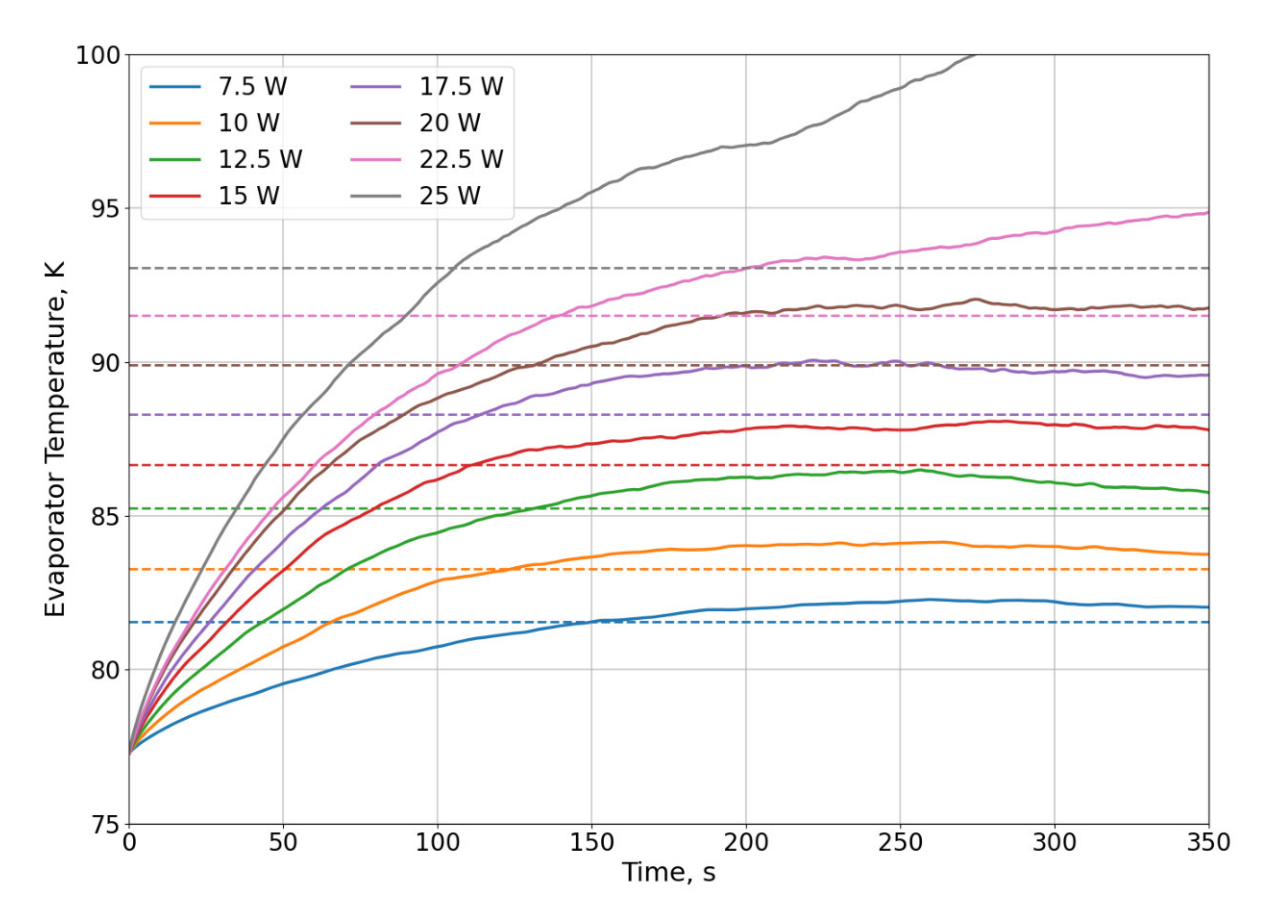


Figure 5.15: Simulated averaged evaporator temperature evolution in a 1.3 mm nitrogen PHP under heat loads ranging from 7.5 to 25 W with a filling ratio of 70%.

Figure 5.16 shows the corresponding pressure evolution for a 70% filling ratio. Pressure oscillations are significantly less pronounced compared to lower filling ratios, which is consistent with experimental observations 4.4. In addition to this, the pressure levels generally agree with the experimental results. However, the increasing deviation at higher heat loads indicates a limitation of the model in predicting performance under strongly vapor dominated conditions, where convective heat transfer governed by strong temperature gradients is dominant.

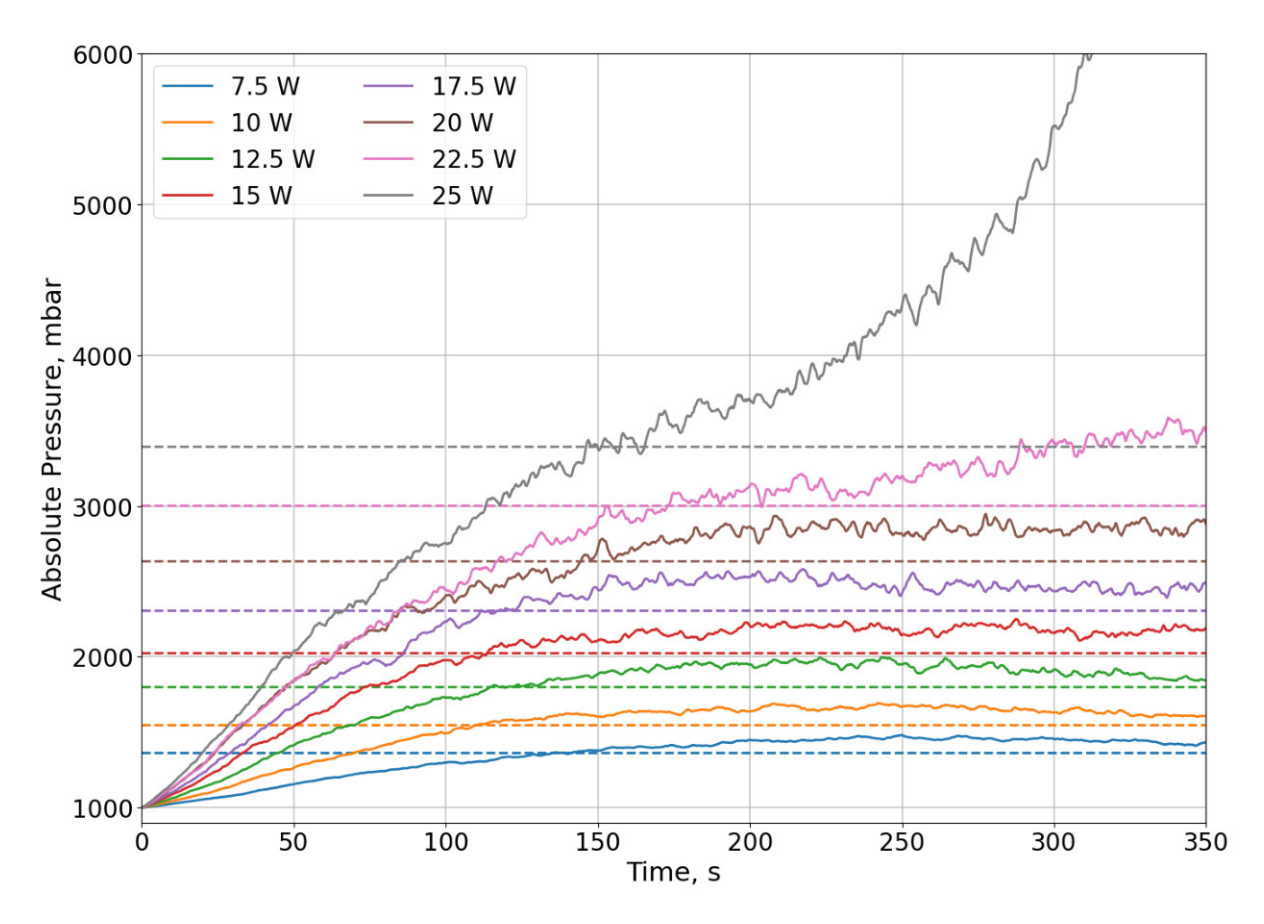


Figure 5.16: Simulated averaged pressure evolution in a 1.3 mm nitrogen PHP under heat loads ranging from 7.5 to 25 W with a filling ratio of 70%.

The comparison between the experimental and numerical results is given in Figure 5.17. Although the error remains acceptable in the range 7.5–20 W, the predictive capability of the model deteriorates significantly above this limit, particularly at 25 W, where the simulation fails to reproduce the correct thermo-hydraulic behavior.

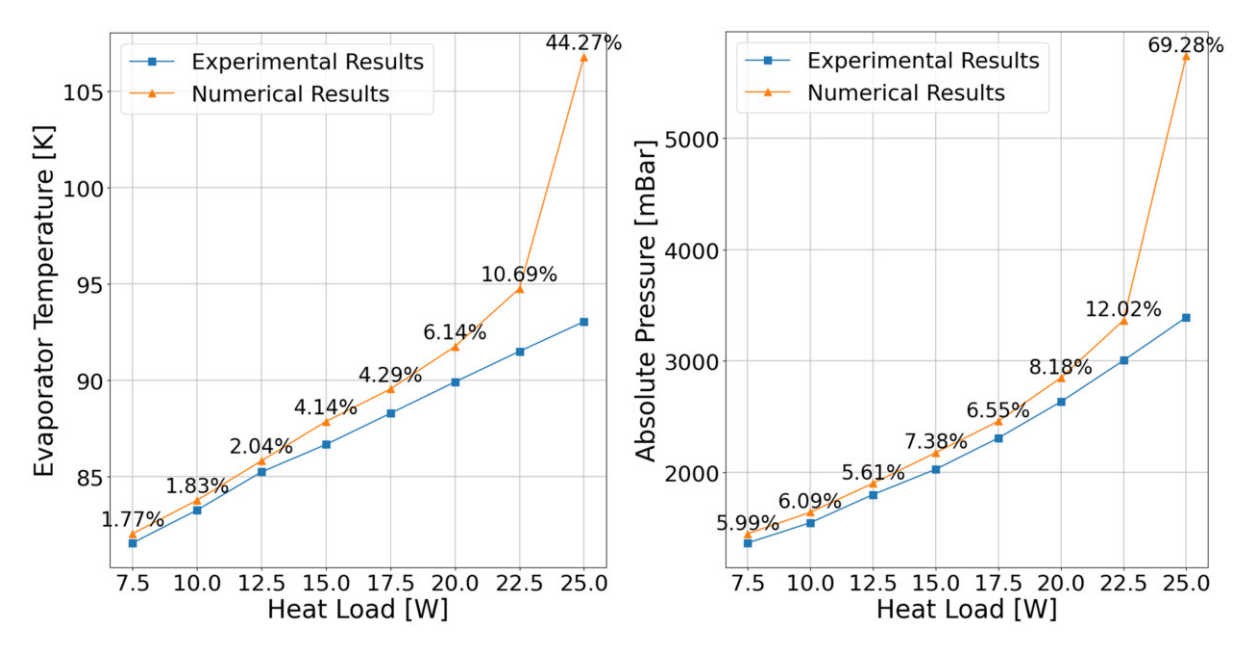


Figure 5.17: Comparison between experimental and simulated results for a 1.3 mm nitrogen PHP with 70% filling ratio under heat loads ranging from 7.5 to 25 W: (left) averaged evaporator temperature, (right) averaged absolute pressure. Percentage values indicate the relative deviation between simulations and experiments.

A cross-comparison of the three filling ratios (30%, 50% and 70%) reveals clear trends. For 30%, PHP reached steady operation throughout the heat load range, with rapid temperature stabilization but a systematic overprediction of pressure. At 50%, good agreement was obtained with moderate heat loads, although agreement was lost at 25 W, showing the onset of model limitations near drying. Finally, in the 70% filling ratio, the divergence between simulations and experiments appeared earlier, already at 22.5 W and full dryout was predicted at 25 W. In general, the best consistency between the experimental and numerical data was obtained in the 30–50% range, whereas high filling ratios led to a reduction in the accuracy and stability of the model under elevated heat loads.

For the 1.7 mm diameter case the transient behavior is noticeably more dynamic compared to the 1.3 mm PHP. The stronger variability at 1.7 mm coincides with a larger Bond number, consistent with diameter controlled regime changes and stability limits described in (207). Figure 5.18 shows that the temperature evolution exhibits pronounced peaks and irregular variations. This pronounced thermal response is attributed to the simplification of the 2D model, which inherently neglects the significant thermal inertia and 3D heat conduction of the physical thermal plate. In the experimental setup, these factors would effectively dampen such local temperature peaks, leading to a more stable behavior.

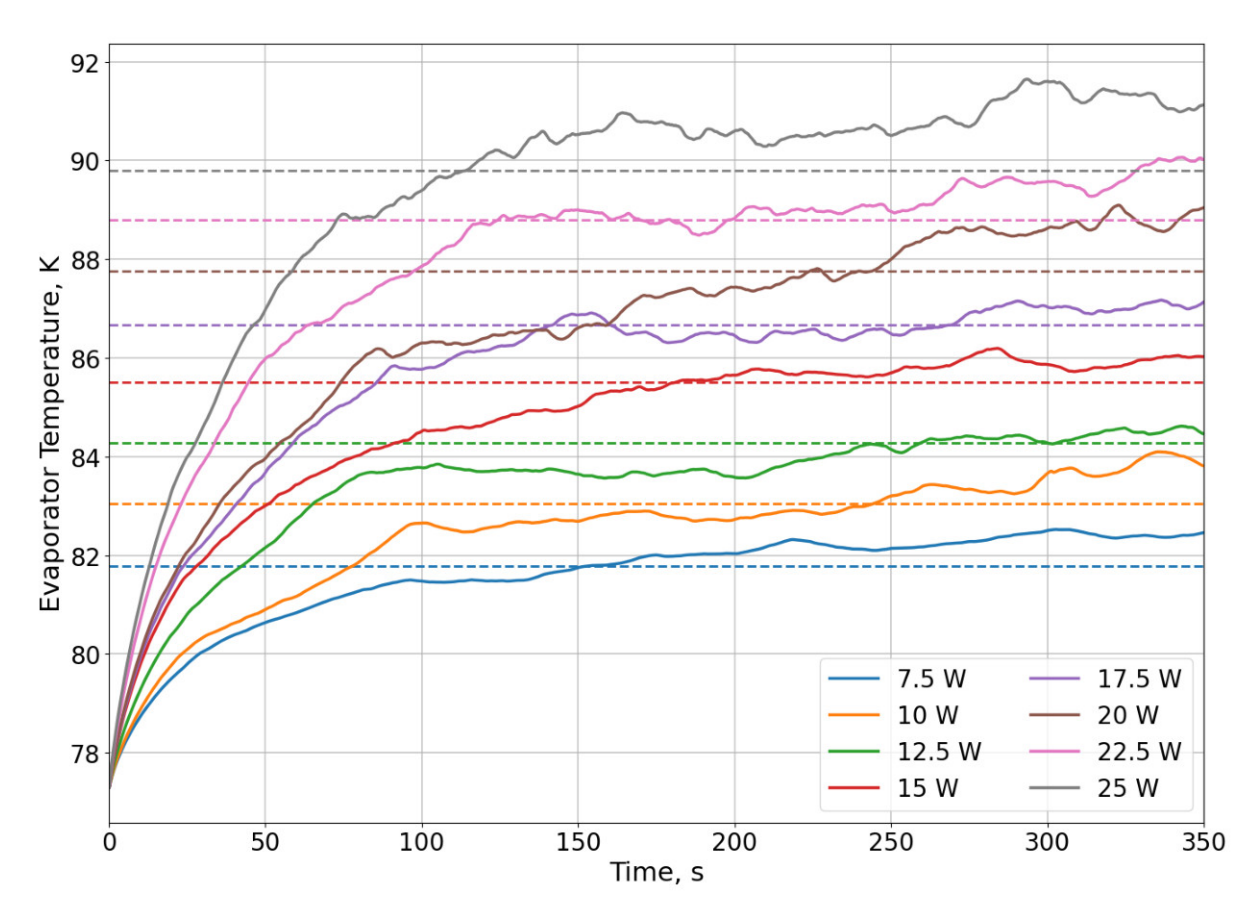


Figure 5.18: Simulated averaged evaporator temperature evolution in a 1.7 mm nitrogen PHP under heat loads ranging from 7.5 to 25 W with filling ratio of 50%.

The corresponding absolute pressure evolution is presented in Figure 5.19. Variations are significantly more dynamic than in the 1.3 mm case and stability decreases with increasing heat load. As in previous cases, the global numerical model overpredicts the absolute pressure compared to the experiment. Here, the explanation is related to the reduced amount of solid material in the 1.7 mm tube. This explanation shifts from the model artifact discussed previously to a physical difference between the tubes. The 1.3 mm tube has a significantly higher solid-to-fluid volume ratio. This greater relative wall mass provides a substantial inherent damping effect, much as the thermal plate was meant to. It effectively smooths out local thermal pulses from phase change, resulting in a more uniform response. The 1.7 mm tube lacks this significant internal thermal buffering. Its walls react much more sharply to local evaporation or condensation, amplifying the thermal-hydraulic feedback loop. This inherent physical instability, particularly visible at 17.5 and 20 W, suggests the system is sensitive not only to physical overheating but also to numerical issues, such as mesh insufficiency leading to the appearance of numerical dry spots.

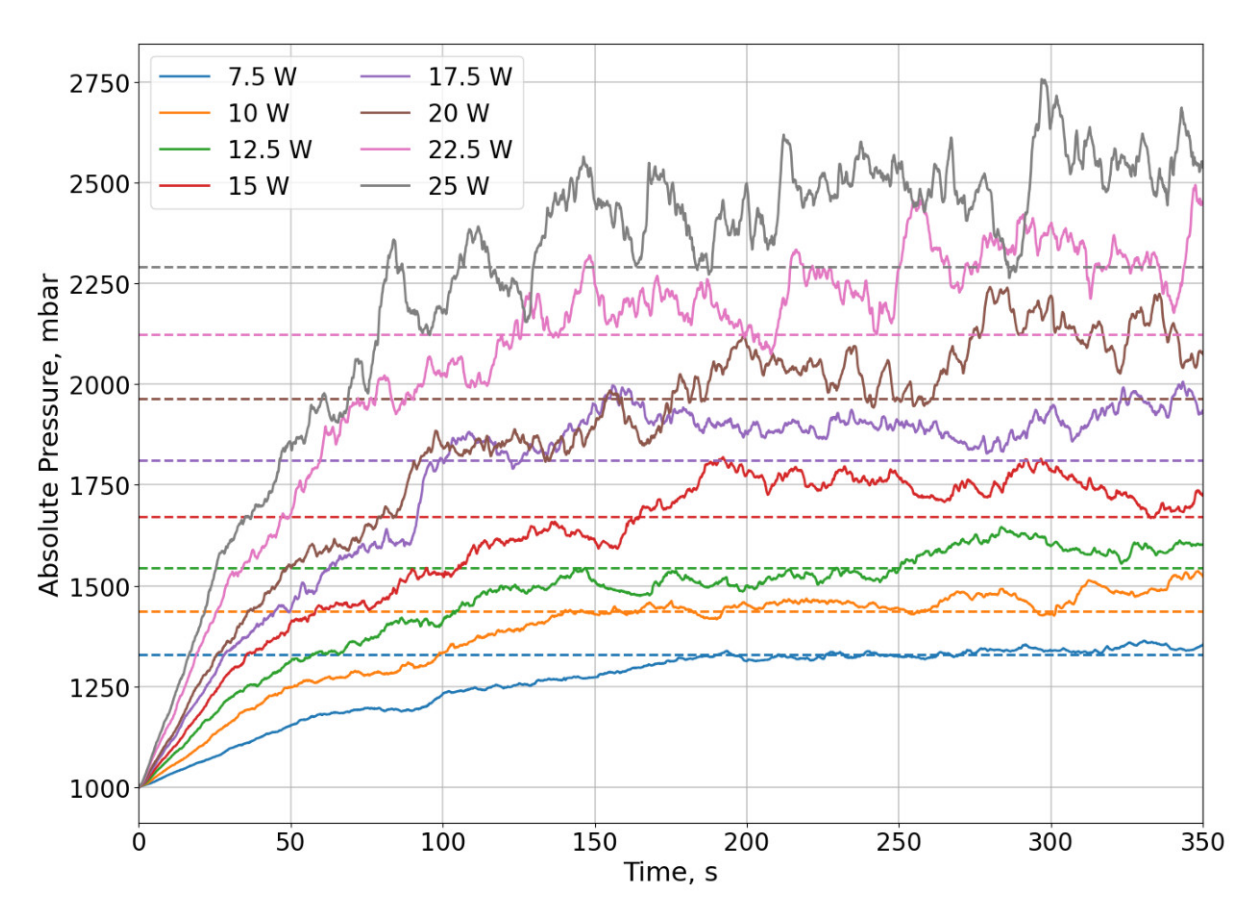


Figure 5.19: Simulated averaged pressure evolution in a 1.7 mm nitrogen PHP under heat loads ranging from 7.5 to 25 W with filling ratio of 50%.

The direct comparison with the experimental results is shown in Figure 5.20. Although the overall shape of the pressure curves remains consistent with the measurements, the temperature predictions are more irregular due to the limitations of the 2D representation. Overall, the results indicate that the accuracy of the model decreases with increasing tube diameter, particularly because of the combined effects of reduced wall damping and numerical sensitivity to local instabilities.

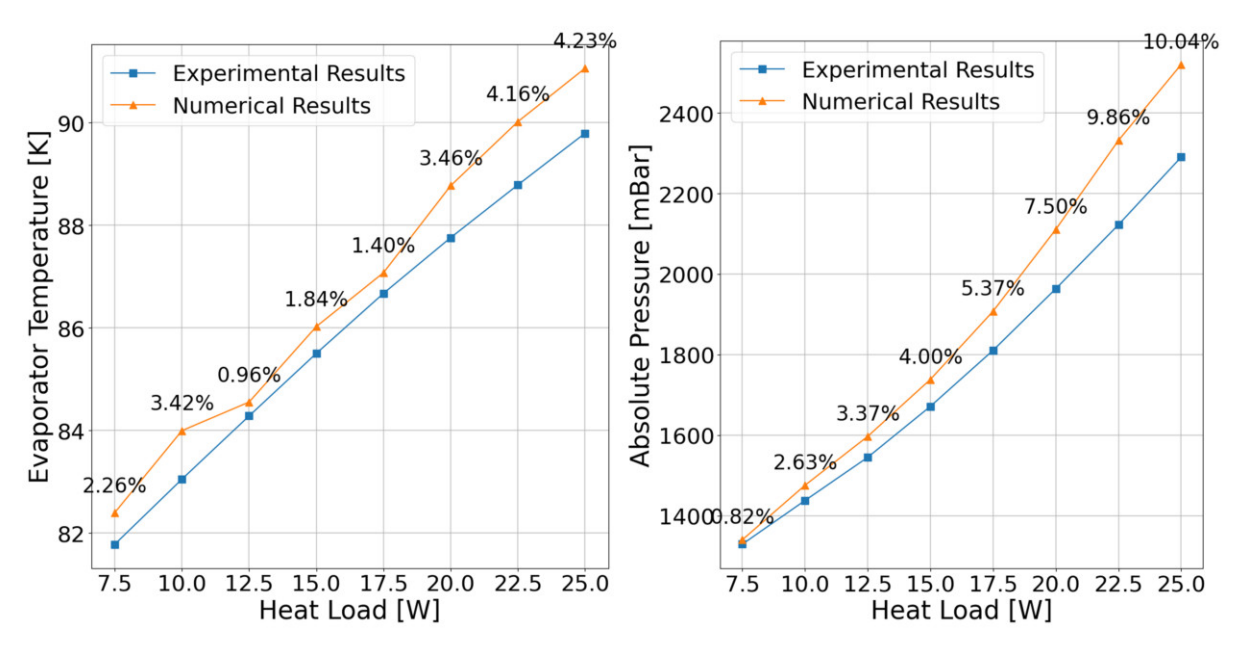


Figure 5.20: Comparison between experimental and simulated results for a 1.7 mm nitrogen PHP with 50% filling ratio under heat loads ranging from 7.5 to 25 W: (left) averaged evaporator temperature, (right) averaged absolute pressure. Percentage values indicate the relative deviation between simulations and experiments.

For argon, the effect of tube diameter (1.3 and 1.7 mm) on thermal performance was investigated. The results for the 1.3 mm case are shown in Figures 5.21–5.23. The transient behavior exhibits a lower dynamics compared to the 1.7 mm nitrogen case (Figure 5.18) and is more consistent with the observations obtained for the 1.3 mm nitrogen PHP (Figure 5.9). Once steady state is reached, a slight decrease in evaporator temperature is visible for some cases. This trend is consistent with the experimental data, where the maximum temperature occurs immediately after a heat load step, followed by a slow reduction to a stable value. For this reason, the last 15 minutes of the experimental runs are used for comparison with the numerical results.

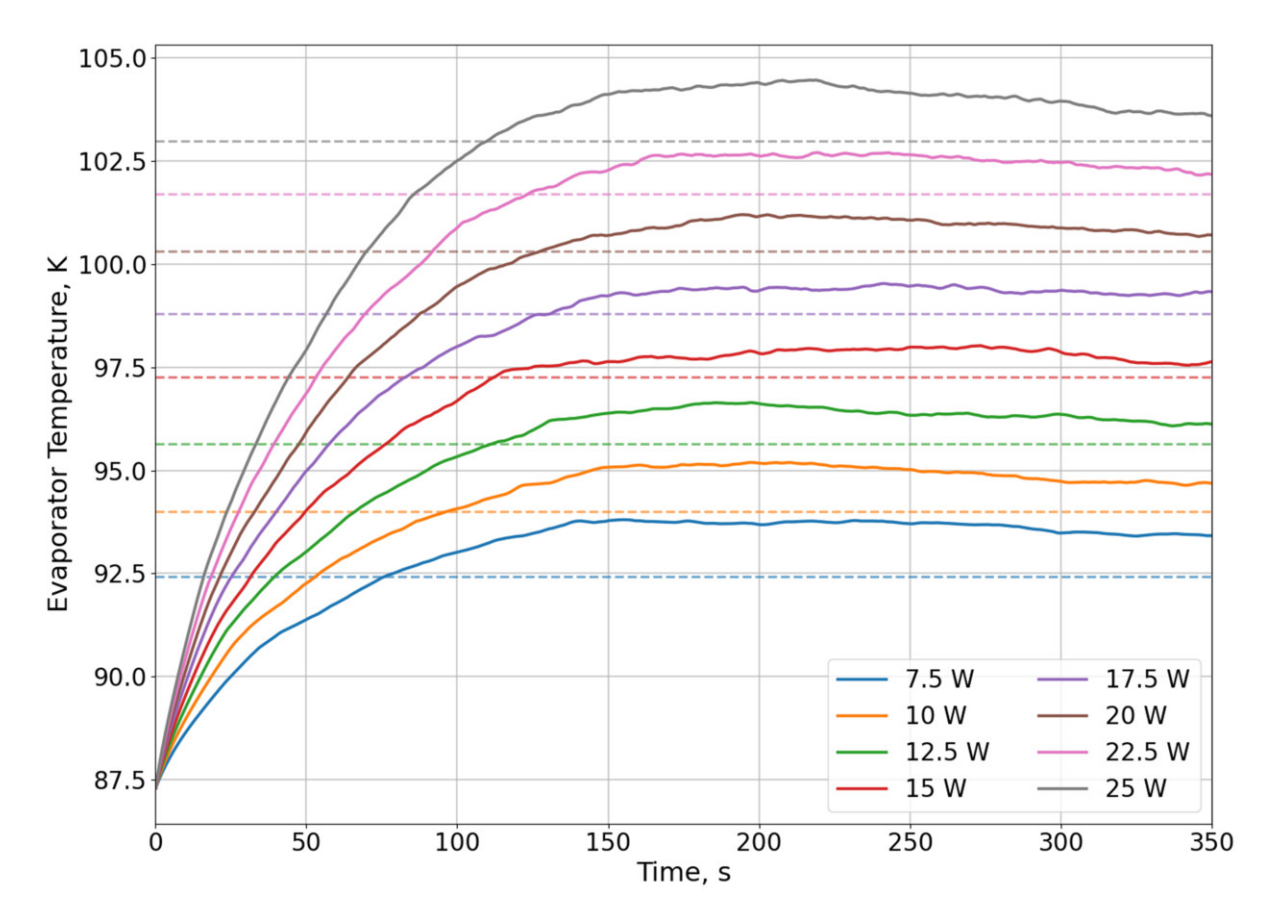


Figure 5.21: Simulated averaged evaporator temperature evolution in a 1.3 mm argon PHP under heat loads ranging from 7.5 to 25 W with filling ratio of 50%.

The corresponding pressure evolution is shown in Figure 5.22. Oscillations increase with the applied heat load, whereas the global trend follows the development of temperature. In all cases, the predicted absolute pressure is higher than in the experiments, which may be related either to the modeling approach or to systematic effects introduced by external pressure measurements outside the cryostat.

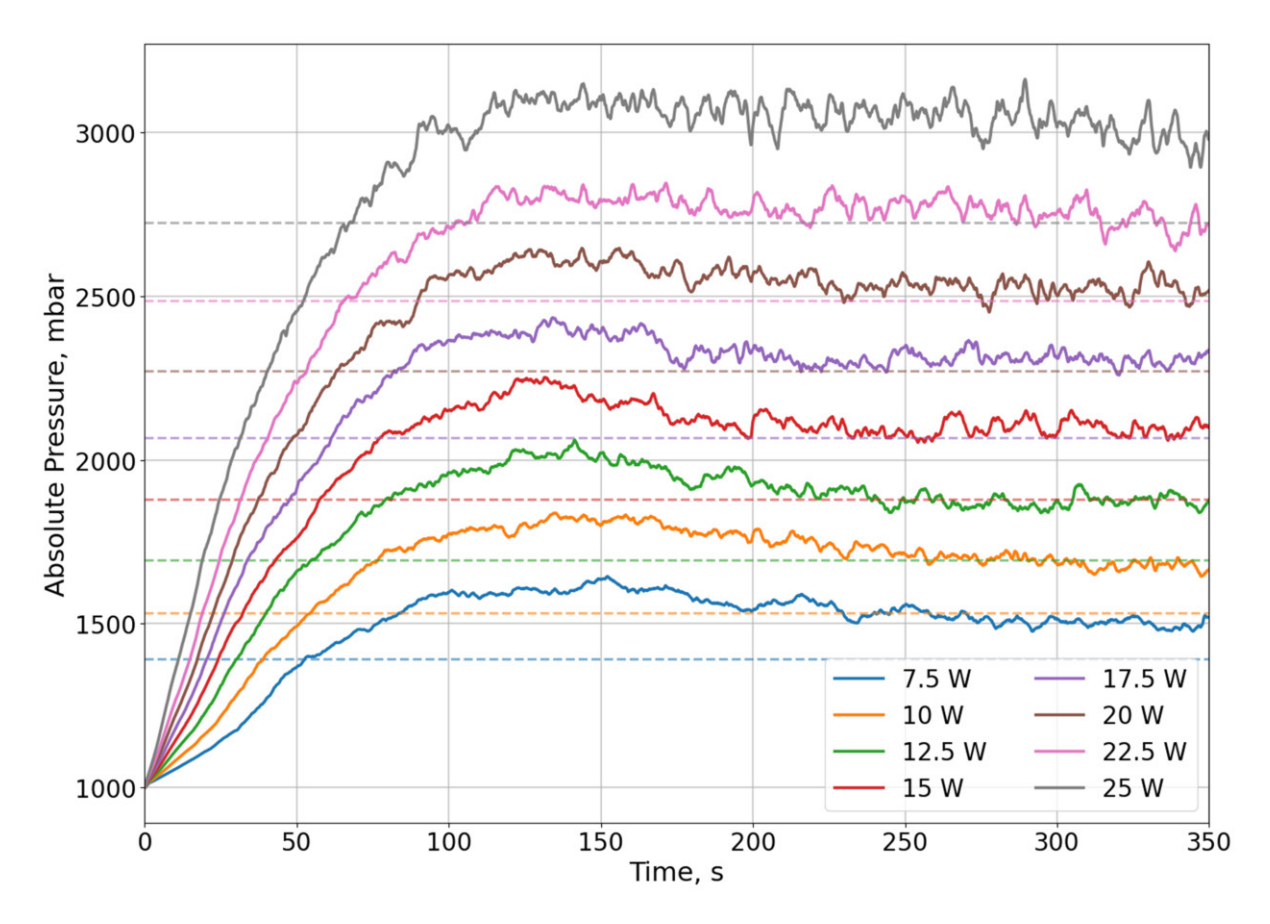


Figure 5.22: Simulated averaged pressure evolution in a 1.3 mm argon PHP under heat loads ranging from 7.5 to 25 W with filling ratio of 50%.

The global comparison with the experimental data is shown in Figure 5.23. The model slightly overpredicts the temperature of the evaporator wall, particularly at the lowest heat load, while the pressure is consistently higher in all cases. However, the relative deviations remain below 10%, which is acceptable from the perspective of evaluating the thermal performance of the PHP.

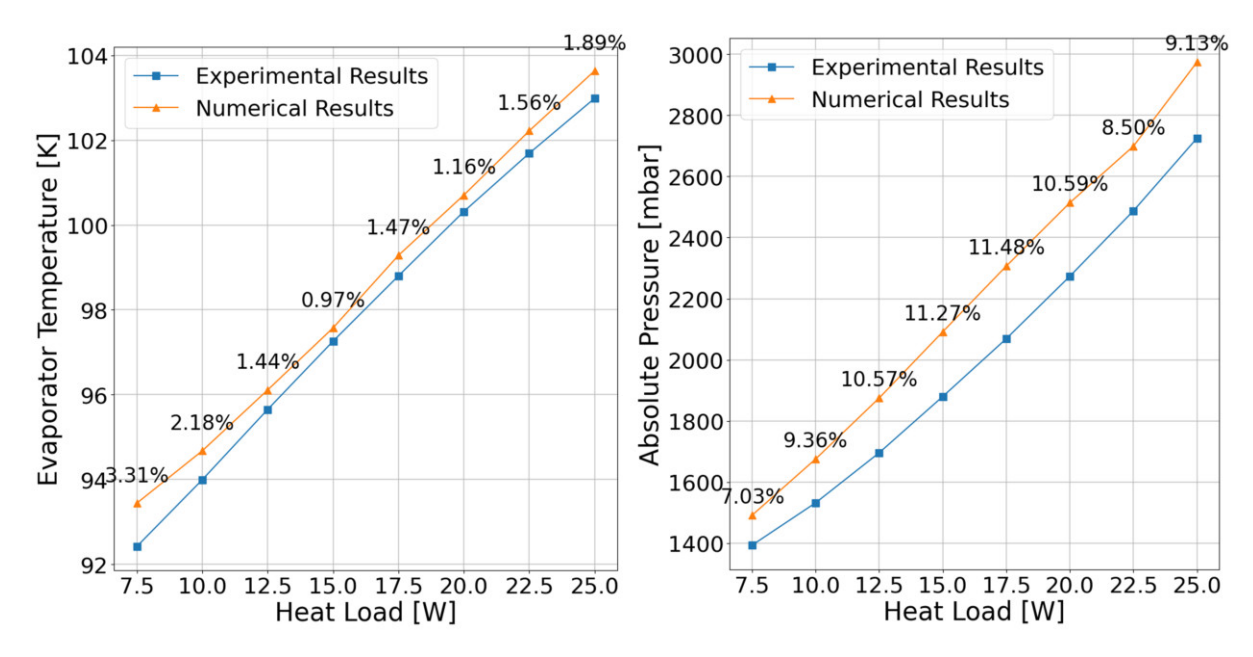


Figure 5.23: Comparison between experimental and simulated results for a 1.3 mm argon PHP with 50% filling ratio under heat loads ranging from 7.5 to 25 W: (left) averaged evaporator temperature, (right) averaged absolute pressure. Percentage values indicate the relative deviation between simulations and experiments.

Figure 5.24 shows the evolution of the evaporator temperature for argon in a 1.7 mm PHP with a filling ratio of 50%. Similarly to nitrogen at the same diameter (Figure 5.18), the temperature variations are more pronounced than in the 1.3 mm cases. The model systematically overpredicts the wall temperature compared to experiments, but the overall correlation with pressure evolution is maintained, particularly at higher heat loads such as 25 W.

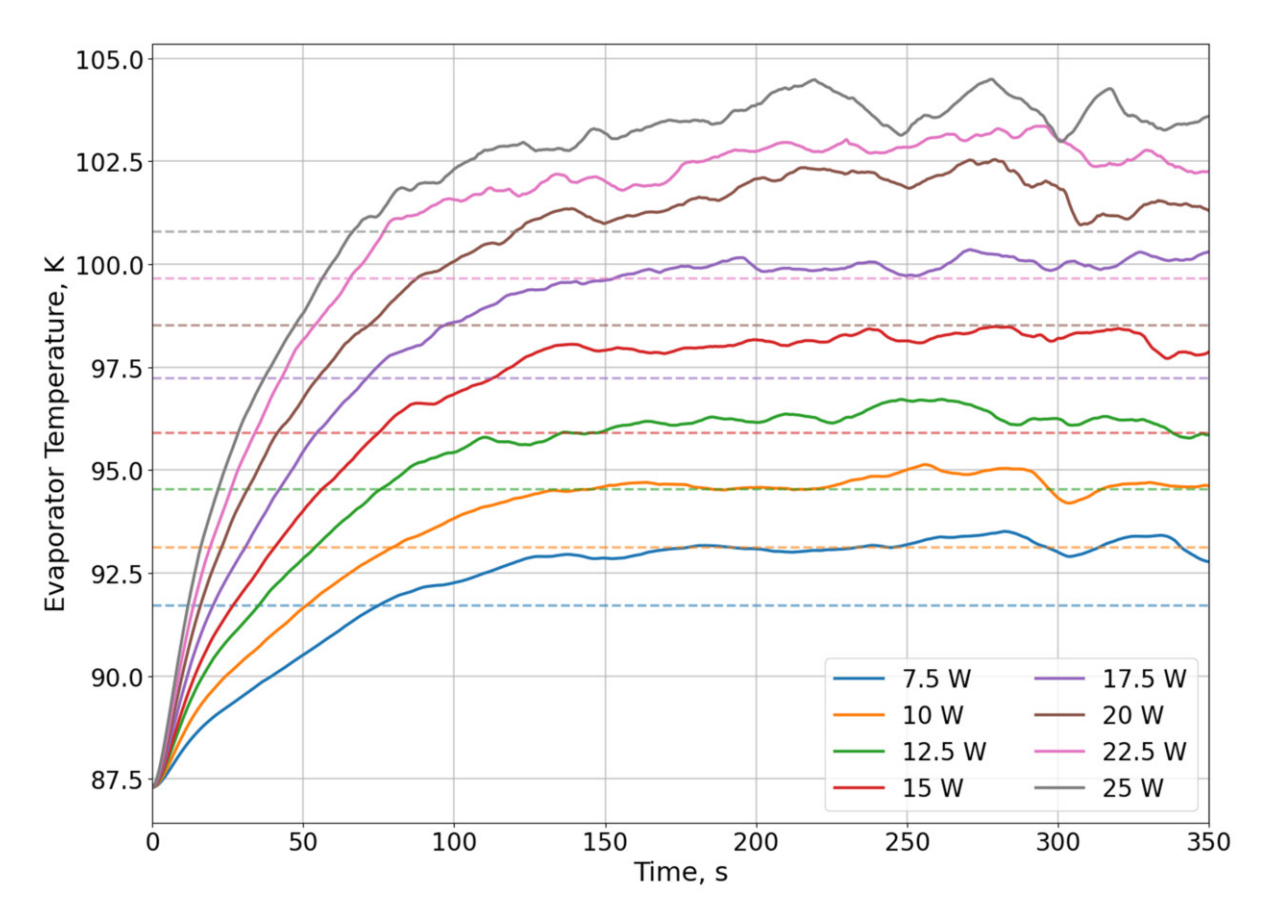


Figure 5.24: Simulated averaged evaporator temperature evolution in a 1.7 mm argon PHP under heat loads ranging from 7.5 to 25 W with a filling ratio of 50%.

The pressure development for argon is presented in Figure 5.25. Compared to nitrogen, the evolution is more dynamic and also exhibits a more ordered structure. This behavior is linked to the weaker influence of the Bond number increase, meaning that mass forces have a reduced impact relative to capillary effects under strong temperature gradients imposed by the condenser. As in nitrogen, enlarging the diameter leads to greater pressure variations, although the absolute pressure levels remain lower. This confirms that the stronger the capillary-driven circulation relative to inertia, the smaller the observed pressure differences.

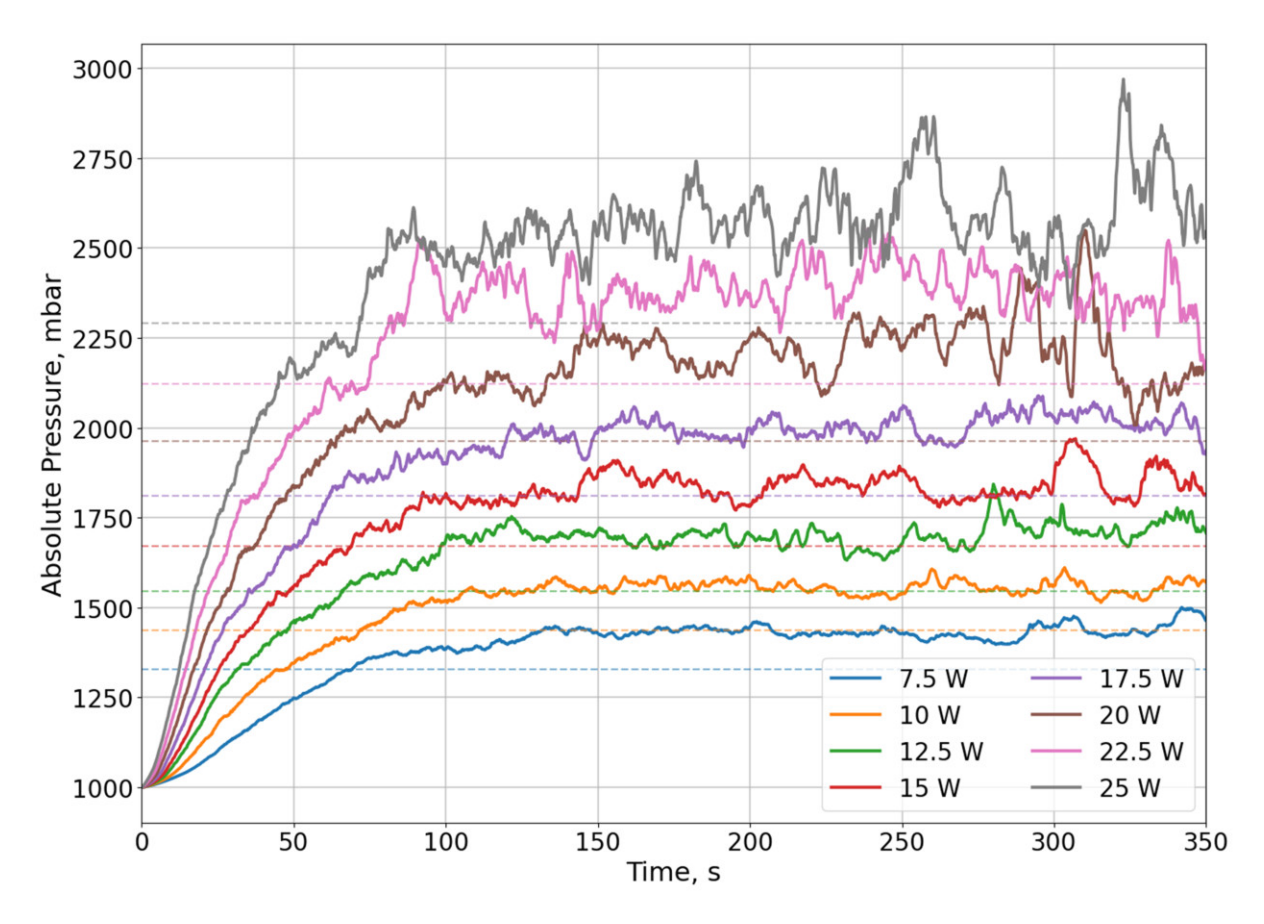


Figure 5.25: Simulated averaged pressure evolution in a 1.7 mm argon PHP under heat loads ranging from 7.5 to 25 W with a filling ratio of 50%.

The comparison between the experimental and simulated results is shown in Figure 5.26. As also seen in previous cases, local increases in pressure are associated with subsequent long-term decreases in the evaporator temperature. This relation reflects the intensification of phase change, as a stronger build-up of pressure enhances condensation through a higher number of computational cells that exceed the threshold in the formulation of the condensation source term (2.28). The overall errors remain below 15%, confirming that the model is still suitable for predicting thermal performance despite the stronger deviations observed at elevated heat loads.

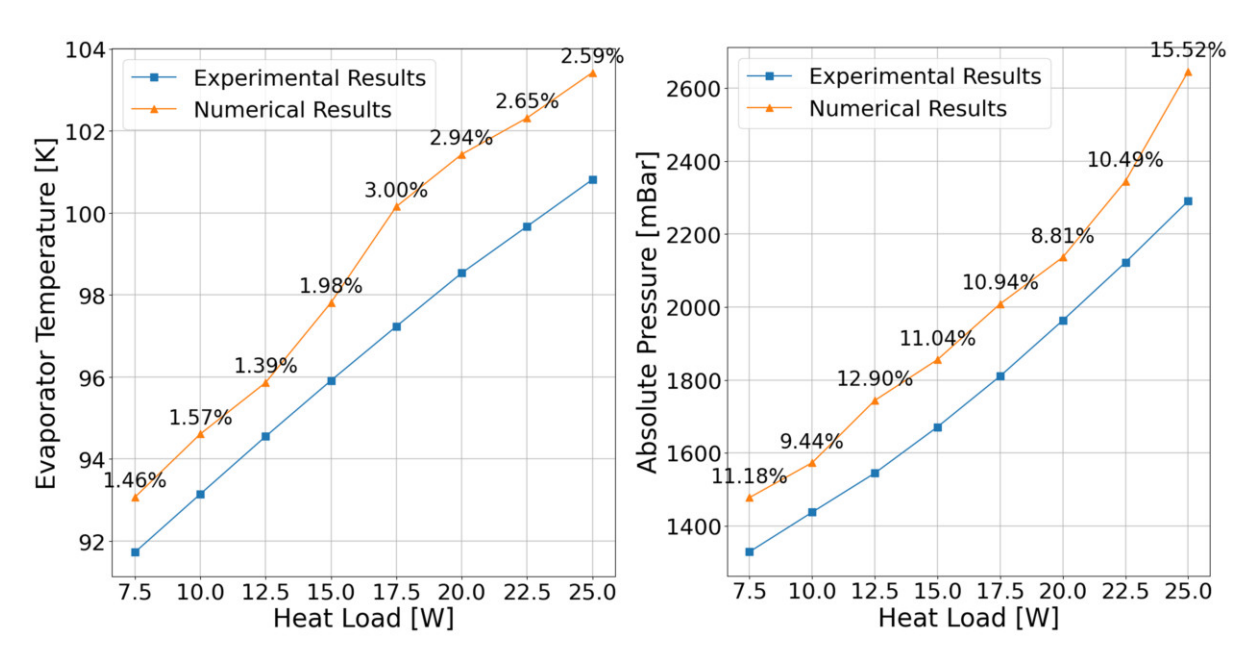


Figure 5.26: Comparison between experimental and simulated results for a 1.7 mm argon PHP with 50% filling ratio under heat loads ranging from 7.5 to 25 W: (left) averaged evaporator temperature, (right) averaged absolute pressure. Percentage values indicate the relative deviation between simulations and experiments.

Figure 5.27 shows the evolution of the average temperature of the evaporator for neon in a 1.3 mm PHP with a filling ratio of 50%. The dynamics are noticeably stronger compared to nitrogen and argon (cf. Figs. 5.9 and 5.21), which can be attributed to the lower heat capacity of the solid wall material and the thermophysical properties of neon itself. In addition, the higher Bond number decrease capillary effects, which result in larger oscillation amplitudes. Local temperature peaks are observed, which may originate from limitations of the two-dimensional model (no copper plate is modeled, while in the experiment it provides a thermal buffer that damps fluctuations) or from local dryout events (Fig. 5.28). After exceeding approximately 4 W, the temperature trends become more regular, indicating that the supplied heat input is sufficient to maintain oscillations and displace liquid plugs through the dryout zones.

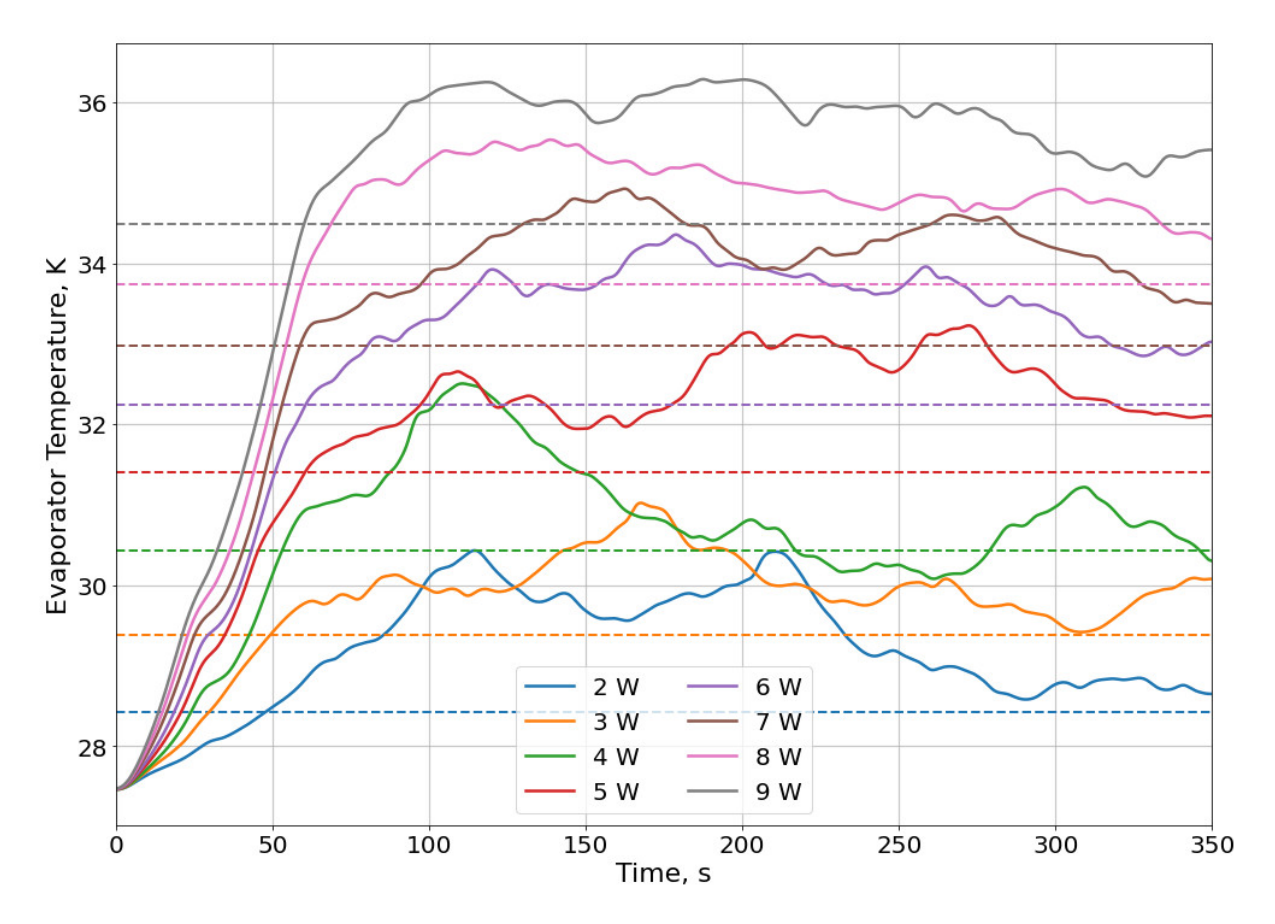


Figure 5.27: Simulated averaged evaporator temperature evolution in a 1.3 mm neon PHP under heat loads ranging from 2 to 9 W with filling ratio of 50%.

Figures 5.28 and 5.29 show the flow structure and the temperature field at 4 W. In region A a capillary segment stays colder because the liquid is immobilized, suppressing convective exchange. In region B a local dryout interrupts the oscillatory circulation. The snapshots at 115 s and 120 s in Fig. 5.29 capture the liquid front that re-wets the dried section, restores the capillary connection between the branches, and triggers sharp temperature and pressure spikes. These transients follow the dynamic film mechanism of Nikolayev (18), where the evolution of thin-walled films controls the onset and amplitude of oscillations. In his model, partial or complete evaporation of the film temporarily suppresses local heat transfer and increases wall temperature, whereas the returning meniscus redeposits a new film that abruptly restores evaporation and leads to large oscillation amplitudes. The same sequence is observed here: film depletion produces local overheating followed by rapid cooling when rewetting occurs. The orientation of the meniscus reveals the direction of motion. During liquid displacement, the advancing interface experiences viscous resistance within the contact-line region, which increases the apparent contact angle, while the receding side is continuously drained, resulting in a smaller angle. This asymmetry arises from the balance between surface tension and viscous stresses near the moving contact line, as described by the hydrodynamic wetting theory of Voinov (208).

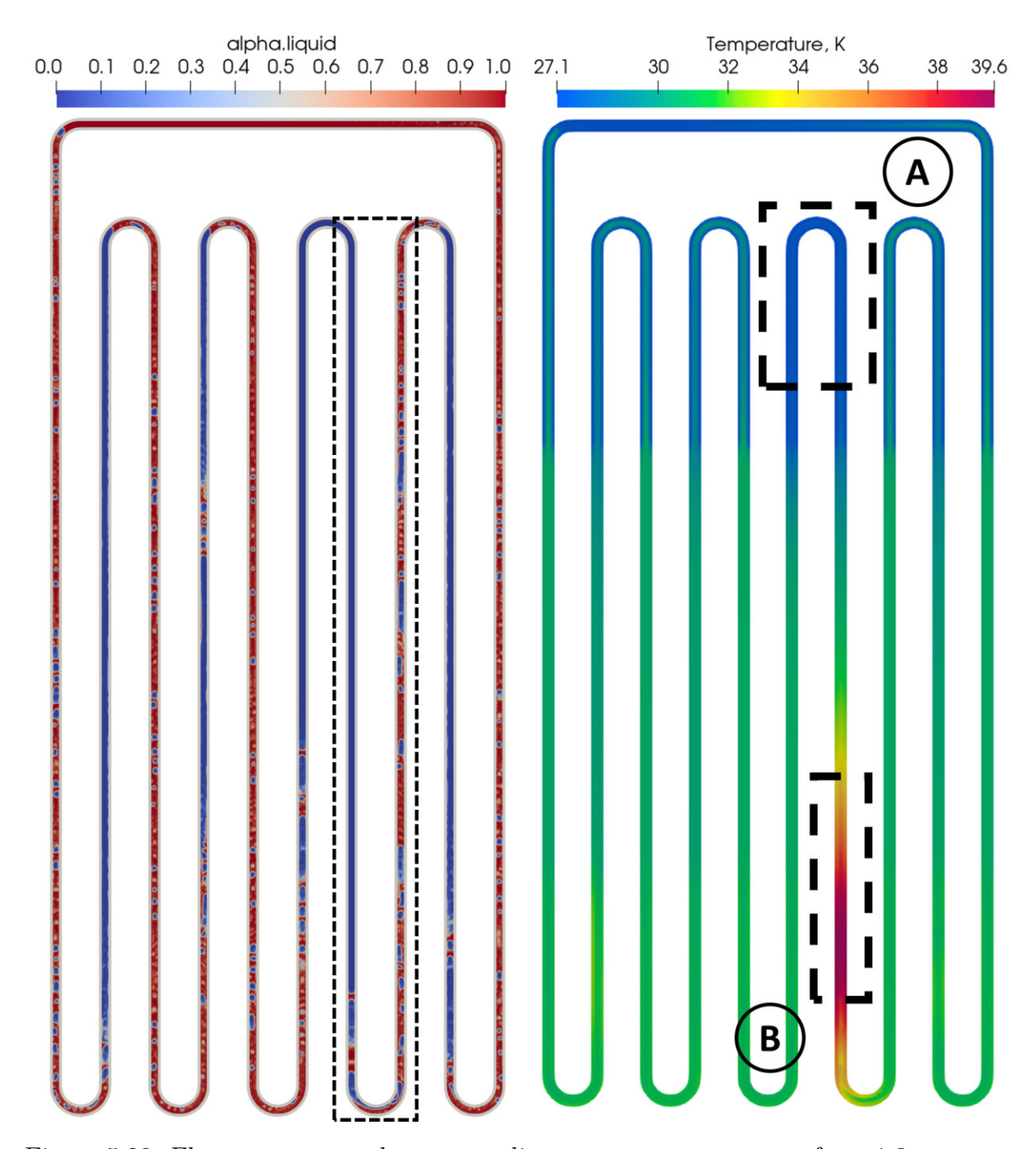


Figure 5.28: Flow structure and corresponding temperature contours for a 1.3 mm neon PHP at 4 W heat load and 50% filling ratio. Regions A and B highlight, respectively, a cooled stagnant arm and a locally dried section blocking oscillatory circulation.

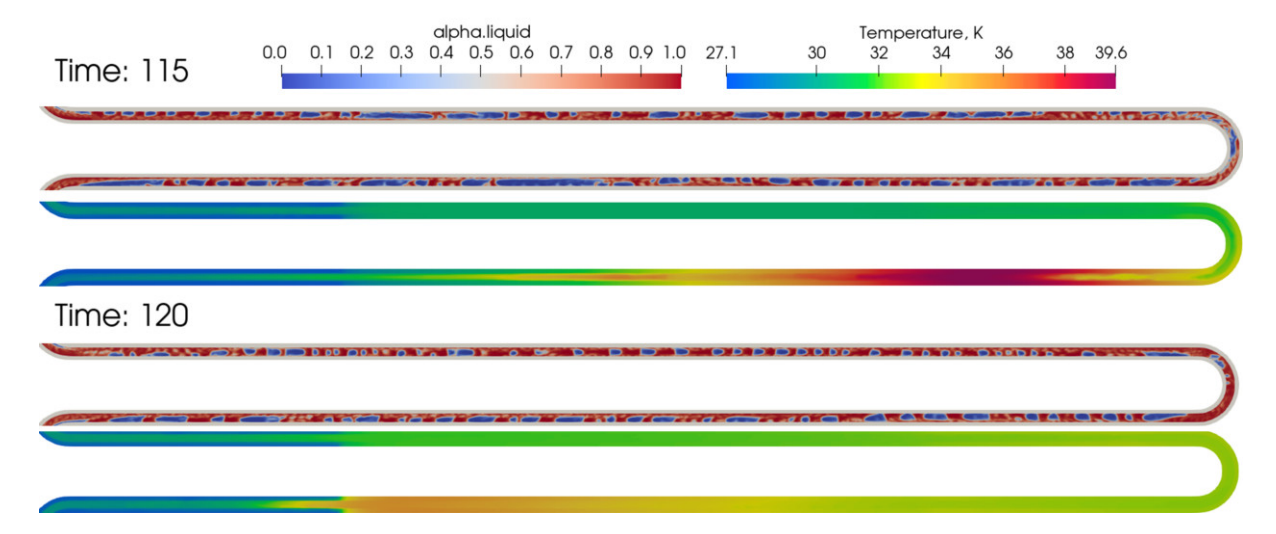


Figure 5.29: Detailed snapshots at 115 s and 120 s for the 4 W neon PHP case, showing displacement of the dried section by liquid inflow. Top: phase fraction field. Bottom: temperature field.

The corresponding absolute pressure (Fig. 5.33) increases in the oscillation amplitude with the applied heat load and shows short spikes that occur together with sudden changes in the wall temperature. In the case of neon, these peaks are stronger because the total heat capacity of the fluid is much smaller than that of argon or nitrogen. The system therefore reacts faster to any temperature disturbance and even a small amount of added heat can cause rapid local evaporation followed by condensation when the liquid returns. These quick transitions generate short pressure pulses visible in the signal. The mean pressure increases steadily with Q, while at the lowest powers the response remains irregular since the oscillations are close to the activation threshold.

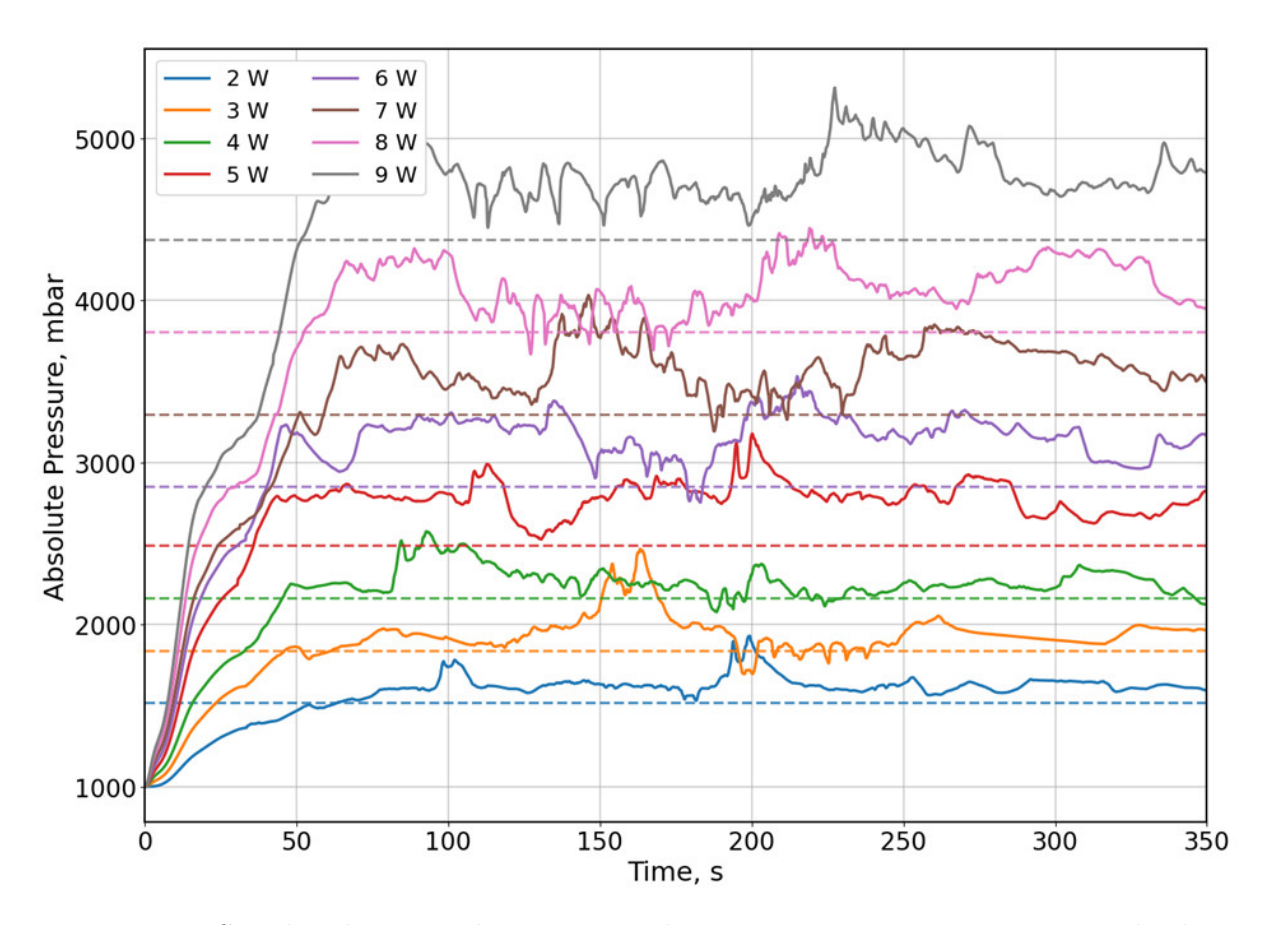


Figure 5.30: Simulated averaged pressure evolution in a 1.3 mm neon PHP under heat loads ranging from 2 to 9 W with filling ratio of 50%.

A comparison with the experimental data is provided in Fig. 5.31. A distinct transition is visible near 5 W, where both the temperature and pressure rise sharply before stabilizing into a more regular regime. The relative error in temperature prediction remains below 4%, while the pressure is consistently overestimated by 7–12%, in line with the tendencies observed for nitrogen and argon.

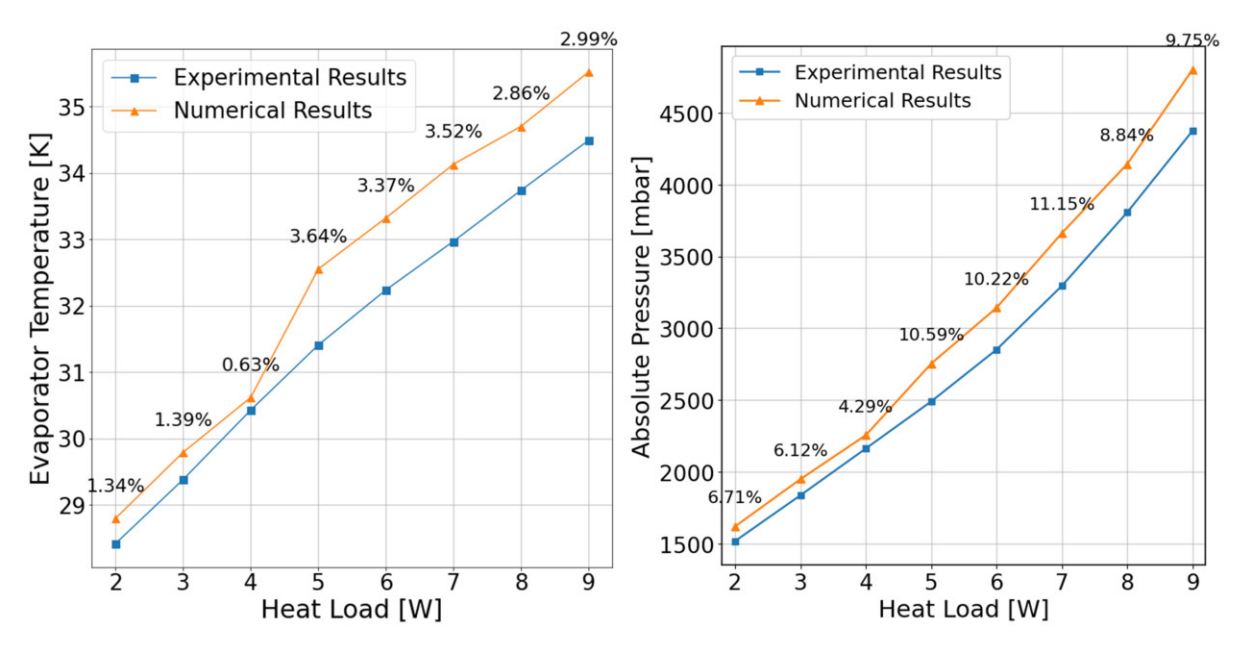


Figure 5.31: Comparison between experimental and simulated results for a 1.3 mm neon PHP with 50% filling ratio under heat loads ranging from 2 to 9 W: (left) averaged evaporator temperature, (right) averaged absolute pressure. Percentage values indicate the relative deviation between simulations and experiments.

Figure 5.32 reports the evolution of the average temperature of the evaporator for neon PHP with 1.3 mm. Pronounced overshoots and intermittent plateaus are observed, particularly at the upper end of the heat-load range. These features originate from repeated dryout–rewetting cycles in the evaporator, which modulate the effective heat-transfer path as the liquid films are depleted and subsequently restored by the incoming plugs. Compared with D=1.3 mm, the larger diameter responding to a higher Bond number which is connected with weaker capillary confinement, while the lower volumetric heat capacity of neon compared to nitrogen and argon reduces thermal buffering. Both effects shorten the characteristic thermal time scale and amplify temperature oscillations for a given Q. In addition, the 2D representation does not include heat spreading in the hot plate, so the damping present in the experiment is absent here, which favors local peaks and longer recovery times.

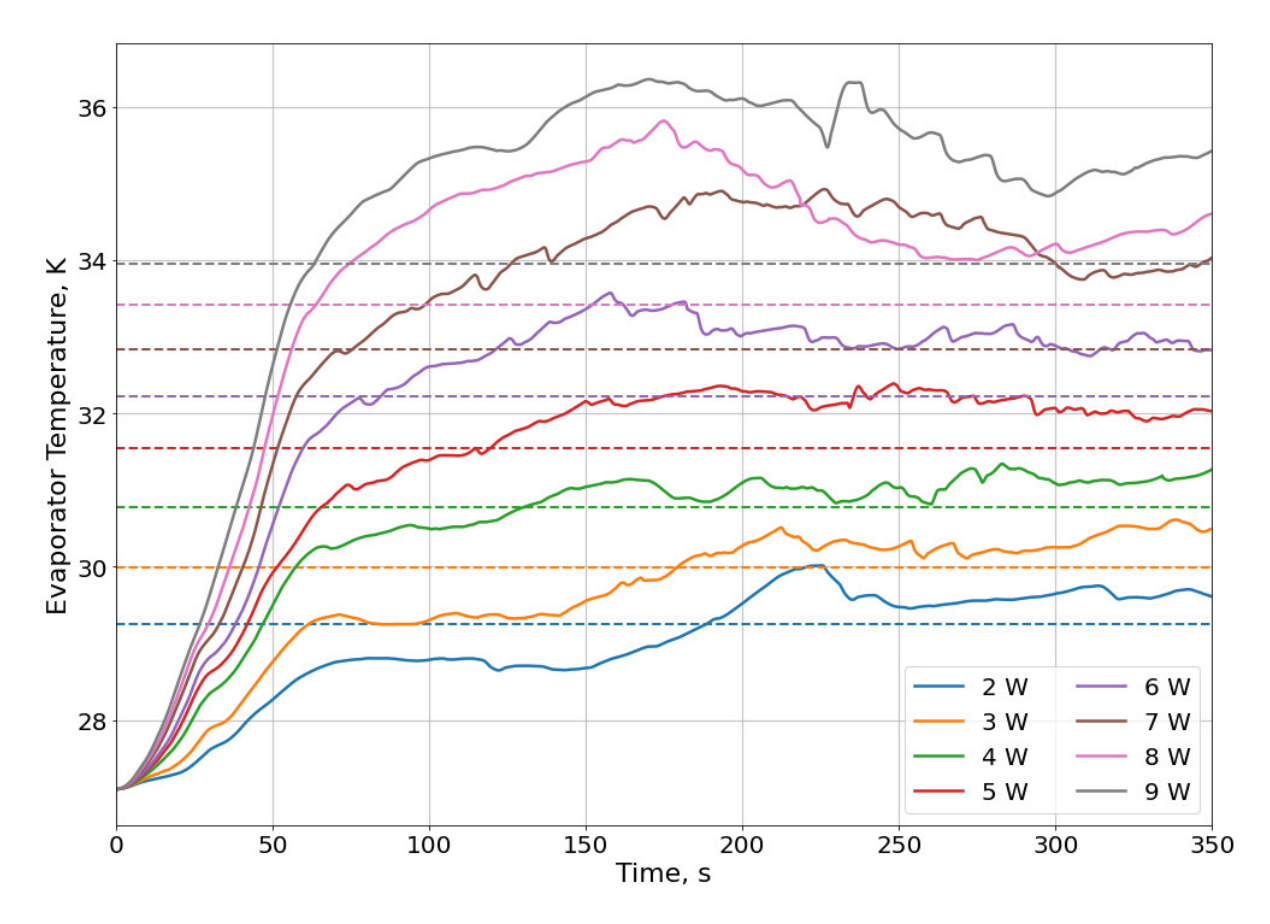


Figure 5.32: Simulated averaged evaporator temperature evolution in a 1.7 mm neon PHP under heat loads ranging from 2 to 9 W with filling ratio of 50%.

The corresponding absolute pressure (Fig. 5.33) exhibits an increase in oscillation amplitude with heat load and sharp spikes that coincide with temperature inflections. These spikes are consistent with capillary pressure jumps $\Delta p \sim \sigma \kappa$, in moving menisci and with rapid rewetting of previously dried segments in U-bends. The long-term mean pressure increases monotonically with Q, while for the lowest powers, the signal remains irregular because the sustained oscillations are close to the threshold.

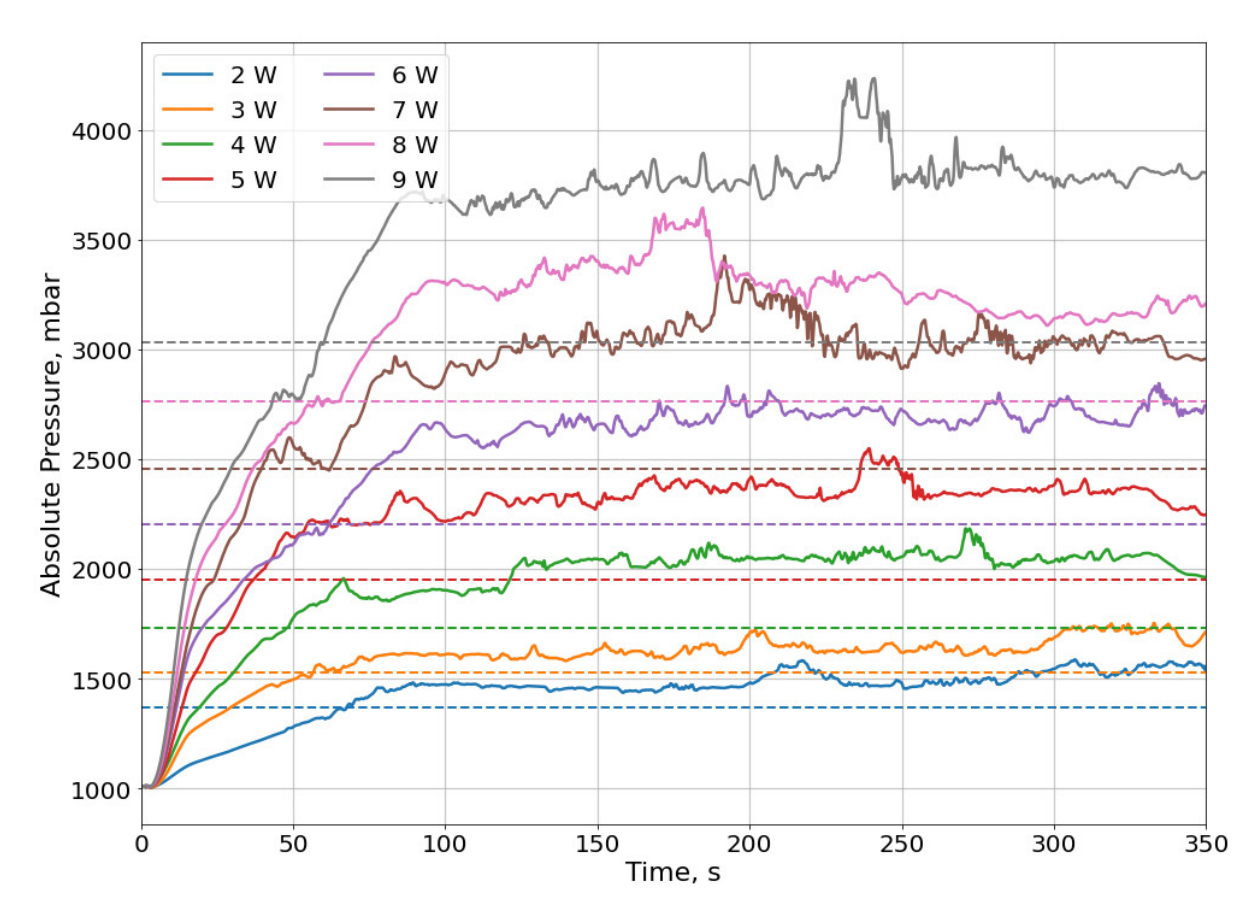


Figure 5.33: Simulated averaged pressure evolution in a 1.7 mm neon PHP under heat loads ranging from 2 to 9 W with filling ratio of 50%.

The quantitative comparison in Fig. 5.34 shows a coupled increase in wall temperature and absolute pressure with Q, but the difference from the experimental results is greater than for D=1.3,mm. The wall temperature is consistently overpredicted and the pressure deviation reaches approximately 10-25% at the highest loads. This behavior results from two-dimensional simplification, which removes the spreading of excessive heat on the hot plate and reduces the effective thermal damping of the loop. It is also amplified by the lower thermal capacity of neon at these temperatures, making the system more sensitive to local temperature variations and small phase-change imbalances. In this modeling framework, the bias can be reduced by refining the mesh and by using smaller time steps to keep the Courant numbers for momentum and phase fraction below the proposed 0.1 limit. Including heat spreading through a three-dimensional conjugate plate or an effective conduction layer would further improve the agreement at high Q.

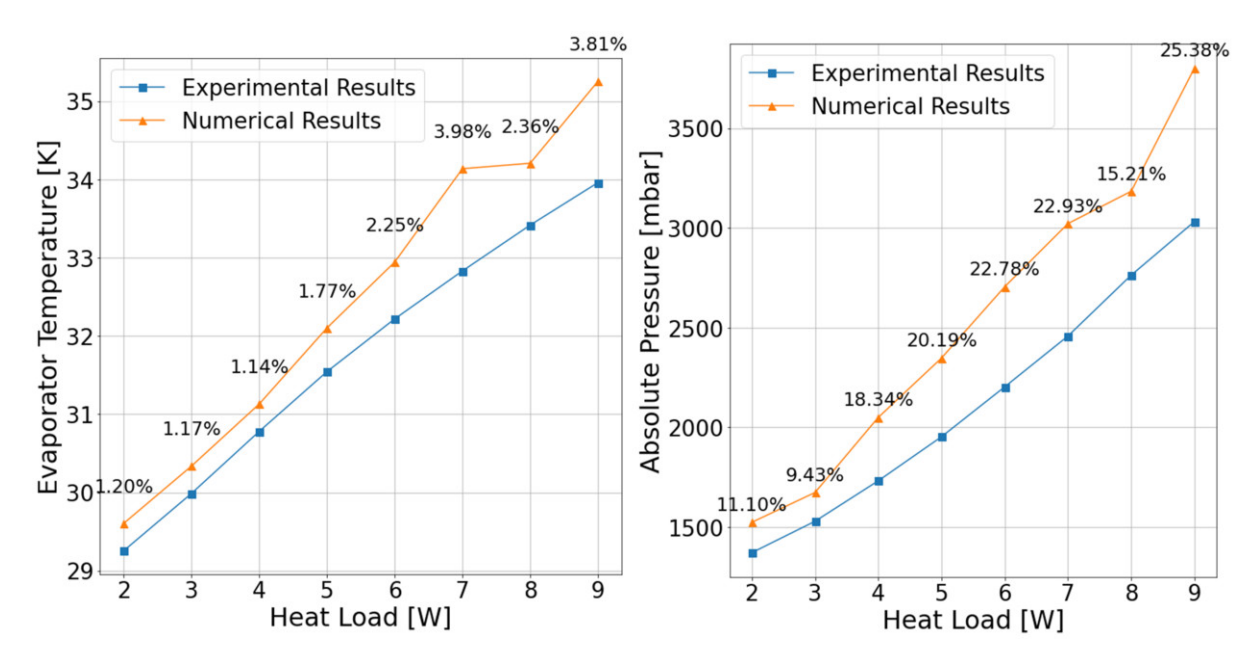


Figure 5.34: Comparison between experimental and simulated results for a 1.7 mm neon PHP with 50% filling ratio under heat loads ranging from 2 to 9 W: (left) averaged evaporator temperature, (right) averaged absolute pressure. Percentage values indicate the relative deviation between simulations and experiments.

The simulations reproduce the observed trends and remain within about 20% of the measured values across the operating range, preserving the coupling between pressure oscillations and evaporator temperature. The wall temperature and absolute pressure are consistently higher than in the experiment. This difference is expected for a formulation that focuses on latent heat transfer without explicitly resolving the thin liquid films along the wall. The discrepancy may also be partly increased by the damping of pressure oscillations in the experimental setup, caused by the compliance and volume of the external pressure line. Within these limits, the model reliably describes the internal flow and phase-change mechanisms, allowing identification of operating regimes and relative performance. The approach is computationally demanding and typically requires several days on a computing cluster rather than on a personal computer. With the continued development of numerical methods and more efficient computational architectures, the predictive capability of this approach is expected to improve.

Chapter 6

Summary, Conclusions and Perspectives

6.1 Summary

This dissertation assembles and analyzes an extensive experimental dataset alongside a CFD-based numerical framework to investigate the heat and mass transfer in cryogenic pulsating heat pipes. The work is structured in five chapters.

Chapter 1 provides an experimental and physical introduction, surveys current knowledge of cryogenic PHP operation from the experimental perspective, outlines the factors that govern PHP behavior, such as geometry and inner diameter, filling ratio, imposed heat flux, and thermophysical properties, and describes the experimental challenges that remain to be addressed.

Chapter 2 focuses on the numerical model, reviews the current modeling approaches for PHPs, identifies numerical gaps and limitations in the literature, and documents the implementation and initial verification of a fully compressible VOF-based phase change solver in OpenFOAMv2106. Beyond the mathematical formulation, the build was verified against canonical problems, namely Scriven bubble growth (166) and the Stefan moving interface case (165), to assess interface tracking and latent heat exchange. Phase-change modeling approach follows an extended Tanasawa formulation (113) with Hardt–Wondratype smoothing (153) and a Galusinski–Vigneaux convergence criterion (149). Although these algorithmic elements have limited direct applicability and known constraints, they allowed controlled checks of solver capabilities such as interfacial localization and evaporation–condensation modeling. The solver was compared with available tools to un-

derscore the thesis novelty, namely a fully compressible VOF model with phase change implemented in OpenFOAM. The complexity of the code and the scope of the doctoral dissertation are reflected in peer-reviewed publications documenting the progressive understanding and progress of the developed framework, as referenced in Chapter 2 (128; 67; 143; 197).

Chapter 3 describes the experimental platform, including the complete fabrication work-flow for capillary assembly and copper plates, fixture design for accurate placement of cylindrical CERNOX® sensors and procedures for thermal anchoring and reduction of parasitic heat leaks that propagate along the instrumentation wiring. Finite element modeling provided a thermal analysis of thermal interfaces between the PHP and the first and second stages of the cryocooler to minimize axial temperature gradients along the condenser plate and guided the integration of the radiation shield within the cryostat. The chapter presents the temperature control approach, the gas filling protocol, calculation of the filling ratio, an uncertainty analysis, a characterization of the cryocooler capacity and cool-down curves.

Chapter 4 reports measurements conducted for three working fluids, argon, nitrogen and neon, using inner diameters of 1.3 mm and 1.7 mm. The tested heat load ranges were 1–12 W for neon, 1–25 W for nitrogen, and 1–32.5 W for argon, bounded by the cry-occoler capacity or the safety limits. The consolidated data set provides performance maps and thermal responses to varying heat flux together with the experimental uncertainties. Within these results, the larger 1.7 mm geometry outperformed the 1.3 mm geometry, including cases for neon where the classical Bond number diameter threshold would suggest limitations. Argon and nitrogen showed comparable performance, with a slight advantage of argon in reduced thermal resistance, whereas neon exhibited visibly lower performance. A correlation was observed between diameter and mean PHP pressure, with pressure decreasing as the diameter increased. The chapter transitions to explain these findings by evaluating the data within a dimensionless framework, using dimensionless numbers and thermophysical properties.

Chapter 5 compares experimental results with that of simulations. Calculations were performed for nitrogen, argon, and neon, with the most extensive parametric studies of filling ratio and diameter sensitivity carried out for nitrogen, while the analysis of argon and neon focused on diameter effects on performance. The simulations were two-dimensional and mesh density selection was supported by mesh convergence checks and diagnostics of interface diffusion as a proxy for resolution adequacy. In all assembled cases, temperature differences between the model and the experiment were typically within $\pm 5 - 10\%$ and pressure differences within $\pm 5 - 25\%$. The overall outcome is a validated framework that reproduces the thermal response to variations in heat flux and changes

in filling ratio with practical accuracy, as well as a clearly defined set of modeling and numerical limitations that provide a framework for future developments.

6.2 Conclusions

This work demonstrates that cryogenic pulsating heat pipes operate with high reproducibility using nitrogen, argon, and neon for both 1.3 mm and 1.7 mm internal diameters over a broad operating range of the cryocooler capacity for different filling ratios from 10% to 90%. At very low heat input, these devices may fail to establish sustained oscillations, while at very high heat input, the operating pressure rises and dryout or a sharp decrease in defective thermal conductivity becomes more likely. In the configuration tested, increasing the internal diameter from 1.3 mm to 1.7 mm reduced the thermal resistance as the heat load increased. Very low filling ratios increased the risk of dryout, while very high filling ratios increased the operating pressure and reduced the thermal resistance within the operating range of safety pressure. The most favorable window was between a 10% and 50% filling ratio, where thermal resistance was low without exceeding pressure safety margins.

Two consistent PHP trends have emerged. First, for a given working fluid and inner diameter, the mean pressure increased with the applied heat input and the filling ratio. Second, the amplitude of the oscillations was a consequence of the internal flow regime rather than the pressure value itself. Although the exact flow structure could not be directly observed due to the absence of a transparent pipe section, synchronized pressure and temperature records successfully identified these regime transitions, including startup, partial dryout characterized by a lack of a liquid film in the evaporator, and occasional global dryout. Presented results suggest that the observed shifts in pressure oscillations are directly related to shifts in the flow type. This mechanism explains the non-monotonic resistance changes at a fixed filling ratio: as the heat input increased to maintain stable oscillations, thermal resistance initially decreased. Beyond a threshold, increasing vapor shear due to higher velocity and intensity of the phase change thinned the wall films, which reduced the effective area for evaporation and therefore worsened thermal performance. Finally, with the larger 1.7 mm pipe, the accessible operating window and pressure margin were larger than for 1.3 mm, consistent with its lower average pressures.

In the uncertainty for the filling ratio, the dominant contribution is coming from buffer volume uncertainty, while the influence of pipe volumes and the evaluation of thermophysical properties were smaller. The dominant contribution to the uncertainty of the resistance was the uncertainty in temperature measurement or the amount of heat applied to the evaporator. This was most pronounced in two specific regimes: first, at low heat load, where unsteady startup conditions caused large temperature fluctuations, making the statistical uncertainty (Type A) higher, and second, at high heat load, where the uncertainty in the amount of applied heat became the dominant (Type B) contribution. The pressure was measured in the feeding tube outside the cryostat, which dampened the signal and partly explains the differences in amplitude relative to the numerical results. Future experimental campaigns should determine the buffer volume directly with higher precision rather than depend on the manufacturer's uncertainty. Additionally, future pressure measurements should be localized inside the PHP to reduce the influence of the feeding tube volume, allowing signal amplitudes and fluctuations to reflect the internal dynamics more accurately.

Finite-element thermal analysis is a useful tool at the design stage of the interface that couples the cryocooler cold head to the condenser plate. Treating the cold head as the heat sink and placing heaters on the interface allows for the selection of heater and sensor locations and the shaping of the interface geometry so that the regulated condenser temperature becomes spatially uniform. In practice, positioning the heater or a pair of heaters closer to the regulated zone on the copper interface produced a faster response with the CTC100, but it resulted in a less uniform condenser temperature than a more distant placement of the heater. This placement is a compromise. Bringing the heat input closer to the regulated area reduces the control-loop delay but increases the local temperature gradients on the condenser surface. Using several heaters can flatten the temperature field. However, it depends on the precision of the manufacturing regarding the uniformity of heating and the consistency of resistance between Kapton heaters, since any variation in a parallel connection might lead to non-uniform temperature control. FEM makes it possible to compare these variants quantitatively and to identify potential layouts and sensor positions.

Mechanical reliability of the PHP depends on the silver-brazed T-joint and vacuum integrity. Therefore, the joint is inspected after thermal cycling and high pressure stress tests. Later, PHPs were checked with the leak detector to confirm that the joint would last within the intended operating range.

Mesh independence was verified by confirming that the wall heating rate, together with the sharpness of the nucleated bubble interfaces, no longer changed significantly with further mesh refinement. Consequently, the chosen resolution preserved meniscus sharpness, accurate interface curvature and physically consistent plug and slug motion at a tractable computational cost. Startup emerged as a gradual build-up of oscillations rather than a distinct event. The two-dimensional setup captured the global thermal response but did not resolve thin liquid films or thermocapillary stresses.

Together, the experiment and the simulations support several coherent outcomes. The 1.7 mm pipes sustained lower thermal resistance and a wider operating window than 1.3 mm. For each diameter, the most stable and repeatable behavior occurred for filling ratios between 30% and 50%, where latent and sensible contributions balance and both the dryout tendency at lower liquid content and the pressure growth at high filling ratios were avoided. The solver showed a systematic over-prediction of pressure and wall temperature.

Mass conservation, with phase change modeling in a sealed and compressible volume based on the VOF method, remains challenging. Stabilization is used here to moderate the accommodation coefficient in the Tanasawa model and to apply a proportional correction to the phase change source terms. The 2D computational domain imposes significant limitations. Firstly, it inherently neglects the 3D heat conduction and the large thermal inertia of the external copper plate. This plate acts as a thermal buffer in the experiment, absorbing heat pulses and damping temperature spikes. In this case, thermal buffering meant that simulated local temperature peaks were nonphysically sharp and significantly larger than those observed in measurements. Contact angle data at cryogenic temperatures are sparse, especially for dynamic values, which add uncertainty to meniscus motion, film deposition, and pressure amplitudes at high loads. Nevertheless, the computational cost was significant and limited both the mesh density and the time step reduction.

The results support practical guidance for design. When the design approaches the capillary confinement limit, expressed by the Bond number, it is generally safer to select the larger value as a candidate for the inner diameter. The classical threshold near a Bond number of 4 should be treated as indicative rather than absolute, since in the present study, oscillations and efficient heat transport were still observed even for doubled threshold values. A mid-range filling ratio provides stable performance and should be used as a reference point when defining operating conditions. Argon and nitrogen with a 1.7 mm inner diameter and a filling ratio close to 50% offered the best compromise between low thermal resistance and sufficient pressure margin. For neon, the usable heat flux window is narrower. For comparisons between similar geometries, it is recommended to report thermal resistance rather than effective thermal conductivity, since the resistance directly links the temperature rise to the imposed heat load, while the conductivity incorporates geometric effects that are redundant when the external dimensions are fixed.

Across the present dataset, no single tested criterion (Bond, Ohnesorge, Jacob numbers, saturation-slope $\mathrm{d}p/\mathrm{d}T|_\mathrm{sat}$) provides a universal connection for thermal performance

across fluids and diameters. Each of them reflects only part of the PHPs behavior and shows trends locally, for a fixed filling ratio and within a limited operating window. However, none of them provides a global conclusion when considered individually. In this sense, the criterial analysis is mainly a way to organize the observations to understand PHPs physics more deeply. As a potential extension, a statistical analysis of the same dataset could help separate local trends from global tendencies and quantify their uncertainty without relying on any single indicator.

The experimental maps and the validated numerical outcomes define the operating windows of cryogenic PHPs and deliver predictions with quantified uncertainty. The framework forecasts operating points and thermal performance and explains the internal flow structure that governs heat transfer. The combination of the simulation results with measurements provides comprehensive validation and demonstrates that the same tool can quantify the influence of inner diameter and other geometric choices, as well as assess changes in working fluid and filling ratio with a single, consistent methodology.

6.3 Perspectives

The next experimental campaign should deliberately approach the capillary–confinement boundary to delineate the practical limits of the Bo=4 threshold (6; 209) under cryogenic conditions. In the present geometry, this suggests testing larger inner diameters for nitrogen and argon (for example $D_i \approx 2.2$ mm for nitrogen and $D_i \approx 2.0$ mm for argon) and a smaller diameter for neon around $D_i \approx 1.0$ mm, corresponding respectively to approximate Bond numbers of 4.2, 4.5 and 0.9. The condenser setpoint should be shifted to sweep the Bond number in fixed geometry while documenting the consequences for operating pressure.

Based on evidence that dynamic contact angle and film deposition can alter thermal resistance in pulsating heat pipes (119), and given the current gaps in cryogenic wetting data such as dynamic contact angle, a targeted measurement campaign is needed to represent interfacial physics quantitatively in models. The general contact line theory is mature (210), yet available cryogenic measurements are sparse. Static angles for nitrogen have been reported on selected substrates (199). Comparable static data for argon and neon are not available and dynamic constant angle datasets are missing for all three fluids. The proposed measurement campaign should determine the relevant materials and surface roughness under static cryogenic conditions for advancing and receding contact angles, their hysteresis, and the velocity dependence of the dynamic contact angle. Such data would enable to provide experimental dataset for the calculation of dynamic wetting and

for film deposition by oscillating slugs, reducing a leading source of uncertainty in phase change modeling and improving the prediction of thermal resistance.

In future studies, a useful direction would be to add flow visualization so that internal structure statistics can be linked directly to the performance maps. High-speed imaging through transparent pipes and cryostat windows, synchronized with pressure and temperature measurements, would enable regime identification and transition maps as functions of the filling ratio, applied heat input and operating pressure. Room-temperature PHP studies already provide practical protocols and taxonomies (204) and recent cryogenic imaging of oscillatory boiling shows that similar approaches are feasible for nitrogen (183; 184). With imaging, each record can be indexed by the instantaneous thermodynamic state and by the velocity of the meniscus derived from the sequences, which in turn enables the use of dimensionless numbers based on velocity. Extending the different fluids would widen the span of surface tension, viscosity, latent heat and heat capacity, allowing statistics on structures to be connected to the governing numbers and to measured thermal resistance and operating pressure. Such experimental data would provide insights into the heat-transfer balance, such as the ratio of latent to sensible components, thereby reducing the present uncertainty of this balance. They would also enable the construction of a statistical model to predict PHP performance under comparable operating conditions.

On the modeling side, a three-dimensional conjugate domain should replace the present two-dimensional representation to restore the normal components of wall films and heat spreading in the copper plates. Interface-resolved capillary studies show that meniscus curvature, capillary pressure jumps and deposited films set the effective evaporation and condensation areas (211; 200). Three-dimensional simulations of Taylor bubbles and slug flow further document the sensitivity of film thickness and heat transfer to geometry and wetting (212; 213). For PHPs, a limited-loop 3D model with periodic replication can control costs while capturing the coupling between the tube and the copper plates and can deliver fields that are inaccessible in two dimensions, namely film thickness and curvature distributions. These outputs would enable direct validation of thin-film closures and a clearer attribution of performance changes to geometry, wetting and operating conditions.

The selected operating points should be recomputed with locally refined meshes that achieve a wall-adjacent resolution of $y^+ \lesssim 1$ and maintain an interface thickness smaller than the expected film scales. This refinement is expected to improve the precision of the calculated meniscus curvature, the prediction of capillary jumps, and the evolution of the deposited films, thus reducing the current bias toward latent transfer and clarifying the shear-induced thinning mechanism that degrades performance at high loads.

The interfacial mass transfer closure requires two advancements. First, the accommodation coefficient in Tanasawa-Schrage-type formulations (113; 111) should be explicitly dependent on the local time step and cell size to avoid stiff over-conversion when $\gamma \to 1$ while remaining consistent with kinetic-theory limits (214). Second, the phase change should be conditioned on co-current deviations of temperature and pressure from saturation and corrected for interface curvature via the Kelvin relation, which arises from surface tension. Consistent with bubble growth simulations that resolve the approach to $T_{\rm sat}$ as in (215), this makes the local equilibrium explicitly dependent on the geometry of the meniscus.

Thermocapillary stresses should be included when reliable $d\sigma/dT$ data are available for the fluid. The driving mechanism is the surface tension gradient along the interface rather than the absolute value, and it must be applied tangentially to the resolved interface as in (216). Given the sensitivity of Marangoni effects to wetting dynamics, their incorporation should follow the acquisition of the dynamic contact angle data outlined above.

Phase-fraction advection can be improved by adopting geometric VOF schemes that maintain boundedness and sharp interfaces with reduced numerical diffusion compared to legacy algebraic limiters. In the OpenFOAM ecosystem, isoAdvector and related geometric methods provide sharper interface transport and better curvature preservation, which improve the accuracy of capillary pressure and reduce spurious currents (217). Migrating the current solver to such advection and modern bounded MULES variants would directly address the residual smearing observed in long sealed runs.

Bibliography

- [1] A. Hisateru, Structure of micro-heat pipe (1993).URL https://www.lens.org/lens/misc/US_4921041_A
- [2] M. Shafii, A. Faghri, Y. Zhang, Thermal modeling of unlooped and looped pulsating heat pipes, Journal of Heat Transfer 123 (6) (2001) 1159 1172. doi:10.1115/1.1409266.
- [3] M. Shafii, A. Faghri, Y. Zhang, Analysis of heat transfer in unlooped and looped pulsating heat pipes, International Journal of Numerical Methods for Heat and Fluid Flow 12 (5) (2002) 585 609. doi:10.1108/09615530210434304.
- [4] M. Alhuyi Nazari, M. H. Ahmadi, R. Ghasempour, M. B. Shafii, How to improve the thermal performance of pulsating heat pipes: A review on working fluid, Renewable and Sustainable Energy Reviews 91 (2018) 630–638. doi:https://doi.org/10.1016/j.rser.2018.04.042.
- [5] M. Arab, M. Soltanieh, M. Shafii, Experimental investigation of extra-long pulsating heat pipe application in solar water heaters, Experimental Thermal and Fluid Science 42 (2012) 6 15. doi:10.1016/j.expthermflusci.2012.03.006.
- [6] S. Khandekar, N. Dollinger, M. Groll, Understanding operational regimes of closed loop pulsating heat pipes: An experimental study, Applied Thermal Engineering 23 (6) (2003) 707 – 719. doi:10.1016/S1359-4311(02)00237-5.
- [7] S. Khandekar, M. Groll, An insight into thermo-hydrodynamic coupling in closed loop pulsating heat pipes, International Journal of Thermal Sciences 43 (1) (2004) 13 20. doi:10.1016/S1290-0729(03)00100-5.
- [8] S. Khandekar, Y. M. Joshi, B. Mehta, Thermal performance of closed two-phase thermosyphon using nanofluids, International Journal of Thermal Sciences 47 (6) (2008) 659 667. doi:10.1016/j.ijthermalsci.2007.06.005.
- [9] M. Mameli, L. Araneo, S. Filippeschi, L. Marelli, R. Testa, M. Marengo, Thermal response of a closed loop pulsating heat pipe under a varying gravity force, In-

- ternational Journal of Thermal Sciences 80 (1) (2014) 11 22. doi:10.1016/j.ijthermalsci.2014.01.023.
- [10] D. Mangini, M. Mameli, A. Georgoulas, L. Araneo, S. Filippeschi, M. Marengo, A pulsating heat pipe for space applications: Ground and microgravity experiments, International Journal of Thermal Sciences 95 (2015) 53-63. doi:https://doi.org/10.1016/j.ijthermalsci.2015.04.001.
- [11] D. Mangini, M. Mameli, D. Fioriti, S. Filippeschi, L. Araneo, M. Marengo, Hybrid pulsating heat pipe for space applications with non-uniform heating patterns: Ground and microgravity experiments, Applied Thermal Engineering 126 (2017) 1029 – 1043. doi:10.1016/j.applthermaleng.2017.01.035.
- [12] M. Mameli, M. Marengo, S. Khandekar, Local heat transfer measurement and thermo-fluid characterization of a pulsating heat pipe, International Journal of Thermal Sciences 75 (2014) 140 – 152. doi:10.1016/j.ijthermalsci.2013.07. 025.
- [13] K. Vontas, M. Andredaki, A. Georgoulas, N. Miché, M. Marengo, The effect of surface wettability on flow boiling characteristics within microchannels, International Journal of Heat and Mass Transfer 172 (2021). doi:10.1016/j. ijheatmasstransfer.2021.121133.
- [14] J. Lee, S. J. Kim, Effect of channel geometry on the operating limit of micro pulsating heat pipes, International Journal of Heat and Mass Transfer 107 (2017) 204 212. doi:10.1016/j.ijheatmasstransfer.2016.11.036.
- [15] J. Kim, S. J. Kim, Experimental investigation on working fluid selection in a micro pulsating heat pipe, Energy Conversion and Management 205 (2020). doi:10. 1016/j.enconman.2019.112462.
- [16] S. Jun, S. J. Kim, Comparison of the thermal performances and flow characteristics between closed-loop and closed-end micro pulsating heat pipes, International Journal of Heat and Mass Transfer 95 (2016) 890 901. doi:10.1016/j.ijheatmasstransfer.2015.12.064.
- [17] J. Jo, J. Kim, S. J. Kim, Experimental investigations of heat transfer mechanisms of a pulsating heat pipe, Energy Conversion and Management 181 (2019) 331 341. doi:10.1016/j.enconman.2018.12.027.
- [18] V. S. Nikolayev, A dynamic film model of the pulsating heat pipe, Journal of Heat Transfer 133 (8) (May 2011). doi:10.1115/1.4003759.

- [19] I. Nekrashevych, V. S. Nikolayev, Pulsating heat pipe simulations: Impact of php orientation, Microgravity Science and Technology 31 (3) (2019) 241–248. doi: 10.1007/s12217-019-9684-3.
- [20] V. S. Nikolayev, Physical principles and state-of-the-art of modeling of the pulsating heat pipe: A review, Applied Thermal Engineering 195 (2021) 117111. doi:https://doi.org/10.1016/j.applthermaleng.2021.117111.
- [21] F. Bonnet, P. Gully, V. Nikolayev, Development and test of a cryogenic pulsating heat pipe and a pre-cooling system, AIP Conference Proceedings 1434 (1) (2012) 607–614. doi:10.1063/1.4706970.
- [22] L. D. Fonseca, F. Miller, J. Pfotenhauer, Design and operation of a cryogenic nitrogen pulsating heat pipe, IOP Conference Series: Materials Science and Engineering 101 (1) (2015) 012064. doi:10.1088/1757-899X/101/1/012064.
- [23] R. Bruce, M. Barba, A. Bonelli, B. Baudouy, Thermal performance of a meter-scale horizontal nitrogen pulsating heat pipe, Cryogenics 93 (2018) 66–74. doi:https://doi.org/10.1016/j.cryogenics.2018.05.007.
- [24] T. Mito, K. Natsume, N. Yanagi, H. Tamura, T. Tamada, K. Shikimachi, N. Hirano, S. Nagaya, Development of highly effective cooling technology for a superconducting magnet using cryogenic ohp, IEEE Transactions on Applied Superconductivity 20 (3) (2010) 2023 – 2026. doi:10.1109/TASC.2010.2043724.
- [25] K. Natsume, T. Mito, N. Yanagi, H. Tamura, T. Tamada, K. Shikimachi, N. Hirano, S. Nagaya, Heat transfer performance of cryogenic oscillating heat pipes for effective cooling of superconducting magnets, Cryogenics 51 (6) (2011) 309–314, special Issue: ACASC 2009. doi:https://doi.org/10.1016/j.cryogenics.2010.07.001.
- [26] L. D. Fonseca, F. Miller, J. Pfotenhauer, A helium based pulsating heat pipe for superconducting magnets, AIP Conference Proceedings 1573 (1) (2014) 28–35. doi: 10.1063/1.4860679.
- [27] R. Bruce, B. Baudouy, Cryogenic design of a large superconducting magnet for astro-particle shielding on deep space travel missions, Physics Procedia 67 (2015) 264–269, proceedings of the 25th International Cryogenic Engineering Conference and International Cryogenic Materials Conference 2014. doi:https://doi.org/ 10.1016/j.phpro.2015.06.085.
- [28] Q. Liang, Y. Li, Q. Wang, Cryogenic oscillating heat pipe for conduction-cooled superconducting magnets, IEEE Transactions on Applied Superconductivity 28 (3) (2018) 1–5. doi:10.1109/TASC.2017.2782783.

- [29] T. Mito, K. Natsume, N. Yanagi, H. Tamura, Y. Terazaki, Enhancement of thermal properties of hts magnets using built-in cryogenic oscillating heat pipes, IEEE Transactions on Applied Superconductivity 23 (3) (2013) 4602905–4602905. doi:10.1109/TASC.2013.2251393.
- [30] M. Barba, R. Bruce, A. Bonelli, B. Baudouy, Experimental study of large-scale cryogenic pulsating heat pipe, IOP Conference Series: Materials Science and Engineering 278 (1) (2017) 012156. doi:10.1088/1757-899X/278/1/012156.
- [31] M. Barba, R. Bruce, F. Bouchet, A. Bonelli, B. Baudouy, Thermal study of a one-meter long neon cryogenic pulsating heat pipe, in: IOP Conference Series: Materials Science and Engineering, Vol. 502, IOP Publishing, 2019, p. 012152.
- [32] M. Barba, R. Bruce, F. Bouchet, A. Bonelli, B. Baudouy, Effect of the thermophysical properties of the working fluid on the performance of a 1-m long cryogenic horizontal pulsating heat pipe, International Journal of Heat and Mass Transfer 187 (2022) 122458. doi:https://doi.org/10.1016/j.ijheatmasstransfer. 2021.122458.
- [33] T. Dixit, G. Authelet, C. Mailleret, F. Gouit, V. Stepanov, B. Baudouy, High performance and working stability of an 18 w class neon pulsating heat pipe in vertical/horizontal orientation, Cryogenics 132 (2023) 103670. doi:https://doi.org/10.1016/j.cryogenics.2023.103670.
- [34] T. Dixit, M. Daval, G. Authelet, C. Mailleret, F. Gouit, V. Stepanov, B. Baudouy, Oversized diameter helium pulsating heat pipe, Applied Thermal Engineering 251 (2024) 123613. doi:https://doi.org/10.1016/j.applthermaleng.2024.123613.
- [35] L. Fonseca, F. Miller, J. Pfotenhauer, Experimental heat transfer analysis of a cryogenic nitrogen pulsating heat pipe at various liquid fill ratios, Applied Thermal Engineering 130 (03 2017). doi:10.1016/j.applthermaleng.2017.11.029.
- [36] L. Fonseca, J. Pfotenhauer, F. Miller, Results of a three evaporator cryogenic helium pulsating heat pipe, International Journal of Heat and Mass Transfer 120 (2018) 1275–1286. doi:10.1016/j.ijheatmasstransfer.2017.12.108.
- [37] B. Mueller, J. Pfotenhauer, F. Miller, Performance of nitrogen pulsating heat pipes as passive thermal switches in a redundant cryocooler application, Applied Thermal Engineering 196 (2021) 117213. doi:https://doi.org/10.1016/j.applthermaleng.2021.117213.

- [38] L. Kossel, J. Pfotenhauer, F. Miller, Experimental investigations and thermodynamic analyses of meter-scale helium pulsating heat pipes, International Journal of Heat and Mass Transfer 236 (2025) 126263. doi:https://doi.org/10.1016/j.ijheatmasstransfer.2024.126263.
- [39] L. Kossel, J. Pfotenhauer, F. Miller, Development of a novel orientation-independent hybrid conventional-pulsating heat pipe using cryogenic helium, International Journal of Heat and Mass Transfer 237 (2025) 126430. doi:https://doi.org/10.1016/j.ijheatmasstransfer.2024.126430.
- [40] N. Nagamoto, A. Kawagoe, T. Mito, Y. Onodera, K. Takahata, N. Yanagi, S. Hamaguchi, N. Hirano, Thermal transport properties of multiple oscillating heat pipes under simultaneous operation, Journal of Physics: Conference Series 1559 (2020) 012091. doi:10.1088/1742-6596/1559/1/012091.
- [41] Q. Liang, Y. Li, Q. Wang, Experimental investigation on the performance of a neon cryogenic oscillating heat pipe, Cryogenics 84 (2017) 7–12. doi:https://doi.org/10.1016/j.cryogenics.2017.03.004.
- [42] Q. Liang, Y. Li, Q. Wang, Effects of filling ratio and condenser temperature on the thermal performance of a neon cryogenic oscillating heat pipe, Cryogenics 89 (2018) 102–106. doi:https://doi.org/10.1016/j.cryogenics.2017.12.002.
- [43] A. Jiao, H. Ma, J. Critser, Experimental investigation of cryogenic oscillating heat pipes, International Journal of Heat and Mass Transfer 52 (15) (2009) 3504–3509. doi:https://doi.org/10.1016/j.ijheatmasstransfer.2009.03.013.
- [44] Y. Li, Q. Wang, S. Chen, B. Zhao, Y. Dai, Experimental investigation of the characteristics of cryogenic oscillating heat pipe, International Journal of Heat and Mass Transfer 79 (2014) 713-719. doi:https://doi.org/10.1016/j. ijheatmasstransfer.2014.08.061.
- [45] H. R. Deng, Y. M. Liu, R. F. Ma, D. Y. Han, Z. H. Gan, J. M. Pfotenhauer, Experimental investigation on a pulsating heat pipe with hydrogen, IOP Conference Series: Materials Science and Engineering 101 (1) (2015) 012065. doi:10.1088/ 1757-899X/101/1/012065.
- [46] Z. Gan, X. Sun, B. Jiao, D. Han, H. Deng, S. Wang, J. M. Pfotenhauer, Experimental study on a hydrogen closed loop pulsating heat pipe with different adiabatic lengths, Heat Transfer Engineering 40 (3-4) (2019) 205–214. doi: 10.1080/01457632.2018.1426223.

- [47] X. Sun, S. Li, B. Jiao, Z. Gan, J. Pfotenhauer, B. Wang, Q. Zhao, D. Liu, Experimental study on hydrogen pulsating heat pipes under different number of turns, Cryogenics 111 (2020) 103174. doi:https://doi.org/10.1016/j.cryogenics. 2020.103174.
- [48] S. Li, X. Sun, D. Liu, B. Jiao, J. Pfotenhauer, Z. Gan, M. Qiu, Experimental study on a hydrogen pulsating heat pipe in different heating modes, Cryogenics 123 (2022) 103440. doi:https://doi.org/10.1016/j.cryogenics.2022.103440.
- [49] V. Patel, N. Mehta, K. Mehta, et al., Experimental investigation of flat plate cryogenic oscillating heat pipe, Journal of Low Temperature Physics 198 (2020) 41–55. doi:10.1007/s10909-019-02243-1.
- [50] K. R. Sagar, H. Naik, H. B. Mehta, Numerical study of liquid nitrogen based pulsating heat pipe for cooling superconductors, International Journal of Refrigeration 122 (2021) 33–46. doi:https://doi.org/10.1016/j.ijrefrig.2020.10.033.
- [51] K. R. Sagar, H. Naik, H. B. Mehta, Novel condenser based cryogenic pulsating heat pipe: Investigations on influence of geometrical parameters, Cryogenics 126 (2022) 103543. doi:https://doi.org/10.1016/j.cryogenics.2022.103543.
- [52] K. R. Sagar, H. Naik, H. B. Mehta, Performance assessment of planar and non-planar cryogenic pulsating heat pipe with novel condenser, Cryogenics 129 (2023) 103614. doi:https://doi.org/10.1016/j.cryogenics.2022.103614.
- [53] B. Taft, A. Williams, B. Drolen, Review of pulsating heat pipe working fluid selection, Journal of Thermophysics and Heat Transfer 26 (2012) 651–656. doi: 10.2514/1.T3768.
- [54] P. R. Pachghare, A. M. Mahalle, Effect of pure and binary fluids on closed loop pulsating heat pipe thermal performance, Procedia Engineering 51 (2013) 624–629, chemical, Civil and Mechanical Engineering Tracks of 3rd Nirma University International Conference on Engineering (NUiCONE2012). doi:https://doi.org/10.1016/j.proeng.2013.01.088.
- [55] E. Babu, G. Reddy, Effect of working fluid and filling ratio on performance of a closed loop pulsating heat pipe, Journal of Engineering Science and Technology 11 (2016) 872–880.
- [56] X. M. Zhang, Experimental study of a pulsating heat pipe using fc-72, ethanol, and water as working fluids, Experimental Heat Transfer 17 (1) (2004) 47–67. doi: 10.1080/08916150490246546.

- [57] N. Kammuang-lue, P. Sakulchangsatjatai, P. Terdtoon, Effect of working fluids and internal diameters on thermal performance of vertical and horizontal closed-loop pulsating heat pipes with multiple heat sources, Thermal Science 20 (2014) 141–141. doi:10.2298/TSCI140904141K.
- [58] D. Y. Han, X. Sun, Z. H. Gan, R. Y. Luo, J. M. Pfotenhauer, B. Jiao, Numerical investigation on pulsating heat pipes with nitrogen or hydrogen, IOP Conference Series: Materials Science and Engineering 278 (1) (2017) 012056. doi:10.1088/1757-899X/278/1/012056.
 URL https://dx.doi.org/10.1088/1757-899X/278/1/012056
- [59] E. W. Lemmon, I. H. Bell, M. L. Huber, M. O. McLinden, NIST Standard Reference Database 23: Reference Fluid Thermodynamic and Transport Properties-REFPROP, Version 10.0, National Institute of Standards and Technology (2018). doi:https://doi.org/10.18434/T4/1502528.
- [60] P. Charoensawan, P. Terdtoon, Thermal performance of horizontal closed-loop oscillating heat pipes, Applied Thermal Engineering 28 (5) (2008) 460–466. doi: https://doi.org/10.1016/j.applthermaleng.2007.05.007.
- [61] N. Kammuang-lue, P. Sakulchangsatjatai, P. Terdtoon, D. J. Mook, Correlation to predict the maximum heat flux of a vertical closed-loop pulsating heat pipe, Heat Transfer Engineering 30 (2009) 961 972.
- [62] H. Y. Noh, S. J. Kim, Numerical simulation of pulsating heat pipes: Parametric investigation and thermal optimization, Energy Conversion and Management 203 (2020) 112237.
- [63] J. Y. Kim, H. Cho, S. Y. Jung, Improvements in performance and durability through surface modification of aluminum micro-pulsating heat pipe using water as working fluid, International Journal of Heat and Mass Transfer 214 (2023) 124445. doi: https://doi.org/10.1016/j.ijheatmasstransfer.2023.124445.
- [64] L. Pagliarini, L. Cattani, M. Mameli, S. Filippeschi, F. Bozzoli, Heat transfer delay method for the fluid velocity evaluation in a multi-turn pulsating heat pipe, International Journal of Thermofluids 17 (2023) 100278. doi:https://doi.org/ 10.1016/j.ijft.2022.100278.
- [65] W.-W. Wang, T. Liu, J.-Z. Guo, B. Li, H.-L. Zhang, Y. Cai, F.-Y. Zhao, D. Liu, Experimental investigation on the thermal performance of high-concentrated photovoltaic module utilizing the thermal sink of a novel fan-shaped plate pulsating heat pipe, Applied Energy 377 (2025) 124365. doi:https://doi.org/10.1016/j.apenergy.2024.124365.

- [66] L. Pietrasanta, G. Postorino, R. Perna, M. Mameli, S. Filippeschi, A pulsating heat pipe embedded radiator: Thermal-vacuum characterisation in the precryogenic temperature range for space applications, Thermal Science and Engineering Progress 19 (2020) 100622. doi:https://doi.org/10.1016/j.tsep.2020.100622.
- [67] M. Opalski, C. Czajkowski, P. Błasiak, A. I. Nowak, J. Ishimoto, S. Pietrowicz, Comprehensive numerical modeling analysis and experimental validation of a multiturn pulsating heat pipe, International Communications in Heat and Mass Transfer 159 (2024) 107990. doi:https://doi.org/10.1016/j.icheatmasstransfer. 2024.107990.
- [68] K. R. Sagar, A. Desai, H. Naik, H. B. Mehta, Experimental investigations on two-turn cryogenic pulsating heat pipe with cylindrical shell-type condenser, Applied Thermal Engineering 196 (2021) 117240. doi:https://doi.org/10.1016/ j.applthermaleng.2021.117240.
- [69] C. Czajkowski, A. I. Nowak, A. Ochman, S. Pietrowicz, Flower shaped oscillating heat pipe at the thermosyphon condition: Performance at different rotational speeds, filling ratios, and heat supplies, Applied Thermal Engineering 212 (2022) 118540. doi:https://doi.org/10.1016/j.applthermaleng.2022.118540.
- [70] F. Jiang, N. Qian, M. Bernagozzi, M. Marengo, B. Zhao, J. Zhang, Y. Fu, Thermal performance prediction of radial-rotating oscillating heat pipe by a novel fusion model: A case study of application in grinding, Case Studies in Thermal Engineering 60 (2024) 104731. doi:https://doi.org/10.1016/j.csite.2024.104731.
- [71] J. Qu, H. Wu, P. Cheng, Start-up, heat transfer and flow characteristics of silicon-based micro pulsating heat pipes, International Journal of Heat and Mass Transfer 55 (21) (2012) 6109-6120. doi:https://doi.org/10.1016/j.ijheatmasstransfer.2012.06.024.
- [72] X. Liu, Q. Sun, C. Zhang, L. Wu, High-speed visual analysis of fluid flow and heat transfer in oscillating heat pipes with different diameters, Applied Sciences 6 (11) (2016). doi:10.3390/app6110321.
- [73] P.-S. Cheng, S.-C. Wong, Detailed visualization experiments on the start-up process and stable operation of pulsating heat pipes: Effects of internal diameter, International Journal of Heat and Fluid Flow 106 (2024) 109325. doi:https://doi.org/10.1016/j.ijheatfluidflow.2024.109325.

- [74] J. Gu, M. Kawaji, R. Futamata, Effects of gravity on the performance of pulsating heat pipes, Journal of Thermophysics and Heat Transfer 18 (2004) 370–378.

 URL https://api.semanticscholar.org/CorpusID:122961069
- [75] J. Gu, M. Kawaji, R. Futamata, Microgravity performance of micro pulsating heat pipes, Microgravity - Science and Technology 16 (2005) 181–185. URL https://api.semanticscholar.org/CorpusID:120368664
- [76] Z. Xue, W. Qu, Experimental study on effect of inclination angles to ammonia pulsating heat pipe, Chinese Journal of Aeronautics 27 (5) (2014) 1122–1127. doi: https://doi.org/10.1016/j.cja.2014.08.004.
- [77] H. Yang, S. Khandekar, M. Groll, Operational limit of closed loop pulsating heat pipes, Applied Thermal Engineering 28 (1) (2008) 49–59. doi:https://doi.org/10.1016/j.applthermaleng.2007.01.033.
- [78] X. Liu, L. Xu, C. Wang, X. Han, Experimental study on thermo-hydrodynamic characteristics in a micro oscillating heat pipe, Experimental Thermal and Fluid Science 109 (2019) 109871. doi:https://doi.org/10.1016/j.expthermflusci. 2019.109871.
- [79] G. Xiahou, S. Zhang, R. Ma, J. Zhang, Y. He, Influence of inclination angle on heat transfer performance of heat pipe radiator with an array of pulsating condensers, Applied Thermal Engineering 191 (2021) 116847. doi:https://doi.org/10.1016/j.applthermaleng.2021.116847.
- [80] Y. Xu, Y. Xue, S. Tang, D. Zhang, W. Cai, Experimental investigation on thermal characteristics and performance enhancement of pulsating heat pipe with ultra-maximum hydraulic diameter, Applied Thermal Engineering 267 (2025) 125702. doi:https://doi.org/10.1016/j.applthermaleng.2025.125702.
- [81] B. Lyu, D. Xu, W. Wang, J. Xin, Y. Shi, Z. Fang, C. Huang, R. Huang, L. Li, Experimental investigation of a serial-parallel configuration helium pulsating heat pipe, Cryogenics 131 (2023) 103668. doi:https://doi.org/10.1016/j.cryogenics. 2023.103668.
- [82] N. Iwata, H. Ogawa, Y. Miyazaki, Experimental study of temperature controllable oscillating heat pipe in space thermal environment, in: Conference: 40th International Conference on Environmental Systems, 2010. doi:10.2514/6.2010-6058.
- [83] M. Ando, A. Okamoto, K. Tanaka, M. Maeda, H. Sugita, T. Daimaru, H. Nagai, On-orbit demonstration of oscillating heat pipe with check valves for space application, Applied Thermal Engineering 130 (2018) 552–560. doi:https://doi.org/10.1016/j.applthermaleng.2017.11.032.

- [84] M. Marengo, M. Abela, L. Araneo, M. Bernagozzi, V. Ayel, Y. Bertin, L. Cattani, F. Bozzoli, A. Cecere, A. Georgoulas, S. Filippeschi, V. Nikolayev, M. Mameli, D. Mangini, M. B. H. Mantelli, N. Miche, L. Pietrasanta, C. Romestant, R. Savino, M. Slobodeniuk, B. Toth, S. Vincent-Bonnieu, Toward Low Earth Orbit (LEO) Applications: the Scientific Journey of the "Space Pulsating Heat Pipe" Experiments, in: 17th International Heat Transfer Conference, IHTC-17, Cape Town, South Africa, 2023, p. ID:228.
 - URL https://cea.hal.science/cea-04344898
- [85] M. Ando, A. Okamoto, H. Nagai, Effect of flow resistance of floating-type check valves on heat transfer characteristics of an oscillating heat pipe, ASME Journal of Heat and Mass Transfer 145 (10) (2023) 101004. doi:10.1115/1.4062783. URL https://doi.org/10.1115/1.4062783
- [86] C. Jung, S. J. Kim, Investigation into the effects of passive check valves on the thermal performance of pulsating heat pipes, International Journal of Heat and Mass Transfer 204 (2023) 123850. doi:https://doi.org/10.1016/j.ijheatmasstransfer.2023.123850.
- [87] Y. S. M. B. Shafii, S. Arabnejad, H. Jamshidi, Experimental investigation of pulsating heat pipes and a proposed correlation, Heat Transfer Engineering 31 (10) (2010) 854–861. doi:10.1080/01457630903547636.
- [88] P. A. Kew, K. Cornwell, Correlations for the prediction of boiling heat transfer in small-diameter channels, Applied Thermal Engineering 17 (8) (1997) 705–715. doi:https://doi.org/10.1016/S1359-4311(96)00071-3.
- [89] L. Yang, X. Song, Y. Xie, Effect of the dryout in tube bundles on the heat transfer performance of falling film evaporators, Procedia Engineering 205 (2017) 2176– 2183, 10th International Symposium on Heating, Ventilation and Air Conditioning, ISHVAC2017, 19-22 October 2017, Jinan, China. doi:https://doi.org/10.1016/ j.proeng.2017.10.041.
- [90] P. Sakulchangsatjatai, M. Siritan, R. Wanison, N. Kammuang-Lue, P. Terdtoon, Correlation to predict thermal characteristics of pulsating heat pipes with long evaporator section, Applied Thermal Engineering 254 (2024) 123868. doi:https://doi.org/10.1016/j.applthermaleng.2024.123868.
- [91] J. Qu, H. Wu, P. Cheng, X. Wang, Non-linear analyses of temperature oscillations in a closed-loop pulsating heat pipe, International Journal of Heat and Mass Transfer 52 (15) (2009) 3481-3489. doi:https://doi.org/10.1016/j.ijheatmasstransfer.2009.03.012.

- [92] N. Qian, X. Wang, Y. Fu, Z. Zhao, J. Xu, J. Chen, Predicting heat transfer of oscillating heat pipes for machining processes based on extreme gradient boosting algorithm, Applied Thermal Engineering 164 (2020) 114521. doi:https://doi.org/10.1016/j.applthermaleng.2019.114521.
- [93] F. K. Kholi, S. Park, J. S. Yang, M. Y. Ha, J. K. Min, A detailed review of pulsating heat pipe correlations and recent advances using artificial neural network for improved performance prediction, International Journal of Heat and Mass Transfer 207 (2023) 124010. doi:https://doi.org/10.1016/j.ijheatmasstransfer. 2023.124010.
- [94] N. Qian, M. Marengo, F. Jiang, X. Chen, Y. Fu, J. Xu, Pulsating heat pipes filled with acetone and water under radial rotation conditions: Heat transfer performance and semi-empirical correlation, International Communications in Heat and Mass Transfer 150 (2024) 107172. doi:https://doi.org/10.1016/j.icheatmasstransfer.2023.107172.
- [95] D. Grunau, S. Chen, K. Egger, A lattice boltzmann model for multi-phase fluid flows, Phys. Fluids A 5 (03 1993). doi:10.1063/1.858769.
- [96] S. Osher, J. A. Sethian, Fronts propagating with curvature-dependent speed: Algorithms based on hamilton-jacobi formulations, Journal of Computational Physics 79 (1) (1988) 12–49. doi:10.1016/0021-9991(88)90002-2.
- [97] T. B. Anderson, R. Jackson, Fluid mechanical description of fluidized beds. equations of motion, Industrial & Engineering Chemistry Fundamentals 6 (1967) 527–539.
 - URL https://api.semanticscholar.org/CorpusID:93338334
- [98] C. Hirt, B. Nichols, Volume of fluid (vof) method for the dynamics of free boundaries, Journal of Computational Physics 39 (1) (1981) 201–225. doi:https://doi.org/10.1016/0021-9991(81)90145-5.
- [99] Z. Guo, C. Shu, Lattice Boltzmann Method and Its Applications in Engineering, WORLD SCIENTIFIC, 2013. doi:10.1142/8806.
 URL https://www.worldscientific.com/doi/abs/10.1142/8806
- [100] Z. Qin, J. Zhu, W. Chen, C. Li, B. Wen, An effective pseudo-potential lattice boltzmann model with extremely large density ratio and adjustable surface tension, Physics of Fluids 34 (11) (2022) 113328. doi:10.1063/5.0123727.
- [101] R. Sharma, J. May, F. Alobaid, P. Ohlemüller, J. Ströhle, B. Epple, Euler-euler cfd simulation of the fuel reactor of a 1mwth chemical-looping pilot plant: Influence of

- the drag models and specularity coefficient, Fuel 200 (2017) 435–446. doi:https://doi.org/10.1016/j.fuel.2017.03.076.
- [102] E. Butaye, A. Toutant, S. Mer, Euler-euler multi-scale simulations of internal boiling flow with conjugated heat transfer, Applied Mechanics 4 (1) (2023) 191–209. doi:10.3390/applmech4010011.
- [103] M. Rafique, P. Chen, M. Duduković, Computational modeling of gas-liquid flow in bubble columns, Reviews in Chemical Engineering 20 (01 2004). doi:10.1515/ REVCE.2004.20.3-4.225.
- [104] A. Faghri, Y. Zhang, Fundamentals of Multiphase Heat Transfer and Flow, Springer, 2020. doi:10.1007/978-3-030-22137-9.
- [105] M. Sussman, E. G. Puckett, A coupled level set and volume-of-fluid method for computing 3d and axisymmetric incompressible two-phase flows, Journal of Computational Physics 162 (2) (2000) 301–337. doi:https://doi.org/10.1006/jcph. 2000.6537.
- [106] M. J. Martinez, R. C. Givler, Computational model of miniature pulsating heat pipes, Tech. rep., Sandia National Lab. (SNL-NM), Albuquerque, NM (United States) (01 2013). doi:10.2172/1177083. URL https://www.osti.gov/biblio/1177083
- [107] D. Gerlach, G. Tomar, G. Biswas, F. Durst, Comparison of volume-of-fluid methods for surface tension-dominant two-phase flows, International Journal of Heat and Mass Transfer 49 (3) (2006) 740–754. doi:https://doi.org/10.1016/j.ijheatmasstransfer.2005.07.045.
- [108] A. Albadawi, On the assessment of numerical interface capturing methods for two fluid flow applications, Ph.D. thesis, Dublin City University, phD thesis, supervised by Yan Delauré (November 2014). URL http://doras.dcu.ie/20019/
- [109] H. Hertz, On the evaporation of liquids, especially mercury, in vacuo, Annalen der Physik (Leipzig) 17 (1882) 177.
- [110] M. Knudsen, Maximum rate of vaporization of mercury, Annalen der Physik (Leipzig) 47 (1915) 69.
- [111] R. W. Schrage, A Theoretical Study of Interface Mass Transfer, Columbia University Press, New York, 1953.

- [112] W. H. Lee, A pressure iteration scheme for two-phase modeling, Technical Report LA-UR 79-975, Los Alamos Scientific Laboratory, Los Alamos, New Mexico (1979).
- [113] I. Tanasawa, Advances in Condensation Heat Transfer, Vol. 21 of Advances in Heat Transfer, Elsevier, 1991, pp. 55–139. doi:10.1016/S0065-2717(08)70334-4.
- [114] B. A. Nichita, J. R. Thome, A level set method and a heat transfer model implemented into fluent for modeling of microscale two-phase flows, in: AVT-178 Specialists' Meeting on System Level Thermal Management for Enhanced Platform Efficiency, Bucharest, Romania, 2010.
- [115] J. Wang, H. Ma, Q. Zhu, Effects of the evaporator and condenser length on the performance of pulsating heat pipes, Applied Thermal Engineering 91 (2015) 1018–1025. doi:10.1016/j.applthermaleng.2015.08.106.
- [116] J. Wang, H. Ma, Q. Zhu, Y. Dong, K. Yue, Numerical and experimental investigation of pulsating heat pipes with corrugated configuration, Applied Thermal Engineering 102 (2016) 158–166. doi:10.1016/j.applthermaleng.2016.03.163.
- [117] J. Wang, X. Bai, The features of clphp with partial horizontal structure, Applied Thermal Engineering 133 (2018) 682–689. doi:10.1016/j.applthermaleng.2018.01.058.
- [118] J. Wang, J. Xie, X. Liu, Investigation on the performance of closed-loop pulsating heat pipe with surfactant, Applied Thermal Engineering 160 (2019) 113998. doi: https://doi.org/10.1016/j.applthermaleng.2019.113998.
- [119] J. Wang, J. Xie, X. Liu, Investigation of wettability on performance of pulsating heat pipe, International Journal of Heat and Mass Transfer 150 (2020) 119354. doi:https://doi.org/10.1016/j.ijheatmasstransfer.2020.119354.
- [120] N. Saha, P. Das, P. Sharma, Influence of process variables on the hydrodynamics and performance of a single loop pulsating heat pipe, International Journal of Heat and Mass Transfer 74 (2014) 238–250. doi:https://doi.org/10.1016/j.ijheatmasstransfer.2014.02.067.
- [121] S. Pouryoussefi, Y. Zhang, Nonlinear analysis of chaotic flow in a three-dimensional closed-loop pulsating heat pipe, Journal of Heat Transfer 138 (12) (2016) 122003. doi:https://doi.org/10.1115/1.4034065.
- [122] S. Pouryoussefi, Y. Zhang, Numerical investigation of chaotic flow in a 2d closed-loop pulsating heat pipe, Applied Thermal Engineering 98 (2016) 617–627. doi: https://doi.org/10.1016/j.applthermaleng.2015.12.097.

- [123] S. Pouryoussefi, Y. Zhang, Analysis of chaotic flow in a 2d multi-turn closed-loop pulsating heat pipe, Applied Thermal Engineering 126 (2017) 1069–1076. doi: 10.1016/j.applthermaleng.2017.01.097.
- [124] D.-T. Vo, H.-T. Kim, J. Ko, K.-H. Bang, An experiment and three-dimensional numerical simulation of pulsating heat pipes, International Journal of Heat and Mass Transfer 150 (2020) 119317. doi:10.1016/j.ijheatmasstransfer.2020. 119317.
- [125] Q. Li, Y. Wang, C. Lian, H. Li, X. He, Effect of micro encapsulated phase change material on the anti-dry-out ability of pulsating heat pipes, Applied Thermal Engineering 159 (2019) 113854. doi:10.1016/j.applthermaleng.2019.113854.
- [126] Q. Li, C. Wang, Y. Wang, Z. Wang, H. Li, C. Lian, Study on the effect of the adiabatic section parameters on the performance of pulsating heat pipes, Applied Thermal Engineering 180 (2020) 115813. doi:10.1016/j.applthermaleng.2020. 115813.
- [127] F. Xie, X. Li, P. Qian, Z. Huang, M. Liu, Effects of geometry and multisource heat input on flow and heat transfer in single closed-loop pulsating heat pipe, Applied Thermal Engineering 168 (2020) 114856. doi:https://doi.org/10.1016/j.applthermaleng.2019.114856.
- [128] P. Błasiak, M. Opalski, P. Parmar, C. Czajkowski, S. Pietrowicz, The thermal—flow processes and flow pattern in a pulsating heat pipe—numerical modelling and experimental validation, Energies 14 (18) (2021). doi:10.3390/en14185952.
- [129] Z. Xu, Y. Zhang, B. Li, J. Huang, Modeling the phase change process for a two-phase closed thermosyphon by considering transient mass transfer time relaxation parameter, International Journal of Heat and Mass Transfer 101 (2016) 614–619. doi:10.1016/j.ijheatmasstransfer.2016.05.075.
- [130] K. Kafeel, A. Turan, Axi-symmetric simulation of a two phase vertical thermosyphon using eulerian two-fluid methodology, Heat Mass Transfer 49 (2013) 1089—-1099. doi:10.1007/s00231-013-1155-6.
- [131] W.-W. Wang, Y.-J. Song, C.-Y. Zhang, H.-L. Zhang, Y. Cai, F.-Y. Zhao, J.-H. Guo, Fluid hydrodynamics and thermal transports in nanofluids pulsating heat pipes applied for building energy exploitations: Experimental investigations and full numerical simulations, Energy and Buildings 290 (2023) 113067. doi:https://doi.org/10.1016/j.enbuild.2023.113067.

- [132] J. Choi, Y. Zhang, Numerical simulation of oscillatory flow and heat transfer in pulsating heat pipes with multi-turns using openfoam, Numerical Heat Transfer, Part A: Applications, An International Journal of Computation and Methodology 77 (8) (2020) 761–781. doi:10.1080/10407782.2020.1717202.
- [133] A. Mucci, F. K. Kholi, J. Chetwynd-Chatwin, M. Y. Ha, J. K. Min, Numerical investigation of flow instability and heat transfer characteristics inside pulsating heat pipes with different numbers of turns, International Journal of Heat and Mass Transfer 169 (2021) 120934. doi:https://doi.org/10.1016/j.ijheatmasstransfer.2021.120934.
- [134] R. Dreiling, V. Dubois, S. Zimmermann, T. Nguyen-Xuan, P. Schreivogel, F. di Mare, Numerical investigation of slug flow in pulsating heat pipes using an interface capturing approach, International Journal of Heat and Mass Transfer 199 (2022) 123459. doi:https://doi.org/10.1016/j.ijheatmasstransfer.2022.123459.
- [135] M. Mameli, Pulsating heat pipes. numerical modelling and experimental assessment, Ph.D. thesis, Università degli studi di Bergamo (2012).
- [136] D. Zhang, L. Wang, B. Xu, Q. Li, S. Wang, Z. An, Experimental and simulation study on flow heat transfer characteristics of flat pulsating heat pipe with wide and narrow interphase channels, Applied Thermal Engineering 245 (2024) 122806. doi:https://doi.org/10.1016/j.applthermaleng.2024.122806.
- [137] K. Sagar, H. Naik, H. Mehta, Cfd analysis of cryogenic pulsating heat pipe with near critical diameter under varying gravity conditions, Theoretical Foundations of Chemical Engineering 54 (2020) 64–76. doi:10.1134/S0040579520010212.
- [138] A. Singh, I. Ghosh, Numerical Investigations of a Single Loop Pulsating Heat Pipe for Cryogenic Applications, ASME Journal of Heat and Mass Transfer (2024) 1– 30doi:https://doi.org/10.1115/1.4066971.
- [139] D. Yang, Z. Bu, B. Jiao, B. Wang, Z. Gan, Numerical study of heat transfer and fluid flow characteristics of a hydrogen pulsating heat pipe with medium filling ratio, Energies 17 (2024) 2697. doi:10.3390/en17112697.
- [140] Z. Bu, S. Li, S. Zhao, B. Jiao, R. Su, B. Wang, Z. Gan, Thermo-hydrodynamic analysis of a nitrogen flat-plate pulsating heat pipe using cfd modeling and visualization experiments, International Communications in Heat and Mass Transfer 159 (2024) 108029. doi:https://doi.org/10.1016/j.icheatmasstransfer.2024.108029.
- [141] Y. Shi, D. Xu, J. Yan, R. Guo, B. Lyu, C. Huang, L. Li, Visualized investigation of a nitrogen pulsating heat pipe, Cryogenics 138 (2024) 103783. doi:https://doi.org/10.1016/j.cryogenics.2024.103783.

- [142] B. Singh, M. Atrey, Numerical investigation of a nitrogen based cryogenic pulsating heat pipe, Cryogenics 115 (2021) 103246. doi:https://doi.org/10.1016/j.cryogenics.2021.103246.
- [143] M. Opalski, T. Dixit, B. Baudouy, P. Błasiak, J. Ishimoto, S. Pietrowicz, Modeling of cryogenic pulsating heat pipe using cfd techniques, Cryogenics 147 (2025) 104061. doi:https://doi.org/10.1016/j.cryogenics.2025.104061.
- [144] H. Scheufler, J. Roenby, Twophaseflow: An openfoam based framework for development of two phase flow solvers (2021). arXiv:2103.00870.
 URL https://arxiv.org/abs/2103.00870
- [145] F. Municchi, I. E. Mellas, O. K. Matar, M. Magnini, Conjugate heat transfer effects on flow boiling in microchannels, International Journal of Heat and Mass Transfer 195 (2022) 123166. doi:10.1016/j.ijheatmasstransfer.2022.123166.
- [146] F. Municchi, C. N. Markides, O. K. Matar, M. Magnini, Computational study of bubble, thin-film dynamics and heat transfer during flow boiling in non-circular microchannels, Applied Thermal Engineering 238 (2024) 122039. doi:10.1016/j. applthermaleng.2023.122039.
- [147] R. Marek, J. Straub, The origin of thermocapillary convection in subcooled nucleate pool boiling, International Journal of Heat and Mass Transfer 44 (3) (2001) 619–632. doi:https://doi.org/10.1016/S0017-9310(00)00124-1.
- [148] M. L. Huber, E. W. Lemmon, I. H. Bell, M. O. McLinden, The nist refprop database for highly accurate properties of industrially important fluids, Industrial & Engineering Chemistry Research 61 (42) (2022) 15449–15472. doi:10.1021/acs.iecr. 2c01427.
- [149] C. Galusinski, P. Vigneaux, On stability condition for bifluid flows with surface tension: application to microfluidics, Journal of Computational Physics, Elsevier 227 (2008) 6140–6164. doi:10.1016/j.jcp.2008.02.023.
- [150] S. S. Deshpande, L. Anumolu, M. F. Trujillo, Evaluating the performance of the two-phase flow solver interfoam, Computational Science & Discovery 5 (1) (2013) 014016. doi:10.1088/1749-4699/5/1/014016.
- [151] Y. Sato, B. Niceno, Nucleate pool boiling simulations using the interface tracking method: Boiling regime from discrete bubble to vapor mushroom region, International Journal of Heat and Mass Transfer 105 (2017) 505–524. doi:https://doi.org/10.1016/j.ijheatmasstransfer.2016.10.018.

- [152] O. Elsayed, R. Kirsch, S. Osterroth, S. Antonyuk, An improved scheme for the interface reconstruction and curvature approximation for flow simulations of two immiscible fluids, International Journal of Multiphase Flow 144 (2021) 103805. doi:https://doi.org/10.1016/j.ijmultiphaseflow.2021.103805.
- [153] S. Hardt, F. Wondra, Evaporation model for interfacial flows based on a continuum-field representation of the source terms, Journal of Computational Physics 227 (11) (2008) 5871–5895. doi:https://doi.org/10.1016/j.jcp.2008.02.020.
- [154] C. Kunkelmann, P. Stephan, Cfd simulation of boiling flows using the volume-of-fluid method within openfoam, Numerical Heat Transfer, Part A: Applications 56 (8) (2009) 631–646.
- [155] OpenFOAM Foundation, OpenFOAM v2106 User Guide (2021). URL https://www.openfoam.com/documentation/user-guide
- [156] H. Yee, R. Warming, A. Harten, Implicit total variation diminishing (tvd) schemes for steady-state calculations, Journal of Computational Physics 57 (3) (1985) 327–360. doi:https://doi.org/10.1016/0021-9991(85)90183-4.
- [157] M. Berger, M. Aftosmis, Analysis of slope limiters on irregular grids, 43rd AIAA Aerospace Sciences Meeting and Exhibit - Meeting Papers (02 2005). doi:10. 2514/6.2005-490.
- [158] H. Jasak, Error analysis and estimation for the finite volume method with applications to fluid flows, Phd thesis, Imperial College London (1996).
- [159] R. Barrett, M. Berry, T. Chan, J. Demmel, J. Donato, J. Dongarra, V. Eijkhout, R. Pozo, C. Romine, H. van der Vorst, Templates for the Solution of Linear Systems: Building Blocks for Iterative Methods, SIAM, Philadelphia, 1994.
- [160] D. C. Wilcox, Turbulence Modeling for CFD, 3rd Edition, DCW Industries, La Canada, California, 2006.
- [161] R. Perna, M. Abela, M. Mameli, A. Mariotti, L. Pietrasanta, M. Marengo, S. Filippeschi, Flow characterization of a pulsating heat pipe through the wavelet analysis of pressure signals, Applied Thermal Engineering 171 (2020) 115128. doi:https://doi.org/10.1016/j.applthermaleng.2020.115128.
- [162] D. Zhang, Z. He, J. Guan, S. Tang, C. Shen, Heat transfer and flow visualization of pulsating heat pipe with silica nanofluid: An experimental study, International Journal of Heat and Mass Transfer 183 (2022) 122100. doi:https://doi.org/10.1016/j.ijheatmasstransfer.2021.122100.

- [163] B. E. Launder, D. B. Spalding, The numerical computation of turbulent flows, Computer Methods in Applied Mechanics and Engineering 3 (2) (1974) 269–289. doi:10.1016/0045-7825(74)90029-2.
- [164] H. K. Versteeg, W. Malalasekera, An Introduction to Computational Fluid Dynamics: The Finite Volume Method, 2nd Edition, Pearson Education, Harlow, England, 2007.
- [165] J. Stefan, Über einige probleme der theorie der wärmeleitung, Sitzungber., Wien, Akad. Mat. Natur 98 (1889) 473–484.
- [166] L. Scriven, On the dynamics of phase growth: Le scriven, chem. engng. sci. 10: 1–13, 1959, Chemical Engineering Science 50 (24) (1995) 3905.
- [167] A. Georgoulas, M. Andredaki, M. Marengo, An enhanced vof method coupled with heat transfer and phase change to characterise bubble detachment in saturated pool boiling, Energies 10 (2017) 272. doi:10.3390/en10030272.
- [168] M. Magnini, Cfd modeling of two-phase boiling flows in the slug flow regime with an interface capturing technique, Ph.D. thesis, University of Bologna (2012).
- [169] H. Gifford, A. W. McMahon, Low temperature apparatus, u.S. misc (May 1964). URL https://miscs.google.com/misc/US3133467A
- [170] Sumitomo Heavy Industries, Ltd., Cryocooler Product Catalogue, SHI Cryogenics Group (June 2023).
 URL https://shicryogenics.com/wp-content/uploads/2023/08/Cryocooler_Product_Catalogue_English_A4_06.23.pdf
- [171] JCGM, Evaluation of measurement data guide to the expression of uncertainty in measurement, JCGM 100:2008, Joint Committee for Guides in Metrology, available at: https://www.bipm.org/documents/20126/2071204/JCGM_100_2008_E.pdf (2008).
- [172] Interalloy AG, Capillary tubes and custom alloy components, Online, https://www.interalloy.ch (2024).
- [173] Lake Shore Cryotronics, CTC100 Cryogenic Temperature Controller User Manual, Westerville, Ohio, USA, firmware version 4.59 (Sep. 2023).

 URL https://www.lakeshore.com
- [174] S. Khandekar, Thermo-hydrodynamics of closed loop pulsating heat pipes, Ph.D. thesis, Institut für Kernenergetik und Energiesysteme, Universität Stuttgart (2004).

- [175] Y. Shi, J. Yan, Y. Zhou, D. Xu, L. Li, Experimental study on nitrogen pulsating heat pipes with different heat transmission distances and configurations, Cryogenics 141 (2024) 103898. doi:https://doi.org/10.1016/j.cryogenics.2024.103898.
- [176] K. Fumoto, K. Ishii, Flat plate pulsating heat pipe operating at ultra-low filling ratio, Applied Thermal Engineering 228 (2023) 120468. doi:https://doi.org/10.1016/j.applthermaleng.2023.120468.
- [177] P. Wang, D. Xu, P. Jia, Y. Shi, R. Guo, L. Li, Multi-parametrical investigation on the start-up of nitrogen pulsating heat pipes for space applications, Cryogenics 150 (2025) 104115. doi:https://doi.org/10.1016/j.cryogenics.2025.104115.
- [178] N. Zuber, Nucleate boiling. the region of isolated bubbles and the similarity with natural convection, International Journal of Heat and Mass Transfer 6 (1) (1963) 53–78. doi:https://doi.org/10.1016/0017-9310(63)90029-2.
- [179] V. S. Nikolayev, Oscillatory instability of the gas-liquid meniscus in a capillary under the imposed temperature difference, International Journal of Heat and Mass Transfer 64 (2013) 313-321. doi:https://doi.org/10.1016/j.ijheatmasstransfer.2013.04.043.
- [180] J. R. Thome, Boiling in microchannels: a review of experiment and theory, International Journal of Heat and Fluid Flow 25 (2) (2004) 128–139, selected Papers from the 5th ECI International Conference on Boiling Heat Transfer. doi:https://doi.org/10.1016/j.ijheatfluidflow.2003.11.005.
- [181] G. F. Hewitt, N. S. Hall-Taylor, Annular Two-Phase Flow, Pergamon Press, Oxford, 1970. doi:https://doi.org/10.1016/C2009-0-06773-7.
- [182] R. Zhang, M. Ding, Thin liquid film method for analyzing gas-liquid annular flow in nonstraight pipe components, Nuclear Engineering and Design 423 (2024) 113199. doi:https://doi.org/10.1016/j.nucengdes.2024.113199.
- [183] S. Li, H. Pei, D. Liu, Y. Shen, X. Tao, Z. Gan, Visualization study on the flow characteristics of a nitrogen pulsating heat pipe, International Communications in Heat and Mass Transfer 143 (2023) 106722. doi:https://doi.org/10.1016/j.icheatmasstransfer.2023.106722.
- [184] S. Li, Z. Bu, T. Fang, Y. Wang, Y. Shen, X. Tao, B. Jiao, Z. Gan, Experimental study on the thermo-hydrodynamic characteristics of a nitrogen pulsating heat pipe, International Communications in Heat and Mass Transfer 146 (2023) 106920. doi:https://doi.org/10.1016/j.icheatmasstransfer.2023.106920.

- [185] M. A. B. Higuera, Study of meter-scale horizontal cryogenic pulsating heat pipes, Phd thesis, Université Paris-Saclay, Saclay, France, nNT: 2019SACLS224 (2019). URL https://www.theses.fr/2019SACLS224
- [186] M. Barba, R. Bruce, F. Bouchet, A. Bonelli, B. Baudouy, Effects of filling ratio of a long cryogenic pulsating heat pipe, Applied Thermal Engineering 194 (2021) 117072. doi:https://doi.org/10.1016/j.applthermaleng.2021.117072.
- [187] Y. Song, J. Xu, Chaotic behavior of pulsating heat pipes, International Journal of Heat and Mass Transfer 52 (13) (2009) 2932-2941. doi:https://doi.org/10.1016/j.ijheatmasstransfer.2009.02.030.
- [188] M. Mameli, G. Besagni, P. K. Bansal, C. N. Markides, Innovations in pulsating heat pipes: From origins to future perspectives, Applied Thermal Engineering 203 (2022) 117921. doi:https://doi.org/10.1016/j.applthermaleng.2021.117921.
- [189] K. Natsume, T. Mito, N. Yanagi, H. Tamura, T. Tamada, K. Shikimachi, N. Hirano, S. Nagaya, Development of cryogenic oscillating heat pipe as a new device for indirect/conduction cooled superconducting magnets, IEEE Transactions on Applied Superconductivity 22 (3) (2012). doi:10.1109/TASC.2012.2185029.
- [190] T. Harirchian, S. V. Garimella, A comprehensive flow regime map for microchannel flow boiling with quantitative transition criteria, International Journal of Heat and Mass Transfer 53 (13) (2010) 2694–2702. doi:https://doi.org/10.1016/j.ijheatmasstransfer.2010.02.039.
- [191] K. Triplett, S. Ghiaasiaan, S. Abdel-Khalik, D. Sadowski, Gas-liquid two-phase flow in microchannels part i: two-phase flow patterns, International Journal of Multiphase Flow 25 (3) (1999) 377–394. doi:https://doi.org/10.1016/S0301-9322(98)00054-8.
- [192] N. Iwata, F. Bozzoli, Investigation of operational limit of a pulsating heat pipe by estimating local heat transfer, Experimental and Computational Multiphase Flow 6 (03 2024). doi:10.1007/s42757-023-0179-5.
- [193] A. Tessier-Poirier, T. Monin, S. Monfray, F. Formosa, L. Fréchette, E. Leveille, How evaporation and condensation lead to self-oscillations in the single-branch pulsating heat pipe, Physical Review Fluids 4 (10 2019). doi:10.1103/PhysRevFluids.4. 103901.
- [194] A. Faghri, Heat pipes: Review, opportunities and challenges, Frontiers in Heat Pipes 5 (04 2014). doi:10.5098/fhp.5.1.

- [195] Y. Okagaki, T. Yonomoto, M. Ishigaki, Y. Hirose, Numerical study on an interface compression method for the volume of fluid approach, Fluids 6 (2) (2021). doi: 10.3390/fluids6020080.
- [196] H. Xian, W. Xu, Y. Zhang, X. Du, Y. Yang, Thermal characteristics and flow patterns of oscillating heat pipe with pulse heating, International Journal of Heat and Mass Transfer 79 (2014) 332–341. doi:https://doi.org/10.1016/j.ijheatmasstransfer.2014.08.002.
- [197] M. Opalski, T. Dixit, B. Baudouy, T. Duraziński, P. Błasiak, S. Pietrowicz, Modeling of thermal performance and flow structures in nitrogen pulsating heat pipes with multiple configurations, Applied Thermal Engineering 280 (2025) 128371. doi:https://doi.org/10.1016/j.applthermaleng.2025.128371.
- [198] G. Gennari, R. Jefferson-Loveday, S. J. Pickering, A phase-change model for diffusion-driven mass transfer problems in incompressible two-phase flows, Chemical Engineering Science 259 (2022) 117791. doi:https://doi.org/10.1016/j. ces.2022.117791.
- [199] D. Corporation, Design and development of a prototype static cryogenic heat transfer system, Contractor Report NASA-CR-121939, NASA Goddard Space Flight Center (1971).
 URL https://ntrs.nasa.gov/api/citations/19710026879/downloads/ 19710026879.pdf
- [200] X. Zhang, V. S. Nikolayev, Physics and modeling of liquid films in pulsating heat pipes, Phys. Rev. Fluids 8 (2023) 084002. doi:10.1103/PhysRevFluids.8.084002.
- [201] K. Krippner, T. Daimaru, M. Kaviany, A simple analytic, slug-deposited liquid film thermal resistance/conductance model for oscillating heat pipe, International Journal of Heat and Mass Transfer 235 (2024) 126139. doi:https://doi.org/10.1016/j.ijheatmasstransfer.2024.126139.
- [202] G. Giustini, Hydrodynamic analysis of liquid microlayer formation in nucleate boiling of water, International Journal of Multiphase Flow 172 (2024) 104718. doi:https://doi.org/10.1016/j.ijmultiphaseflow.2023.104718.
- [203] D. Pal, I. Perez-Raya, Simulating film boiling with sharp interface and direct calculation of mass transfer to investigate the hydrodynamic and thermal transport phenomena near the interface, International Journal of Heat and Mass Transfer 235 (2024) 126179. doi:https://doi.org/10.1016/j.ijheatmasstransfer. 2024.126179.

- [204] L. Pagliarini, N. Iwata, F. Bozzoli, Pulsating heat pipes: Critical review on different experimental techniques, Experimental Thermal and Fluid Science 148 (2023) 110980. doi:https://doi.org/10.1016/j.expthermflusci.2023.110980.
- [205] F. P. Bretherton, The motion of long bubbles in tubes, Journal of Fluid Mechanics 10 (2) (1961) 166–188. doi:10.1017/S0022112061000160.
- [206] X. Han, X. Wang, H. Zheng, X. Xu, G. Chen, Review of the development of pulsating heat pipe for heat dissipation, Renewable and Sustainable Energy Reviews 59 (2016) 692–709. doi:https://doi.org/10.1016/j.rser.2015.12.350.
- [207] J. Qu, Q. Wang, Q. Sun, Lower limit of internal diameter for oscillating heat pipes: A theoretical model, International Journal of Thermal Sciences 110 (2016) 174–185. doi:https://doi.org/10.1016/j.ijthermalsci.2016.07.002.
- [208] O. V. Voinov, Hydrodynamics of wetting, Fluid Dynamics 11 (5) (1976) 714–721. doi:10.1007/BF01012963.
- [209] V. Nikolayev, M. Marengo, Pulsating Heat Pipes: Basics of Functioning and Modeling, Vol. 1: Modeling of Two-Phase Flows and Heat Transfer, World Scientific Publishing Company, 2018, p. 63–139. doi:10.1142/9789813234406\ 0002.
- [210] J. Snoeijer, B. Andreotti, Moving contact lines: Scales, regimes, and dynamical transitions, Annual Review of Fluid Mechanics 45 (2013) 269–292. doi:10.1146/annurev-fluid-011212-140734.
- [211] M. Magnini, J. Thome, A cfd study of the parameters influencing heat transfer in microchannel slug flow boiling, International Journal of Thermal Sciences 110 (2016) 119–136. doi:https://doi.org/10.1016/j.ijthermalsci.2016.06.032.
- [212] L. A. M. Rocha, J. M. Miranda, J. B. L. M. Campos, Wide range simulation study of taylor bubbles in circular milli and microchannels, Micromachines 8 (5) (2017). doi:10.3390/mi8050154.
- [213] M. F. Silva, J. B. L. M. Campos, J. M. Miranda, J. D. P. Araújo, Numerical study of single taylor bubble movement through a microchannel using different cfd packages, Processes 8 (11) (2020). doi:10.3390/pr8111418.
- [214] G. Liang, I. Mudawar, Review of pool boiling enhancement by surface modification, International Journal of Heat and Mass Transfer 128 (2019) 892–933. doi:https://doi.org/10.1016/j.ijheatmasstransfer.2018.09.026.
- [215] W. Linkai, G. Bois, V. Pandey, V. Nikolayev, Effect of contact line evaporation during nucleate boiling studied by multiscale numerical simulation, Applied Thermal Engineering 275 (2025) 126690. doi:10.1016/j.applthermaleng.2025.126690.

- [216] M. Moezzi, M. Sajjadi, S. H. Hejazi, Thermally driven marangoni effects on the spreading dynamics of droplets, International Journal of Multiphase Flow 159 (2023) 104335. doi:https://doi.org/10.1016/j.ijmultiphaseflow.2022. 104335.
- [217] J. Roenby, H. Bredmose, H. Jasak, A computational method for sharp interface advection, Royal Society Open Science 3 (11) (2016) 160405. doi:10.1098/rsos. 160405.